

Rare-Earth Doping in Nanostructured Inorganic Materials

Bingzhu Zheng, Jingyue Fan, Bing Chen, Xian Qin, Juan Wang,* Feng Wang,* Renren Deng,* and Xiaogang Liu*

Cite This: <https://doi.org/10.1021/acs.chemrev.1c00644>

Read Online

ACCESS |

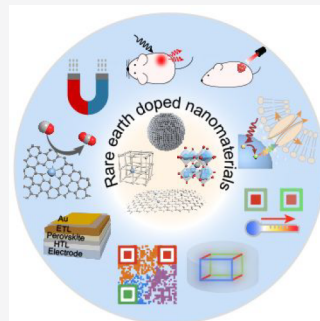


Metrics & More



Article Recommendations

ABSTRACT: Impurity doping is a promising method to impart new properties to various materials. Due to their unique optical, magnetic, and electrical properties, rare-earth ions have been extensively explored as active dopants in inorganic crystal lattices since the 18th century. Rare-earth doping can alter the crystallographic phase, morphology, and size, leading to tunable optical responses of doped nanomaterials. Moreover, rare-earth doping can control the ultimate electronic and catalytic performance of doped nanomaterials in a tunable and scalable manner, enabling significant improvements in energy harvesting and conversion. A better understanding of the critical role of rare-earth doping is a prerequisite for the development of an extensive repertoire of functional nanomaterials for practical applications. In this review, we highlight recent advances in rare-earth doping in inorganic nanomaterials and the associated applications in many fields. This review covers the key criteria for rare-earth doping, including basic electronic structures, lattice environments, and doping strategies, as well as fundamental design principles that enhance the electrical, optical, catalytic, and magnetic properties of the material. We also discuss future research directions and challenges in controlling rare-earth doping for new applications.



CONTENTS

1. Introduction	B	4.1. Bioapplications	Y
2. Characteristics of Rare-Earth Elements	C	4.1.1. Bioimaging	Y
2.1. Electronic Structures and Basic Properties	C	4.1.2. Photothermal Therapy	AC
2.2. Characteristic Properties	C	4.1.3. Photodynamic Therapy and Photocemo- therapy	AD
2.2.1. Sc^{3+} , Y^{3+} , La^{3+} , and Lu^{3+}	C	4.1.4. Drug Delivery	AF
2.2.2. Ce^{3+} and Ce^{4+}	C	4.1.5. Optogenetics	AF
2.2.3. Pr^{3+}	D	4.2. Optical Sensing	AG
2.2.4. Nd^{3+}	F	4.2.1. Temperature Sensing	AH
2.2.5. Pm^{3+} and Sm^{3+}	F	4.2.2. Pressure Sensing	AJ
2.2.6. Eu^{3+} and Eu^{2+}	F	4.2.3. pH Sensing	AM
2.2.7. Gd^{3+}	F	4.2.4. Molecular Detection	AM
2.2.8. Tb^{3+}	G	4.3. Catalysis	AN
2.2.9. Dy^{3+}	G	4.3.1. Ceria-Based Catalysis	AN
2.2.10. Ho^{3+} , Er^{3+} , and Tm^{3+}	G	4.3.2. Photocatalysis	AO
2.2.11. Yb^{3+}	H	4.3.3. Single-Atom Catalyst	AQ
3. Doping Strategies	H	4.4. Lighting and Displays	AQ
3.1. Principal Factors in Doping	H	4.4.1. Nanoparticle Lasing	AQ
3.1.1. Ionic Size	H	4.4.2. Displays	AQ
3.1.2. Valency	I	4.4.3. Information Storage	AR
3.1.3. Reactivity	I	4.4.4. Anticounterfeiting	AS
3.1.4. Doping in Nanostructures	I	4.5. Photodetectors	AT
3.2. Doping in Various Substrates	J		
3.2.1. Rare-Earth Compounds	J		
3.2.2. Alkaline-Earth Compounds	P		
3.2.3. Semiconductor Quantum Dots	R		
3.2.4. Metal–Organic Frameworks	U		
3.2.5. 2D Layered Nanomaterials	W		
4. Technological Applications	Y		

Received: July 21, 2021

4.5.1. Microwaves	AT
4.5.2. Infrared	AU
4.5.3. Ultraviolet–Visible	AU
4.5.4. X-rays and γ -rays	AU
4.6. Photovoltaics	AV
4.7. Nanomagnets and Magneto-optic Devices	AX
5. Summary and Outlook	AY
Author Information	AY
Corresponding Authors	AY
Authors	AZ
Notes	AZ
Biographies	AZ
Acknowledgments	AZ
Abbreviations and List of Acronyms	AZ
References	BA

1. INTRODUCTION

Impurity doping is a technique that can be used to modify material properties. Doping rare-earth ions into nanomaterials can modulate the crystallographic phases, morphologies, sizes, and electronic configurations of inorganic nanomaterials. In addition, doping with rare-earth ions can impart rich optical, electrical, magnetic, and catalytic properties, making doped nanomaterials attractive for many technological applications. The rare-earths are a group of 17 elements composed of scandium, yttrium, and 15 lanthanides (ranging from lanthanum to lutetium) that have many similar physical/chemical properties and often coincide in geological deposits. The history of rare-earth elements can be traced back to 1751, when the first rare-earth mineral was discovered in Sweden.¹ However, this mineral was initially mistaken for a calcium iron silicate. In 1787, another similar mineral was found by Carl Arrhenius at Ytterby in Sweden. In 1794, a Finnish chemist Johan Gadolin first isolated a new oxide from the Ytterby ore and named it ytterbia. Later in 1842, Mosander further separated the ytterbia oxide into yttria, erbia, and terbia, although later studies revealed that these three oxides were also rare-earth mixtures. Because rare-earth elements have similar chemical properties, isolation of all 17 rare-earths was not accomplished until 1908–1909, when a repetitive fractional crystallization technique was implemented. In 1914, Henry Moseley used X-ray spectroscopy to confirm all rare-earth elements, except for radioactive element promethium (Pm). Promethium was not characterized until 1945 at Clinton Laboratories, now Oak Ridge National Laboratory.

Although all rare-earth elements have been identified, the isolation and large-scale production of individual rare-earth compounds remained a challenge. Prior to World War II, only europium could be extracted on an industrial scale as EuSO_4 because europium ions are more easily reduced from trivalent to divalent than other rare-earths.² As a result of rapid scientific and technological development during the war, the first effective rare-earth isolation technique was developed based on ion exchange chromatography. This technique exploited the differences in stability between different rare-earth citrate chelates. In about 1954, another effective method, liquid–liquid extraction, was developed and successfully used in commercial production.³

The mass production of rare-earth compounds provides a solid foundation for their practical application in modern society. For instance, Eu^{3+} -doped yttrium vanadate became the first red phosphor, enabling the development of color

television screens. Since the 1950s, rare-earths have facilitated the advancement in the materials industry in many categories, including phosphors, magnets, metallurgy, catalysts, and glass. In many cases, rare-earths are used as additives or dopants in materials. The beauty of using rare-earths is that even in small quantities, they can significantly alter material properties. As a result, rare-earths have been recognized as “vitamins” of modern industry, and the development of rare-earth-doped materials has become one of the most essential components of technological progress.

Since the 1990s, when the study of nanoscience and nanotechnology entered the fast lane, the potential of rare-earth-doped nanomaterials for diverse applications has been gradually recognized. Initial work was mainly devoted to rare-earth-doped luminescent nanoparticles, inspired by the invention of colloidal quantum dots and other inorganic nanophosphors.^{4–7} The initial motivation was to reduce the size of conventional rare-earth-doped luminophores to make them dispersible in colloidal suspension for new applications, such as biolabeling and biosensing. One of the first attempts was reported in 1990 by Beverloo et al., who used 0.1–0.3 μm $\text{Y}_2\text{O}_2\text{S}:\text{Eu}$ microparticles as luminescent biolabels for immunoassays.⁸ The advantages of using rare-earth-doped luminescent materials include high photochemical stability, narrow emission bandwidth, and long luminescence lifetime, as well as the ability to achieve UV/visible emission upon near-infrared (NIR) excitation through a unique process known as upconversion.^{9–11} However, at the outset, these nanophosphors could only be prepared by crushing bulk phosphors through ball milling. This limited the minimum size of the phosphors to a few hundred nanometers, which prevented wider use of these materials.

It was not until the beginning of the 21st century that new synthetic approaches to producing high-quality crystals less than 100 nm in size spurred growth in this area. Thanks to recent advances in new synthetic strategies such as thermal decomposition, coprecipitation, and hydro(solvo)thermal processing, monodisperse rare-earth-doped nanomaterials with easily controllable size, morphology, and crystallinity can now be prepared reliably with rationally designed structures.^{12–15} Rare-earth-based nanomaterials have become a highly interdisciplinary field of research that straddles the boundary between materials science and solid-state chemistry (Figure 1). Because of their intriguing material properties, a wide range of applications have been developed, from healthcare (bioimaging and therapy) to environmental protection (catalytic treatment of pollutants and clean energy development) to breakthrough science and technology (optical communications and three-dimensional displays).

Despite an enormous number of publications on the subject, previous reviews focused mainly on the optical properties of these nanomaterials. In particular, much attention has been paid to the applications of rare-earth-doped nanocrystals. There is a lack of a comprehensive review that summarizes the developments of rare-earth-doped nanomaterials in a broader context. To this end, we hope that this review can be a useful guide to the recent development of rare-earth-doped inorganic nanomaterials. This review highlights the unique properties of rare-earth-doped materials at the nanoscale and their applications. The review is organized as follows. In section 2, we provide an overview of the basic properties of all rare-earths and briefly summarize the utility of each rare-earth for various applications. In section 3, we discuss strategies for doping

various nanosized substrates with rare-earth ions. We highlight recent advances in the strategic design of these nanomaterials (core–shell structures, spatially confined doping strategies, and organic–inorganic hybrid nanocomposites) to generate multifunctional materials with remarkable properties. In section 4, we review a wide range of applications that arise from material properties. We conclude with a brief overview of the prospects for the future development of rare-earth-doped inorganic nanomaterials.

2. CHARACTERISTICS OF RARE-EARTH ELEMENTS

The properties of doped materials depend largely on the doping elements. Because of their chemical similarity, different rare-earth ions can be incorporated simultaneously into a substrate with controlled concentrations and compositions. In material design, it is essential to choose the right doping formula to achieve the desired property. This section summarizes the general properties and most common applications of individual rare-earth dopants in nanomaterial hosts.

2.1. Electronic Structures and Basic Properties

By definition, rare-earths are the 15 lanthanides (La–Lu) and 2 group IIIB elements (Sc and Y), all of which have a similar ground state electronic configuration. For Sc and Y, the ground state configurations are $[\text{Ar}]3d^14s^2$ and $[\text{Kr}]4d^15s^2$, respectively. For the 15 lanthanides, La, Ce, Gd, and Lu share the $[\text{Xe}]4f^{0-1}5d^16s^2$ configurations, while other lanthanides share $[\text{Xe}]4f^06s^2$ configurations (Figure 2). Although electrons in the 5s and 5p orbitals of lanthanides have lower energy than those in the 4f orbitals, the 5s and 5p orbitals are more dispersive than the 4f orbitals. Consequently, fully filled $5s^2$ and $5p^6$ closed subshells are still outside the 4f orbitals, resulting in weak shielding of the 4f electrons.⁴⁷

In similar $4f^{0-1}5d^16s^2$ or $4f^06s^2$ outer electron configurations, the two electrons on the 6s orbital and one electron on the 5d or 4f orbital of rare-earths are relatively easy to lose. As a result, rare-earths exhibit stable trivalent ionic states. Trivalent lanthanide ions from La^{3+} to Lu^{3+} have the same configuration $[\text{Xe}]4f^{0-1}$. This causes the ionic radius to decrease systematically across the lanthanide series, which is known as lanthanide contraction.⁴⁸ Therefore, the ionic radii fall into a small range across the lanthanide series, with the radius of Ho^{3+} being close to that of Y^{3+} (Table 1). This makes it possible to incorporate different rare-earth ions into a single-phase material, which is essential for the development of crystalline multicomponent materials with exciting and diverse properties.

Although the trivalent rare-earths are the most stable oxidation states, Ce^{4+} ($[\text{Xe}]4f^0$), Eu^{2+} ($[\text{Xe}]4f^7$), Tb^{4+} ($[\text{Xe}]4f^7$), and Yb^{2+} ($[\text{Xe}]4f^{14}$) can also be found in certain compounds. This is because the electronic states involving empty ($4f^0$), half-filled ($4f^7$), and fully filled ($4f^{14}$) 4f orbitals are more stable than other configurations. In addition, the thermochemical properties of lanthanide elements also contribute significantly to the stability of their oxidation states.

Another attractive property of rare-earths in doped nanomaterials is their narrow-band optical absorption and emission originating from intra-atomic 4f–4f electron transitions. Due to the shielding effect of the 5s and 5p electrons, the 4f electrons are not directly involved in bonding with surrounding molecules. Therefore, emission energies from 4f–4f transitions are rather stable to environmental changes and exhibit quasi-atomic behavior. When a lanthanide ion is doped into a crystal

lattice, its 4f–4f transition energies retain almost the same as those of the corresponding free ion.

Moreover, most trivalent lanthanides are paramagnetic in the ground state, with the exception of La^{3+} and Lu^{3+} , which are diamagnetic. This discrepancy is attributed to unpaired 4f electrons. The shielding effect also makes the magnetic moments of lanthanides independent of the coordination environment. Rare-earths generally exhibit strong spin–orbital coupling and weak ligand-field splitting, leading to zero-field splitting and magnetic anisotropy in given crystals. This characteristic property has driven the development of rare-earth permanent magnetic materials. In nanomaterials research, rare-earth-doped paramagnetic nanomaterials have been widely used as contrast agents in magnetic resonance imaging (MRI).

2.2. Characteristic Properties

In this section, we summarize the characteristic properties (optical, magnetic, and catalytic) of each rare-earth ion and their main applications in doped nanomaterials.

2.2.1. Sc^{3+} , Y^{3+} , La^{3+} , and Lu^{3+} . Sc^{3+} and Y^{3+} have no 4f electrons, while the 4f orbitals of La^{3+} and Lu^{3+} are either empty or completely filled. These ions have no unpaired 4f electrons and are all diamagnetic and free of 4f–4f transition-based photoluminescence. Therefore, these four ions are ideal host cations for lanthanide doping to achieve luminescence and magnetic modulation. Indeed, many nanomaterials are based on these cations, such as rare-earth fluorides, alkaline rare-earth oxyhalides, rare-earth oxysulfides, rare-earth oxides, and alkaline rare-earth fluorides.

Rare-earth ions can also act as Lewis acids and catalyze organic synthesis. For instance, La^{3+} ions have been doped into nanostructured catalysts to enhance their photocatalytic activity toward organic pollutants by reducing bandgaps, trapping photoinduced electrons, and suppressing electron–hole recombination.⁵¹ In addition, nanometric La–Na–Cu–O perovskite-like complex oxides have been shown to be effective in removing soot and simultaneously accelerating NO_x reactions.⁵² Lu^{3+} ions have been doped into CeO_2 to oxidize soot and incorporated into Ni to produce carbon nanotubes.^{53,54}

2.2.2. Ce^{3+} and Ce^{4+} . Owing to its allowed 4f–5d transition, Ce^{3+} can be efficiently excited by UV photons.⁵⁵ The luminescence of Ce^{3+} ions usually shows a tunable emission band in the UV-blue region, depending on the crystal structures of host materials.⁵⁶ Compared to the parity forbidden 4f–4f transitions of other rare-earth ions, the 4f–5d transition of Ce^{3+} is markedly efficient with a much larger absorption coefficient. Therefore, Ce^{3+} ions in many doped luminophores serve as sensitizers to absorb UV excitation and transfer energy to other lanthanide ions (Pr^{3+} , Sm^{3+} , Dy^{3+} , Eu^{3+} , and Tb^{3+}) for luminescence.^{57–59} Ce^{4+} ions have no emission or absorption in the visible spectral region.

The experimental magnetic moment of Ce^{3+} is $2.4 \mu_B$, whereas Ce^{4+} has no magnetic moment. However, Ce^{3+} and Ce^{4+} can coexist in some hosts. Unlike bulk paramagnetic CeO_2 materials, nanostructured CeO_2 materials are ferromagnetic.^{60,61} Ferromagnetism is thought to arise from exchange interactions between unpaired 4f electrons of Ce^{3+} and oxygen vacancies on nanostructured surfaces.^{62,63} Ce^{3+} -doped BiFeO_3 nanoparticles exhibit weak ferromagnetism at room temperature, while undoped BiFeO_3 counterparts display antiferromagnetic behavior.⁶⁴ In Ce^{3+} -doped BiFeO_3 nanoparticles, the

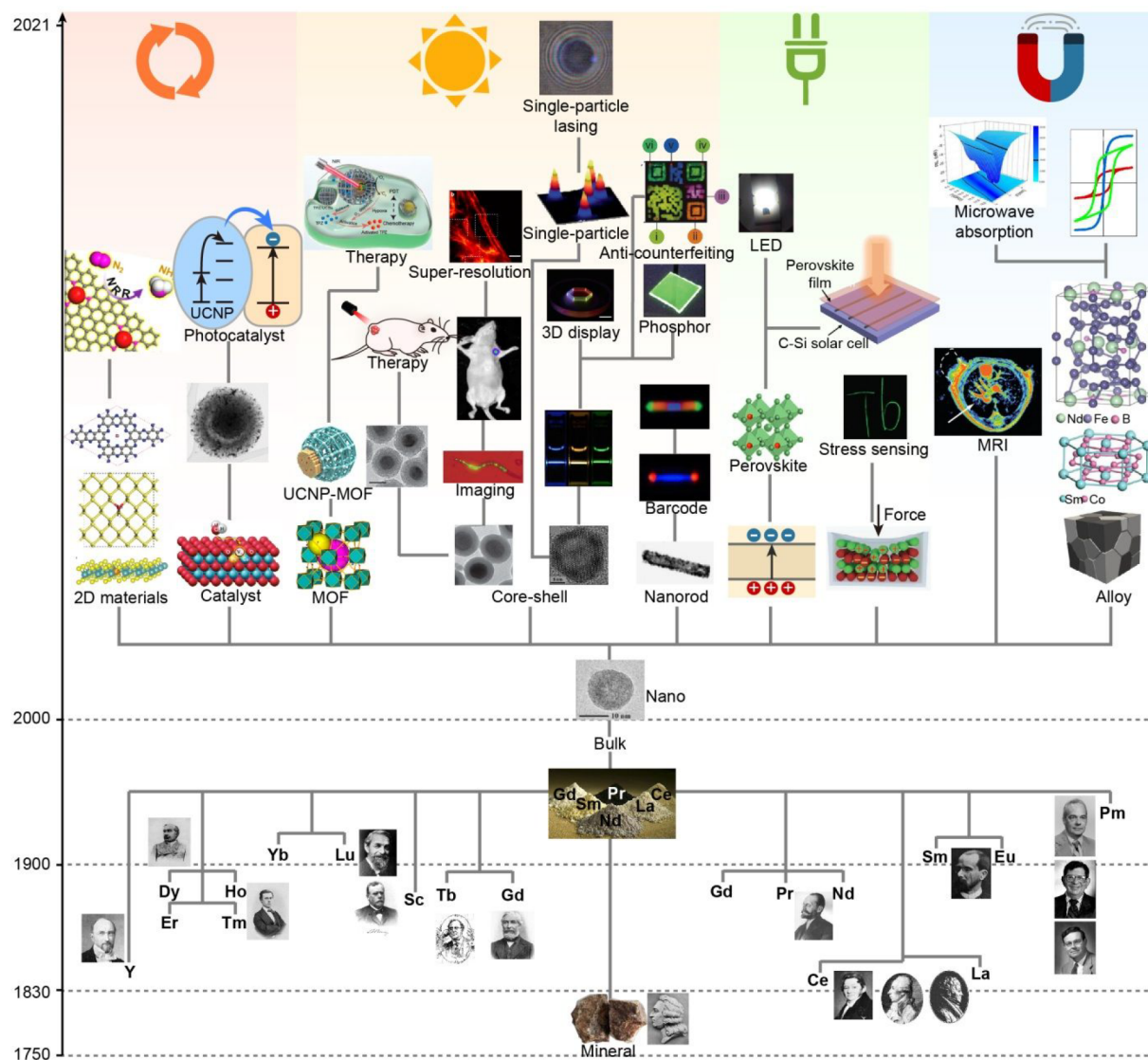


Figure 1. Development and application of rare-earth-based nanomaterials. The history of rare-earths begins with the discovery of rare-earth minerals and their separation and purification by scientists. Since the advent of nanotechnology, doping of rare-earths in nanomaterials of different morphology and composition has enabled many technological applications (Adapted with permission from refs 16–46. Copyright 2006, 2012, 2013, 2017, 2018, 2019, 2020 American Chemical Society; Copyright 2016 the Owner Societies; Copyright 2006, 2016 The Royal Society of Chemistry; Copyright 2019 AIP Publishing; Copyright 2015, 2016, 2017, 2018 WILEY-VCH Verlag GmbH & Co. KGaA, Weinheim; Copyright 2020 American Association for the Advancement of Science; Copyright 2012, 2015, 2017, 2018, 2020 Nature Publishing Group; Copyright 2012 The Royal Society of Chemistry; Copyright 2005 Elsevier Ltd.; Copyright 2021 the Partner Organisations; Copyright 2018 IOP Publishing Ltd.).

collapse of the cycloidal spin structure of BiFeO_3 caused by doping and the size effect leading to increased uncompensated surface spins contribute to the ferromagnetism. In Ce^{3+} -doped SnO_2 nanofibers, the room-temperature ferromagnetism is believed to arise from strong coupling between the f electrons of Ce^{3+} and the s electrons of the SnO_2 host.⁶⁵

Among rare-earth-doped materials, Ce-based compounds, especially CeO_2 , are widely used for catalysis. Nanostructured CeO_2 has been used as a primary or auxiliary catalyst in various catalytic oxidations, such as soot combustion,^{53,66,67} three-way catalysis,⁶⁸ conversion of CO ,^{69,70} steam reforming of methane,⁷¹ selective oxidation of organic molecules,^{72,73} and water–gas shift reaction.⁷⁴ Ce undergoes rapid redox/oxidation cycling between Ce^{3+} and Ce^{4+} states. This enables the local storage/release of oxygen in Ce-based compounds and influences catalytic reactions through synergistic effects.⁷⁴ In bioapplications, CeO_2 nanoparticles have also been used as

nanoenzymes that mimic the function of biological enzymes, such as superoxide dismutase and catalase.⁷⁵

2.2.3. Pr^{3+} . Pr^{3+} has the ground state $^3\text{H}_4$ and the main excited states $^3\text{P}_0$, $^1\text{D}_2$, and $^1\text{G}_4$. Pr^{3+} typically shows blue emission at ~ 483 nm ($^3\text{P}_0 \rightarrow ^3\text{H}_4$ transition),⁷⁶ orange emission at ~ 610 nm ($^3\text{P}_0 \rightarrow ^3\text{H}_6$ and $^1\text{D}_2 \rightarrow ^3\text{H}_4$ transitions),^{77,78} and red emission at ~ 643 nm ($^3\text{P}_0 \rightarrow ^3\text{F}_2$ transition).⁷⁹ Although the $^3\text{P}_0 \rightarrow ^3\text{H}_5$ and $^3\text{P}_0 \rightarrow ^3\text{F}_{3,4}$ transitions can also be detected with emission at ~ 540 and ~ 725 nm, respectively, their emission intensities are usually relatively weak.^{80,81}

In addition to the radiative relaxation paths, Pr^{3+} in combination with Yb^{3+} can be used for downconversion emission, also called quantum cutting, because the $^1\text{G}_4$ intermediate state of Pr^{3+} and the $^2\text{F}_{5/2}$ state of Yb^{3+} are almost at the same level. During the process, a high-energy photon from the $^3\text{P}_0 \rightarrow ^3\text{H}_4$ transition of Pr^{3+} splits into two

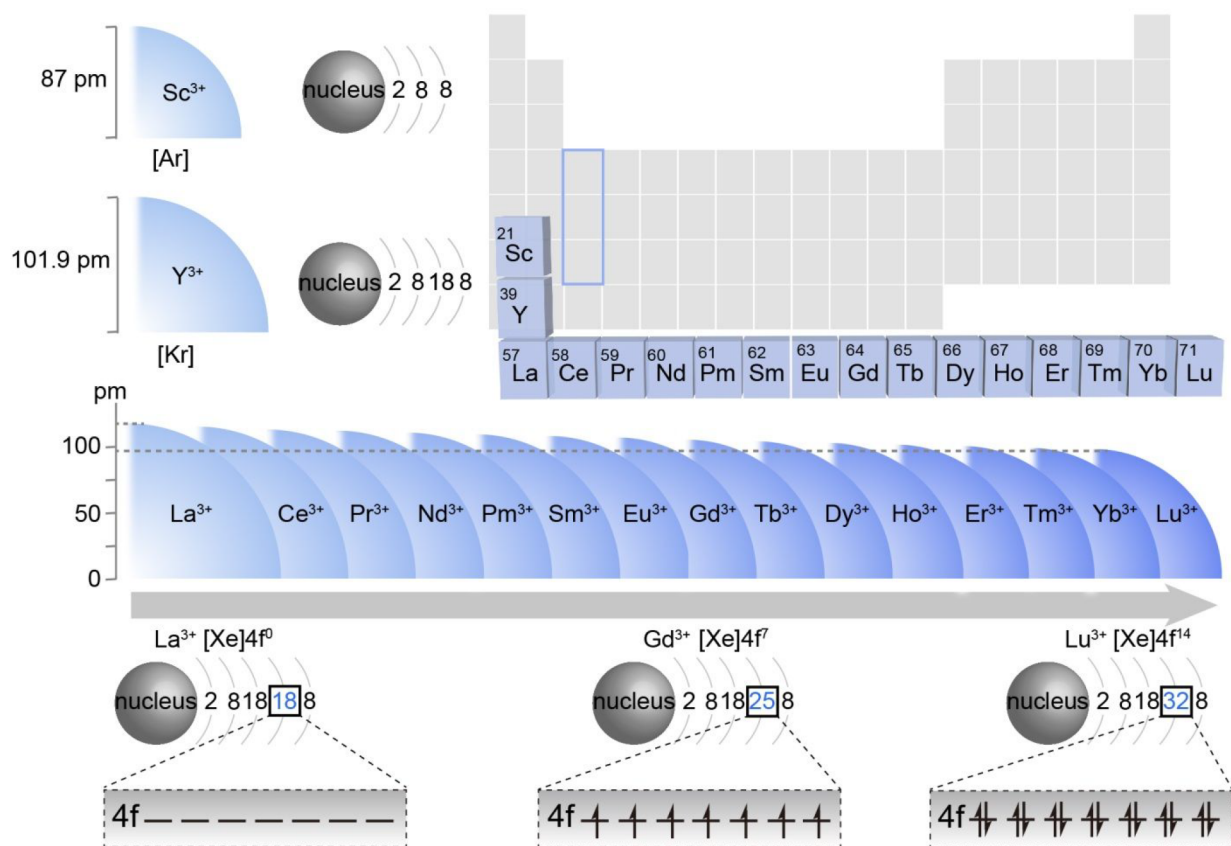


Figure 2. Ionic radius and valence configuration of rare-earths. From La³⁺ to Lu³⁺, the number of electrons on the 4f orbitals increases with increasing atomic number. The electron configurations of La³⁺, Gd³⁺, and Lu³⁺ show empty, half-filled, and completely filled 4f orbitals, respectively.

Table 1. Basic Properties of Rare-Earth Elements

atomic number (Z)	name	symbol	ground state configuration	metal radius (pm) ^a	electron configuration of RE ³⁺	ionic radius (pm) ^b +2		application	
21	scandium	Sc	[Ar]3d ¹ 4s ²	164.06	[Ar]	/	87	/	host material; catalysis; magnet; ferroelectricity; piezoelectricity
39	yttrium	Y	[Kr]4d ¹ 5s ²	180.12	[Kr]	/	101.9	/	host material; catalysis; ferrimagnetism; superconductivity; ferroelectricity
57	lanthanum	La	[Xe]5d ¹ 6s ²	187.91	[Xe]4f ⁰	/	116	/	host material; catalysis; superconductivity
58	cerium	Ce	[Xe]4f ¹ 5d ¹ 6s ²	182.47	[Xe]4f ¹	/	114.3	97	sensitizer; catalysis; ferromagnetism
59	praseodymium	Pr	[Xe]4f ³ 6s ²	182.79	[Xe]4f ³	/	112.6	96	quantum cutting; ferromagnetism; catalysis
60	neodymium	Nd	[Xe]4f ⁴ 6s ²	182.14	[Xe]4f ⁴	129	110.9	/	sensitizer; down conversion
61	promethium	Pm	[Xe]4f ⁵ 6s ²	181.10	[Xe]4f ⁵	/	109.3	/	radioactive
62	samarium	Sm	[Xe]4f ⁶ 6s ²	180.41	[Xe]4f ⁶	127	107.9	/	magnetism; catalysis
63	europium	Eu	[Xe]4f ⁷ 6s ²	204.18	[Xe]4f ⁷	125	106.6	/	downconversion; catalysis; phosphor
64	gadolinium	Gd	[Xe]4f ⁷ 5d ¹ 6s ²	180.13	[Xe]4f ⁷	/	105.3	/	host material; MR imaging; magnetism; catalysis
65	terbium	Tb	[Xe]4f ⁹ 6s ²	178.33	[Xe]4f ⁹	/	104	88	upconversion; phosphor; ferromagnetism
66	dysprosium	Dy	[Xe]4f ¹⁰ 6s ²	177.40	[Xe]4f ¹⁰	119	102.7	/	MR imaging; ferromagnetism; catalysis
67	holmium	Ho	[Xe]4f ¹¹ 6s ²	176.61	[Xe]4f ¹¹	/	101.6	/	upconversion; MR imaging
68	erbium	Er	[Xe]4f ¹² 6s ²	175.66	[Xe]4f ¹²	/	100.4	/	upconversion; photocatalysis; MR imaging; NIR II imaging
69	thulium	Tm	[Xe]4f ¹³ 6s ²	174.62	[Xe]4f ¹³	/	99.4	/	upconversion; photocatalysis
70	ytterbium	Yb	[Xe]4f ¹⁴ 6s ²	193.92	[Xe]4f ¹⁴	114	98.5	/	sensitizer; MR imaging; NIR imaging
71	lutetium	Lu	[Xe]4f ¹⁴ 5d ¹ 6s ²	173.49	[Xe]4f ¹⁴	/	97.7	/	host material

^aWith a coordination number of 12. ^bWith a coordination number of 8.^{49,50}

low-energy photons from the ²F_{5/2} → ²F_{7/2} transition of Yb³⁺ by energy transfer, resulting in a photoluminescence quantum yield of 200%.^{82,83}

Pr³⁺ ion with a magnetic moment of 3.5 μ_B has been used to tune antiferromagnetic hosts, such as BiFeO₃, from magnetic

to ferromagnetic.^{84,85} Pr(OH)₃ nanowire bundles exhibit ferromagnetic behavior at room temperature.⁸⁶

Pr₆O₁₁ can enhance the catalyst performance for ethanol electrooxidation.⁸⁷ Pr³⁺ ions can be incorporated as aliovalent dopants in a CeO₂ host to introduce oxygen vacancies and thus improve the oxygen storage capacity and catalytic properties of the hosts.⁸⁸ Doping semiconductor hosts, such as TiO₂ and CdSe, with Pr³⁺ ions in can also enhance the photocatalytic activity of these semiconductors.^{89,90}

2.2.4. Nd³⁺. Upon energy absorption, Nd³⁺ ions in the ground state (⁴I_{9/2}) can be excited to the ²P_{1/2} and ⁴G_{7/2} states. Nd³⁺ typically emits at approximately 413 nm (²D_{5/2}, ²P_{1/2} → ⁴I_{9/2} transitions), 523 nm (⁴G_{7/2}, ²K_{13/2}, ⁴G_{9/2} → ⁴I_{9/2} transitions), 588 nm (²G_{7/2}, ²G_{5/2} → ⁴I_{9/2} transitions), 640 nm (²H_{11/2} → ⁴I_{9/2} transition), 661 nm (⁴F_{9/2} → ⁴I_{9/2} transition), 869–900 nm (⁴F_{3/2} → ⁴I_{9/2} transition), 1060 nm (⁴F_{3/2} → ⁴I_{11/2} transition), and 1330 nm (⁴F_{3/2} → ⁴I_{13/2} transition).^{91–93} Nd³⁺ is usually used for its efficient NIR emission at ~1060 nm when excited at 740 or 800 nm.⁹¹ Since both the excitation and emission are within the optical window (700–1100 nm), Nd³⁺-doped nanoparticles are ideal NIR nanophosphors for biological imaging.⁹⁴

In addition to downshifting emission, Nd³⁺ can be employed to upconvert luminescence. Given its relatively large absorption coefficient of the ⁴I_{9/2} → ⁴F_{5/2} transition, Nd³⁺ can serve as sensitizers in Yb³⁺/Er³⁺, Yb³⁺/Tm³⁺, or Yb³⁺/Ho³⁺-codoped upconversion systems under 800 nm excitation.^{31,93,95,96} With rationally designed core–shell structures, upconversion emission of Nd³⁺ can be achieved at ~382 nm (⁴D_{3/2} → ⁴I_{11/2} transition) and at ~413 nm (⁴D_{3/2} → ⁴I_{13/2} transition).⁹⁷

Nd–Fe–B-based compounds are among the most prominent rare-earth permanent magnets and have captured a large portion of the global market share.⁹⁸ Nanosized Nd–Fe–B compounds, such as Nd₂Fe₁₄B nanoparticles, have been prepared using a sol–gel method.⁹⁹ These magnetic nanoparticles have potential applications in ferrofluids, coolants, high-density information storage, and biomedicine.¹⁰⁰

Nd³⁺ ions have been doped into wide bandgap semiconductors, such as TiO₂,¹⁰¹ and ZnO,¹⁰² to make them available for visible-light photocatalysis.¹⁰³ In some cases, Nd³⁺ can be directly excited and acts as an electron sink to improve the catalytic performance by suppressing electron–hole recombination in photocatalysts.¹⁰⁴ Beyond photocatalysts, Nd³⁺ has been doped into nanostructured hosts to impart novel catalytic activities for various applications, including selective hydrogenation,¹⁰⁵ CO conversion,¹⁰⁶ and asymmetric nitroaldol reactions.^{107,108}

2.2.5. Pm³⁺ and Sm³⁺. Promethium is radioactive and can be used for applications such as radiotherapy, but current studies on Pm³⁺-related nanomaterials are rather limited. For this reason, we will focus only on Sm³⁺ in this subsection.

Sm³⁺ has the ground state ⁶H_{15/2} and a well-utilized excited state ⁴G_{5/2}. Typical emissions from excited Sm³⁺ are ⁴G_{5/2} → ⁶H_{5/2} at ~566 nm, ⁴G_{5/2} → ⁶H_{7/2} at ~602 nm, ⁴G_{5/2} → ⁶H_{9/2} at ~649 nm, and ⁴G_{5/2} → ⁶H_{11/2} at ~728 nm.^{109–111} Sm³⁺ is mainly used as a downshifting emitter for red/orange emission.

Due to the exchange interaction between the conduction electrons of transition metals and the local spin-polarized electrons of Sm,¹¹² a transition metal–Sm alloy, such as Co–Sm, is one of the best known permanent magnets at room temperature and is widely used for high-density magnetic recording and energy storage. In nanomaterials, Sm–Co

nanoparticles (e.g., Sm₂Co₁₇ and SmCo₅) exhibit size-dependent magnetic properties.¹¹³ Sm³⁺ ions have been used to enhance the magnetization of BiFeO₃ nanosubstrates.⁶¹

Sm³⁺ has been doped into nanostructured catalysts, such as manganese ferrite,¹¹⁴ zinc spinel ferrite,¹¹⁵ perovskite bismuth ferrite,¹¹⁶ and TiO₂,¹¹⁷ to enhance the photocatalytic activity toward organic pollutants by narrowing the bandgap, trapping photoinduced electrons, and suppressing the recombination of electrons and holes. Considering the UV-absorbing ability of Sm³⁺, several Sm compounds, such as Sm(OH)₃,¹¹⁸ can also serve as photocatalysts for photodegradation reactions.

2.2.6. Eu³⁺ and Eu²⁺. Eu³⁺ has a ground state of ⁷F₀ and excited states of ⁵D_J (J = 0–3). It is the most common dopant used to achieve red emission. Typical emission bands of Eu³⁺ are ⁵D₂ → ⁷F₃ at ~510 nm, ⁵D₁ → ⁷F₁ at ~536 nm, ⁵D₁ → ⁷F₂ at ~555 nm, ⁵D₁ → ⁷F₃ (⁵D₀ → ⁷F₀) at ~584 nm, ⁵D₀ → ⁷F₁ at ~591 nm, ⁵D₀ → ⁷F₂ at ~615 nm (most intense), ⁵D₀ → ⁷F₃ at ~645 nm, and ⁵D₀ → ⁷F₄ at ~696 nm.^{110,119,120}

Eu³⁺ is paramagnetic at room temperature. Although its ⁷F₀ ground state is diamagnetic, the experimental magnetic moment of Eu³⁺ at room temperature is around 3.4 μ_B, which is due to the close proximity of the ⁷F₁ and ⁷F₂ states. Doping of Eu³⁺ in nanosized barium hexaferrite enhances superexchange interactions and magnetocrystalline anisotropy, which increases the saturation magnetization and coercivity of the doped sample.¹²¹ Eu³⁺ ions have been doped in Bi₂WO₆, ZnO, MoO₃, YVO₄, Bi₂S₃, and TiO₂ to promote catalytic activity toward organic molecules.^{122–127}

Eu²⁺ ions are commonly used as inorganic luminophores for blue–green emission arising from the 4f⁶5d¹ → 4f⁷ transition.¹²⁸ The ionic radius of Eu²⁺ is around 17% larger than that of Eu³⁺, which makes difficult to incorporate a large amount of Eu²⁺ into many host materials that can accommodate trivalent RE³⁺ at high doping concentrations. Typical nanomaterials for Eu²⁺ include SrAl₂O₄, CaS, and Sc₂O₃.^{129–132} Another interesting property of Eu²⁺ is its persistent luminescence when codoped with other lanthanides, such as Dy³⁺, Ce³⁺, and Tm³⁺.^{133,134}

2.2.7. Gd³⁺. The energy levels of Gd³⁺ ions have been studied in great detail. By virtue of the large energy gap between the ⁸S_{7/2} ground state and the ⁶P_{7/2} first excited state (~32 000 cm⁻¹), direct excitation of Gd³⁺ ions to the ⁶P_{7/2} state can be achieved by UV irradiation at ~310 nm. Due to the relatively high energy of the ⁶P_{7/2} state, excited Gd³⁺ ions can serve as an energy reservoir to realize energy migration-mediated emission of other activators.¹³⁵ Typical emissions of excited Gd³⁺ ions include ⁶D_J → ⁸S_{7/2} (J = 1/2, 3/2, 5/2, 7/2) at 246 nm, ⁶D_{9/2} → ⁸S_{7/2} at 253 nm, ⁶I_J → ⁸S_{7/2} (J = 7/2–15/2) at ~270–281 nm, ⁶P_{5/2} → ⁸S_{7/2} at ~305 nm, ⁶P_{7/2} → ⁸S_{7/2} at ~311 nm (particularly intense).^{136,137} NaGdF₄ nanocrystals are excellent host materials for doping lanthanide emitters with emissions in the visible or NIR region. In some cases, Gd³⁺ can be used as a sensitizer to facilitate the emission of Eu³⁺, Tb³⁺, Dy³⁺, and Sm³⁺ ions through energy migration.¹³⁵

Gd³⁺ has a highly symmetric ground state with seven unpaired 4f electrons and the largest magnetic moment of any lanthanide. Accordingly, this ion is strongly paramagnetic. Gd³⁺-containing nanomaterials, such as NaGdF₄, Gd₂O₃, GdF₃ and GdPO₄, are the most efficient positive contrast agents (T₁), widely used in magnetic resonance imaging.^{138–142} Gd₂O₃ and Gd₂BaNiO₅ nanoparticles have also found potential applications in cryomagnetic refrigeration due to their magnetocaloric effect.^{62,143} KGdF₄ nanoparticles have

been reported to exhibit temperature-dependent magnetic properties: paramagnetic at 300 K and superparamagnetic at 2 K.¹⁴⁴

Gd₂O₃ nanorods show high catalytic activity for the conversion of CO even at a low temperature of 100 °C.¹⁴⁵ Gd³⁺ has also been doped into semiconducting nanomaterials, such as TiO₂ and CdSe, to enhance the photocatalytic capacity.^{146–148} Gd(OH)₃ nanorods can support Pd nanoparticles for hydrogenation or serve as main catalysts for Cr(VI) photoreduction in water.^{149,150} When Gd³⁺ or Gd₂O₃ are doped into ZSM-5 zeolite catalysts, the coking effect, which blocks active sites and deactivates the catalysts, is effectively suppressed, making the composite catalysts coke-compatible and having a long service life.^{151–153} Gd₂O₃ and Gd(OH)₃ nanorods exhibit peroxidase-like enzyme activity.¹⁵⁴ Gd₂O₃ nanoparticles have also been used as catalysts for the electrochemical reduction of CO₂ to CO.¹⁵⁵

2.2.8. Tb³⁺. Tb³⁺ is a highly efficient green emitter in rare-earth-doped luminophores. Energy transitions from the excited states ⁵D₃/⁵D₄ to the ground state ⁷F₆ are mainly investigated in Tb³⁺-doped phosphors. Typical emissions from excited Tb³⁺ are ⁵D₃ → ⁷F₆ at ~380 nm, ⁵D₃ → ⁷F₅ at ~414 nm, ⁵D₃ → ⁷F₄ at ~435 nm, ⁵D₄ → ⁷F₆ at ~486 nm, ⁵D₄ → ⁷F₅ at ~541 nm (most intense), ⁵D₄ → ⁷F₄ at ~587 nm, and ⁵D₄ → ⁷F₃ at ~622 nm.¹⁵⁶ Nanoparticles codoped with Ce³⁺/Tb³⁺ show a strong downward shift in the luminescence of Tb³⁺ under UV excitation.¹⁵⁷ Tb³⁺ can also be coupled with Yb³⁺ to generate upconversion emission through a Yb-assisted cooperative process under 980 nm excitation.^{156,158} Moreover, Tb³⁺/Yb³⁺-encoded systems are known to exhibit downconversion photoluminescence. When Tb³⁺ is excited with a high energy visible photon, two NIR photons from Yb³⁺ can be emitted by energy transfer from one Tb³⁺ ion to two Yb³⁺ ions.¹⁵⁹

Tb³⁺ is paramagnetic at room temperature and has a magnetic moment of 9.5 μ_B. Tb³⁺ has been frequently used to tune the magnetic behavior of nanomaterials. For example, Tb³⁺ can impart paramagnetic properties to nanostructured diamagnetic hosts, such as ZnS.¹⁶⁰ ZnO:Tb³⁺ nanorod bundles have been reported to exhibit superparamagnetism at room temperature and ferromagnetism at 5 K.¹⁶¹ ZnO:Tb³⁺ nanoparticles with an average size of less than 20 nm also possess ferromagnetism at room temperature.¹⁶² Compared to undoped nanoparticles, multiferroic BiFeO₃ nanoparticles doped with Tb³⁺ exhibit increased magnetic saturation.¹⁶³ Doping Nd₂Fe₁₄B with Tb³⁺ ions increases the coercivity due to the higher anisotropy field when Nd³⁺ is partially replaced by Tb³⁺.¹⁶⁴ It has been reported that Tb₂O₃ nanoparticles exhibit ferromagnetism at 5 K.¹⁶⁵

When Tb³⁺ is doped into a Pd-containing catalyst, it tends to lose electrons and reduce Pd ions to Pd metals, which improves the performance of Pd-based catalysts.¹⁶⁶ In ethanol electrooxidation, doping with Tb³⁺ can increase the adsorption of OH⁻, which enhances the catalytic activity of the Pb–Tb composite.¹⁶⁷ Furthermore, when doping Ca₂Ta₃O₁₀ nanocrystals, Tb³⁺ can stabilize the charge separation state, which benefits the catalytic activity of the main catalyst for hydrogen production from water.¹⁶⁸ Tb³⁺ ions have also been doped into semiconductors such as ZrO₂ to promote photocatalytic degradation of organic molecules.¹⁶⁹

2.2.9. Dy³⁺. Dy³⁺ with ground state ⁶H_{15/2} shows efficient emission due to transitions between I and F levels. There are two intense emissions of Dy³⁺: ⁴F_{9/2} → ⁶H_{15/2} at ~480 nm and ⁴F_{9/2} → ⁶H_{13/2} at ~570 nm.¹⁷⁰ There are also two less intense

emissions: ⁴F_{9/2} → ⁶H_{11/2} at ~673 nm and ⁴F_{9/2} → ⁶H_{9/2} at ~756 nm.^{171,172} Dy³⁺ has a high magnetic moment due to its unpaired 4f electrons. Dy³⁺-doped ZnO nanoparticles exhibit tunable ferromagnetism at room temperature, which depends on the concentration of Dy³⁺ dopants.¹⁷³ Many Dy³⁺-based nanoparticles, including DyF₃, NaDyF₄, and Dy₂O₃, have been employed as T₂ contrast agents for MRI.^{174–176}

Dy₂O₃ nanorods are efficient catalysts for the conversion of CO.¹⁴⁵ Dy³⁺ dopants facilitate the separation of electron and hole pairs in Bi₂MoO₆ or ZnO host materials and improve their photocatalytic performance.^{177–179} Dy₂O₃ nanoparticles can be used as catalysts for the electrocatalytic reduction of CO₂.¹⁵⁶ Dy³⁺ has also been doped in chitosan as a nanocatalyst for the synthesis of hexahydropyrimidine derivatives.¹⁸⁰

2.2.10. Ho³⁺, Er³⁺, and Tm³⁺. Ho³⁺, Er³⁺, and Tm³⁺ are best known in the lanthanide series for their upconversion properties. These three ions all have ladder-like, well-ordered energy levels with almost uniformly distributed energy gaps between adjacent levels. Since their energy gaps resemble the ²F_{5/2} → ²F_{7/2} transition of Yb³⁺, ion pairs of Er³⁺–Yb³⁺, Tm³⁺–Yb³⁺, and Ho³⁺–Yb³⁺ can achieve efficient energy transfer upconversion with the Yb³⁺ ion as the sensitizer.¹¹

Ho³⁺ has a ground state of ⁵I₈ and exhibits excited states of ⁵F₄, ⁵F₅, and ⁵I₆. Typical emissions include ⁵F₄ → ⁵I₈ at ~525 nm, ⁵F₅ → ⁵I₈ at ~650 nm, and ⁵I₆ → ⁵I₈ at ~1150 nm.¹⁸¹ Ho³⁺-doped nanoparticles such as HoF₃ and NaHoF₄ exhibit much larger r₂ than r₁, making them promising candidates as T₂ MRI contrast agents.^{174,182} Ho³⁺ ions have also been doped into TiO₂ and ZnO to enhance their catalytic activity.^{183,184}

Besides the direct doping strategy, YF₃:Ho@TiO₂ core–shell nanoparticles have been prepared to facilitate visible absorption by upconversion of Ho³⁺.¹⁸⁵ Moreover, Ho³⁺ ions have been used to prepare bimetallic Ni/Ho catalysts for the synthesis of carbon nanotubes.¹⁸⁶

Er³⁺ has a ground state of ⁴I_{15/2} and features excited states of ²H_{9/2}, ²H_{11/2}, ⁴S_{3/2}, and ⁴F_{9/2} as the most useful excited states. Typical emissions are ²H_{11/2} → ⁴I_{15/2} at ~525 nm, ⁴S_{3/2} → ⁴I_{15/2} at ~546 nm, ⁴F_{9/2} → ⁴I_{15/2} at ~660 nm, ²H_{9/2} → ⁴I_{15/2} at ~410 nm, and ⁴I_{13/2} → ⁴I_{15/2} at ~1550 nm.^{181,187} The emission of ⁴I_{13/2} → ⁴I_{15/2} at ~1550 nm is interesting due to its transparency in biological tissue.¹⁸⁸ Moreover, Er³⁺ can be used as a sensitizer for excitation at 1550 nm to achieve upconversion emission from Er³⁺ alone¹⁸⁹ or from other lanthanides (e.g., Yb³⁺, Ho³⁺, Tm³⁺).^{190,191}

Due to its large intrinsic magnetic moment, NaErF₄ nanomaterials have been used as T₂ contrast agents for magnetic resonance imaging.¹⁹² Doping of ZnO nanostructures with Er³⁺ ions leads to magnetic transition from diamagnetism to ferromagnetism at room temperature.¹⁹³ Pure NaErF₄ nanocrystals have been shown to be effective contrast agents for T₂-weighted magnetic resonance imaging.¹⁹⁴ BiFeO₃ nanoparticles doped with Er³⁺ exhibit enhanced ferromagnetism compared to undoped BiFeO₃.¹⁹⁵

Er³⁺ ions have been doped into semiconductors, such as TiO₂, In₂O₃, Bi₂WO₆, ZnO, PbSe, ZnS, and ZnSe, to improve their catalytic performance.^{196–202} When Er³⁺ was codoped with Yb³⁺, the enhanced upconversion process and energy transfer to the primary catalyst improved catalytic efficiency through NIR harvesting.²⁰³ NaYF₄:Er nanoparticles served as a cataluminescent sensor for ketones.²⁰⁴ Er(OH)₃ nanoparticles served as a catalyst for the photocatalytic reduction of Cr(VI) ions.²⁰⁵ When Er³⁺ was codoped with Yb³⁺ into fluorine-doped

tin oxides to fabricate counter electrodes in dye-sensitized solar cells, the overall cell efficiency was improved due to photocatalytic I^-/I_3^- circulation and accelerated I^- regeneration.²⁰⁶ Er_2O_3 nanorods showed high catalytic activity in the dehydration of 1,4-butanediol.²⁰⁷ Er^{3+} served as both catalyst and dopant in the preparation of optically active silica nanowires.²⁰⁸

Typical emissions of Tm^{3+} ions include $^1D_2 \rightarrow ^3H_4$ at ~ 359 nm, $^1D_2 \rightarrow ^3F_4$ at ~ 450 nm, $^1G_4 \rightarrow ^3H_6$ at ~ 477 nm, $^1G_4 \rightarrow ^3F_4$ at ~ 650 nm, $^3F_2 \rightarrow ^3H_6$ at ~ 695 nm, and $^3H_4 \rightarrow ^3H_6$ at ~ 800 nm.^{209,210} The transition from the 3H_4 to the 3H_6 manifold dominates the 800 nm emission at low pump powers, while the 800 nm emission at high-power excitation is likely due to the $^1G_4 \rightarrow ^3H_6$ transition. Research on the magnetic properties of Tm^{3+} -doped nanomaterials is still limited. As with other lanthanide ions, doping with Tm^{3+} causes nanoscale $BiFeO_3$ to exhibit ferromagnetic behavior.²¹¹

For catalytic applications, Tm^{3+} ions are usually codoped with Yb^{3+} into various inorganic host materials ($NaYF_4$, YF_3 , $NaLuF_4$, and $BiPO_4/BiVO_4$),^{212–217} which are then combined with TiO_2 or graphitic C_3N_4 to form nanocomposite catalysts.^{218,219} Through an upconversion process, composite catalysts can convert NIR light to ultraviolet or visible light and subsequently increase catalytic efficiency.^{220,221}

2.2.11. Yb^{3+} . Yb^{3+} has an electronic configuration of $[Xe]4f^{13}$ with only one unpaired electron, leading to a characteristic $4f-4f$ transition at ~ 980 nm. Owing to its efficient absorption and energy level matching Er^{3+} , Tm^{3+} , and Ho^{3+} emitters, Yb^{3+} effectively absorbs the excitation energy and transfers that energy to the intermediate energy levels of those emitters. Therefore, Yb^{3+} ions have been widely used as sensitizers and codoped with other lanthanides.²²² In addition, Yb^{3+} has been used as an emitter in conjugation with sensitizers such as Ce^{3+} , Pr^{3+} , Tb^{3+} , Tm^{3+} and Er^{3+} , for the downconversion of visible/UV to infrared light.^{40,223,224} On a separate note, Yb^{3+} can be used as a paramagnetic ion to develop $NaYbF_4$ -based T_2 -MRI contrast agents.²²⁵

The unique properties of individual rare-earth ions are determined by their electronic structures. Sc^{3+} , Y^{3+} , La^{3+} , and Lu^{3+} ions are optically and magnetically inert and are mainly employed as host cations for doping with metal ions. Although each rare-earth ion behaves differently, different rare-earth ions can be combined to form nanocrystals with controlled optical, electrical, and magnetic properties. This combination makes rare-earth-doped nanocrystals special and is the reason for their enormous potential, which has been tapped in recent decades. Furthermore, rare-earth dopants can undergo reversible valence changes (e.g., Ce^{3+}/Ce^{4+}) and improve the performance of nanocatalysts by modulating the electrical properties of the host lattice.

3. DOPING STRATEGIES

Doping, which enables one or more types of atoms or ions to be incorporated into a host material, has a long and distinguished history of imparting diverse properties to solids. In the past, metallic dopants such as iron (Fe^{2+} and Fe^{3+}), chromium (Cr^{3+}), cobalt (Co^{2+} and Co^{3+}), manganese (Mn^{2+} and Mn^{4+}), and copper (Cu^+ and Cu^{2+}) ions were employed to endow glass with vivid colors in the visible spectrum. Impurity doping also makes possible to control the transport of electrons and holes in semiconductors, which is the most critical concept of modern electronic and information technology. Rare-earths have become an important class of

dopants for glasses or crystalline materials to control optical, electrical, catalytic, and magnetic properties. In recent years, the advent of nanostructured materials, together with advances in chemical synthesis, has greatly expanded the scope of rare-earth doping. The precise incorporation of rare-earths can now be achieved in a broad spectrum of nanomaterials ranging from crystalline insulators and semiconductors to inorganic–organic hybrid materials, leading to many remarkable properties and functionalities.

3.1. Principal Factors in Doping

Rare-earth doping is often carried out simultaneously with the synthesis of host materials. Alternatively, doping can be performed by cation exchange on preformed substrates. In both cases, the effectiveness of doping is determined by the degree of chemical similarity between the host cations and the rare-earth dopants.

3.1.1. Ionic Size. Ionic size is determined by the distance between ions in different compounds.²²⁶ The crystal structure of an ionic compound is primarily dictated by the ratio of ionic radii of the cation and anion, as stable crystal structures are formed when a central cation is surrounded by a maximum number of anions in contact with each other. Therefore, the size of ions is one of the most critical parameters to be considered in the substitution of host cations by rare-earth dopants.

In general, ions of similar size can substitute for each other in a crystalline compound without any noticeable change in crystal structure. Because of the similar size of rare-earth ions (Table 1), most of their compounds can form complete solid solutions, allowing convenient doping with other rare-earth ions at arbitrary concentrations. For example, in an early study, Haase and co-workers doped $LaPO_4$ nanocrystals with 60 mol % Ce^{3+} and Tb^{3+} .²²⁷ The efficient luminescence process observed in these nanocrystals ($QY > 60\%$) suggests that heavy doping has negligible deleterious effects. In recent years, heavy doping with rare-earths has been demonstrated in a variety of nanocrystals and hierarchical nanostructures, such as $NaYF_4$ and $NaGdF_4@NaYF_4$, which have become indispensable for achieving unprecedented luminescence phenomena.^{228–231}

Although rare-earth ions of similar size can replace one another over a considerable compositional range, extensive substitution of host cations can lead to significant changes in the thermodynamic properties of the crystal. For example, van Veggel and co-workers found that doping GdF_3 with 30 mol % La^{3+} can trigger a phase transformation from an orthorhombic to a trigonal structure that is thermodynamically more stable.²³² In another representative demonstration, Liu and co-workers observed simultaneous changes in the phase (cubic to hexagonal) and size (~ 30 to 10 nm) of $NaYF_4:Yb/Er$ nanocrystals after gadolinium doping, due to changes in the dipole polarizability and surface charge.²³³ According to density functional theory calculations, the substitution of Y^{3+} ions with Gd^{3+} increased the formation energy per atom by about 0.7 eV, indicating that $NaGdF_4$ is more energetically stable than $NaYF_4$ in the hexagonal phase. Moreover, the electron charge density of the crystal surface also increased after Gd^{3+} doping, which effectively enhanced charge repulsion and delayed the deposition of F^- on the crystal surface. These findings have inspired a versatile approach to controlling the nanocrystal formation of various nanomaterials, such as CaF_2 , $NaLuF_4$, $NaYbF_4$, In_2O_3 , and $ScOOH/Sc_2O_3$.^{234–240} For example, Yan and co-workers reported that doping a $NaYbF_4$

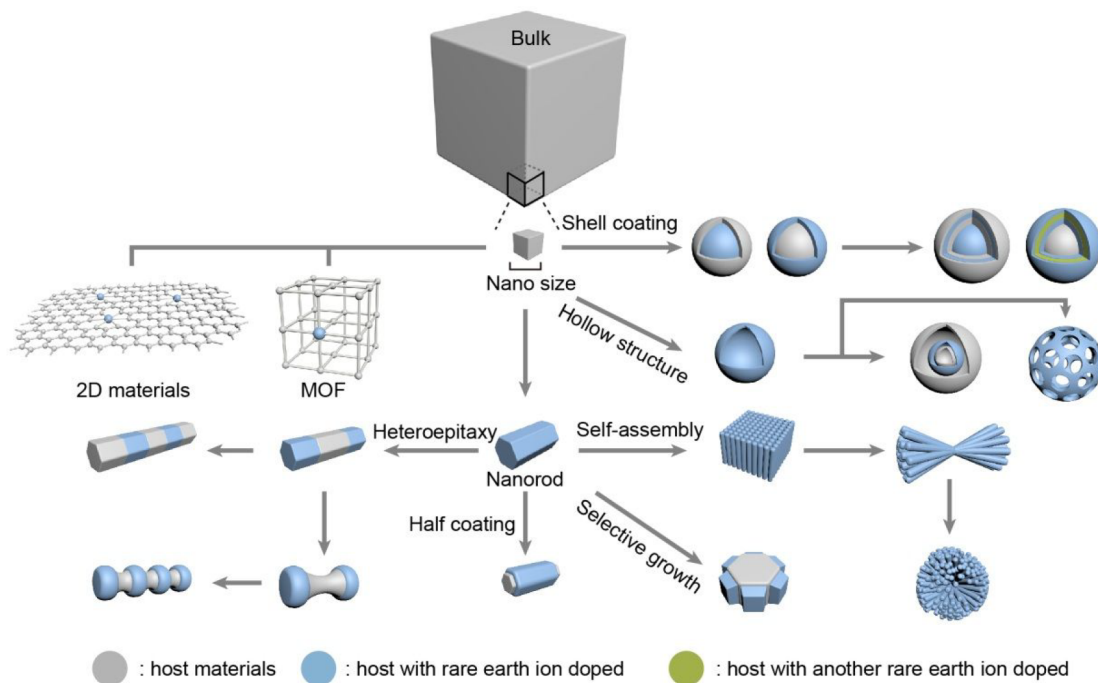


Figure 3. Selective doping of rare-earth ions in various nanomaterials via diverse strategies.

lattice with Gd^{3+} ions facilitates the phase transformation from cubic to hexagonal.²⁴¹ Furthermore, increasing the Gd^{3+} content decreases the average size of hexagonal $\text{NaYb}_{1-x}\text{Gd}_x\text{F}_4$ nanocrystals. Rare-earth dopants such as Dy^{3+} , Tb^{3+} , Eu^{3+} , Sm^{3+} , Nd^{3+} , Pr^{3+} , Ce^{3+} , and La^{3+} with larger radii than Yb^{3+} usually show similar effects to Gd^{3+} .²³³

Nevertheless, doped ions may not penetrate the host lattice if the size differences between the rare-earth dopant and the host cation are significant. In addition, rare-earth dopants are preferentially stabilized at cationic sites with high coordination numbers ($\text{CN} \geq 6$), such as octahedral sites ($\text{CN} = 6$) and cubic sites ($\text{CN} = 8$). However, for semiconductors with sphalerite, chalcopyrite, and wurtzite structures such as InP , CuInS_2 , ZnS , and CdSe , tetragonal coordination ($\text{CN} = 4$) is unfavorable for rare-earth doping because their cationic sites are too small to accommodate large dopants. Only a small percentage (typically less than 1 mol %) of rare-earth ions can be doped in these crystals, and most of the dopants are located on crystal surfaces.²⁴²

3.1.2. Valency. In general, it is easy to dope a rare-earth ion into an isovalent cation site, because the local structure of the host is least disturbed. However, the valences of the dopant and the substituted host cation are not necessarily identical. For instance, rare-earth ions, although unfavorable, can be doped into CdS and CdSe at divalent cationic sites.^{243,244} Aliovalent substitution often introduces point defects to maintain charge neutrality. Typical charge balancing defects include interstitial ions and vacancies.²⁴⁵

Compounds such as CaF_2 and SrF_2 with large cationic sites and a high coordination environment ($\text{CN} = 8$) are excellent candidates for rare-earth dopant incorporation.^{246–248} However, due to charge balancing and the associated local lattice distortion, the upper limit of the dopant concentration can be reduced. For example, the ion sizes of Ca^{2+} and Eu^{3+} are relatively close (1.12 vs 1.07 Å). Due to the intercalation of interstitial F^- ions, the CaF_2 host typically takes up less than 20

mol % Eu^{3+} dopants.²⁴⁹ Further increasing the dopant concentration requires careful control of experimental variables.²⁵⁰

3.1.3. Reactivity. In order to penetrate the host lattice and form stable substitutes, rare-earth dopants must have similar reactivity to the host cations. A large difference in chemical reactivity leads to the exclusion of ions that are not in equilibrium from the crystal lattice. For example, halides are less reactive with rare-earths than with lead. Accordingly, the substitution of Pb^{2+} by rare-earth ions in perovskite crystals such as CsPbBr_3 is characterized by low doping efficiency despite the small differences in ion size. In the wet chemical synthesis of $\text{CsPbBr}_3:\text{Ce}$ nanocrystals, the actual doping ratio of Ce^{3+} was 2.88%, as opposed to a 30% reaction ratio, corresponding to a relatively low doping efficiency of about 10%.²⁵¹ A similar mechanism could apply to the ineffective incorporation of rare-earth ions into Bi-based hosts such as Bi_2S_3 .²⁵²

3.1.4. Doping in Nanostructures. Unlike doped bulk materials, rare-earth doping in nanoscale crystals is not limited to single-phase materials. The development of nanostructures with various dimensions and shapes (e.g., nanoparticles, nanoplates, nanosheets, nanorods, nanowires, and irregular nanostructures) has allowed researchers to spatially limited doping sites to a few nanometers, enabling diverse strategies for multicomponent dopant incorporation (Figure 3).

For example, doped nanoparticles can be fabricated with core–shell architectures in which different dopants are incorporated into the inner core and the outer shell. One example is the synthesis of $\text{NaYF}_4:\text{Yb}/\text{Er}@/\text{NaYF}_4$ and $\text{NaGdF}_4:\text{Yb}/\text{Tm}@/\text{NaGdF}_4$ upconversion nanoparticles (UCNPs), in which the active Yb^{3+} , Er^{3+} , and Tm^{3+} dopants in the core are covered with an inert NaYF_4 shell to separate them from surface quenching sites, such as nonradiative surface defects, ligands, and solvent molecules.^{253,254} Another prominent example is core–shell nanocomposites that

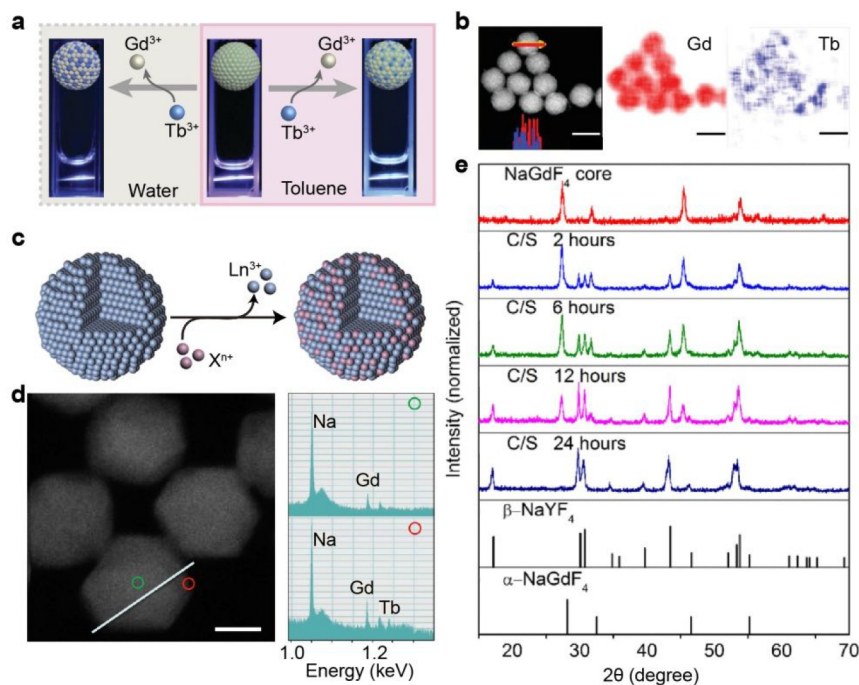


Figure 4. (a) Luminescence photos of UCNPs during cation exchange in water. (b) HRTEM and EELS images of NaGdF₄:Yb/Tm UCNPs after cation exchange. Scale bars are 25 nm. (c) Schematic of a typical cation exchange process occurring at the particle surface. (d) Typical STEM imaging of UCNPs after cation exchange and EELS point analysis taken at the green and red circles in the left image. The scale bar is 10 nm. (e) XRD patterns of NaGdF₄ core nanocrystals and NaGdF₄@NaYF₄:Yb/Er nanocrystals with different reaction times (Reprinted with permission from refs 286–288. Copyright 2018 The Royal Society of Chemistry; Copyright 2016 Nature Publishing Group; Copyright 2017 Springer).

combine hard and soft magnetic materials such as SmCo₅@Sm₂O₃ nanoparticles.²⁵⁵ The coupling of hard- and soft-magnetic components enables the formation of high-performance magnets based on exchange coupling for many applications.

In addition, spherical nanoparticles can be further transformed into hollow or mesoporous structures, such as Gd₂O₃, GdPO₄, and CeO₂ nanoparticles.^{256–258} With a larger surface-to-volume ratio, these nanostructures can have more dopants on the surface, which is crucial for applications such as catalysis and drug loading.

On the other hand, doped nanomaterials with anisotropic structures such as segmented nanorods, nanohourglasses, nanoblooms, nanodumbbells, and nanocylinders can be developed.²⁵⁹ Controlled epitaxial growth can selectively introduce multiple dopants into different segments of these heterogeneous structures. Moreover, rare-earth ions can be dispersed as single atoms onto two-dimensional (2D) supports such as graphitic carbon nitrides,²⁶⁰ or incorporated as metal centers in metal–organic frameworks.²⁶¹

3.2. Doping in Various Substrates

A large collection of materials is available for rare-earth doping, such as metal oxides, metal fluorides, metal oxyhalides, metal oxysulfides, metal oxysalts, and inorganic minerals. Moreover, various heterogeneously structured host materials have been developed to control the spatial distribution of rare-earths. Depending on the composition and structure of the host materials, different synthesis protocols and doping strategies are required.

3.2.1. Rare-Earth Compounds. Rare-earth compounds are ideal hosts for doping all types of rare-earth ions, because the physicochemical properties of the rare-earth series are

similar. Common rare-earth-based nanomaterials include fluorides, oxyhalides, oxysulfides, and oxysalts.

3.2.1.1. Rare-Earth Fluorides and Tetrafluorides. Fluorides are the most commonly used hosts for rare-earth dopants due to their mild synthesis conditions, high photochemical stability, and low phonon energy. Early studies on fluoride hosts mainly employed simple rare-earth fluorides such as LaF₃ and GdF₃ because they are easy to synthesize. For example, well-crystallized LaF₃ nanoparticles can be readily synthesized in an aqueous solution above room temperature.^{262,263} Subsequently, efforts have been made to incorporate rare-earth ions into various rare-earth fluorides, such as Na_xScF_{3+x}, KSc₂F₇, BaYF₅, BaGdF₅, KYb₂F₇, K₂GdF₅, and NaLaF₄.^{264–270} Nevertheless, current studies primarily focus on tetrafluoride hosts (e.g., LiLnF₄, NaLnF₄, KLnF₄; Ln = Y, Gd, Lu) because of their well-established synthetic approaches and efficient luminescence processes, such as photon upconversion.^{12,271–280}

Although rare-earth fluoride nanocrystals can be synthesized according to various protocols, high-quality synthesis is typically performed in organic solvents at elevated temperatures (~250–300 °C). A commonly used solvent is 1-octadecene (ODE) in combination with oleic acid (OA) and oleylamine (OM) as capping ligands.^{12,281} Reactions involved include coprecipitation of metal oleate precursors with fluoride and thermal decomposition of metal trifluoroacetate. Rare-earth doping can be achieved quite simply by partially replacing the host precursor with doping ions during synthesis. Elemental analysis can help determine the dopant concentrations in the resulting nanocrystals, and a satisfactory match with the feed ratio in the precursor largely reflects the chemical similarity between dopants and host ions.²⁸²

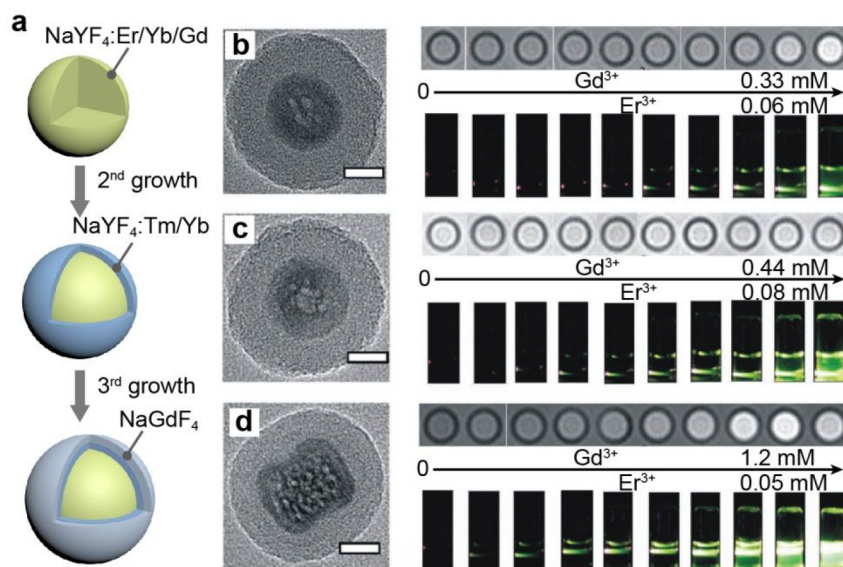


Figure 5. (a) Schematic representation of the synthesis of core–multishell UCNPs. (b–d) TEM images, T_1 -weighted MRI contrast images, and digital photographs, respectively, of core, core–shell, and core–shell–shell samples with different Gd/Er concentrations. The scale bar is 10 nm (Adapted with permission from ref 300. Copyright 2011 Wiley VCH Verlag GmbH & Co. KGaA, Weinheim).

Hexagonal-phase NaYF_4 ($\beta\text{-NaYF}_4$) is considered one of the most efficient host materials for achieving efficient lanthanide luminescence, especially for upconversion emission. Accordingly, many efforts have been made to dope $\beta\text{-NaYF}_4$ nanoparticles with rare-earth ions of different composition and concentration. For example, Wang and Liu synthesized NaYF_4 nanocrystals doped with ten different concentration ratios of Yb^{3+} , Er^{3+} , and Tm^{3+} .²⁸³ Hirsch and Resch-Genger and co-workers prepared $\text{Yb}^{3+}/\text{Er}^{3+}$ -encoded NaYF_4 nanoparticles by thermal decomposition.²⁸⁴ Gd^{3+} ions at various concentrations (0–60%) were also introduced into the NaYF_4 host to tune the resulting particle sizes.²³³

Doping of rare-earth fluoride nanoparticles can alternatively be achieved by cation exchange. Dong and van Veggel found that La^{3+} ions could replace Gd^{3+} ions in GdF_3 by dispersing citrate-stabilized GdF_3 nanocrystals in a solution containing an excess of La^{3+} and citrate.²⁸⁵ This cation-exchange reaction was relatively fast, and about 92% of the Gd^{3+} ions were replaced by La^{3+} in 1 min. Similarly, La^{3+} ions in LaF_3 nanocrystals could also be replaced by Gd^{3+} ions, but the degree of exchange was relatively small. The authors found that cationic exchange can occur between many pairs of LnF_3 and Ln^{3+} , such as EuF_3 with Gd^{3+} and NdF_3 with La^{3+} . Based on these cation exchange features, it can be argued that controlling the reaction time and diffusion rate of dopant ions can regulate the doping depth of lanthanide ions in fluoride hosts.

Doping via cation exchange has also been realized in tetrafluoride UCNPs. van Veggel et al. used cation exchange to replace the surfaces of $\beta\text{-NaYF}_4\text{:Yb/Tm}$ nanoparticle with thin NaGdF_4 shells.²⁸⁶ Recently, cation exchange has been demonstrated as a general approach to rapidly introduce various luminescent dopants (e.g., Tb^{3+} , Eu^{3+} , Mn^{2+} , Dy^{3+} , and Ce^{3+}) into $\beta\text{-NaGdF}_4\text{:Yb/Tm}@NaGdF_4$ nanoparticles and modulate the luminescence (Figure 4a–d).^{287,288} It has also been reported that heterogeneous $\alpha\text{-NaGdF}_4@beta\text{-NaYF}_4\text{:Yb/Er}$ structures can be fabricated by cation exchange at the interface (Figure 4e).²⁸⁹

Occasionally, nanoparticle units can be assembled into a hierarchical structure by controlling experimental variables

such as extending the reaction time, increasing reaction temperature, or adjusting the pH of the reaction. In one exciting example, olive-shaped GdF_3 nanoparticles doped with Eu^{3+} , Tb^{3+} , and Dy^{3+} ions were assembled into a series of hierarchical structures by simply changing the pH of the reaction.²⁹⁰

In addition to the aggregates of homogeneous nanoparticles, hierarchical core–shell nanostructures were also used for rare-earth doping. A prominent feature of the core–shell technique is that different rare-earth ions can be spatially confined in separate layers, leading to controllable interactions between the dopants and their environment. The manufacture of rare-earth-doped, core–shell nanoparticles typically requires a layer-by-layer growth process in which the doping ions are added during layer growth. It is unlikely that precise doping in core–shell nanostructures can be achieved by cation exchange, especially if multiple shell layers are required, as the exchange reaction occurs predominately at nanoparticle surfaces.

Core–shell nanostructures were initially developed to enhance luminescence intensity by eliminating surface quenching, i.e., nonradiative decay of dopant ions caused by high-energy surface oscillators.²⁹¹ Organic groups of surface capping ligands (e.g., $-\text{OH}$ and $-\text{NH}_2$) can serve as vibrational deactivation centers to quench excited lanthanide dopants via multiphonon relaxation. By coating the luminescent core with an inert protective shell, the lanthanide-doped core can be shielded from environmental influences.²⁹² For example, Skripka et al. reported that the absolute PLQY of $\text{NaGdF}_4\text{:Nd}$ nanoparticles increased from 8.2% to 17.4% after coating with NaGdF_4 in hexane.²⁹³

An important mechanism responsible for concentration quenching is energy migration through a dopant network that brings excitation energy to the surface quenchers.²⁹⁴ The core–shell engineering thus provides a simple solution to concentration quenching by isolating the luminescent core from the surface quenchers. Several groups have observed strong attenuation of quenching in core–shell UCNPs doped with high concentrations of Yb^{3+} or Er^{3+} in the core.^{30,192,295,296} Control experiments by Almutairi and co-

workers verified that strong concentration quenching can be induced by incorporating Yb³⁺ or Nd³⁺ dopants into the inert shell, which bridges energy transfer from the core to the surface quenchers.²⁹⁷

For core–shell nanoparticles, the surface passivation efficiency is positively correlated with the shell thickness. Emission intensity typically saturates at a critical shell thickness at which surface quenching is sufficiently suppressed. Chen et al. prepared highly uniform LiLuF₄:Yb/Ln@LiLuF₄ (Ln = Tm, Er) UCNPs.²⁷⁷ They showed that thicker LiLuF₄ shells lead to high quantum yields of 5.0 and 7.6% for Er³⁺ and Tm³⁺ emission, respectively. Li et al. investigated the optimal shell thickness in two sets of NaYF₄:Yb/Tm@NaYF₄ nanocrystals prepared by coprecipitation.²⁹⁸ The surfaces of the nanocrystals were coated with hydrophobic OA molecules or hydrophilic OH groups. They found that the OH groups have a stronger quenching effect due to their high vibrational energy. Hence, a thicker shell is required to suppress the quenching by OH groups. The optimal shell thickness is 3.5 nm. In contrast, the optimal thickness of OA-coated nanocrystals is 1.6 nm. Notably, thicker shells (>10 nm) are usually required to protect heavily doped cores, likely due to intense interactions between the surface quenchers and heavily doped ions.²⁹⁹

Among the various core–shell nanostructures, partially inert Gd-based shells are widely used by the upconversion community. The paramagnetic Gd³⁺ ion has seven unpaired 4f⁷ electrons, which alter the longitudinal relaxation of the surrounding water protons. Therefore, shell layers containing Gd³⁺ ions can be used as T₁-weighted MRI contrast agents in clinical diagnosis. Note that the position of Gd³⁺ ions in the core–shell structure greatly affects the MRI capabilities of the nanoparticles. Shi, Bu, and co-workers designed a NaYF₄:Yb/Er/Gd core continuously coated with an epitaxial NaYF₄:Yb/Tm inner shell and a NaGdF₄ outer shell (Figure 5).³⁰⁰ The growth of the epitaxial shells increased the total emission intensity (7.4- and 37.3-fold, respectively) compared to the bare NaYF₄:Yb/Er/Gd core. The authors attributed this emission increase to the lattice shielding of the shell. However, the NaYF₄:Yb/Tm shell (~4 nm thick) almost completely shielded the longitudinal relaxivity of the Gd³⁺ dopants in the core. The authors concluded that the rigid crystal of the core–shell nanostructure almost completely isolated the Gd³⁺ ions in the core from the surrounding water protons. This isolation was interpreted as a negative lattice shielding effect for Gd³⁺ dopants. The longitudinal relaxivity of the Gd-doped UCNPs was restored by coating the second epitaxial shell with NaGdF₄. Moreover, the authors also prepared Gd³⁺-free NaYF₄:Yb/Er cores with NaGdF₄ shells of different thicknesses (0.2–3.7 nm). They found that a thicker NaGdF₄ shell has a more negative shielding effect on Gd³⁺ ions. There are also many other reports of Gd³⁺-based core–shell structures for MRI, and the Gd³⁺ ions are generally distributed in the outermost layer of the shell to provide high water accessibility, such as NaGdF₄:Yb/Er@NaGdF₄:Nd/Yb, NaYF₄@NaNdF₄@NaYF₄@NaGdF₄, and NaYbF₄:Er@NaGdF₄.^{301–303}

Outer layers of core–shell nanoparticles can be doped with optically active lanthanide ions to harvest excitation energy and sensitize the emitter in the core. Vetrone et al. demonstrated this effect by coating NaGdF₄:Yb/Er core nanoparticles with an undoped NaGdF₄ shell and an active NaGdF₄:Yb shell.³⁰⁴ They found that the emission from NaGdF₄:Yb/Er@NaGdF₄:Yb nanoparticles was more intense than that from a NaGdF₄:Yb/Er@NaGdF₄ counterpart. In addition, a control

sample of NaGdF₄:Yb/Er nanoparticles was prepared with the same total Yb³⁺ dopant concentration as NaGdF₄:Yb/Er@NaGdF₄:Yb nanoparticles. The emission intensity of the control sample was much lower than that of the nanoparticles with active cores and active shells. It was concluded that the active NaGdF₄:Yb shell not only protects the luminescent core from nonradiative decay but also transfers the absorbed NIR energy to the upconversion core. Moreover, Zhu et al. reported that the active-core/active-shell structure can also promote downconversion luminescence in NaGdF₄:Yb/Pr@NaYF₄:Yb nanoparticles. They found that intense NIR luminescence can be achieved by downconversion of Yb³⁺ when additional Yb³⁺ ions are doped into the shell layer.³⁰⁵

Inspired by the active-core/active-shell structure, the effect of the doping site on the luminescence properties of core–shell nanoparticles has been studied. Bhuckory et al. recently prepared three types of NaGdF₄:Yb/Er-based UCNPs, including a NaGdF₄:Yb/Er nanoparticle without a shell, an active NaGdF₄:Yb/Er core with a passivating NaGdF₄ shell, and an undoped NaGdF₄ core with an active NaGdF₄:Yb/Er shell.³⁰⁶ The strongest luminescence was emitted by NaGdF₄:Yb/Er@NaGdF₄ nanoparticles, followed by NaGdF₄:Yb/Er and NaGdF₄@NaGdF₄:Yb/Er nanoparticles. The passivating NaGdF₄ shell of NaGdF₄:Yb/Er@NaGdF₄ nanoparticles protected the emitters in the core from surface quenching. In contrast, the other two types of nanoparticles had no such structural advantage. Abnormally, the photoluminescence decay time of NaGdF₄@NaGdF₄:Yb/Er nanoparticles was the largest, followed by NaGdF₄:Yb/Er@NaGdF₄ and NaGdF₄:Yb/Er nanoparticles. The authors offered two explanations for this order of decays. One was that some Yb³⁺ and Er³⁺ dopants migrated into the boundary layer of the shell and even into the inner core during the coating of the active shell. Therefore, Er³⁺ ions were effectively sensitized and protected at the interface of NaGdF₄@NaGdF₄:Yb/Er nanoparticles. The other reason was that the confinement of Yb³⁺ ions in the thin NaGdF₄ shell can suppress luminescence quenching by nonradiative defects. As a result, the sensitization of Er³⁺ ions with excited Yb³⁺ ions was enhanced, leading to long decay times.

Core–shell nanostructures are also frequently used to regulate energy exchange interactions between dopants. In an early study, Ballato and co-workers investigated the energy transfer between Eu³⁺ and Tb³⁺ dopants in a series of LaF₃ core–shell architectures, including LaF₃:Eu/Tb@LaF₃, LaF₃:Eu@LaF₃:Tb@LaF₃, and LaF₃:Eu@LaF₃@LaF₃:Tb@LaF₃.³⁰⁷ In these particles, the outermost LaF₃ shell acted as a passivation layer to prevent surface quenching. The intercalated LaF₃ layer in LaF₃:Eu@LaF₃@LaF₃:Tb@LaF₃ nanoparticles served as an energy barrier to tune the energy transfer between Eu³⁺- and Tb³⁺-ions confined in different layers. They demonstrated that the energy exchange between Eu³⁺ and Tb³⁺ can be completely blocked when a LaF₃:Eu@LaF₃@LaF₃:Tb@LaF₃ nanostructure with a thick inner LaF₃ layer (>2 nm) is used. A similar multilayer design allowed diverse luminescence processes to be integrated into a single class of nanoparticles without noticeable crosstalk, resulting in orthogonal or multimodal emissions.^{34,308–314}

An exciting achievement using a core–shell nanostructure to regulate complex energy transfer between lanthanide dopants was demonstrated by Liu and co-workers.¹³⁸ In their study, Yb³⁺, Tm³⁺, and Tb³⁺ (or Eu³⁺, Dy³⁺, Sm³⁺) were incorporated into core and shell layers, respectively, of NaGdF₄@NaGdF₄

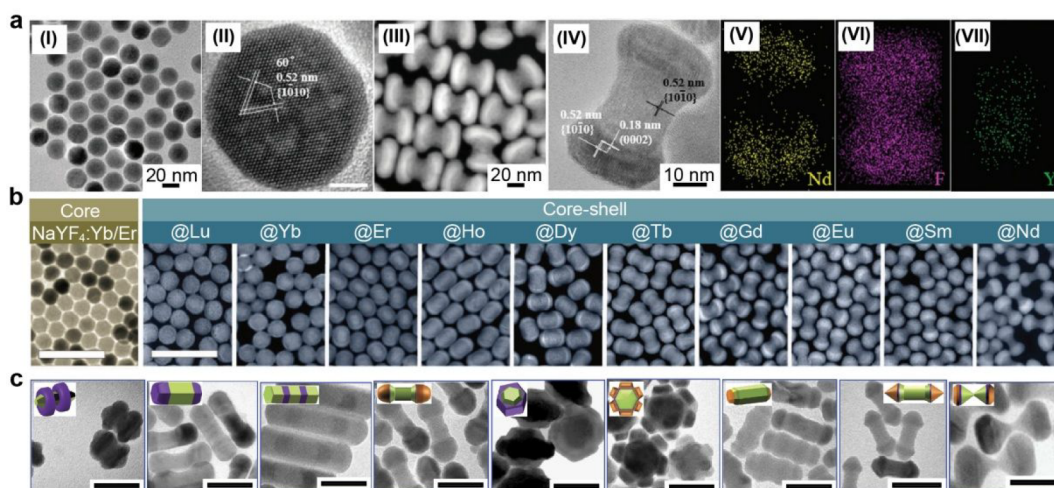


Figure 6. (a) (I) TEM and (II) HRTEM images of core nanoparticles (the scale bar in II is 5 nm). (III) STEM and (IV) HRTEM images of dumbbell-shaped core-shell nanoparticles. (V–VII) Elemental mapping of the distribution of Nd³⁺, Y³⁺, and F⁻ ions within a single dumbbell-shaped nanocrystal. (b) TEM imaging of the NaYF₄:Yb/Er core and HAADF-STEM imaging of the corresponding NaYF₄:Yb/Er@NaREF₄ core-shell nanoparticles. Scale bars are 100 nm. (c) Complex NaLnF₄ nanostructures synthesized under different reaction conditions. Scale bars are 50 nm (Adapted with permission from refs 259, 320, and 322. Copyright 2016 The Royal Society of Chemistry; Copyright 2019 Wiley VCH Verlag GmbH & Co. KGaA, Weinheim; Copyright 2016 Nature Publishing Group).

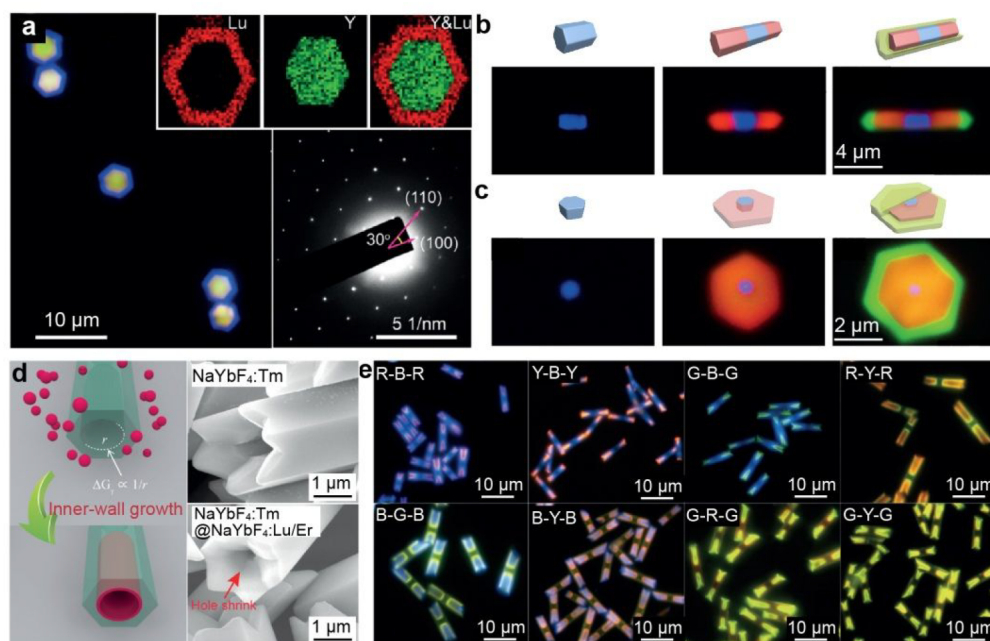


Figure 7. (a) Upconversion luminescent micrographs of core-shell crystals under 980 nm excitation. (top inset) Elemental mapping performed on a single core-shell crystal. (bottom inset) Electron diffraction pattern of a selected region recorded at the edge of a core-shell crystal. (b) Diagrams and optical micrographs showing the evolution from microrod seed to tricolor microrod. (c) Diagrams and optical micrographs showing evolution from microrod seed to three-color microplate. (d) Growth of the inner wall on tubular microrods because of the relatively low surface energy of the concave wall. (e) Optical micrographs of microrods fabricated with different combinations of substrate microrods and coating layers (Adapted with permission from refs 36 and 324. Copyright 2016 and 2017 Wiley-VCH Verlag GmbH & Co. KGaA, Weinheim).

nanoparticles. The spatial separation of the two doped groups eliminated the nonradiative quenching caused by deleterious cross-relaxation. Meanwhile, energy migration through the Gd³⁺ sublattice at the core-shell interface bridged the selective energy transfer from the core to the shell, resulting in unprecedented upconversion emission of Tb³⁺, Eu³⁺, Dy³⁺, and Sm³⁺ ions without intermediate energy levels.³¹⁵ The strategy of core-shell engineering combined with energy migration is

now routinely used to generate novel luminescence processes.^{34,316–319}

Besides conformal core-shell nanoparticles, anisotropic epitaxial nanostructures have been synthesized by controlling the epitaxial growth process. The epitaxial shape is governed by both intrinsic mismatches between the core and shell lattices and synthetic variables.^{320,321} Xu et al. prepared dumbbell-shaped NaYF₄:Yb/Er@NaNdF₄:Yb heterostructures.³²² The Yb³⁺/Er³⁺ and Yb³⁺ dopants were individually distributed in

different regions of the nanocrystal, and the doping concentration of Yb^{3+} in the NaYF_4 domain was higher than that in the NaNdF_4 domain (Figure 6a). The authors concluded that the dumbbell morphology is more advantageous for photodynamic therapy than the conformal core-shell structure.

Zhao et al. have shown that epitaxial growth on hexagonal phase NaREF_4 nanocrystals is subject to anisotropic interfacial strain.³²⁰ In general, epitaxial deposition on the [001] facet is subject to less mismatch strain than that on the [100] facet. As a result, preferential epitaxial growth is often observed along the *c*-axis. Due to anisotropic interfacial tension, the prism shell may eventually decompose to minimize the global free energy, resulting in dumbbell-shaped morphologies (Figure 6b). The biaxial strain in the dumbbell-shaped $\text{NaYF}_4:\text{Yb}/\text{Er}@/\text{NaGdF}_4$ UCNPs affected the relative intensity of red and green emissions from the Er^{3+} dopants.

In addition to interfacial strain, surface capping ligands also have an important function in forming core-shell nanocrystals with the desired morphology. Liu et al. found that the oleate anion (OA^-) tends to bind to the (100) facet of NaREF_4 crystals in hexagonal phase, while the oleic acid (OA) molecule has a particular affinity for the (001) facet.²⁵⁹ They choose a hexagonal NaYF_4 nanocrystal as a model and designed epitaxial growth of the NaLnF_4 ($\text{Ln} = \text{Y}, \text{Gd}, \text{Nd}, \text{Lu}$) shell on the NaYF_4 core by controlling the ratio of OA^-/OA . The high concentration of NaOH resulted a large ratio of OA^-/OA , which promoted epitaxial growth along the longitudinal direction of the NaYF_4 nanocrystal. Epitaxial growth along the transverse direction of the hexagonal NaYF_4 nanocrystal can be achieved by decreasing the NaOH concentration, which increases the OA concentration (Figure 6c).

Anisotropic core-shell morphology offers a new dimension for controlling the optical properties of nanoparticles as well as their interactions with the surroundings. Carefully selection of core nanoparticles and precise control of synthesis methods can achieve highly directional epitaxial growth, leading to segmented nanostructures.^{36,311,323,324} For example, Zhang et al. prepared multicolored rod- and plate-shaped upconversion barcodes based on precise control of the shell thickness and growth direction of epitaxial layers on $\beta\text{-NaYbF}_4$ seeds.³⁶ The authors synthesized small $\beta\text{-NaYbF}_4$ nanorods and epitaxially grew different lanthanide dopants in horizontal or vertical orientation. The epitaxial growth of RE^{3+} was carried out by mixing cubic-phase NaLuF_4 or NaYF_4 nanoparticles with $\beta\text{-NaYbF}_4$ microrods under hydrothermal conditions. Multicolored $\beta\text{-NaYF}_4$ microrods and microplates with localized Ln^{3+} dopants were obtained, and the growth direction was tuned by controlling favorable growth along different facets of the nanocrystals (Figure 7a–c). Wang and co-workers prepared NaYbF_4 microrods in hexagonal phase with isolated holes along the longitudinal axis.³²⁴ They succeeded in controlling epitaxial growth in the inner walls of holes to obtain multicolor emission from different sections of the microrods (Figure 7d and e). In another interesting example, Li, Zhang, and co-workers synthesized a series of $\text{NaYF}_4:\text{Yb}/\text{Er}@/\text{NaGdF}_4:\text{Yb}@/\text{NaNdF}_4:\text{Yb}$ core-shell-shell nanoplates with controllable surface roughness.³²⁵ The authors employed a successive layer-by-layer strategy to grow NaLnF_4 shells on nanoplates and then control the kinetics of shell coating during the process. In this way, hexagonal disk and multipetal core-shell nanoplates with different degrees of surface roughness were obtained. Interestingly, the authors demonstrated that

nanostructures with the highest surface roughness were able to pass blood-brain barriers in living mice, which was impossible with conventional core-shell nanostructures.

3.2.1.2. Rare-Earth Oxyhalides. The excited-state energy and transition probability of rare-earth dopants are largely influenced by the host materials. In recent years, rare-earth oxyhalides have been recognized as a significant class of host materials for rare-earth dopants. Several methods have been reported for fabrication of rare-earth-doped oxyfluorides nanocrystals, including hydrothermal synthesis followed by heat treatment,^{326,327} coprecipitation,³²⁸ thermolysis of rare trifluoroacetate,³²⁹ and the sol-gel Pechini methods.³³⁰

In 2009, Yan's group reported the synthesis of sub-2 nm EuOF nanowires by decomposition of the corresponding trifluoroacetates at elevated temperatures.³²⁹ The authors used $\text{Eu}(\text{CF}_3\text{COO})_3$ as a precursor to obtain Eu^{3+} and F^- by thermolysis in a mixed solvent containing OA and OM. During the synthesis, a $\text{Eu}(\text{CF}_3\text{COO})_{3-x}(\text{OA})_x$ intermediate was generated to control the nucleation and further growth of EuOF nanowires in subsequent steps. In a later study, Chen, Tu, and co-workers doped Ce^{3+} , Eu^{3+} , $\text{Ce}^{3+}/\text{Tb}^{3+}$, $\text{Yb}^{3+}/\text{Er}^{3+}$, and $\text{Yb}^{3+}/\text{Ho}^{3+}$ into LaOBr nanocrystals by a modified thermal decomposition approach.³³¹ By analyzing the downshifting emission of $\text{LaOBr}:\text{Eu}^{3+}$, the authors identified several doping site symmetries in nanocrystals, including C_{4v} , C_1 , C_s , C_2 , and C_{2v} . In a recent demonstration, Du et al. synthesized $\text{Pr}^{3+}/\text{Gd}^{3+}$ -encoded $\text{Lu}_6\text{O}_5\text{F}_8$ nanocrystals by thermal decomposition.³³² The host lattice was chosen so that the $4f^2 5d^1$ energy level can be tuned to achieve upconversion emission from Pr^{3+} in the deep ultraviolet region via sequential absorption of two blue excitation photons through $^3\text{H}_4 (4f^2) \rightarrow ^3\text{P}_0 (4f^2)$ and $4f^2 \rightarrow 4f^1 5d^1$ transitions.

Lin and co-workers reported the synthesis of LaOF nanocrystals by a hydrothermal method followed by heat treatment.³²⁶ Doping nanocrystals with a series of lanthanide dopants, including Eu^{3+} , Tb^{3+} , Sm^{3+} , Dy^{3+} , Tm^{3+} , and Ho^{3+} , yielded characteristic f–f emissions with red, blue–green, orange, yellow, blue, and green colors under ultraviolet and low-voltage electron beam excitation. Two-step hydrothermal methods have also been utilized to prepare rare-earth oxyfluorides in the Vernier phase, such as V-YOF ($\text{Y}_6\text{O}_5\text{F}_8$), V-YbOF ($\text{Yb}_6\text{O}_5\text{F}_8$), and V-LuOF ($\text{Lu}_6\text{O}_5\text{F}_8$) nanoparticles.^{327,333–335} With multiple low-symmetry doping sites (C_1 , C_2 , and C_s), V-rare-earth oxyfluorides are essential for the development of highly efficient multicolor nanophosphors.

In 2016, You's group developed a topotactic transformation route to prepare $\text{GdOF}:\text{Ln}^{3+}$ ($\text{Ln} = \text{Eu}, \text{Tb}, \text{Ce}/\text{Tb}, \text{Yb}/\text{Er}$, and Yb/Tm) nanocrystals.³³⁶ Brucite-like $\text{Gd}_2(\text{OH})_5\text{NO}_3 \cdot 0.9\text{H}_2\text{O}$ was first converted into layered $\text{Gd}(\text{OH})_2\text{F}$ with large {0001} facets by ion exchange. Topotactic *in situ* growth of GdOF from $\text{Gd}(\text{OH})_2\text{F}$ was then achieved by thermal decomposition due to the structural correspondence between [0001] $\text{Gd}(\text{OH})_2\text{F}$ and [110] GdOF facets. In a parallel development, You, Liu, and colleagues used $\text{RE}(\text{OH})\text{CO}_3$ as both precursor and template.³³⁷ By calcining $\text{RE}(\text{OH})\text{CO}_3$ together with KHF_2 , they obtained porous $\text{REOF}:\text{Ln}^{3+}$ spheres ($\text{RE} = \text{Y}, \text{Gd}, \text{Lu}$; $\text{Ln} = \text{Ce}, \text{Eu}, \text{Tb}, \text{Ce}/\text{Tb}, \text{Yb}/\text{Er}, \text{Yb}/\text{Ho}$, or Yb/Tm). These structures exhibit a large surface-to-volume ratio and have the potential for applications in photocatalysis and drug delivery.

Rare-earth-doped oxyfluoride nanoparticles can be prepared with heterogeneous nanoscale architectures. Gao and co-workers synthesized $\text{YOF}:\text{Yb}/\text{Er}@/\text{YOF}$ nanoparticles by

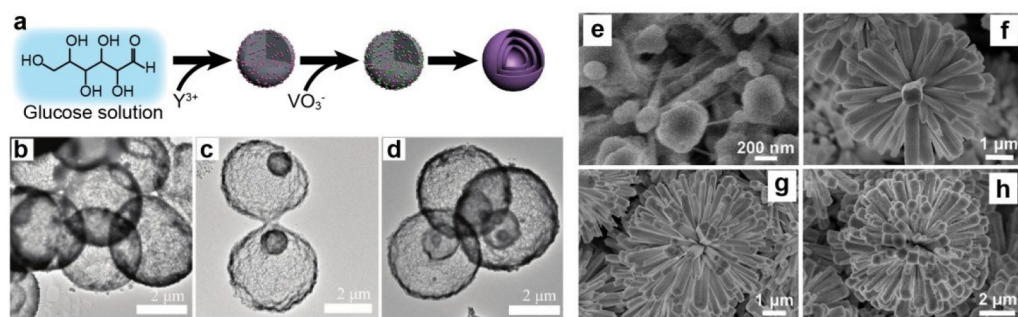


Figure 8. (a) Schematic synthesis of multilayered YVO_4 hollow spheres. (b–d) TEM images of single-, double-, and triple-shell YVO_4 hollow spheres, respectively. (e–h) SEM images of the samples, prepared at $260\text{ }^\circ\text{C}$ for 5 h with different molar ratios of $\text{Na}_2\text{H}_2\text{L}/\text{Gd}^{3+}$: (e) 2, (f) 2.60, (g) 2.76, and (h) 2.80 (Adapted with permission from refs 341 and 342. Copyright 2017 Wiley-VCH Verlag GmbH & Co. KGaA, Weinheim; Copyright 2016 Elsevier B.V.).

thermolysis of rare-earth trifluoroacetates.³³⁸ These as-prepared core–shell nanoparticles exhibited stronger red upconversion emission than their core-only counterparts. These nanoparticles can be further rendered hydrophilic and conjugated with antibodies to label and image cancer cells. Yan et al. produced ultrasmall ($\sim 5\text{ nm}$) GdOF nanoparticles that can be readily functionalized with peptides to specifically image the cytoplasm and nucleus.³³⁹ Lin's group established a protocol to prepare yolkl-like, mesoporous GdOF:Ln@ SiO_2 (Ln = Yb, Er, Mn) nanoparticles with various functional groups and demonstrated their utility as a multifunctional platform for multimodal image-guided therapies.³⁴⁰

3.2.1.3. Oxysulfides. Oxysulfides such as $\text{Gd}_2\text{O}_2\text{S}$, $\text{Y}_2\text{O}_2\text{S}$, $\text{Tb}_2\text{O}_2\text{S}$, $\text{La}_2\text{O}_2\text{S}$, $\text{Eu}_2\text{O}_2\text{S}$, and $\text{Lu}_2\text{O}_2\text{S}$ are popular host materials for rare-earth doping.^{343–353} Traditional doping methods with oxysulfides include solid–gas reaction, solid thermal evaporation, liquid thermal decomposition, sol–gel processing, laser ablation, and solvothermal treatment. In the last two decades, special synthetic methods have been reported. For example, in 2000, Qian and co-workers reported a solvothermal gel method for the preparation of nanocrystalline $\text{La}_2\text{O}_2\text{S}$ in polar solvents.³⁵⁴ In 2006, Gao's group developed the facile colloidal synthesis of monodisperse $\text{Eu}_2\text{O}_2\text{S}$ and $\text{Gd}_2\text{O}_2\text{S}:\text{Eu}$ nanocrystals with tunable size and shape.³⁵¹ The entire preparation process was conducted under ambient atmosphere. The size and shape of the doped $\text{RE}_2\text{O}_2\text{S}$ nanocrystals were precisely controlled by surfactants of OA and OM. With the help of a mild, self-templating approach, Huang and co-workers used supramolecular lanthanide–cholate hydrogels to prepare Eu^{3+} -doped $\text{Gd}_2\text{O}_2\text{S}$ and $\text{Y}_2\text{O}_2\text{S}$ nanotubes, which exhibited efficient luminescence.³⁵⁵ Ding et al. demonstrated that doping with Na^+ can facilitate the formation of high-quality monodisperse, ultrathin $\text{La}_2\text{O}_2\text{S}$ nanoplates.³⁵⁶ The authors found that Na^+ can be doped into $\text{La}_2\text{O}_2\text{S}$ nanocrystals at a high concentration, determined by the trapped-dopant model. Theoretical calculations revealed that introduction of Na^+ significantly reduced the repulsion in the sublattice, resulting in doped $\text{La}_2\text{O}_2\text{S}$ nanocrystals.

3.2.1.4. Rare-Earth Oxysalts. Rare-earth oxysalts represent a broad class of host materials, characterized by high thermal stability. However, many RE oxysalts must crystallize at temperatures above $500\text{ }^\circ\text{C}$ and are unlikely to form uniform nanocrystals by wet chemical synthesis. Commonly studied rare-earth oxysalt nanoparticles include orthophosphates, vanadates, borates, tungstates, and molybdates.

Orthophosphates, a series of inorganic hosts that exist in the form of three free ions, H_2PO_4^- , HPO_4^{2-} , and PO_4^{3-} , have found widespread applications as phosphors, laser materials, humidity sensors, biomarkers, and catalysts.^{357–363} For example, Haase and co-workers used the core–shell nanostructure in the preparation of colloidal $\text{CePO}_4:\text{Tb}@\text{LaPO}_4$ nanoparticles by a wet chemical method.³⁶⁴ Growth of a LaPO_4 shell around the core nanoparticles significantly increased the luminescence quantum yield of Tb^{3+} from 43 to 70%. Recently, You's group developed a topotactic transformation method to prepare $\text{YPO}_4:\text{Ln}^{3+}$ (Ln = Ce, Eu, Tb) micro/nanocrystals.³⁶⁵ In this strategy, the topotactic structure of the precursor determines the resulting phase of $\text{YPO}_4:\text{Ln}$ nanoparticles. Indeed, layered $\text{Y}_2(\text{OH})_5\text{NO}_3$ induced the formation of hexagonal-phase $\text{YPO}_4:\text{Ln}$, while amorphous $\text{Y}(\text{OH})\text{CO}_3$ favored the formation of tetragonal $\text{YPO}_4:\text{Ln}$. They also found that additives such as Na_2CO_3 and NH_4HCO_3 determined precursor structures. The ratio of additives to Na_3PO_4 can be varied to tune the crystal size of the resulting products.

Precursor engineering is suitable for imparting a specific structure to the rare-earth-doped oxysalt nanoparticles. For example, Jia et al. prepared a rare-earth hydroxycarbonate precursor by homogeneous precipitation of $\text{RE}(\text{NO}_3)_3$ with urea.³⁶⁶ Hydroxycarbonates can be converted in the liquid phase into more thermodynamically stable structures containing precursor counteranions, such as fluorides, phosphates, or vanadates. Therefore, hydroxycarbonates can serve as templates for the formation of dispersible inorganic nanostructures by wet chemical methods. Jia et al. treated rare-earth hydroxycarbonates with PO_4^{3-} and VO_4^{3-} anions to obtain rare-earth-doped YPO_4 and YVO_4 nanospheres with hollow structures.

Many strategies have accelerated the development of rare-earth orthovanadates for applications in optical devices.^{367–373} In principle, rare-earth orthovanadates have two polymorphs, the monoclinic monazite and the tetragonal zircon structures. Large rare-earth ions prefer the monazite type because of its higher oxygen coordination number (CN = 9) than the zircon type (CN = 8). However, the monazite host is neither suitable for luminescence activators nor promising for catalysis compared to zircon-type orthovanadates. Hence, the design of an effective strategy for preparing metastable orthovanadates, such as zircon-type LaVO_4 , is of great interest. In that regard, Zhao's group prepared Ln^{3+} -doped zircon-type LaVO_4 by a simple hydrothermal method without the need for

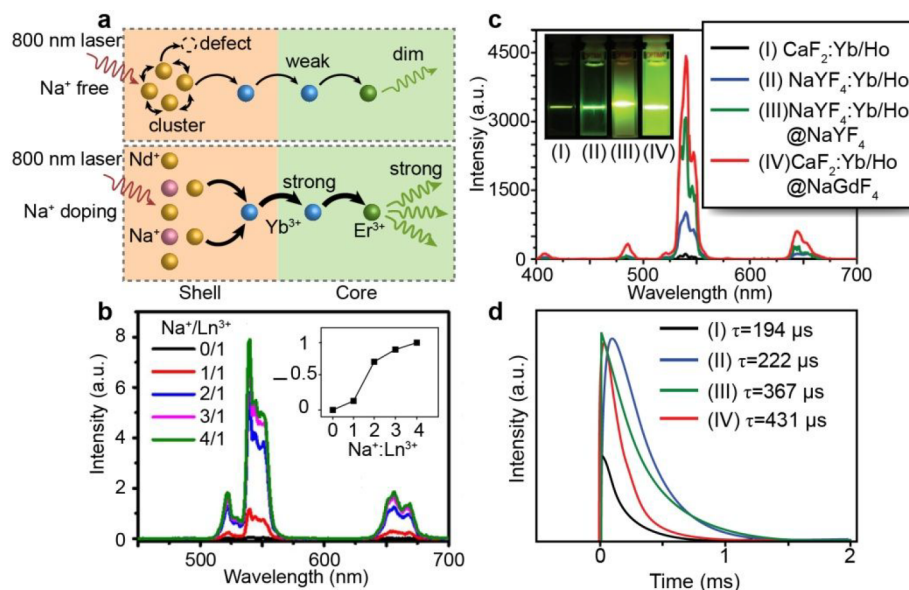


Figure 9. (a) Schematic of energy transfer in $\text{CaF}_2\text{:Yb/Er@CaF}_2\text{:Nd/Yb}$ nanoparticles with and without Na^+ ions in the shell. (b) UCL emission spectra of $\text{CaF}_2\text{:Yb/Er@CaF}_2\text{:Nd/Yb}$ nanoparticles synthesized at different molar ratios of $\text{Na}^+/\text{Ln}^{3+}$ upon excitation at 800 nm. (c) UC PL spectra and corresponding photographic digital images of colloidal (I) cubic $\text{CaF}_2\text{:20\%Yb/2\%Ho}$, (II) hexagonal $\text{NaYF}_4\text{:20\%Yb/2\%Ho}$, (III) hexagonal $(\text{NaYF}_4\text{:20\%Yb/2\%Ho})@\text{NaYF}_4$, (IV) cubic $(\text{CaF}_2\text{:20\%Yb/2\%Ho})@\text{NaGdF}_4$. (d) Decay behavior of photoluminescence at 540 nm in colloidal (I), (II), (III), and (IV), respectively (Adapted with permission from refs 391 and 398. Copyright 2017 American Chemical Society; Copyright 2015 The Royal Society of Chemistry).

catalysts or templates.³⁷⁴ They found that the variation of pH can control the phase and shape of LaVO_4 . When the pH was less than 3.5, only irregular nanoparticles of $\text{LaVO}_4\text{:Ln}$ with the monazite phase were obtained. When the pH was between 4.5 to 6.0, uniform $\text{LaVO}_4\text{:Ln}$ nanorods with the tetragonal zirconium phase were obtained. When the pH was further increased to above 6.0, the obtained $\text{LaVO}_4\text{:Ln}$ nanocrystals exhibited particlelike morphology. To control the dimension of orthovanadates, Lin's group utilized an electrospinning technique after a sol-gel process to prepare one-dimensional $\text{YVO}_4\text{:Ln}^{3+}$ ($\text{Ln} = \text{Eu, Sm, Dy}$) nanofibers.¹⁰⁹ Antić et al. employed a pulsed laser deposition technique to fabricate zirconia thin films of $\text{GdVO}_4\text{:Dy}$ on thermally grown SiO_2 substrates.³⁷⁵ These physical techniques can effectively construct Ln^{3+} -doped nanocrystals with various shapes.

Rare-earth orthovanadate nanocrystals may self-assemble into ordered structures that provide great opportunities for device applications as well as mechanistic investigations of optical and electronic properties. Weng et al. reported a hydrothermal synthesis of LnVO_4 ($\text{Ln} = \text{La, Ce, Pr, Nd, Sm, Eu, Gd}$) nanorods that can self-assemble into different aggregates, depending on pH, reaction time, and EDTA concentration.³⁷⁶

In another interesting study, Zong et al. used yttrium-carbon spheres as templates to build $\text{YVO}_4\text{:Yb/Er}$ hollow structures with single shells, double shells, and triple shells (Figure 8a–d).³⁴¹ The number of shell layers could depend on the calcination temperature and time, heating rate, and concentration of VO^{3-} . By adjusting the ratio of surfactants ($\text{Na}_2\text{H}_2\text{L}$) and rare-earths, Amurisana et al. developed a one-pot hydrothermal route that enabled the synthesis of GdVO_4 superstructures with well-controlled flowerlike morphology (Figure 8e–h).³⁴²

Apart from orthophosphates and orthovanadates, attempts have also been made to prepare other types of nanocrystals

based on rare-earth oxysalts such as borates, tungstates, and molybdates. Yan, Sun, and co-workers employed a sol-gel pyrolysis method to prepare hexagonal-phase $\text{YBO}_3\text{:Eu}$ (0–30 mol %) nanocrystals with different sizes and size-dependent coloration.³⁷⁷ Li and co-workers developed a solvothermal liquid-solid solution method and prepared YBO_3 nanocrystals with better monodispersity.³⁷⁸ In 2013, a triclinic form of $\text{GdBO}_3\text{:Eu}$ nanocrystals was synthesized by Szczeszak et al. via a hydrothermal method.³⁷⁹

Rare-earth tungstates and molybdates form in several variants, such as $\text{NaRE}(\text{MO}_4)_4$, $\text{RE}_2\text{M}_3\text{O}_{12}$, and RE_2MO_6 , where M stands for W^{6+} or Mo^{6+} . The compositional variability provides great flexibility in tailoring the material properties. For example, orthorhombic $\text{RE}_2\text{M}_3\text{O}_{12}$ crystals such as $\text{Yb}_2\text{W}_3\text{O}_{12}$ and $\text{Sc}_2\text{Mo}_3\text{O}_{12}$ exhibit negative thermal expansion, which is critical for attenuating luminescence quenching at elevated temperatures.^{380,381} However, as with many other rare-earth oxysalts, only a small number of nanocrystalline rare-earth tungstates and molybdates have been reported. In 2016, Zhong, Meijerink, and co-workers synthesized sub-50 nm $\text{NaRE}(\text{WO}_4)_2$ nanocrystals with a uniform diamond shape using a solvothermal method.³⁸² The researchers used hexacarbonyl tungsten as a W^{6+} source and mixed it with rare-earth acetate and sodium hydroxide in a mixed solution of OA, OM, and ODE. The new synthetic route for nanosized tungstates may promote new applications for these hosts in the future.

3.2.2. Alkaline-Earth Compounds. Host materials containing alkaline-earth metal ions can provide different chemical environments to control the valence of rare-earth dopants. Owing to the considerable size similarity between rare-earths and alkaline-earths (e.g., Ca^{2+} , Sr^{2+} , Ba^{2+}), alkaline-earth compounds can readily accommodate high doping concentrations (>10%) of rare-earth ions.

3.2.2.1. Alkaline-Earth Halides. Alkaline-earth fluorides (MF_2 , $\text{M}^{2+} = \text{Ca}^{2+}, \text{Sr}^{2+}, \text{Ba}^{2+}$) have received considerable attention for rare-earth doping due to their high optical transparency and high chemical and thermal stability.^{283,383–388} Rare-earth-doped MF_2 nanoparticles can be prepared using protocols similar to those developed for preparing rare-earth fluorides and tetrafluorides.

In a representative example from Wang's group, ~ 3 nm $\text{BaF}_2:\text{Yb}/\text{Tm}$ nanoparticles were prepared by a solvothermal method and subsequently used as core nanoparticles for the epitaxial growth of $\text{SrF}_2:\text{Nd}$ shells by thermal decomposition.⁹⁴ In this architecture, the SrF_2 shell not only contributed to the enhancement of the NIR-to-NIR upconversion luminescence of the $\text{BaF}_2:\text{Yb}/\text{Tm}$ core but also acted as a host for the realization of the NIR-to-NIR downshifting of the Nd^{3+} emission. Wang's group also reported that aliovalent rare-earth dopants can control the size and shape of alkaline-earth fluoride nanocrystals (MF_2 , $\text{M} = \text{Ca}, \text{Sr}, \text{Ba}$).^{389,390} Substitution of M^{2+} by Ln^{3+} in MF_2 required an additional F^- for charge compensation. Introduction of such F^- ions into the grain surface can induce transient electric dipoles with their negative poles directed outward. These transient electric dipoles hinder the diffusion of F^- ions, which are required for crystal growth, from the solution to the grain surface, thus retarding the growth of MF_2 .

For charge compensation, it is possible to introduce Na^+ together with rare-earth ions into CaF_2 host lattices. Xu et al. reported an enhancement of upconversion emission in $\text{CaF}_2:\text{Yb}/\text{Er}@\text{CaF}_2:\text{Nd}/\text{Yb}$ nanoparticles by Na^+ doping (Figure 9a,b).³⁹¹ The researchers argued that doping a CaF_2 lattice with rare-earth and Na^+ ions can maintain charge neutrality and reduce defect formation in the host, leading to high upconversion efficiency.

MF_2 materials are widely used as hosts for isovalent rare-earth dopants such as Eu^{2+} . Hong and Kawano treated $\text{CaF}_2:\text{Eu}^{3+}$ nanoparticles in a thermal carbonaceous atmosphere at 500–900 °C, which reduced Eu^{3+} into Eu^{2+} .³⁹² They found that the particle size and $\text{Eu}^{2+}/\text{Eu}^{3+}$ ratio increased with increasing temperature from 600 to 900 °C. Eu^{2+} ions enter the cubic CaF_2 lattice by Ca^{2+} substitution, and each Eu^{2+} ion coordinates with eight fluorine anions. The octahedral crystal field splits the 5d level of Eu^{2+} into two orbital groups with different energies. Consequently, the $4f^7-4f^65d$ transition of Eu^{2+} is highly sensitive to chemical bonding between Eu^{2+} and F^- ions.

Obtaining Eu^{2+} -doped nanoparticles usually requires post-synthetic annealing to reduce the oxidation state of europium from trivalent to divalent. The heating process often leads to undesirable coalescence of the particles, resulting in increased particle size and the formation of hard agglomerates. To overcome this problem, Wickleder and co-workers have recently developed a simple strategy using ionic liquid that harnesses the power of ultrasonic waves to synthesize $\text{BaFCl}:\text{Eu}^{2+}$ nanocrystals under mild conditions.³⁹³ This sonochemical technique produces Eu^{2+} -doped BaFCl nanocrystals with a relatively narrow size distribution.

Interestingly, it is easy to grow epitaxially heterogeneous $\text{NaREF}_4@\text{CaF}_2$ core-shell nanostructures using conventional wet chemical methods because the CaF_2 crystal is isostructural to NaREF_4 tetrafluorides in cubic phase. A variety of $\text{NaREF}_4@\text{CaF}_2$ nanocomposites, such as $\text{NaYbF}_4:\text{Tm}@\text{CaF}_2$, $\text{NaYbF}_4:\text{Tm}/\text{Nd}@\text{CaF}_2:\text{Nd}@\text{CaF}_2:\text{Nd}/\text{Yb}/\text{Er}$ nanoparticles, $\text{NaYbF}_4:\text{Tm}@\text{CaF}_2@$ alpha- NaDyF_4 , $\text{NaYbF}_4@\text{CaF}_2$, and

$\text{CaF}_2@\text{NaGdF}_4$ nanoparticles, have been developed (Figure 9c,d).^{394–398} Despite dissimilar crystal structures, the group of Yan and Sun synthesized $\beta\text{-NaLnF}_4@\text{CaF}_2$ core-shell nanoparticles.³⁹⁹ The authors demonstrated that the evolution of nanoparticle surfaces from hexagonal to cubic was triggered by the preferential exchange between Ca^{2+} and Na^+ cations. This removed the large barrier and allowed heteroepitaxial growth of cubic CaF_2 shell on the hexagonal NaLnF_4 . Compared to homogeneous $\text{NaREF}_4@\text{NaREF}_4$, the heterogeneous $\text{NaREF}_4@\text{CaF}_2$ core-shell structures can suppress the ion leakage between core and shell layers.⁴⁰⁰ In addition, the CaF_2 shell is considered to be more biocompatible than rare-earth fluorides for *in vivo* biological applications.

3.2.2.2. Alkaline-Earth Sulfides. Alkaline-earth sulfides are useful for the uptake of divalent rare-earth dopants. The most representative examples are Eu^{2+} -doped CaS and SrS synthesized by alkoxide and coprecipitation.^{131,401,402} Due to the high sensitivity of the f–d transition of Eu^{2+} to the local lattice environment, the emission wavelength of Eu^{2+} can be used to verify the incorporation of Eu^{2+} into the octahedral site of the CaS lattice. Meijerink and co-workers reported an approach to doping CaS and SrS materials with Eu^{2+} using one precursor.⁴⁰¹ They found that the reactivity of the dopant and the host precursor determines the doping efficiency. Precursors with low reactivity require a relatively high decomposition temperature to promote the diffusion of Eu^{2+} through the SrS lattice.

Moreover, Eu^{2+} -doped CaS nanomaterials exhibited persistent luminescence when codoped with other trivalent lanthanides. For example, Capobianco's group prepared $\text{CaS}:\text{Eu}^{2+}/\text{Dy}^{3+}$ nanophosphors that showed persistent red emission.⁴⁰³ They demonstrated that Eu^{2+} dopants can produce shallow traps below the conduction band of CaS , while the addition of Dy^{3+} as a codopant can produce shallow and deeper traps, resulting in prolonged afterglow of 5 h. Chen's group has codoped Eu^{2+} and Sm^{3+} into CaS nanocrystals.⁴⁰⁴ They found that the resulting nanocrystals exhibit intense luminescence of Eu^{2+} at 650 nm, which responds quickly to NIR stimulation, lasts longer than 2 h, and has a low power density threshold of 10 mW cm^{-2} .

Owing to their low phonon energies, alkaline-earth sulfides are also suitable hosts to achieve NIR luminescence by rare-earth doping. For example, Chen and co-workers reported the synthesis of $\text{Ce}^{3+}/\text{Er}^{3+}$ - and $\text{Ce}^{3+}/\text{Nd}^{3+}$ -codoped CaS nanoparticles that exhibited blue-LED-excitable NIR luminescence.⁴⁰⁵ Ce^{3+} ions in CaS can be efficiently excited by blue-light through the 4f–5d transition and can subsequently sensitize the 4f–4f emissions of Er^{3+} and Nd^{3+} in the NIR region.

3.2.2.3. Alkaline-Earth Oxides/Nitrides. Alkaline-earth oxides and nitrides are commonly used to accommodate rare-earth ions and can also accommodate unusual valences such as Ce^{4+} and Eu^{2+} . The resulting materials are mainly for catalysis and photoluminescence.

For example, the lattices of alkaline-earth aluminates are suitable for isovalent doping with Eu^{2+} ions.⁴⁰⁶ Co-combustion of $\text{Al}(\text{NO}_3)_3$, $\text{Sr}(\text{NO}_3)_2$, $\text{Eu}(\text{NO}_3)_3$, and $\text{CO}(\text{NH}_2)_2$ incorporated Eu^{2+} ions into the SrAl_2O_4 host.⁴⁰⁷ This combustion reaction was an exothermic process that avoided extensive thermal treatment. Meanwhile, $\text{CO}(\text{NH}_2)_2$ produced a reducing atmosphere to convert Eu^{3+} to Eu^{2+} . Coprecipitation of metal nitrates with $(\text{NH}_4)_2\text{CO}_3$ followed by annealing led to the production of $\text{Sr}_4\text{Al}_{14}\text{O}_{25}$ nanoparticles encoded with Eu^{2+}

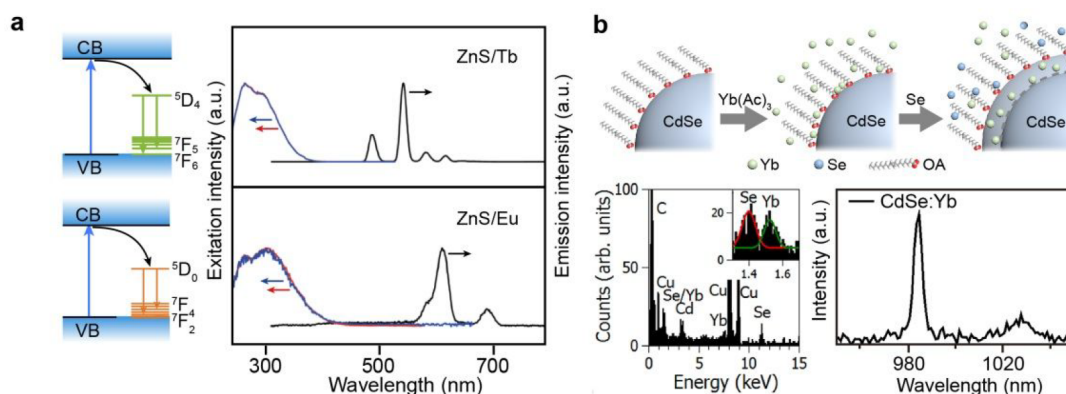


Figure 10. (a) Illustration of the energy transfer process from ZnS to rare-earth ions and normalized time-gated excitation and emission spectra of ZnS/Tb [$\lambda_{\text{ex}} = 300$ nm (black), $\lambda_{\text{em}} = 490$ nm (red), $\lambda_{\text{em}} = 545$ nm (blue)] (top panel) and ZnS/Eu [$\lambda_{\text{ex}} = 300$ nm (black), $\lambda_{\text{em}} = 616$ nm (red), $\lambda_{\text{em}} = 696$ nm (blue)] (bottom panel) nanoparticles. (b) Illustration of the three-step synthesis process, EDS analysis, and emission spectrum of CdSe:Yb (Adapted with permission from refs 242 and 244. Copyright 2010 and 2013 American Chemical Society).

and Dy³⁺.⁴⁰⁸ Other examples of isovalent Eu²⁺ doping include BaMgAl₁₀O₁₇:Eu²⁺ by solution combustion methods^{409,410} and Sr₈CaSc(PO₄)₇:Eu²⁺ by thermal treatment in a reducing atmosphere CO at high temperatures.⁴¹¹ Another notable example is Sr₂Si₃N₈ phosphors doped with Eu²⁺ used in solid-state lighting.⁴¹²

Ce⁴⁺ can be incorporated into cation sites (IV) in oxometallates. For example, Zhang et al. investigated the preparation of Ce⁴⁺-doped BaZrO₃ phosphors by a hydrothermal method,⁴¹³ in which Ce⁴⁺ doping was achieved by replacing Zr⁴⁺ sites in the crystal lattice. Incorporation of Ce⁴⁺ into the BaZrO₃ lattice enhanced the dual-frequency sonocatalytic generation of reactive oxygen species in aqueous solvents. Extensive studies have explored the isovalent doping of Ce⁴⁺ in TiO₂ and ZrO₂ nanostructures.^{414–418} Because the ionic size of Ce⁴⁺ is much larger than that of Ti⁴⁺ (1.02 versus 0.68 Å), the doping process can cause lattice defects, such as dislocations, in TiO₂, leading to changes in the binding energies of Ti and O.⁴¹⁹

3.2.3. Semiconductor Quantum Dots. Semiconductor quantum dots (QDs) are characterized by large absorption coefficients ($\epsilon > 10^5$ M⁻¹ cm⁻¹) and tunable emission energies. It has been shown that efficient energy transfer between QDs and rare-earth ions can be readily achieved in hybrid systems.⁴²⁰ Doping QDs with rare-earth ions can greatly enhance the luminescence of rare-earth dopants due to the antenna effect of the QD host. On the other hand, doping with rare-earth ions can affect the crystalline and electronic structures of QDs and alter their excitonic properties, resulting in enhanced band-edge emission or improved photocatalysis.⁴²¹ Based on various element combinations, QDs of group II–VI and halide perovskites are commonly explored for rare-earth doping.

3.2.3.1. Group II–VI Quantum Dots. Group II–VI QDs, such as CdSe, CdTe, and ZnS, have attracted the most attention and can now be routinely prepared by several synthetic protocols with precise control over particle size and morphology. However, it remains challenging to incorporate rare-earth ions into these QDs due to the wide large variation in ionic radii and charge imbalance between the Ln³⁺ ions and the host cations.

In most doping processes, rare-earth ions are mainly located at the surface of the host QDs. For example, Døssing et al. have attempted to dope CdSe QDs with Ln³⁺ (Ln = Tb, Eu, Gd) by

a thermal decomposition reaction.⁴²² In their method, the temperature and the addition of amine were two crucial factors in the preparation of Ln³⁺-modified CdSe QDs. The surface-doped Ln³⁺ ions decreased the quantum yield and shortened the lifetime of the excited states of CdSe QDs. In addition, sensitization of surface dopants required high-energy excitation larger than the lowest absorption band of the CdSe QDs. The researchers treated the surface dopants as energy traps with decay kinetics independent of the dopants in the core. They also proposed that Ln³⁺-related traps are associated with the surface of CdSe hosts. Therefore, surface dopants quench the photoluminescence, but hot excitons produced at the dopant sites can trigger the sensitization and emission of Ln³⁺ dopants.

Petoud, Waldeck, and colleagues successfully doped Ln³⁺ (Ln = Tb, Eu) ions onto the surface of ZnS QDs by a postsynthetic modification, based on the addition of excess Ln(NO₃)₃ salts into the reaction during thermal decomposition (Figure 10a).⁴²³ To locate Ln³⁺ dopants, they measured the luminescence decay rate of excited Eu³⁺ ions and the intensity ratio of ⁵D₀ → ⁷F₂ to ⁵D₀ → ⁷F₁ as a standard of comparison. Since these two factors depend on the symmetry of the Eu³⁺ coordination environment, the ⁵D₀ → ⁷F₂ transition (~616 nm) of Eu³⁺, which has an electric dipole character, is usually forbidden in a perfectly octahedral environment, while it is allowed in a less symmetric environment and has a higher oscillator strength. In contrast, the ⁵D₀ → ⁷F₁ transition (~590 nm) of Eu³⁺ is a magnetic dipole transition that is insensitive to its environment. Surface sites are more asymmetric than inner core sites. According to emission data, Eu³⁺ dopants are mainly located at particle surfaces. In addition, ZnS QDs can act as antennae to sensitize Ln³⁺ emission that is stable for several weeks.

Organic molecules have been used to control rare-earth doping on the surfaces of QDs. To investigate the effect of spatial confinement on the energy transfer between ZnS QDs and Tb³⁺ ions, a reverse micelle method (water/sulfosuccinate/isooctane) was used to synthesize different types of ZnS QDs in the presence of Tb³⁺ ions.⁴²⁴ Tb³⁺ ions and ZnS nanoparticles were separated by an organic sulfosuccinate layer, and ZnS sensitized the Tb³⁺ emission through an intramolecular energy transfer mechanism.

To improve rare-earth doping of QDs, Martín-Rodríguez et al. adopted a three-step method to incorporate Yb³⁺ ions into CdSe QDs.²⁴⁴ First, CdSe nanocrystals were prepared by

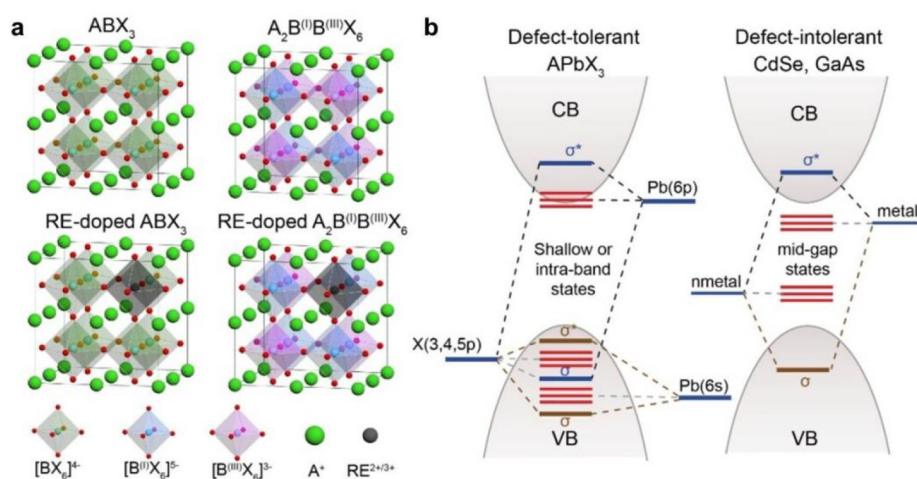


Figure 11. (a) Structural diagrams of the untreated perovskites ABX_3 and $A_2B^{(II)}B^{(III)}X_6$ and their rare-earth-doped counterparts. (b) Schematic diagrams of the electronic band structures of defect-tolerant ABX_3 perovskites and defect-intolerant semiconductors (CdSe and GaAs). σ and σ^* refer to bonding and antibonding orbitals, respectively (Adapted with permission from ref 426. Copyright 2017 American Chemical Society).

heating Cd-oleate and Se powder in trioctylphosphine. Yb^{3+} ions were then adsorbed onto nanocrystal surfaces, followed by the growth of a CdSe shell (Figure 10b). In a similar process, a model with trapped doping was used to fabricate Eu-encoded ZnS QDs.⁴²⁵ In this model, a new strategy was also used to adsorb Eu^{3+} ions onto the surface of ZnS QDs. Incorporation of Eu^{3+} ions into ZnS nanocrystals was achieved by further growth of an additional ZnS shell.

For Cd-based QDs, the significant toxicity usually hinders the practical application of these phosphors in the biological field. To improve the cytocompatibility of CdTe QDs, Schiff base ligands were employed to coordinate them with Ln^{3+} ($Ln = Yb, Tb, \text{ and } Gd$) ions by a microwave-assisted method.^{426,427} These doped QDs possess greater cytocompatibility than their unmodified counterparts and show potential for biolabeling in various environments.

In addition, divalent rare-earth ions such as Eu^{2+} , which allow $4f-5d$ transitions with stronger oscillator strengths, can be doped into QDs of Groups II–VI. For example, doping of ZnS nanoparticles with Eu^{2+} has been achieved by coprecipitation at elevated temperatures.^{428,429} Despite numerous efforts to dope II–VI QDs with rare-earth ions, the emission performance of the resulting nanoparticles is relatively modest. A more comprehensive summary of this field can be found in a recent review by Marin and Jaque.⁴³⁰

3.2.3.2. Halide Perovskite Quantum Dots. ABX_3 -type perovskites have become popular in recent years, owing to their excellent photoluminescence and photoelectronic properties, such as high quantum yield (>90%), narrow emission bandwidth (<100 meV), large absorption coefficient ($\sim 10^4 \text{ cm}^{-1}$), and tunable bandgaps (1.5–3 eV).⁴³¹ In cubic ABX_3 perovskite lattices, the A site is occupied by either cesium (Cs^+), methylammonium ($MA; CH_3NH_3^+$), or formamidinium ($FA; CH(NH_2)_2^+$). The B site is usually occupied by Pb^{2+} , and the X site by halide anions such as Cl^- , Br^- , and I^- . The $[BX_6]^{4-}$ octahedra are connected in a three-dimensional network, while the A-site cations reside in the large voids between them (Figure 11a). The structural stability of halide perovskites can be evaluated by the Goldschmidt tolerance factor. The maximum tolerance factor, as mentioned above, limits the choice of A-site cations, considering the suitability of

12-coordinate geometry for the tightest possible packing configuration.⁴³²

An attractive feature of these perovskites is their unique “defect tolerance.” Lead halide perovskite nanocrystals retain good photoluminescent or photoelectric properties even when they contain a high density of defects (e.g., vacancies and interstitials, up to 1–2 at %).^{432,433} Such defect-tolerance has been attributed to the antibonding nature in the valence band (VB) maximum and the strong spin–orbit coupling in the conduction band (CB) minimum.⁴³⁴ Theoretical calculations suggest that lattice defect-induced impurity states reside either in the VB or CB bands or slightly below these bands, forming shallow or intraband states with no states in the middle of the bandgap (Figure 11b).⁴²⁶ This is thus quite different from the cases in conventional semiconductors such as CdSe and InP, whose defect states are mainly located within the bandgap.

Because of the high defect tolerance, it is expected that rare-earth ions can be doped into perovskite hosts without significant lattice distortion.^{435–437} First, the six-coordinate environment of the Pb^{2+} site is suitable for rare-earth substitution, and the slightly smaller size of rare-earth ions compared to Pb^{2+} (ionic radius 1.19 Å) makes them viable as dopants (Table 1). On the other hand, introduction of emitting lanthanide dopants is expected to broaden the luminescence spectrum of perovskites. In addition, defect tolerance has enabled analogs of $AB^{(I)}B^{(III)}X_6$ halide double perovskites such as $Cs_2AgInCl_6$ and $Cs_2AgBiBr_6$.^{438–442} Bi^{3+} and In^{3+} sites are also suitable for occupation by trivalent rare-earth ions.

Rare-earth-doped halide perovskites can be prepared using conventional synthetic approaches derived directly from the preparation of pristine halide perovskites. For instance, colloidal rare-earth-doped halide perovskite nanocrystals have been prepared by ultrasonic treatment,⁴⁴³ hot injection method,^{40,251,444,445} room-temperature supersaturated recrystallization,⁴⁴⁶ and *in situ* generation.^{39,447,448} Among these techniques, the hot injection method has the advantage of providing nanocrystals with good colloidal dispersibility and size tuning.

In 2017, Song and co-workers reported the synthesis of rare-earth-doped $CsPbX_3$ ($X = Cl, Br$) nanocrystals by hot injection.⁴⁰ In their work, $CsPbCl_xBr_{3-x}$ nanocrystals doped

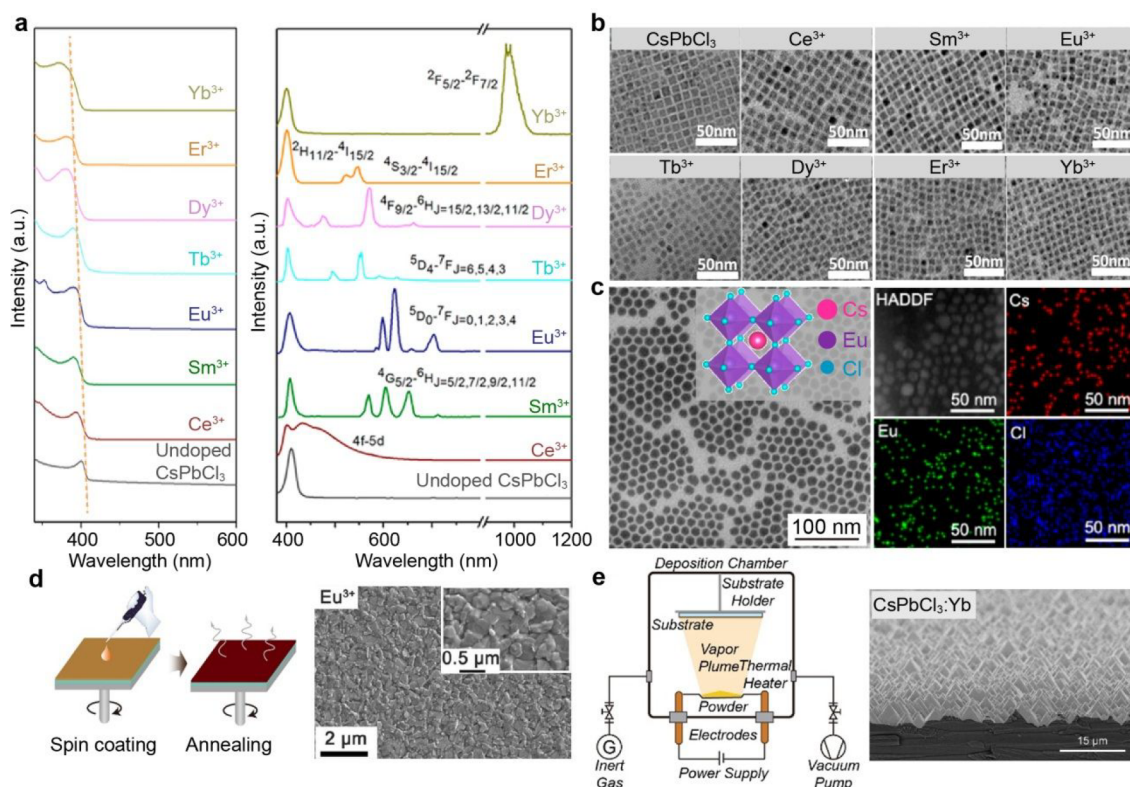


Figure 12. (a) Absorption and emission spectra of CsPbCl₃ nanocrystals doped with different rare-earth ions. (b) TEM images of CsPbCl₃ nanocrystals doped with various rare-earth ions. (c) TEM image and EDS mapping of CsEuCl₃ nanocrystals. (inset) Extended unit cell of CsEuCl₃. (d) Schematic of spin-coating method and SEM images of a typical CsPbI₃:Eu²⁺ formation by chemical vapor deposition. (e) Schematic of the chemical vapor deposition method and SEM images of typical CsPbCl₃:Yb³⁺ films formed by chemical vapor deposition (Adapted with permission from refs 444 and 449–451. Copyright 2017, 2019, 2020 American Chemical Society; Copyright 2019 American Association for the Advancement of Science).

with Yb³⁺/Er³⁺/Ce³⁺ were fabricated by injecting a hot Cs-oleate precursor into a mixed solvent of ODE, OM, and OA in the presence of lanthanide chlorides and PbBr₂ at 200 °C. The existence of lanthanide elements in CsPbCl₃Br_{3-x} hosts was confirmed by XRD, ICP-OES, XPS, and photoluminescence characterizations. In another study, Song and co-workers extended rare-earth doping in the CsPbCl₃ host system to almost the entire lanthanide family, including Ce³⁺, Sm³⁺, Eu³⁺, Tb³⁺, Dy³⁺, Er³⁺, and Yb³⁺, using a similar protocol (Figure 12a,b).⁴⁴⁴ CsPbCl₃ quantum dots doped with rare-earths exhibited cubic shapes with an average size of 7.8 to 6.3 nm. The particle size decreased with increasing atomic number of the rare-earth dopant. XRD characterization showed that diffraction peaks of rare-earth-doped nanocrystals gradually shifted toward large angles in contrast to untreated samples, which was attributed to lattice contraction caused by the smaller ionic radii of lanthanide dopants (1.03 Å for Ce³⁺ and 0.86 Å for Yb³⁺) compared to Pb²⁺ (1.19 Å).⁴⁵²

In addition to CsPbCl₃ hosts, rare-earth-doped CsPbBr₃ nanocrystals can also be synthesized using metal bromides as precursors. This was well exemplified by Yao et al., who reported the synthesis of CsPbBr₃:Ce³⁺ nanocrystals by injecting the Cs-oleate precursor into a hot mixture of ODE, OM, and OA in the presence of metal bromides at 185 °C.²⁵¹ The successful doping with Ce³⁺ was confirmed by EDS mapping. Notably, the actual doping concentration of Ce³⁺ in the host was an order of magnitude lower than the feed ratio in the reaction precursor, which can be attributed to the

unbalanced reaction activities between Pb²⁺ and RE³⁺ with halide anions.

Intriguingly, divalent rare-earths are more easily incorporated into CsPbX₃ hosts, as manifested by extremely high doping concentrations. In 2019, Lee and co-workers discovered that injection of a Cs-oleate precursor at 180 °C into organic solvents in the presence of YbI₂ and PbI₂ leads to cubic CsYbI₃ nanocrystals in which Pb²⁺ sites are completely replaced by Yb²⁺ ions.⁴⁵³ The Goldschmidt tolerance factor (*t*) and octahedral factor (*μ*) were calculated to be 0.86 and 0.46, indicating that cubic CsYbI₃ is highly stable at room temperature. High-resolution TEM images of the synthesized nanocrystals revealed a monodisperse cubic morphology with an average diameter of 9.5 nm, consistent with the calculated and experimental XRD patterns. Similar results were also shown in a recent study of Eu²⁺-doped CsPbCl₃ nanocrystals, in which 100% substitution of Pb²⁺ by Eu²⁺ was achieved (Figure 12c).⁴⁴⁹

During hot injection, metal bromide and iodide species decompose at high temperatures, limiting reaction temperatures to below 200 °C and disfavoring the formation of high-crystallinity products. To address this problem, a reverse injection route at relatively high temperatures for rare-earth doping has been developed by several groups using metal acetates in organic solvents. For example, the Gamelin,^{454,455} Wu,⁴⁵⁶ and Artizzu⁴⁵⁷ groups independently reported doping CsPbCl₃Br_{3-x} nanocrystals with La³⁺, Yb³⁺, or Er³⁺ by injecting a trimethylchlorosilane (TMS-Cl) or trimethylbromosilane (TMS-Br) precursor into a mixture of ODE, OM, and OA with

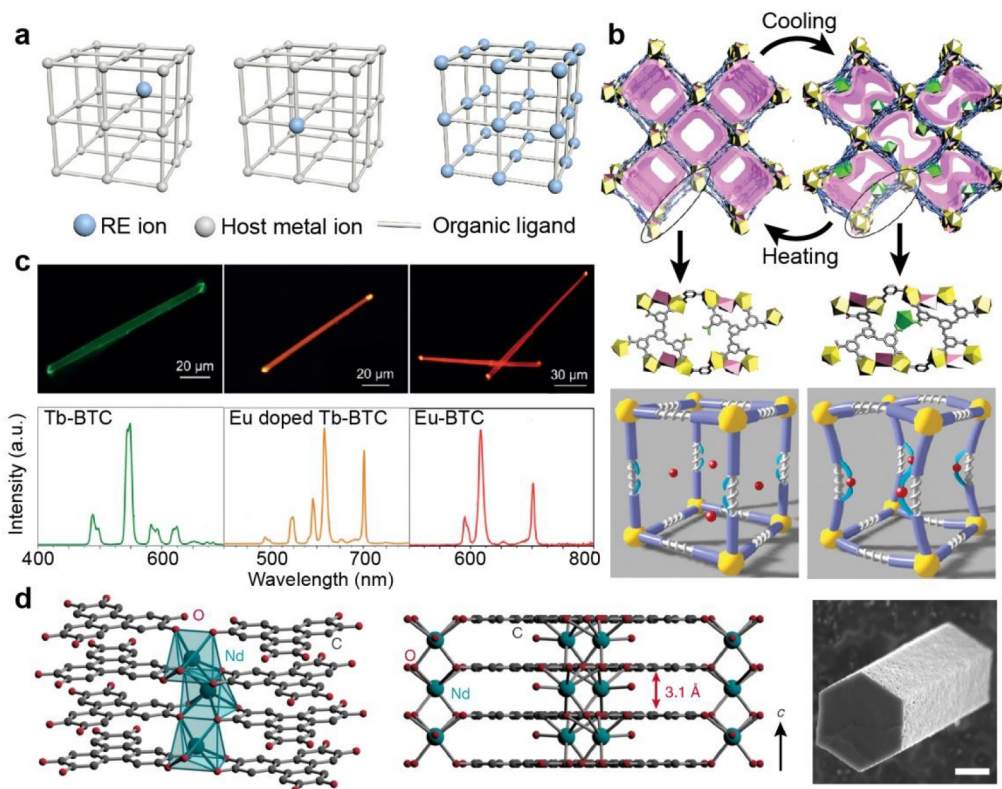


Figure 13. (a) Schematics of MOFs with absorbed, doped, or lattice-occupied rare-earth ions. (b) Schematic of the temperature-induced single-crystal to single-crystal transformations of rare-earth-doped MOFs. (c) Photoluminescence microscopy images and emission spectra of crystalline RE-BTC microrods. (d) Structural representation and SEM image of a NdHHTP crystal. The scale bar is 1 μm (Adapted with permission from refs 476–478. Copyright 2015, 2017 Wiley-VCH Verlag GmbH & Co. KGaA, Weinheim; Copyright 2020 Nature Publishing Group).

lanthanide and lead acetates at ~ 240 $^{\circ}\text{C}$. This approach yielded larger nanocrystals with a typical size over 10 nm. Importantly, this protocol can be easily extended to the synthesis of rare-earth-doped halide double perovskites, such as $\text{Cs}_2\text{AgInCl}_6$, $\text{Cs}_2\text{AgBiCl}_6/\text{Cs}_2\text{AgBiBr}_6$, and $\text{Cs}_2\text{AgIn}_x\text{Bi}_{1-x}\text{Cl}_6$ nanocrystals.^{458–460} It is worth noting that the reaction temperature for the preparation of halide double perovskites is generally lower than that for lead halide perovskites due to the low decomposition temperature of the silver precursors.

Apart from colloidal nanocrystals, rare-earth-doped halide perovskite thin films have also been prepared by spin coating or chemical vapor deposition (CVD). In typical spin coating, precursors of metal halides (lead, rare-earth, and cesium halides) or MA and FA halides were first dissolved in a polar solvent (e.g., DMF and DMSO). The solutions were then spin-coated on a substrate, after which the remaining solvent was removed by annealing to obtain dense perovskite films with uniform grain size (Figure 12d).⁴¹⁹ Using this protocol, Tang and co-workers doped Sm^{3+} , Tb^{3+} , Ho^{3+} , Er^{3+} , and Yb^{3+} ions into CsPbBr_3 thin films on fluorine-doped TiO_2 substrates.⁴⁶¹ These rare-earth dopants were incorporated into the CsPbBr_3 lattice, as confirmed by combined characterizations including XRD, ICP-AES, and XPS. Additionally, $\text{MAPbI}_3:\text{Eu}^{2+}$, $\text{MAPbI}_3:\text{Eu}^{2+}/\text{Eu}^{3+}$, $\text{MAPbI}_3:\text{Nd}^{3+}$, $\text{CsPbI}_3:\text{Eu}^{3+}$, and $\text{CsPbBr}_3:\text{Eu}^{2+}$ were also successfully prepared by spin coating.^{450,462–465}

Despite its usefulness, spin coating is a solution-based process that may impose certain limitations on film manufacture. For example, although the precursors PbBr_2 , PbI_2 , and MAI are readily soluble in common solvents, Cs-

based halide salts generally disperse poorly in liquids, limiting the range of compositions available for synthesis. Moreover, spin coating cannot be performed on substrates with irregular topology. This limitation can be resolved by the solvent-free CVD method, which allows thin film deposition on arbitrary substrates. Gamelin and co-workers have recently demonstrated a single-source CVD method for preparing $\text{CsPbCl}_3:\text{Yb}^{3+}$ and $\text{CsPbCl}_{1.5}\text{Br}_{1.5}:\text{Yb}^{3+}$ films on substrates suspended 5–20 cm above the source at rates ranging from ~ 0.05 to ~ 1000 \AA s^{-1} (Figure 12e).⁴⁵¹ A crucial point is that the feedstocks were mechanochemically prepared prior to deposition using a planetary ball mill, circumventing the nonstoichiometry caused by unbalanced decomposition temperatures in conventional multisource coevaporation routes. The perovskite film preserved the features of the patterned submicron structures in the silicon substrates, which is useful for photon absorption.^{466,467}

3.2.4. Metal–Organic Frameworks. Metal–organic frameworks (MOFs) are organic–inorganic hybrid crystalline porous materials consisting of a three-dimensional network of metal ions or clusters connected by multidentate organic molecules.^{468–470} These organic molecules typically contain carboxylate, phosphonate, and pyridyl functional groups. The bonding energy between the metal ion and the organic molecule is moderate, which allows reversible bond formation and dissolution during MOF synthesis.²⁶¹ MOFs have large pore sizes (3–100 \AA), high porosity (up to 90%), large surface areas (up to 7000 $\text{m}^2 \text{g}^{-1}$), and low densities (~ 0.13 g cm^{-3}).^{471,472} In addition, many organic ligands with large light absorption coefficients can act as antennas to sensitize

luminescent metal centers in the systems. In principle, rare-earth ions can be directly incorporated into MOF hosts, either as guests (rare-earth-absorbing MOFs), as dopants (rare-earth-doped MOFs), or as metal nodes (rare-earth-based MOFs) (Figure 13a). Incorporated rare-earth ions can work as luminescent centers, while connecting ligands can serve as luminescent antennas that participate in energy transfer processes.^{473,474}

3.2.4.1. Rare-Earth-Absorbed MOFs. The large pore structure in MOFs can accommodate RE ions. In a representative example, Rosi and co-workers developed a series of “bio-MOFs-1” ($\text{Zn}_8(\text{ad})_4(\text{BPDC})_6\text{O}\cdot 2\text{Me}_2\text{NH}_2$, 8DMF, 11H₂O) with columnar zinc-adeninate assemblies and biphenyl dicarboxylate linkers.⁴⁷² The bio-MOF-1 was anionic with mobile DMA cations located in 1-D channels.⁴⁷⁵ Therefore, labile DMA cations can be easily replaced with lanthanide ions by soaking them in DMF solutions of lanthanide nitrate salts. Successful incorporation of lanthanide ions in bio-MOFs-1 was made evident by fluorescence measurements. The emission spectra of the chromophoric structure in the bio-MOF-1 clearly showed characteristic $f-f$ transitions of Sm^{3+} , Tb^{3+} , Eu^{3+} , and Yb^{3+} under 340 nm excitation. It is noteworthy that rare-earth emissions can be detected even under aqueous conditions, although they are strongly attenuated by water molecules. This suggests that the bio-MOF-1 scaffold can sensitize rare-earth dopants and protect guest ions from extraction by solvents.

In another study, Yan and co-workers reported the preparation of Eu^{3+} -encapsulated MIL-53-COOH(Al)MOFs by immersing pristine MOFs in corresponding lanthanide salt solutions.⁴⁷⁹ Trivalent rare-earths were encapsulated in the one-dimensional pore channels of MOFs due to interactions with the carboxyl groups of the ligands. These Eu^{3+} -encapsulated MOFs can be used to detect Fe^{3+} ions because the luminescence of Eu^{3+} emission is quenched by energy transfer. Similarly, Cui, Qian, and co-workers reported Tb^{3+} -encapsulated MIL-100(In)MOFs with strong oxygen-sensitive emission of Tb^{3+} , which makes them attractive for the development of highly sensitive oxygen sensors.⁴⁸⁰

Incorporation of rare-earth ions into MOFs can alter local structures. This was illustrated by Zhang and co-workers, who prepared Eu^{3+} -encapsulated MOFs in the form of (H_3O^+) - $\text{Eu}_{0.5}[\text{EuNa}_{0.5}\text{L}(\text{DMF})(\text{H}_2\text{O})]\cdot(\text{solvent})_x$ (**EuL**).⁴⁷⁶ Due to structural transformation by cleavage and formation of dynamic Eu–O bonds, **EuL** MOFs can transform between $C2/c$ and $P2_1/n$ space groups, which is accompanied by rapid release or deposition of free Eu^{3+} ions in the channels. This reversible structural transformation can be triggered by varying the temperature. At a low temperature (193 K), free Eu^{3+} ions can be trapped by free carboxylate groups, leading to immediate conformational changes in the **EuL** MOFs. When the temperature is gradually increased to room temperature, trapped Eu^{3+} ions gradually escape from the encapsulation, and the MOFs return to their original structures (Figure 13b).

3.2.4.2. Rare-Earth-Doped MOFs. Apart from occupying the pores of MOFs, rare-earth ions often occupy nodal points as dopants. The main methods for preparing rare-earth-doped MOFs are cation exchange and hydrothermal synthesis.

An early example is the preparation of Dy^{3+} -doped $\text{Cd}_{1.5}(\text{H}_3\text{O})_3[(\text{Cd}_4\text{O})_3(\text{hett})_8]\cdot 6\text{H}_2\text{O}$ MOFs through cation exchange by soaking pristine MOFs in lanthanide nitrate solution for 3 weeks.⁴⁸¹ Crystallographic studies showed that the original topology was preserved after Dy^{3+} doping, except

that hydroxybridged square planar $\{\text{Dy}_4(\mu_2\text{-OH})\}^{11+}$ units replaced the $\{\text{Cd}_4(\mu_4\text{-O})\}^{6+}$ units at vertices of the octahedron in the parent MOFs. Because of aliovalent substitution, positively charged MOFs were assumed to be compensated by negatively charged NO_3^- anions confined in MOF channels.

Cation exchange at room temperature is usually time-consuming but can be accelerated by heating. For example, Lejaeghere and co-workers demonstrated a fast and simple microwave method for doping UiO-66 MOFs with rare-earth ions (Ce^{4+} , Nd^{3+} , Eu^{3+} , and Yb^{3+}).⁴⁸² Incorporation of rare-earth ions into the Zr sites of MOFs was confirmed by XRD characterization, which showed a shift of the diffraction peaks to low angles. Dopant distributions were further verified by EDX elemental mapping, which showed homogeneous distribution of Ce^{4+} ions with some aggregations at the edges, probably due to limited diffusion of rare-earth precursors in the materials. Doping of rare-earth ions in inorganic nodes can change the electronic structure of UiO-66 MOFs, improving the photocatalytic activity of the hosts. Doping induces a new energy band within the bandgap and promotes ligand-to-metal charge transfer (LMCT) between the metal node and the ligand.

Hydrothermal synthesis is a straightforward synthetic method for rare-earth-doped MOFs, by which the solubility of organic linkers in the solvent can be greatly promoted at high temperatures to facilitate material synthesis.^{483–485} For example, Nenoff and co-workers prepared Eu^{3+} -doped SMOF-1 ($\text{In}(\text{BTB})_{2/3}(\text{OA})(\text{DEF})_{3/2}$) by reacting $\text{In}(\text{NO}_3)_3$ and EuCl_3 directly with 1,3,5-tris(4-carboxyphenyl)benzene (BTB) and oxalic acid in a mixture of N,N' -diethylformamide and ethanol at 115 °C for 4 days.⁴⁸⁶ The eight-coordinated indium sites in SMOF-1 can accommodate large Eu^{3+} ions. The pristine SMOF-1 showed broad emission centered at ~500 nm under excitation at 380 nm, which was attributed to the ligand-based $\pi-\pi^*$ transition and subsequent LMCT transition. Introduction of Eu^{3+} dopants resulted in a particularly narrow red emission band, offering new opportunities for the development of MOF-based solid-state illumination.

3.2.4.3. Rare-Earth-Based MOFs. Rare-earth-based MOFs refer to a special type of MOFs with nodes or lattice sites completely occupied by rare-earth ions or secondary building units.^{24,487} These MOFs have several advantages over conventional transition-metal-based MOFs.⁴⁸⁸ First, rare-earth ions have a high coordination number and flexible coordination geometry.⁴⁸⁹ Second, lanthanide ions are hard Lewis acids, with their coordination chemistry dominated by multidentate ligands featuring hard donor atoms such as oxygen and nitrogen.^{490,491} Last, rare-earth doping enables incorporation of multiple types of rare-earth ions into individual MOF hosts without causing noticeable crystal imperfections.⁴⁹² By doing so, tunable luminescence with controllable energy transfer processes can be achieved.⁴⁹³

Rare-earth-based MOFs are commonly synthesized by mixing organic ligands and rare-earths at mild temperatures (below 150 °C). For example, Eddaoudi and co-workers have prepared a series of RE-1,4-NDC-MOFs (RE = Eu, Tb) by heating 1,4-H₂NDC, $\text{Y}(\text{NO}_3)_3$, and 2-fluorobenzoic acid in a mixed solution of DMF, H₂O, and HNO₃ at 115 °C for 60 h.^{494,495} The size and morphology of the resulting MOFs can be regulated by reaction time, temperature, and solvent ratio.

Energy transfer processes and multicolor emissions have been extensively studied in MOFs containing $\text{Eu}^{3+}/\text{Tb}^{3+}$ ion pairs. An excellent example is Ln-BTC (Ln = Tb^{3+} , Eu^{3+} ; BTC

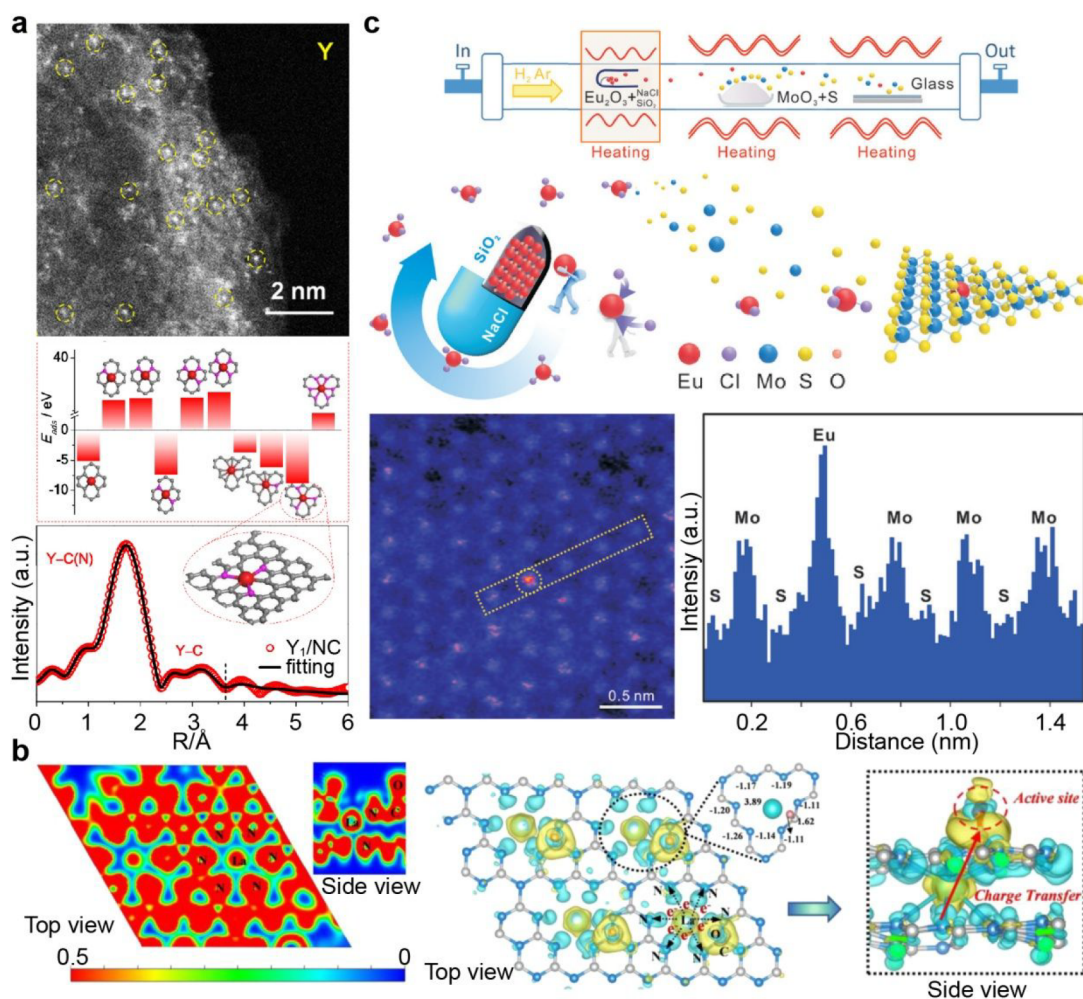


Figure 14. (a) HAADF-STEM images of Y₁/NC, calculated active site structures of a single yttrium atom and corresponding adsorption energies, as well as FT-EXAFS fit in R-space of Y₁/NC. (b) Electronic site function and differential charge density analysis of O/La-CN (the blue region indicates charge accumulation and the yellow region indicates charge loss), C, N, O, and La atoms are gray, blue, red, and green spheres, respectively. (c) Schematic of the MASR-CVD synthesis process for Eu-embedding MoS₂ single crystals, HAADF-STEM atomic image of Eu-embedding MoS₂, and intensity profile of the region marked with a dotted box (Adapted with permission from refs 16, 260, and 519. Copyright 2020 American Chemical Society; Copyright 2018 Wiley-VCH Verlag GmbH & Co. KGaA, Weinheim).

= 1,3,5-benzenetricarboxylic acid) MOFs, in which luminescence spectra can be fine-tuned by adjusting the Eu³⁺/Tb³⁺ ratio (Figure 13c). Other examples include Eu_xTb_{1-x}-DMBDC (DMBDC = 2,5-dimethoxy-1,4-benzenedicarboxylate), Eu_xTb_{1-x}-BDC (BDC = 1,4-benzenedicarboxylate), Eu_xTb_{1-x}-DSB (DSB = 3,5-disulfobenzate), Eu_xTb_{1-x}-L (L = 1,3-bis(4-carboxyphenyl)imidazolium), Eu_xTb_{1-x}-hfa (hfa = hexafluoroacetylacetonate), and Eu_xTb_{1-x}-BTC (BTC = 1,3,5-benzenetricarboxylate).^{496–502}

Rare-earth-based MOFs are generally considered to have low conductivity because linking organic groups are mostly insulators with small π -orbital conjugation. Recently, it has been found that these special MOFs exhibit proton conductivity.^{503–505} For example, Dincă and co-workers reported that Ln-HHTP MOFs (Ln = La, Nd, Ho, Yb; HHTP = 2,3,6,7,10,11-hexahydroxytriphenylene) exhibited efficient and tunable one-dimensional charge transport properties (Figure 13d).⁴⁷⁸ Among Ln-HHTP MOFs, Ho-HHTP MOFs exhibited the highest electrical conductivity of 0.05 S cm⁻¹ at 29 °C, which is within the range of the most conductive MOFs to date. In another representative work, Zaworotko and co-workers found that coordinate-saturated Gd

zeolite-like MOFs (Gd-ZMOFs) exhibit high longitudinal relaxivity.⁵⁰⁶ Compared with conventional Gd(III) complex-based contrast agents, these Gd-ZMOFs show higher stability and better contrast performance for MRI, which makes them attractive as potential contrast agents for clinical use.

3.2.5. 2D Layered Nanomaterials. Since the first isolation of graphene in 2004,⁵⁰⁷ two-dimensional (2D) layered nanomaterials have attracted great attention owing to their excellent chemical and physical properties. Recently, there has been growing research interest in doping 2D layered nanomaterials with rare-earth elements. They include graphene/graphene oxides,⁵⁰⁸ graphitic carbon nitrides,^{16,260,509–511} transition metal dichalcogenides (MoS₂, WS₂, WSe₂, or In₂Se₃),^{512–515} and layered metal oxides (layered RE hydroxides and 2D rare-earth oxides).^{516,517} Rare-earth dopants have been mainly introduced in these hosts as luminescent guests. They can also be employed to modify the electric and magnetic properties of 2D substrates. Owing to their high surface-to-volume ratios, rare-earth-doped 2D nanomaterials have great potential for miniaturization and intelligentization of functional devices in heterogeneous catalysis and optoelectronic applications.

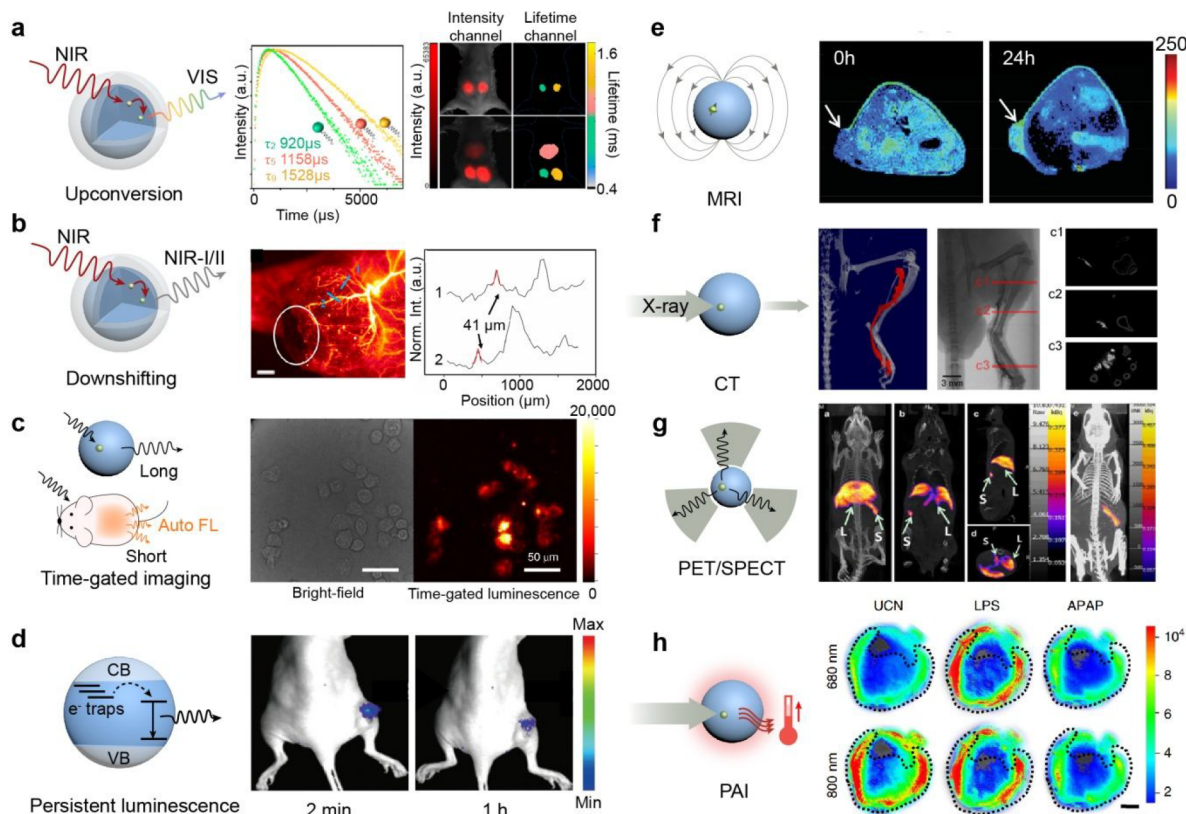


Figure 15. Schematic illustration of the principles of imaging modes and corresponding (a) visible fluorescence imaging, (b) near-infrared fluorescence imaging (scale bar, 2 mm), (c) time-gated imaging (scale bars, 50 μm), (d) persistent luminescence imaging, (e) magnetic resonance imaging (MRI), (f) computed tomography (CT scale bar, 3 mm), (g) positron emission computed tomography/single-photon emission computed tomography (PET/SPECT), and (h) photoacoustic imaging (PAI) of rare-earth-doped nanomaterials (Adapted with permission from refs 533–540. Copyright 2011, 2019, 2020 American Chemical Society; Copyright 2019 Nature Publishing Group; Copyright 2016 Wiley-VCH Verlag GmbH & Co. KGaA, Weinheim; Copyright 2013 Ivyspring International Publisher; Copyright 2012 Elsevier).

Graphene oxide nanosheets and rare-earth ions can form strong complexes through oxygen–metal coordination at the surface.⁵¹⁸ Shinde et al. synthesized graphene oxide nanosheets doped with La^{3+} , Eu^{3+} , or Yb^{3+} using a two-step method.⁵⁰⁸ Rare-earth ions were absorbed onto graphene in an acidic aqueous solution and then thermally exfoliated at high temperature. Successful doping the graphene substrate with rare-earths was mapped by EDS. Eu^{3+} -doped graphene improved the electrocatalytic performance, which can be attributed to additional doping sites and tuning the physical properties of the graphene substrate.

Moreover, rare-earth dopants can be atomically incorporated into layered carbon nitride structures via metal–nitrogen bonds. Shui and co-workers doped dispersed Y and Sc atoms into amorphous carbon supports.¹⁶ They showed that Y and Sc atoms were stabilized in large carbon voids by the coordination of six nitrogen and carbon atoms. This is in contrast to the conventional $\text{M}-\text{N}_4$ coordination structures ($\text{M} = \text{Fe}, \text{Co}, \text{Mn}$, etc.) in transition metal–carbon nitrides (Figure 14a). Y- and Sc-doped carbon nitrides were excellent single-atom catalysts, with high nitrogen and carbon dioxide reduction activity. In a parallel study, Dong and co-workers fabricated La single atoms on graphitic carbon nitrides using a one-step calcination method.²⁶⁰ XAS measurements and DFT calculations showed that La was complexed by both N and O groups in the substrates. In the structure, La–N facilitated energy transfer, which improved the selectivity in photocatalytic CO_2 reduction (Figure 14b).

Rare-earths can be introduced into 2D transition metal dichalcogenides. In 2016, Hao's group applied a two-step CVD method to fabricate large $\text{MoS}_2\text{:Er}$ thin films.⁵¹⁵ They first deposited Er^{3+} -doped Mo thin films on SiO_2/Si substrates and then sulfurized the samples by CVD. In a later study, Xu et al. designed a one-step matrix-assisted CVD method to synthesize Eu^{3+} -doped MoS_2 single crystals.⁵¹⁹ NaCl was added as a salt-assisted medium with Eu_2O_3 . The addition of salt supported the sustained release of Eu precursor and ensured the growth of high-quality Eu-doped MoS_2 single crystals on glass substrates (Figure 14c). The properties of doped 2D transition metal dichalcogenides are highly dependent on the nature of rare-earth dopants. While luminescent dopants such as Yb^{3+} , Er^{3+} , Eu^{3+} , and Ho^{3+} confer photoluminescence properties,^{513,520,521} doping MoS_2 with Dy^{3+} confers room-temperature ferromagnetism to the substrates.⁵²²

Layered rare-earth hydroxides (LRHs) are another type of promising 2D layered metal oxide for rare-earth doping. They typically contain layered $\text{RE}_x(\text{OH})_y \cdot n\text{H}_2\text{O}$ polyhydroxide structures with intercalated anions between the hydroxide layers.⁵²³ Suspended colloidal LRHs have been prepared mainly by top-down methods through exfoliation of bulk layered hydroxide crystals. Lee et al. first isolated thin nanosheets of LRHs from bulk $[\text{Gd}_2(\text{OH})_5(\text{H}_2\text{O})_x]\text{Cl}$ crystals by ultrasonic treatment in deionized water.⁵²⁴ Subsequent studies led to various colloidal LRHs, including Eu-hydroxide nanosheets,⁵²⁵ LGdH:RE ($\text{RE} = \text{Eu}^{3+}, \text{Tb}^{3+}, \text{Dy}^{3+}$) nanosheets,⁵²⁶ LYH:Tb nanosheets,^{527,528} and LTbH/LEuH nano-

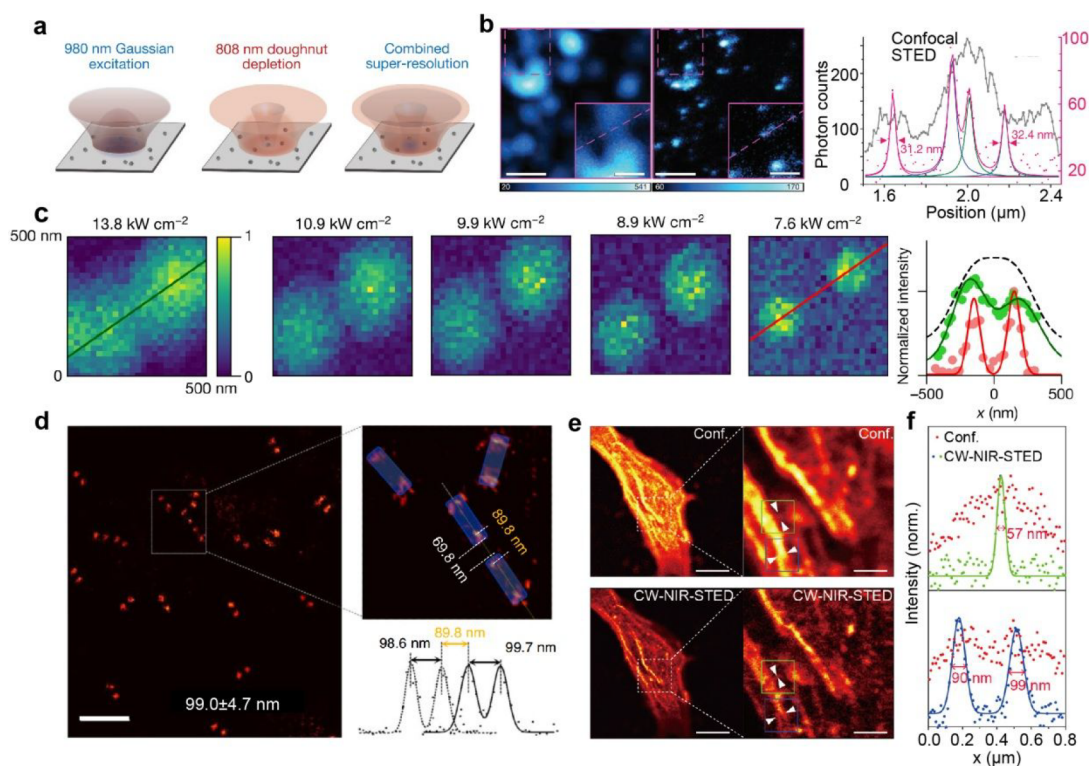


Figure 16. (a) Diagrams of upconversion-STED super-resolution imaging. (b) Comparison of confocal and super-resolution images and corresponding intensity profiles of 40 nm 8% Tm-doped UCNPs. Scale bars are 500 nm (main images) and 200 nm (insets). (c) Photon-avalanche single-beam super-resolution images and corresponding intensity profiles of Tm³⁺ avalanche nanoparticles. (d) Super-resolution image of heterogeneous nanorods. The scale bar is 400 nm. (e) Standard (top) and super-resolution (bottom) images of HeLa cells stained with Nd-doped nanoprobe. Scale bars are 10 μm (original images) and 2 μm (enlarged images). (f) Intensity profiles of selected areas from e (Adapted with permission from refs 543–546. Copyright 2017, 2020, 2021 Nature Publishing Group).

sheets.^{529,530} As an added benefit, LRHs can serve as templates for the synthesis of other ultrathin rare-earth substrates, such as Tm₂O₃ nanosheets and YPO₄:Eu nanophosphors.^{531,532}

4. TECHNOLOGICAL APPLICATIONS

To realize practical applications of rare-earth-doped nanomaterials, it is generally necessary to further functionalize these materials by assembling them with other types of nanostructured building blocks or integrating them into micro/nanosized devices. In the following, we provide an overview of a wide range of applications for rare-earth nanomaterials enabled by the complex interplay between the dynamics of doping and the underlying composite structures.

4.1. Bioapplications

There is particular interest in using rare-earth-doped nanomaterials for bioapplications, including bioimaging, single-particle biomarking, and therapeutics. Most current work focuses on rare-earth fluorides and oxysalt-based nanomaterials for bioapplications because they are chemical stable and biocompatible.

4.1.1. Bioimaging. Bioimaging is a subfield of biology that aims to image and understand the spatiotemporal mechanisms of biological processes, whether *in vivo*, *in vitro*, systematic, or cellular, for research and clinical purposes. Bioimaging is often combined with bioanalytical techniques to quantify these phenomena for meaningful interpretation. It is also combined with therapeutics to achieve image-guided treatment and intervention.⁵⁴¹ To date, a wide range of luminescent bioimaging techniques have been developed, including

upconversion luminescence, downshifting emission, time-gated luminescence imaging, and persistent luminescence imaging (Figure 15a–d).⁵⁴² Moreover, rare-earth-doped nanomaterials have been used as contrast agents to enhance the observability of specific targets for clinical imaging such as MRI, computed tomography (CT), positron-emission computed tomography/single-photon emission computed tomography (PET/SPECT), and photoacoustic imaging (PAI) (Figure 15e–h). Advances in the chemical and physical properties of rare-earth-doped nanomaterials can help address current bioimaging challenges. Developments in rare-earth-doped nanomaterials can improve chemical functionality for targeting, increase luminescence stability for long-term imaging, and push the boundaries of imaging biological events with unprecedented spatial and temporal resolution.

4.1.1.1. Upconversion Luminescence Imaging. Since the early 2000s, nanomaterials doped with rare-earth ions have served as luminescent probes for tissue and cell imaging. Upconversion luminescence imaging benefits from the NIR excitation of rare-earth-doped nanophosphors, which provides enhanced tissue penetration and suppression of the autofluorescence background.⁵⁴⁷ This technique has been widely applied to visualize biological activity for many applications. Many specific reports on upconversion nanophosphors for bioimaging have been written in the last decades.^{548–552} In the last five years, the application of upconversion luminescence imaging has been extended to include new features, such as spectral and temporal multiplexing⁵³³ and super-resolution imaging.^{29,553}

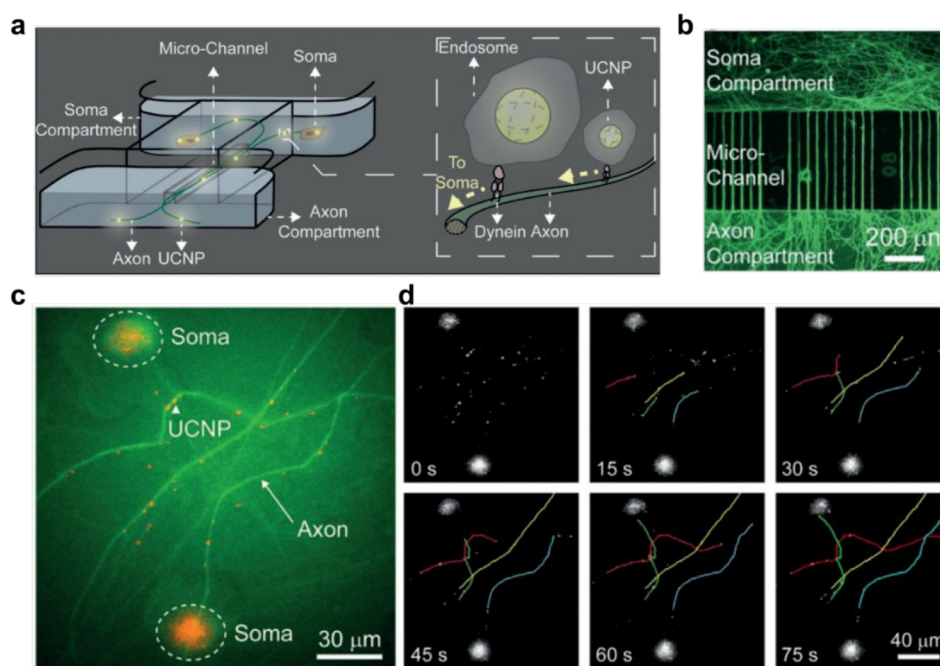


Figure 17. (a) Schematic illustration of a dual-chamber microchamber and tracking process. (b) Fluorescence microscopic image of calcein-labeled neurons. (c) Luminescence microscopic image showing typical dynein tracking. (d) Tracking of four individual upconversion luminescence spots (Adapted with permission from ref 560. Copyright 2019 Wiley-VCH Verlag GmbH & Co. KGaA, Weinheim).

In 2017, Liu et al. reported the use of $\text{Yb}^{3+}/\text{Tm}^{3+}$ -codoped NaGdF_4 nanoparticles for super-resolution imaging with stimulated emission depletion (STED).⁵⁴³ High Tm^{3+} doping (8 mol %) was used to induce strong cross-relaxation between activators and population inversion relative to the $^3\text{H}_6$ ground state of Tm^{3+} . The optimized spatial resolution is 28 nm, and the power of the depletion beam is much lower than conventional organic STED probes (Figure 16a and b). This method requires dual laser excitation at 980 and 808 nm to realize emission depletion for STED imaging. Single-beam super-resolution imaging has also been developed based on photon-avalanche upconversion.^{544,554} In 2019, Bednarkiewicz and co-workers theoretically predicted that photon-avalanching can constrain the point spread function in imaging.⁵⁵⁴ They investigated photon avalanche in Nd^{3+} -doped nanoparticles under nonresonant 1064 nm photoexcitation. The simulations resolved to 20 nm features when the avalanching-induced nonlinearity exceeded 80. In 2021, Lee et al. went a step further and experimentally demonstrated such an effect in Tm^{3+} -doped nanocrystals.⁵⁴⁴ In their experimental study, the avalanching emission from nanoparticles could scale nonlinearly with the 26th power of the pump intensity. Spatial resolution below 70 nm was achieved with single-beam excitation without the need for computational analysis (Figure 16c). In 2021, Liang et al. reported NIR-STED imaging based on downshifting lanthanide nanoparticles.⁵⁴⁶ This technique exploits population inversion through slow parity-forbidden transitions of quasi-four-level Nd^{3+} emitters and enables super-resolution imaging with lateral resolution below 20 nm and without photobleaching. The rapid development of super-resolution imaging techniques has found many applications, such as single-element analysis,⁵⁵⁵ structural decoding of heterogeneous nanoparticles,⁵⁴⁵ and super-resolution cell imaging (Figure 16d–f).⁵⁴⁶

Because of the high photostability of hosts, rare-earth-doped nanophosphors allow detailed molecular activities to be

visualized at the single-particle level.^{556–559} Rare-earth-doped NaREF_4 nanophosphors have recently been used for real-time tracking of motor proteins for axonal transport.⁵⁶⁰ Figure 17a,b shows a microchamber with a soma compartment, interconnected microchannels, and an axonal compartment. When UCNPs are introduced into the axonal compartment, they can be transported by motor proteins along axonal tracts, allowing in situ tracking of motor protein movement. Snapshots of emission were recorded in real-time at 7 Hz (Figure 17c,d). Continuous imaging of moving nanoparticles under wide-field illumination could be achieved because of the zero-autofluorescence and nonblinking properties of UCNPs. $\text{Yb}^{3+}/\text{Tm}^{3+}$ -codoped NaYF_4 nanophosphors have also been used to track and assess the biodistribution of natural killer cells *in vivo*.⁵⁶¹ Moreover, upconversion nanophosphors have been used as injectable retinal photoreceptors to enable NIR vision in mammals.⁵⁶² Nevertheless, most of the nanoparticles studied are much larger than organic probes, with the smallest sizes ranging from 5 to 10 nm. Any smaller size will affect the brightness of the luminescence due to surface quenching. Therefore, the development of smaller but brighter rare-earth-doped inorganic phosphors for targeting single molecules will be a significant step forward.^{32,563,564}

4.1.1.2. Downshifting Luminescence Imaging. Luminescence imaging in the NIR-II range (1000–1700 nm) has become another hot topic in bioimaging in last five years. NIR-II light offers deeper tissue penetration and lower scattering than UV/vis excitation.⁵⁶⁵ Rare-earth-doped nanomaterials are important candidates for NIR-II imaging because many dopants (e.g., Nd^{3+} , Pr^{3+} , Ho^{3+} , Tm^{3+} , Er^{3+} , and Yb^{3+}) exhibit downward emission due to deeper 4f–4f transitions.^{566–569} For example, Song et al. fabricated single-layered graphene-oxide-modified $\text{NaYF}_4:\text{Yb}/\text{Er}@/\text{NaYF}_4$ nanocrystals and realized efficient cell uptake, excellent biocompatibility, flexible surface modifiability, and NIR-II imaging at 1532 nm.⁵⁷⁰ Zhao et al. combined NIR imaging at 1060 nm with ROS-activated

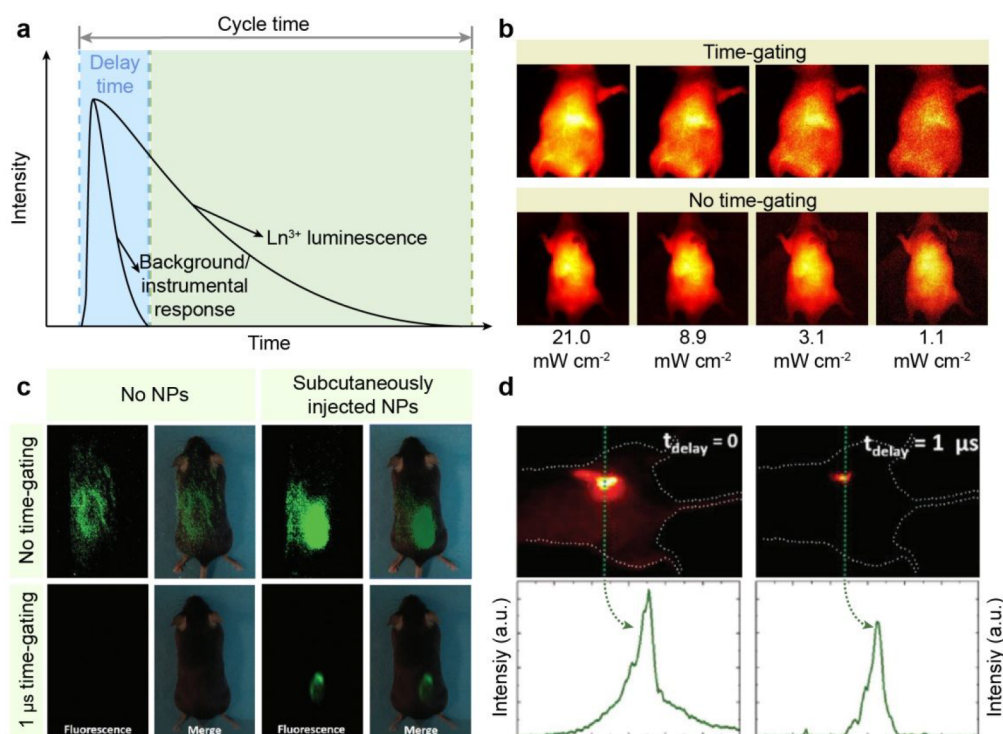


Figure 18. (a) Schematic of time-gated imaging. (b) Comparison of time-gated imaging (top) and normal imaging (bottom) of $\alpha\text{-NaYbF}_4\text{@CaF}_2$ nanoparticles (NIR τ -dots). (c) Optical and NIR images of mice with and without Yb/Nd-doped nanoparticles, recorded at 0 and 1 μs delay times. (d) NIR images and corresponding intensity profiles collected for a mouse subcutaneously injected with $\text{NaGdF}_4\text{:Nd}$ nanoparticles with 0 and 1 μs delay (Adapted with permission from refs 535, 567, and 580. Copyright 2019 Nature Publishing Group; Copyright 2018 The Royal Society of Chemistry; Copyright 2016 Wiley-VCH Verlag GmbH & Co. KGaA, Weinheim).

cross-linking of luminescent probes to image inflammatory sites with greatly improved signal-to-noise ratios.⁵⁷¹

Many downshift NIR-II emitters such as Yb^{3+} , Er^{3+} , Ho^{3+} , and Tm^{3+} suffer from luminescence quenching due to high-energy vibrations of solvent molecules. To improve NIR-II emission, Prasad, Chen, and co-workers developed dye-sensitized nanocrystals with enhanced emission in the NIR-II window.⁵⁷² They modified downshifting NaYF_4 core-shell nanocrystals with NIR dyes (indocyanine green) to gain more excitation energy through dye absorption, and the excitation energy was then transferred to nanocrystals. This approach enables enhanced NIR-II emission from a collection of rare-earth activators, such as Yb^{3+} , Er^{3+} , Ho^{3+} , Tm^{3+} , and Pr^{3+} . In 2017, Dai and colleagues enhanced the downshifting emission of Er^{3+} by codoping with Ce^{3+} in $\text{NaYbF}_4\text{@NaYF}_4$ nanoparticles. Ce^{3+} -doping modulated the intermediate 4f–4f transitions of Er^{3+} , which increased luminescence at 1550 nm by 9-fold.⁵⁷³ Through efficient Yb–Er–Ce energy transfer, Chen’s group achieved a maximum downshifting quantum yield of 32.8% of 1530 nm emission in $\text{NaCeF}_4\text{:Er/Yb}$ nanocrystals upon excitation at 980 nm.⁵⁷⁴ Such a high NIR-II emission yield allows detection at a tissue depth of 10 mm, which offers the possibility of imaging organs and hindlimbs of mice at high resolution.

The development of efficient downshifting nanoprobe with rare-earth dopants has expanded the applicability of NIR-II imaging in many ways. For instance, these NIR-II phosphors have been used to visualize tiny metastatic tumors and brain vessels in living mice (Figure 15b).⁵³⁴ They have also been used to decipher complex biological processes such as

immunotherapeutic responses and *in situ* ATP metastases.^{575,576}

4.1.1.3. Time-Gated Imaging. Time-gated imaging techniques can be implemented with rare-earth-activated nanophosphors due to their long-lived luminescence. The 4f–4f luminescence lifetime of rare-earth activators is generally 2–3 orders of magnitude longer than that of organic dyes (typically several nanoseconds), ranging between microseconds and milliseconds. To improve image contrast due to long-lived phosphorescence, it is possible to eliminate interference from short-lived emissions, such as autofluorescence or light scattering, by collecting the luminescent signal from the phosphors after the background signal has completely decayed (Figure 18a).^{577–579}

Interestingly, the luminescence lifetime of rare-earth ions depends on many factors, including dopant concentration, susceptibility to surface quenching, phonon density, and specific crystal-field environment. Altogether, these factors provide a unique opportunity to multiplex the luminescence lifetime.^{581–584} As a typical example, Hao et al. have demonstrated the use of a multicompart ment core/shell structure to generate upconversion nanophosphors with tunable luminescence lifetimes.³¹⁰ Liu et al. have combined rare-earth emission with energy migration to achieve multiplexed lifetime tuning.³⁴ Recently, Gu et al. combined time-gated imaging with NIR excitation/emission to achieve multiplexed lifetime imaging in deep tissue (Figure 18b–d).^{535,567,580,585} They developed $\alpha\text{-NaYbF}_4\text{@CaF}_2$ NIR τ -dots for time-gated imaging in the NIR-II window and demonstrated the utility of such imaging probes for visualization of internal organs at a power density of 1 mW cm^{-2} (Figure 18b).

A strong autofluorescence background was observed in the absence of time delay between the laser pulse and image acquisition (Figure 18c). At a delay of 1 μ s, the autofluorescence disappeared completely, allowing high-contrast imaging in deep tissue. Rosal et al. also performed time-gated imaging using NaGdF₄:Nd nanoparticles with an emission band centered at approximately 1060 nm upon 808 nm excitation. Accurate location of the subcutaneously injected nanoparticles was possible with a delay of 1 μ s. The intensity profiles also confirmed the elimination of the autofluorescence background (Figure 18d).

4.1.1.4. Persistent Luminescence Imaging. Persistent luminescence imaging with rare-earth-doped nanoparticles has recently drawn much interest. Persistent luminescent materials are characterized by ultralong decay times, which can be as long as several months. These materials are attractive for bioimaging because persistent luminescence does not require excitation during imaging, completely eliminating background interference.^{536,586} In 2007, le Masne de Chermont et al. demonstrated persistent luminescence imaging *in vivo* using Ca_{0.2}Zn_{0.9}Mg_{0.9}Si₂O₆:Eu²⁺/Dy³⁺/Mn²⁺ nanoparticles.⁵⁸⁷ In 2013, Abdulkayum et al. demonstrated ultralong NIR persistence luminescence of Zn_{2.94}Ga_{1.96}Ge₂O₁₀:Cr/Pr nanoparticles for 15 days after 5 min of UV irradiation.⁵⁸⁸ After further PEGylation and subcutaneous injection, these nanoparticles showed good biocompatibility and NIR imaging practicality in rodents.

To maximize applicability *in vivo*, persistent luminescent nanoprobes should be re-excitabile after injection into tissues. In this regard, several distinct NIR-excitabile upconversion persistent luminescent nanophosphors, such as Zn₃Ga₂GeO₈:Cr/Yb/Er and (Zn₂SiO₄:Mn):Y/Yb/Tm nanoparticles have been developed.^{589,590} Because of the deeper tissue penetration with NIR excitation, these nanophosphors can be recharged by an upconversion process to generate persistent bioimaging signals *in vivo*. However, the upconversion process still suffers from low conversion efficiency.

Recently, there has been a growing trend to use X-rays as an excitation source for *in vivo* persistent luminescence imaging. In 2017, Song et al. presented the use of soft X-ray excitation for repeatable activation of SrAl₂O₄:Eu²⁺ nanophosphors *in vivo* imaging.⁵⁹¹ They demonstrated a maximum tissue penetration of 2.5 cm by X-ray excitation. Since then, X-rays have been utilized to activate various persistent luminescent nanophosphors *in vivo*, such as MgGeO₃:Mn²⁺/Yb³⁺/Li⁺, Zn₂GeO₄:Mn, and ZnGa₂O₄:Cr³⁺.^{592–594}

A major challenge in the development of persistent luminescent nanophosphors is that their brightness decreases significantly as the particle size decreases into the nanometer range. Surface passivation can improve the efficiency of persistent luminescence by preventing the energy loss due to surface quenching. However, most persistent luminescent nanomaterials currently in use were prepared under harsh conditions (>800 °C) that prevent core–shell modification. In 2021, Ou et al. reported persistent luminescence of NaLuF₄:Tb@NaYF₄ nanoparticles with a size of 27 nm upon X-ray irradiation.⁵⁹⁵ Compared with NaLuF₄:Tb core nanoparticles, these core–shell nanoparticles increased the radio-luminescence intensity by 1.5-fold. Shortly thereafter, Zhang, Yang, Fan and their collaborators developed NaY₂GdF₄:Ln@NaY₂GdF₄ (Ln = Er, Nd, Ho, Tm) nanoparticles that exhibit strong X-ray-activated persistent luminescence in the NIR-II region.⁵⁹⁶ The core–shell design enables tunable NIR-II

persistent luminescence from 1064 to 1525 nm and bioimaging at deep tissue depth (2–4 mm) with a 4-fold higher signal-to-noise ratio and 3-fold higher contrast. These findings shed light into the development of highly efficient persistent luminescent nanophosphors for bioimaging and therapeutics.

4.1.1.5. Contrast Agents. In addition to luminescence imaging, rare-earth-doped nanomaterials can serve as contrast agents for imaging modalities such as MRI, CT, PAI and cathodoluminescence microscopy. For instance, paramagnetic Gd³⁺ has the highest number of unpaired electrons (7), making it suitable as a positive (T_1) contrast agent for MRI.^{597,598} It shortens the spin–lattice relaxation time (or longitudinal relaxation time) of water protons. The other main class of MRI contrast agents works by changing the spin–spin (or transverse) relaxation time. They are negative (T_2) contrast agents because the image is obscured by the accumulation of contrast agents. Superparamagnetic iron oxide nanoparticles are the best known negative T_2 contrast agents.

For nanosized T_1 MRI contrast agents, it has been shown that only paramagnetic ions located near nanocrystal surfaces can contact water protons, thereby enhancing T_1 -weighted MRI contrast. Consequently, paramagnetic dopants need to be concentrated in the outermost layer to further improve the contrast performance. Two approaches have been used to increase surface dopants. One is the synthesis of small nanocrystals with a very high surface-to-volume ratio. The other is to dope metal ions locally on the surface using a surface doping strategy. For example, the r_1 relaxivity of Gd³⁺ nanoparticles can be increased by either using ultrasmall NaGdF₄ nanocrystals (sub-5 nm)⁵⁹⁹ or coating NaYF₄ nanocrystals with an ultrathin layer of NaGdF₄ (<1 nm).²⁸⁹ Furthermore, loading a nanocrystalline matrix with multiple Gd³⁺ ions allows a dramatic increase in the local surface concentration, which improves the imaging contrast.^{600,601} Cheung et al. made PAA-stabilized Gd³⁺ nanoparticle aggregates to increase the surface-to-volume ratio while maintaining a large size that promotes vascular retention at tumor sites.⁶⁰² Multifunctional MRI nanoparticles have also been reported. Wu et al. designed Eu³⁺-doped Gd₂O₃ nanoscrolls with encapsulated doxorubicin (DOX) drug molecules, which enabled dual MRI imaging and targeted tumor chemotherapy.⁶⁰³

Other paramagnetic rare-earth ions, such as Dy³⁺ and Ho³⁺, are suitable as negative (T_2) contrast agents because of their high magnetic moments ($\sim 10.6 \mu_B$) and short electronic relaxation times (~ 0.5 ps).⁶⁰⁴ Unlike Gd³⁺, the relaxation enhancement for Dy³⁺ is a bulk effect. Larger nanoparticles generally have a higher contrast effect. For instance, van Veggel and co-workers found that the T_2 contrast of NaDyF₄ and NaHoF₄ nanoparticles increased with increasing particle size and magnetic field strength.^{178,605} Size-dependent evaluation of T_2 relaxivity showed that imaging contrast increased with larger NaDyF₄ nanoparticles and higher field strength. Specifically, the largest nanoparticles (~ 20 nm) showed ~ 64 -fold higher contrast per nanoparticle and ~ 6 -fold higher contrast per Dy³⁺ ion at 9.4 T, compared to 3 T. Compared to clinically used T_2 contrast agents such as iron oxides, Dy³⁺/Ho³⁺-based nanoparticles provide higher signal-to-noise ratio and better spatial resolution for high-field MRI (>7 T) of vasculitis in the central nervous system.

Additionally, nanomaterials doped with rare-earths have long been utilized as contrast agents for X-ray CT imaging. Because of their high atomic number and lanthanide contraction,

lanthanide elements exhibit high electron density and thus high X-ray attenuation. Among lanthanides, lutetium (Lu) has the largest atomic number and is expected to have a large X-ray absorption coefficient. Lu³⁺-based nanoparticles, such as NaLuF₄ and LiLuF₄, have proven as efficacious CT contrast agents.^{277,539,606} In practical applications, rare-earth-doped nanoproboscopes have been used mostly in CT alongside other imaging modalities, such as MRI, luminescence imaging, PET, and SPECT.^{537,607–609}

In separate developments, research groups have demonstrated the use of rare-earth-doped nanoparticles as contrast agents for PAI.^{610,611} PAI is a relatively less explored modality compared to MRI and luminescence imaging. Based on current understanding, the observed photoacoustic property is attributed to nonradiative relaxation by surface quenching of excited lanthanide dopants, such as Yb³⁺ and Er³⁺ in NaYF₄. Apparently, the signal strength of the reported nanoparticle composition is rather weak compared with organic photoacoustic probes. Improvement by changing the host lattice or dopant composition might be possible. To improve the spatial and temporal resolution of imaging *in vivo*, Xing, Gao, and co-workers combined multispectral optoacoustic tomography with upconversion nanoproboscopes.⁵⁴⁰ They coupled UCNPs with radical-sensitive cyanine dyes to produce hybrid nanoproboscopes. These nanoproboscopes can respond orthogonally to disparate forms of oxidative and nitrosative stimulation, allowing *in vivo* visualization of endogenous redox biomarkers with high spatiotemporal resolution (Figure 15h).

Cathodoluminescence refers to optical emission under electronic beam excitation. It can be realized in scanning electron microscopy with a photomultiplier detector. Previous research has used rare-earth complexes to visualize multiple biological molecules in electron microscopy.⁶¹² However, the previous research requires a specific sensitizer for each type of rare-earth complex. In 2019, Prigozhin et al. examined the cathodoluminescence of rare-earth-doped nanoparticles with an average size of less than 20 nm.⁶¹³ They showed bright optical emissions under direct electron beam excitation. Although the emission spectra of individual particles show significant variations even among samples of the same batch and under the same illumination conditions, this study was an excellent demonstration of the cathodoluminescence of rare-earth-doped inorganic nanomaterials. Future mechanistic studies on factors affecting the cathodoluminescence intensity and line shape are needed.

4.1.1.6. Multifunctional Imaging Probes. Multimodal imaging provides different types of information about the same objects with a single dose of probes. There is a considerable interest in integrating multiple imaging modalities through rare-earth-doped nanoproboscopes.^{542,614} For instance, Sun et al. have developed multifunctional NaLuF₄:Yb/Tm@NaGdF₄(¹⁵³Sm) nanoproboscopes that integrate four modalities for tumor angiogenesis assays.⁶⁰⁷ The core structure is codoped with Yb³⁺, Tm³⁺ to achieve upconverted NIR emission at 800 nm. The Lu³⁺, Yb³⁺, and Gd³⁺ ions in the core and cladding layer provide X-ray attenuation and CT contrast. In addition, Gd³⁺ ions in the cladding layer provide T₁ contrast for MRI. Lastly, radioactive ¹⁵³Sm³⁺ dopants in the shell release γ rays to provide the fourth imaging contrast for SPECT.

It is interesting to selectively detect biological targets to obtain better imaging contrast and more detailed structural information. An effective strategy to impart molecular

specificity to imaging contrast agents is to develop imaging probes that can respond to changes in the environment.⁶¹⁵ For example, it is useful to design multifunctional rare-earth-doped nanoproboscopes whose luminescent signal responds to local pH or signal molecules. Combined with an external optical control for photoactivation, these multifunctional nanoproboscopes have been widely used in diagnostics and nanomedicine.^{616–618}

A potential limitation of rare-earth-doped nanoparticles for *in vivo* imaging is short circulation due to nanoparticle accumulation in the liver and spleen. To overcome this problem, Peng et al. reported an increase in blood circulation of rare-earth-doped nanoparticles to over half an hour using polyphosphoric acid ligands.⁶¹⁹ They administered nanoparticles functionalized with polyphosphoric acid to mice by injection into the tail vein. Upconversion luminescence and SPECT imaging allowed visualization of the main arteries and heart within the first half-hour after injection, whereas nanoparticle accumulation in the liver and spleen occurred later. For targeted bioimaging, Rao et al. recently reported precise tumor imaging by coating UCNPs with cancer cell membranes.⁶²⁰ This surface modification reduced nanoparticle uptake by the phagocyte-enriched reticuloendothelial system, leading to much improved specific nanoparticle accumulation at tumor targets.

Another limitation of rare-earth-doped nanoproboscopes for luminescence bioimaging is their low absorption coefficient. Several methods exist to improve light absorption, such as dye sensitization and plasmonic enhancement.^{621–625} Although luminescence intensity could be increased by more than 3–4 orders of magnitude in organic solvents, dye-sensitized nanoparticles become only a few dozen times brighter in the aqueous phase. In 2020, a team led by Liu and Li discovered that aggregation-induced quenching is the major limitation of dye-sensitized upconversion luminescence.⁶²⁶ By using hydrophobic interactions instead of direct coordination between the dye molecules on the surface and the lanthanide nanoparticles, aggregation-induced quenching can be reduced. The researchers modified the dye structure to minimize the retransfer of energy from the rare-earth ions to the dye. Overall, a more than 600-fold increase in luminescence was achieved.

4.1.2. Photothermal Therapy. Photothermal therapy (PTT) is a noninvasive treatment for diseases based on photothermal agents. Photothermal agents can convert absorbed light into heat to cause thermal ablation of damaged tissue, such as tumors and infected tissue (Figure 19a). PTT can be accomplished by combining rare-earth-doped nanoproboscopes with photothermal conversion materials.^{627,628}

Au and Ag nanostructures with strong heating effects due to surface plasmon resonance have been widely utilized as photothermal agents for PTT. Therefore, combining rare-earth-doped nanomaterials with Au or Ag nanoparticles could be an efficacious approach for improved PTT.^{629–633} In 2011, Liu, Shao, and co-workers constructed multifunctional UCNP-Fe₃O₄-Au nanomaterials for *in vivo* dual-mode upconversion luminescence/MR imaging and magnetically targeted PTT.⁶³⁴ Chan et al. coupled Au nanorods with Nd³⁺-sensitized UCNPs.⁶³⁵ This design enables upconversion emission and photothermal energy conversion at a single wavelength of 808 nm.

Furthermore, materials with strong light absorption, such as graphene oxide (GO), Cu_xS, and organic light absorbers, have been combined with rare-earth-doped nanomaterials as photothermal agents for PTT in refs 636–642. For instance,

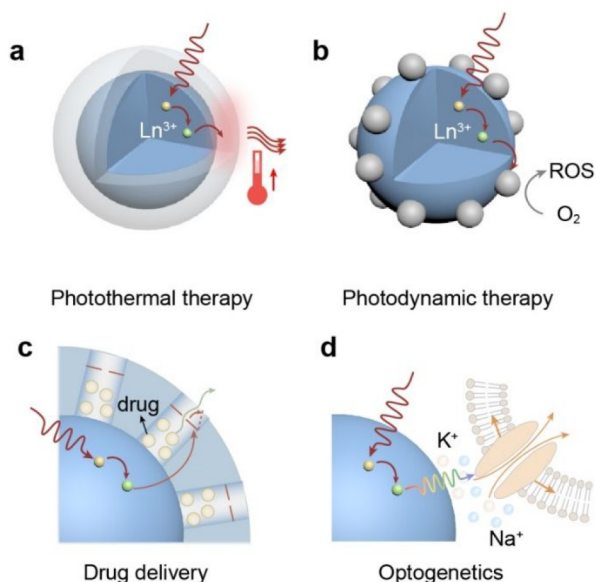


Figure 19. Schematics of rare-earth-doped nanomaterials for (a) photothermal therapy, (b) photodynamic therapy, (c) drug delivery, and (d) optogenetics.

Wang et al. reported the use of GO-covalently grafted UCNPs as a thermal platform for bioimaging and PTT.⁶⁴³ Lin and co-workers presented the synthesis of hollow $Y_2O_3:Yb/Er-Cu_xS$

nanospheres for image-guided PTT.⁶⁴⁴ Xu et al. recently combined CuS , $g-C_3N_4$ and UCNPs to achieve efficient PTT under NIR excitation.⁶⁴⁵ The researchers functionalized composite nanoparticles with polyethylene glycol and folic acid to target cancer cells and improve biocompatibility. In 2020, He and co-workers assembled poly(selenoviologen) on $NaYF_4$ UCNPs for PTT-based antibacterial therapy.⁶⁴⁶ These polymer-modified nanoparticles show good efficacy in killing methicillin-resistant *Staphylococcus aureus* both *in vitro* and *in vivo* (Figure 20a).

To minimize overheating during PTT, Zhu et al. demonstrated temperature-controllable PTT using $NaLuF_4:Yb/Er@NaLuF_4@carbon$ nanoparticles.⁶⁴⁷ They used UCNPs with temperature feedback to monitor the local temperature in PTT. They found that the local temperature around nanoscale photothermal converters was sufficient to kill cancer cells if the temperature of the lesions was kept low enough to prevent damage to normal tissue. This allowed PTT-mediated tumor ablation with high spatial resolution and minimal damage to normal tissue. This PTT strategy has been combined with chemotherapy and immunotherapy to improve therapeutic performance.^{648,649}

4.1.3. Photodynamic Therapy and Photochemotherapy. Similar to PTT, photodynamic therapy (PDT) and photochemotherapy offer potential options for cancer treatment with minimal off-target effects.⁶⁵⁰ Both approaches typically use photosensitizers that can be activated by irradiation at specific wavelengths. These activated photo-

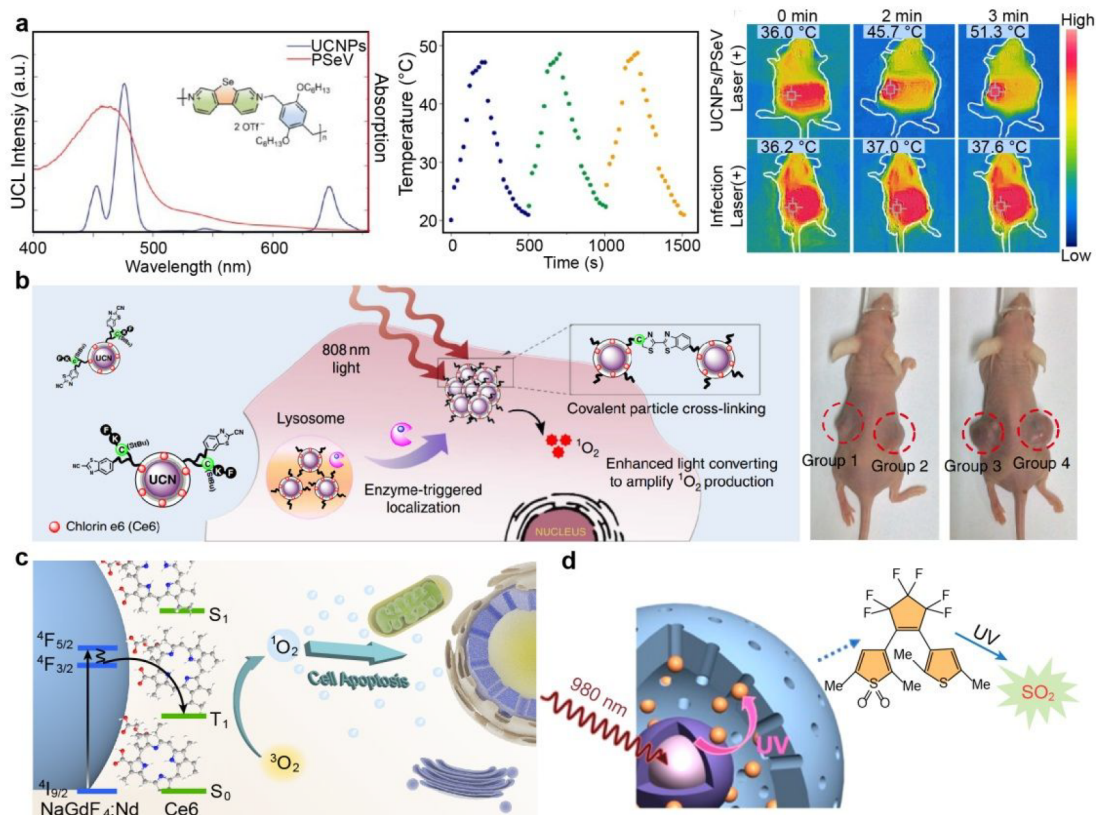


Figure 20. (a) Photothermal therapy with UCNPs/PSeV nanoconjugates under 980 nm irradiation. (b) Illustration of photodynamic therapy with covalent cross-linking of peptide-premodified UCNPs and photographs of tumor-bearing mice after treatment with UCNPs (group 1) and other control groups. (c) Proposed mechanism of nanoparticle-based photodynamic therapy with direct energy transfer from the excited triplet states of rare-earths. (d) Schematic of NIR-triggered SO_2 generation for gas therapy (Adapted with permission from refs 646 and 663–665. Copyright 2020 American Chemical Society; Copyright 2016 Nature Publishing Group; Copyright 2021 Elsevier Inc.).

sensitizers mediate *in situ* chemical reactions to generate cytotoxic species, such as reactive oxygen species (ROS). One of the main challenges for conventional photosensitizers is that they can only absorb light in the UV–visible range and therefore have limited penetration into biological samples. To overcome this problem, rare-earth-doped nanoparticles have been used as light transducers to enable PDT and photochemotherapy deep within tissues (Figure 19b).^{651–654}

For example, Xie and co-workers demonstrated X-ray-induced *in vivo* PDT for cancer treatment using Eu²⁺-doped SrAl₂O₄ nanoparticles.⁶⁵⁵ They coupled SrAl₂O₄:Eu²⁺ nanoscintillators with merocyanine 540, a photosensitizing dye. Under X-ray irradiation, SrAl₂O₄:Eu²⁺ nanoscintillators emitted visible photons, which subsequently photoactivated merocyanine 540 to generate cytotoxic singlet oxygen (¹O₂). This X-ray induction method overcame the shallow penetration limitation associated with conventional light sources for PDT.^{656,657} Scintillating nanoparticles with various compositions, such as SrAl₂O₄:Eu²⁺, LaF₃:Tb/Ce, Tb₂O₃, NaGdF₄:Tb, NaCeF₄:Gd/Tb, and Gd₂(WO₄)₃:Tb, have proven effective as X-ray transducers when combined with organic photosensitizers for PDT.^{658–664}

In addition to organic photosensitizers, rare-earth-doped nanoscintillators can also activate inorganic semiconductor photocatalysts. Zhang et al. prepared multilayer LiYF₄:Ce@SiO₂@ZnO nanoparticles that exhibited efficient energy transfer from Ce³⁺ (emission at 305 and 325 nm) to ZnO under X-ray irradiation.⁶⁶⁸ Such energy transfer facilitated the production of hydroxyl radicals in the presence of water, leading to deep-tissue PDT of tumor cancers. The core–shell design can make nanoscintillators multifunctional. For example, Chang and co-workers prepared NaLuF₄:Eu@NaLuF₄:Gd@NaLuF₄:Tb nanoparticles in conjugation with Rose Bengal and PEG-folic acids.⁶⁶⁹ These nanoparticles exhibited dual emission, one from Tb³⁺ at 543 nm for Rose Bengal activation and the other from Eu³⁺ at 614 and 695 nm for image-guided PDT. Rare-earth-doped nanoscintillators could also enable photochemotherapy by X-ray-controlled generation of peroxynitrite in tumors.⁶⁷⁰

For clinical use, the safe radiation dose of X-rays needs to be carefully evaluated, taking into account the potential photo-disturbances due to high ionization energy. Alternatively, NIR irradiation can be used as a safer light source than visible light to accomplish therapeutic treatment in deep tissue. An example of this in nanoscience is the use of UCNP to convert NIR excitation to short-wavelength UV/visible emission.⁶⁵³ Since the early 2010s, upconversion-based PDT has been extensively explored, with significant advances in precision therapy, image-guided therapy, and multimodal synergistic therapy.^{25,671–676} In the last five years, research in this field has mainly focused on expanding the applicability of upconversion-based PDT through various approaches. For instance, to minimize the heating effect, Chan et al. demonstrated the use of Nd³⁺-sensitized UCNP for PDT under 808 nm irradiation.⁶⁷⁷ Compared with the 980 nm irradiation employed for conventional Yb³⁺-sensitized upconversion, 808 nm NIR light achieved a high excitation amount for upconversion with minimal tissue overheating, which is more efficacious for cancer treatment. Nd³⁺-sensitized nanoparticles can be further modified with IR-808 and ICG dyes to increase absorbance and improve PDT performance at 808 nm irradiation.^{301,569}

To achieve targeted PDT, Sun et al. developed DNA-modified hierarchical nanocomposites comprising Au nanorods, UCNP, and Ce6.⁵³⁷ These nanocomposites can be visualized and tracked *in vivo* by upconversion luminescence imaging, CT scanning, PAI, and T₁-MRI, enabling image-guided combination phototherapy. In 2020, Lin, Yang, and co-workers fabricated NaGdF₄:Lu/Yb/Er/Ce nanoparticles coated with copper and manganese silicate nanospheres. These exhibited combined chemodynamic/photodynamic effects and bright downshifting NIR-II luminescence suitable for image-guided phototherapy.⁶⁷⁸ To enhance site-specific, on-demand, antitumor activity, Xing and co-workers incorporated a peptide sequence that recognizes cathepsin B into Nd³⁺-sensitized UCNP.⁶⁶⁵ This peptide modification confers sensitivity to the tumor microenvironment, triggering specific nanoparticle accumulation in cancer cells and subsequently enhancing ROS generation at targeted tumor sites (Figure 20b). In addition, upconversion PDT can be enhanced by improving the specificity of UCNP to mitochondria, which promotes mitochondrial damage by ROS to induce apoptosis.^{679,680}

Upconversion-based PDT can respond to the tumor microenvironment. The microenvironment of a solid tumor has specific characteristics, such as low pH, high H₂O₂ and glutathione concentrations, and hypoxic conditions. These factors strongly influence *in situ* ROS generation and phototherapeutic performance. For instance, the anoxic environment of a solid tumor suppresses the efficacy of PDT due to the lack of oxygen for ¹O₂ production. To overcome this challenge, UCNP have been modified with MnO₂, CeO₂, platinum(IV)–diazido complexes, Fe(OH)₃, etc.^{258,601,681–683} These materials are able to catalyze the degradation of endogenous H₂O₂ to O₂ and thus promote ¹O₂ production in tumor cells. It is also possible to combine UCNP-based PDT with hypoxia-activated prodrugs, such as tirapazamine or immune-responsive species, to enhance anticancer therapy.^{22,684–686}

Despite its usefulness, upconversion-based PDT generally requires a relatively high irradiance (typically >100 mW cm⁻²). Moreover, the conversion efficiency is low due to the significant energy loss during multiphoton upconversion. Therefore, it is essential to develop highly efficient NIR-responsive PDT platforms that operate at relatively low excitation intensities. In 2021, Zheng et al. reported a novel concept to achieve PDT at ultraweak NIR irradiation that directly activates excited triplet states of organic photosensitizers without the need for intersystem crossing of higher singlets of the organics (Figure 20c).⁶⁶⁷ The researchers demonstrated an unusual energy transfer pathway via short-range Dexter-type interactions to realize photosensitization for ¹O₂ production via energy transfer from lanthanides to triplets. This approach enables the activation of a series of porphyrin and phthalocyanine sensitizers under low NIR irradiance (~10–80 mW cm⁻²) of Nd³⁺- or Yb³⁺-doped NaGdF₄ nanoparticles. This work could expand the repertoire of rare-earth-doped materials for PDT and other biomedical applications.⁶⁸⁷

In addition to ROS, UCNP can trigger the release of specific gas molecules for NIR-sensitive therapy. For example, upconverted visible emission can activate the production of nitric oxide (NO) from Roussin's black salt [Fe₄S₃(NO)₇]⁻ (RBS).^{688–691} In 2017, Zhang et al. combined Nd³⁺-sensitized UCNP with RBS to trigger NO release.⁶⁹² Under 808 nm

excitation, this nanoplatfrom releases large amounts of NO that effectively destroy cancer stem cells *in vivo*. Apart from NO therapy, Li et al. recently demonstrated sulfur dioxide (SO₂) cancer therapy enabled by NIR-responsive UCNPs.⁶⁶⁶ The researchers constructed porous silica-coated upconversion nanoparticles and then loaded them with an SO₂ prodrug. These assembled nanostructures not only enable intracellular and *in vivo* delivery of the SO₂ prodrug but also on-demand release of SO₂ into deep tissue (Figure 20d).

4.1.4. Drug Delivery. Targeted drug delivery can be accomplished by conjugating nanomaterials with acceptor molecules that specifically recognize receptors on target organs and cells via ligand–acceptor or antigen–antibody interactions (Figure 21). Additionally, surface modification of nanomaterials

Strategy	Modification moiety	Function
SiO ₂ coating	SiO ₂ , mesoporous SiO ₂	Hydrophilicity, molecule loading and release
Yolk-shell SiO ₂ capsulation	Mesoporous SiO ₂	Hydrophilicity, molecule loading and release, gas release
Polymer coating	PAA, PEI, PEG, PVP...	Hydrophilicity, molecule encapsulation
Liposome	Membrane, lipid	Hydrophilicity, molecule encapsulation
Amphiphilic polymer coating	DSPE-PEG, pluronic F127...	Hydrophilicity, molecule loading and release
Protein modification	Bovine serum albumin, linker-protein G, enzyme, antibody...	Biocompatibility, connection with other materials, targeting
Nucleic acid modification	DNA	Hydrophilicity, connection with other materials, molecule loading, biosensing, DNA delivery
	RNA	Hydrophilicity, gene silencing, RNA delivery
Targeted molecule	Folic acid, hyaluronic acid...	Targeting

Figure 21. Strategies for surface modification of rare-earth-doped nanomaterials for bioapplications: PAA poly(acrylic acid); PEI poly(ether imide); PEG poly(ethylene glycol); PVP poly(vinylpyrrolidone); DSPE distearoylphosphoethanolamine.

als through postsynthesis or *in situ* functionalization greatly enhances the efficacy of pharmaceutical payloads and alter drug solubility, stability, and metabolic pathways in living systems.^{695–698}

A unique feature of rare-earth-doped nanomaterials for drug delivery is that they provide additional external stimuli to manipulate pharmacokinetics and drug release (Figure 19c).^{697,699,700} This enables site-specific, spatiotemporally controlled drug release and localized functional regulation in nanomaterial-based delivery systems. As a representative example, UCNPs have been combined with photocleavable prodrugs for NIR-activated drug release.^{701–706} Recently, Chen et al. demonstrated NIR-controlled delivery of an enzyme inhibitor in living cells using hollow mesoporous silica nanocomposites containing NaYF₄:Tm/Yb@NaYF₄ UCNPs and photoactivatable Ru complexes.⁷⁰⁷ The photocaged Ru complex is designed to be photochemically cleaved to release the enzyme inhibitor upon stimulation with blue-emitting UCNPs. The released enzyme inhibitor inhibits the enzyme cathepsin K in living cells and controls local cell functionality

in deep tissue. In a separate study, Li and co-workers developed a gene delivery system that enabled NIR-initiated hybridization chain reaction (HCR) for spatiotemporally resolved imaging of mRNA in living cells.⁷⁰⁸ The researchers loaded HCR-functional DNA hairpins onto rare-earth-doped nanoparticles and introduced them into living cells. One of the DNA hairpins was modified by adding a short photocleavable linker to block the HCR reaction. After the cells endocytosed the DNA hairpins, HCR was restored by light-induced photolysis of the photocleavable linker. To date, NIR-activated delivery systems have found many applications, such as *in vivo* release of CRISPR-Cas9 for gene editing, localized DNA delivery to eliminate senescent cells, controlled release of small molecules to drive multidirectional differentiation of mesenchymal stem cells, and targeted delivery of drugs that trigger local antitumor immunity.^{709–714}

Another prominent approach for photoactivated drug-release can be realized by conformational changes, such as *cis–trans* isomerism in azobenzene derivatives (Figure 22).^{693,694,718} For instance, Zhang et al. encapsulated the anticancer drug DOX on the surface of NaYF₄:Tm/Yb@NaYF₄ nanoparticles using azo-functionalized DNA strands (Figure 22a).⁶⁹³ Under NIR excitation, these nanoparticles emitted UV and visible photons to initiate isomerization of the azo-compound, which triggered the continuous release of DOX from the nanocomposites. The researchers demonstrated a release of 86.7% of the compound after 30 min of irradiation. Yao et al. inlaid amphiphilic azobenzene derivatives into liposomes with encapsulated DOX and Yb/Tm-encoded UCNPs (Figure 22b,c).⁶⁹⁴ Upon irradiation at 980 nm, the blue/visible upconverted emission immediately excited the photosensitive azobenzene molecules. The reversible isomerization of the azobenzene disrupted the liposome scaffold and allowed the controlled release of DOX (Figure 22d). In addition to photochemical reactions, the photothermal effect of rare-earth-doped nanoparticles can also trigger targeted drug release.^{719,720} Han et al. reported a photothermal drug release system based on UCNPs prefunctionalized with gold nanoparticles and hairpin DNA. The DOX drug, intentionally entrapped in the DNA hairpins, can be released from nanoparticle surfaces upon laser irradiation at 980 nm.⁷¹⁹

4.1.5. Optogenetics. Optogenetics is a revolutionary technique that uses light as a modality of biological control to manipulate cellular activities, neuronal functions, and even the behavior of living animals. This technique typically uses visible light to regulate the influx of ions such as Ca²⁺, Na⁺, and K⁺ through light-gated ion channels on cell membranes. This process is of particular interest in neuromodulation.^{721,722} By selective expressing light-sensitive channelrhodopsins (ChR) in neurons, light stimulation can precisely control the activation or inhibition of target neurons within milliseconds. Optogenetics can enable clinical exploration of numerous neuronal states and remediation of neuronal dysfunction. One of the challenges in optogenetics is the short working distance of light stimulation. This is because conventional ChR receptors can only absorb light in the visible range, typically between 430 and 650 nm, which penetrates tissue poorly.^{723,724} This challenge can be overcome by coupling optogenetics and rare-earth-doped nanoparticles that can convert NIR excitation into visible emission (Figure 19d).

Upconversion-mediated optogenetics was first demonstrated in 2015. Hososhima et al. reported using NaYF₄:Sc/Yb/Er UCNPs as NIR optical donors to stimulate C1 V1-expressing

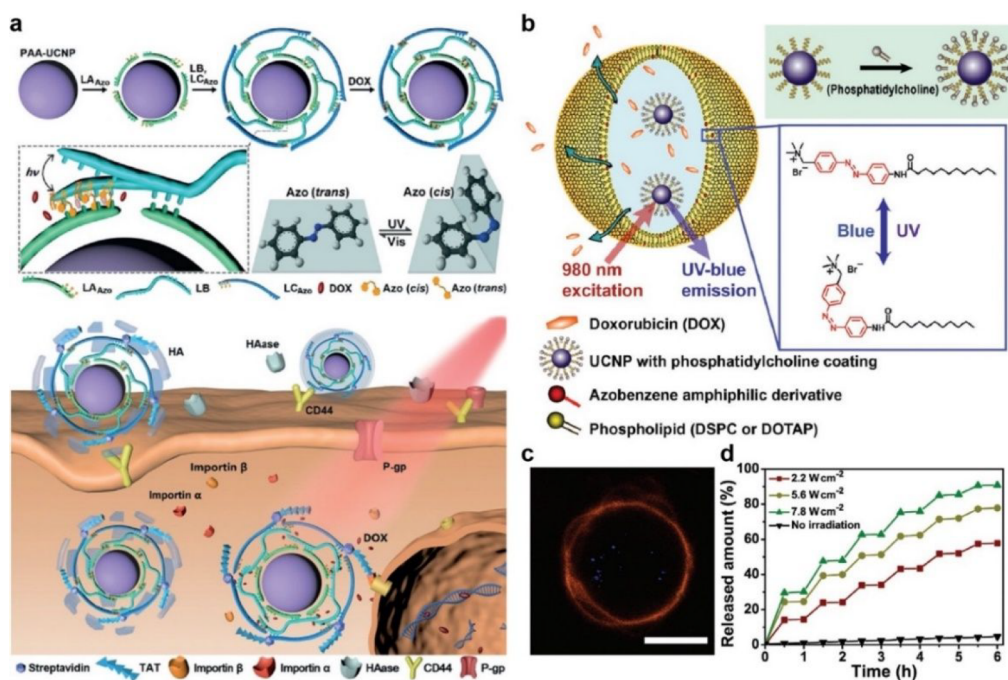


Figure 22. (a) Schematic of UCNPs-LA_{Azo}/BC_{Azo}/DOX assembly and NIR-triggered drug release in living cells. (b) Schematic of NIR-triggered drug delivery using azobenzene-liposome/UCNP hybrid vesicles. (c) Confocal cross sections of azobenzene-liposome/UCNP/CdSe hybrid vesicles. The scale bar is 5 μm. (d) Power-dependent drug release curves in buffer under intermittent irradiation with 980 nm light (Adapted with permission from refs 693 and 694. Copyright 2016 and 2019 Wiley-VCH Verlag GmbH & Co. KGaA, Weinheim).

ND7/23 cells at 975 nm irradiation.⁷²⁵ At the same time, Pang, Lee, and their co-workers used blue-emitting NaYF₄:Yb/Tm@NaYF₄ UCNP to facilitate optogenetic activation of Chr2-expressing neuronal cells.⁷²⁶ Han and co-workers designed IR-806-sensitized NaYF₄:Yb/Er@NaYF₄:Yb UCNP as optical transducers for enhanced optogenetics under 800 nm excitation.⁷²⁷ They demonstrated efficient NIR activation of ReaChR in cultured hippocampal neurons.

Although UCNP have proven useful for *in vitro* NIR-activated optogenetics in cultured neurons, the overheating caused by NIR light still hinders the application of this technique *in vivo*. To address this problem, Zhang's group proposed quasi-CW NIR irradiation to improve the efficiency of multiphoton upconversion, while reducing the overheating caused by high-energy excitation.⁷²⁸ NaYF₄:Yb/Tm@SiO₂ nanoparticles can be used to activate Chr2 in Hek293t cells at a low pump intensity under quasi-CW 980 nm excitation.

Under 980 nm laser irradiation, *in vivo* optogenetic manipulation has been demonstrated in Chr2-expressing *C. elegans* using UCNP. However, activation of Chr2 in this study requires a relatively high irradiance to trigger the reversal behavior of *C. elegans*. It is difficult to determine whether the observed reversal behavior is caused by activation of Chr2-expressing neurons or by an innate avoidance response to thermal or blue light irradiation. To avoid the photophobic response of *C. elegans*, Ao et al. employed a more sensitive optogenetic sensor Chrimson to manipulate the behavior of the *C. elegans* motor circuit with Nd³⁺-sensitized green-emitting UCNP.⁷¹⁵ In that study, Chrimson protein was expressed in GABAergic class D motor neurons (D-MNs) and glutamatergic DVC interneurons. Upon NIR irradiation at 800 nm, D-MNs released GABA in muscle arms, inhibiting action potentials in body wall muscles and preventing locomotion. These nanoparticles exhibit negligible toxicity to neuron

development, growth, and reproduction. The 800 nm NIR energy required to elicit physiological responses does not activate the temperature response of *C. elegans* (Figure 23a). In another work, Ai et al. demonstrated NIR-activated optogenetic manipulation in zebrafish.⁷¹⁶ They activated Chr2 cell membrane channels under 808 nm irradiation with Nd³⁺-sensitized UCNP (Figure 23b).

Upconversion-mediated optogenetics can be employed *in vivo* in mammals. For example, Wang, Shi, and co-workers embedded UCNP in a glass micropipette to form an ultrasmall, fully implantable device for optogenetic inhibition of target neurons in the mouse brain.⁷²⁹ The opto-gated inhibitory sensor was an enhanced Natronomonas halorhodopsin (eNpHR) protein expressed in the subthalamic nucleus of the rat brain. When the upconversion device was placed near the target sites in the brain, the electrical activities of eNpHR-expressing neurons were remotely inhibited by NIR illumination. The neurons' signals could be immediately restored after the NIR stimulation was turned off. In 2018, Chen, McHugh, Liu, and co-workers injected blue-emitting NaYF₄:Yb/Tm@NaYF₄@SiO₂ nanoparticles directly into dopaminergic neurons in the ventral tegmental area of Chr2-expressing rats.⁷¹⁷ Transcranial NIR irradiation was able to trigger blue upconverted emissions that elicited dopamine release from genetically labeled neurons in the ventral tegmental area. Activation of inhibitory neurons in the hippocampus of the medial septum induced brain oscillation, which a suitable means for seizure suppression (Figure 23c).

4.2. Optical Sensing

In recent decades, nanomaterial-based sensors have evolved into a suite of technologies for precise and sensitive detection of changes in the microenvironment (temperature, pressure, and pH). Due to their unique chemical and optical properties, rare-earth-based nanoparticles enable exquisite detection of

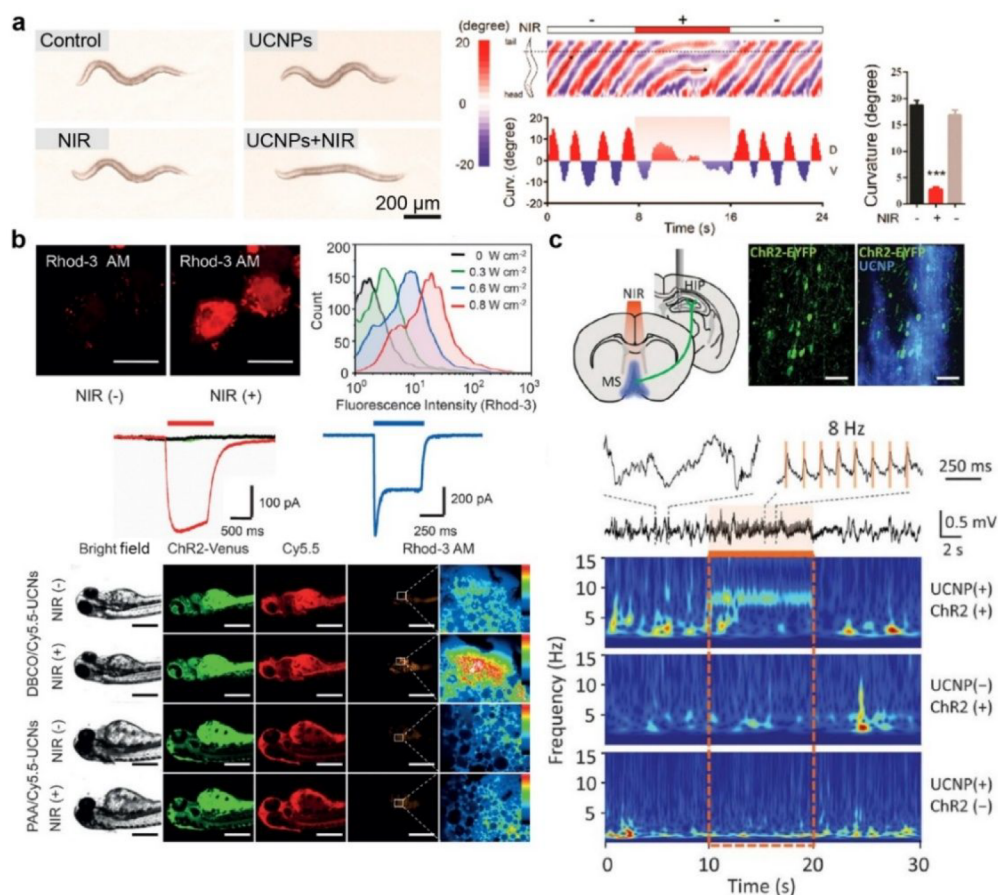


Figure 23. (a) NIR-triggered postural changes in *C. elegans* exposed to UCNPs. (b) *In vitro* and *in vivo* regulation of cell activities of zebrafish incubated with Cy5.5-UCNPs at 808 nm illumination. Scale bars are 20 μm (top) and 400 μm (bottom). (c) UCNP-mediated upconversion optogenetics for deep brain stimulation. The scale bar is 50 μm (Adapted with permission from refs 713–715. Copyright 2019 American Chemical Society; Copyright 2017 Wiley-VCH Verlag GmbH & Co. KGaA, Weinheim; Copyright 2018 American Association for the Advancement of Science).

changes in the microenvironment with unprecedented sensitivity. Moreover, they enable noncontact molecular detection of biomolecules, metal ions, anions, gases, and small molecules in deep tissue.

4.2.1. Temperature Sensing. In order to achieve highly accurate temperature measurements over wide ranges, non-contact luminescence nanothermometry has been explored.^{730,731} Given characteristic temperature-dependent luminescence properties, a plethora of rare-earth ions, including Pr^{3+} , Nd^{3+} , Sm^{3+} , Eu^{3+} , Tb^{3+} , Ho^{3+} , Er^{3+} , and Tm^{3+} , have been doped into different host materials for temperature sensing.^{732,733} Many variable optical parameters such as peak intensity ratio, emission wavelength, and luminescence lifetime have been used to probe temperature changes.^{381,734,735} The commonly studied mechanisms of temperature-dependent luminescence changes can be divided into two categories: (i) thermally coupled redistribution of excitation energy within a rare-earth emitter controlled by Boltzmann statistics and (ii) energy transfer between multiple dopants mediated by thermally induced phonon oscillations.

Among rare-earth emitters, Er^{3+} is the most studied element for temperature sensing and has been frequently coupled with Yb^{3+} and Nd^{3+} in nanocrystal hosts to improve the efficiency of upconversion from NIR to visible light. Temperature sensing with Er^{3+} is generally achieved by energy redistribution between the excited states ${}^2\text{H}_{11/2}$ and ${}^4\text{S}_{3/2}$. When the

temperature changes, the fluorescence intensity ratio (FIR) of the two transitions (${}^2\text{H}_{11/2} \rightarrow {}^4\text{I}_{15/2}$ at 525 nm and ${}^4\text{S}_{3/2} \rightarrow {}^4\text{I}_{15/2}$ at 545 nm) changes according to the Boltzmann distribution law, which can be expressed as follows⁷³⁶

$$\text{FIR} = \frac{I_1}{I_2} = B \exp\left(-\frac{\Delta E}{kT}\right) \quad (1)$$

where B is a constant, ΔE is the energy difference between the two emission bands, and k is the Boltzmann constant. To evaluate the thermometric capacity, the absolute sensitivity (S_a) and the relative sensitivity (S_r) can be calculated as⁷⁴²

$$S_a = \frac{d\text{FIR}}{dT} = \text{FIR} \times \frac{\Delta E}{kT^2} \quad (2)$$

$$S_r = \frac{1}{\text{FIR}} \frac{d\text{FIR}}{dT} \times 100\% = \frac{\Delta E}{kT^2} \times 100\% \quad (3)$$

Since S_r is used on a larger scale, it allows comparison of the thermometric sensitivities of thermometers of different types and principles. The emission intensity of Er^{3+} -doped luminophores at 525 nm increases with increasing temperature, accompanied by a decrease in emission intensity at 545 nm. For instance, Brites et al. reported a nanothermometer based on $\text{NaYF}_4:\text{Yb}/\text{Er}@\text{NaYF}_4$ with a relative thermal sensitivity of 1.15% K^{-1} at 296 K.⁷³⁷ Thanks to its remarkable thermometric capacity and high spatial resolution ($<1 \mu\text{m}$), the

Table 2. Summary of Rare-Earth-Doped Nanomaterials for Temperature Sensing

host	dopant	exc (nm)	ratio of ems (nm)	maximum Sr^a (% K^{-1})	T (K)	range (K)	ref
NaYF ₄	Yb, Er	980	525/545	1.15	296	300–330	737
NaYF ₄	Yb, Er	980	525/545	1.8	/	298–343	738
NaYF ₄	Yb, Er	980	525/545	1.24	300	300–773	739
NaYbF ₄	Er	980	525/545	3.46	175	175–475	740
NaYF ₄ @SiO ₂	Yb, Er	975	525/545, 1010/810, 1010/660	1.10, 1.44, 0.79	313	299–337	741
YF ₃	Yb, Er	975	525/545	1.2	295	295–478	732
Bi ₃ IO ₇	Er	980	525/545	1.36	303	303–543	742
Bi ₂ SiO ₅ @SiO ₂	Yb, Er	977	525/545	1.1	300	80–800	743
SrF ₂	Yb, Er	980	525/545	1.2	298	298–383	744
α -NaGdF ₄	Yb, Er	980	525/550	/	/	293–363	745
β -NaGdF ₄							
β -NaGdF ₄ @SiO ₂							
LaPO ₄ /YPO ₄	Yb, Tm	975	700/800	/	/	293–773	352
α -NaYbF ₄ :Tm@CaF ₂ @NaYF ₄ :Yb/Er@CaF ₂	Yb, Tm, Er	980	801/820, 521/538	3.06	150	10–295	746
Bi ₂ O ₃	Yb, Tm	980	799/808	/	/	98–373	747
LaF ₃	Yb, Er	378	988/1540	6.6092	15	15–105	748
	Yb, Pr	/	/	1.08	25		
GdOF/SiO ₂	Yb, Nd, Er	808	534/543	1.6	260	260–490	749
Yb ₂ W ₃ O ₁₂ , Yb ₂ WO ₆	Er	980	523/660	/	573	303–573	381
SrF ₂	Yb, Tm	975	795/769	0.24	/	/	750
	Nd	808	869/905	0.17	/	/	
NaGdF ₄ :Yb/Er/Ho@NaGdF ₄ :Yb@ NaGdF ₄ :Yb/Nd@NaGdF ₄	Yb, Er, Ho, Nd	806	1180/1340, 1550/1340	1.17, 1.1	/	293–323	751
KLu(WO ₄) ₂	Yb, Ho	980	545/650	0.54	300	297–673	752
NaGdF ₄	Yb, Ho, Ce	980	650/543	/	500	300–500	753
CsPbBr ₃ /EuPO ₄	Eu	393	611/516	1.8	420	303–480	754
Sc ₂ O ₃	Eu ²⁺ , Eu ³⁺	254	403/612	3.06	267	77–267	132
Mn:Zn ₂ SiO ₄ –Eu:Gd ₂ O ₃	Eu	260	612/520	3.05	303	303–623	755
SrZrO ₃	Eu	237	616/470	2.22	460	300–550	756
LaF ₃	Nd	808	865/885	0.25	/	303–343	757
Y ₃ Al ₅ O ₁₂	Nd	808	938/945	0.15	/	283–343	758
LiLuF ₄	Nd	808	862/866	0.62	77	77–275	759
LiLa _{0.4} Nd _{0.1} Yb _{0.5} P ₄ O ₁₂	Nd, Yb	808	870/980	0.4	330	93–663	760
TiO ₂	Eu	360	613/438	2.43	/	307–533	761
ZnSe	Er	980	656/547	8.61	77	77–298	762
TiO ₂	Sm	360	612/438	10.54	330.5	297–383	763
MoS ₂	Eu	282	612/437	1.4904	180	30–360	513
Eu _{0.2} Tb _{0.8} L	Eu, Tb	322	543/615	0.15	300	40–300	499
[Eu ₂ (QPTCA)(NO ₃) ₂ (DMF) ₄ ·(CH ₃ CH ₂ OH) ₃]perylene	Eu	388	615/473	1.28	293	293–323	764
Eu _{0.0066} Tb _{0.9934} L	Eu, Tb	335	542/612	3.76	450	77–450	765
Eu _{0.0089} Tb _{0.9911} L	Eu, Tb, Gd			2.71		430	
Eu _{0.013} Tb _{0.060} Gd _{0.927} L				6.11		400	
Eu _{0.033} Tb _{0.085} Gd _{0.882} L				3.62			
UiO-bpydc	Eu	395	530/614	2.99	293	293–353	766
(Me ₂ NH ₂) ₃ [Ln ₃ (FDC) ₄ (NO ₃) ₄ ·4H ₂ O	Eu	365	475, 575, 605, 640	2.7	170	12–320	767
Nd _{0.577} Yb _{0.423} BDC-F ₄	Nd, Yb	808	1060/980	0.816	313	293–313	768

^aRelative sensitivity.

researchers demonstrated that this nanothermometer can measure the instantaneous ballistic velocities of Brownian nanocrystals in colloidal suspensions.

There is growing interest in exploiting the anomalous effect of thermally enhanced luminescence in rare-earth-based nanothermometry.^{769–772} Normally, elevated temperatures are detrimental to nanophosphor luminescence because they enhance nonradiative pathways (phonon relaxation). Nevertheless, several groups have recently observed anomalous thermally enhanced upconversion luminescence in rare-earth-

doped crystals, such as NaGdF₄:Yb/Eu, NaYF₄:Yb/Tm, NaY(WO₄)₂:Yb/Er, and Yb₂W₃O₁₂:Er.^{381,773–775} Thermal enhancement has been linked to material properties such as particle size, dopant composition and concentration, crystal structure, and surface modification. Zhou et al. argued that the oxygen component on Yb³⁺/Tm³⁺-doped nanoparticle surfaces can form a stable [Yb···O] complex with Yb³⁺.⁷⁴⁴ The coupling of phonon vibrations with the excited intermediate state of Tm³⁺ could further facilitate the upconversion process at elevated temperatures. Lei et al. attributed this thermal

Table 3. Summary of Rare-Earth-Doped Nanomaterials for pH Sensing

host	dopant	exc (nm)	em (nm)	pH indicator	pH range	ref
NaYF ₄	Yb, Er	980	656/542	ETH 5418	6–11	793
NaYF ₄	Yb, Er	980	540	graphene oxide	5–8	794
NaYF ₄	Yb, Er	980	590/550	pHrodo Red	3–7	795
NaYF ₄	Yb, Er	980	540	pHAb	4–6	796
NaGdF ₄	Yb, Er	980	795/540	Ag ₂ S	4–9	797
NaGdF ₄	Yb, Er	980	650	bromothymol blue	6–8	798
NaYF ₄	Yb, Tm	980	528/648	BODIPY dye	5–9	799
NaGdF ₄	Yb, Tm	980	670	DNA	5.5–7.2	800
NaYF ₄	Yb, Tm	980	450/646	xylene orange	5–8	801
NaGdF ₄ @NaYF ₄ :Yb/Tm@NaYF ₄	Yb, Tm	980	650/513	hemicyanine dye	4–9	802
NaGdF ₄ :Yb/Tm@NaGdF ₄ :Nd/Yb@NaYF ₄	Nd, Yb, Tm	808	515/645	fluorescein	5–8	803
NaYF ₄ :Yb/Tm@NaYF ₄ :Yb@NaYF ₄ :Yb/Nd	Nd, Yb, Tm	808	474/643	FITC	3–8	804
NaGdF ₄	Ce, Tb	254	550	citric acid	3–10	805
NaGd(WO ₄) ₂	Eu	250, 490	512/611	fluorescein	4–10	806
NaGd(WO ₄) ₂ IOPC	Tb, Eu	280	620	phenol red	5–10	807
carbon quantum dots	Eu, Tb	365	438	/	1–14	808
JXNU-3 (MOF)	Tb	327	~550	/	3–7	809
[Eu ₅ (OH) ₆ (TZI) ₃ (DMA) _{1.5}](H ₂ O) _{10.5} ·DMA·0.5H ₂ O	Eu	/	616	/	3–10	810
MOF-253-Eu-TTA	Eu	375	614	/	5–7.2	811
[Ln ₂ (D-cam)(Himdc) ₂ (H ₂ O) ₂]	Eu	277	616	/	6.8–8.0	812
[Tb ₄ (μ ₃ -OH) ₄ L ₃ (H ₂ O) ₇]Cl _{0.63} ·(NO ₃) _{4.37} ·3H ₂ O	Tb	336	542	/	2–7	813

enhancement effect to the release of trapped electrons, while Hu et al. argued that the desorption of H₂O molecules was the key factor.^{776,777} Although the mechanism is still under debate,⁷⁷² this temperature effect has facilitated the design of rare-earth-based thermometers with ultrahigh thermal sensitivity. For example, Mi et al. reported combining thermal enhancement and thermal quenching within a nanoparticle to achieve high relative sensitivity.⁷⁷⁸ In their design, NaYF₄:Yb/Nd@NaYF₄@NaYF₄:Yb/Er nanoparticles with a core–shell–shell structure were prepared, in which Nd³⁺ luminescence was enhanced by phonon-assisted Yb³⁺-to-Nd³⁺ energy transfer and Er³⁺ luminescence was thermally quenched at elevated temperatures. A ratiometric thermometer with a maximum relative sensitivity of 9.6% K⁻¹ at room temperature was obtained. New analytical methods in combination with ratiometric approaches will further improve the relative sensitivity of multiparametric luminescence thermometers.⁷⁷⁹ Other examples of recently developed rare-earth-based thermometers are summarized in Table 2.

Rare-earth-based optical thermometry has been combined with clinical therapeutic protocols to synchronously monitor lesion temperature.^{647,648} There is also a growing demand for the development of NIR-I/II luminescence nanothermometers capable of detecting localized microenvironments in biological systems. In this context, Yb³⁺, Nd³⁺, Ho³⁺, Er³⁺, and Tm³⁺ emitters have been used for NIR-based thermometry, which enables temperature sensing and luminescence lifetime measurements in deep tissues.^{757,780–783} For example, Nd³⁺–Yb³⁺ is a typical NIR-to-NIR emission system that has shown great potential for subcutaneous thermal biosensing based on phonon-assisted energy transfer from Nd³⁺ to Yb³⁺. Ximendes et al. found that thermal sensitivity was increased 4-fold when Nd³⁺ and Yb³⁺ were separated in the core and shell layers, respectively.⁷⁸⁰ These core–shell nanoparticles were used to measure subcutaneous temperatures in the NIR optical window with high accuracy.

4.2.2. Pressure Sensing. In addition to temperature sensing, rare-earth-doped nanomaterials have also been used to

measure pressure changes. Optical stress nanosensors have recently emerged for applications in robotics and materials research. It has long been known that the emission properties of certain rare-earth ions respond to pressure stimuli.^{784,785} To date, the pressure-stimulated responses of rare-earth-doped inorganic materials are thought to be mainly due to piezoelectric and crystal field effects. The application of pressure creates a piezoelectric field due to strong electron–lattice coupling, which triggers the separation of charge carriers trapped by defects in a transient state.⁷⁸⁶ Due to the slope of the energy bands below the internal piezoelectric potential, electrons in lattice defects can be easily detrapped after moving to a lower energy. Recombination of the released electron and hole pairs enables nonradiative energy transfer to doped rare-earth emitters, leading to spontaneous photon emission. This process, also known as mechanoluminescence, does not require additional photoexcitation to emit photons. Moreover, under high pressure, the interatomic distances and bond lengths shorten, the local symmetry around the rare-earth ions changes, and a phase transition can even occur, leading to altered luminescence characteristics upon photoexcitation.

CaZnOS, *m*CaO·Nb₂O₅, SrZn₂S₂O, and SrZnSO host crystals have been combined with rare-earth emitters to achieve efficient mechanoluminescence.^{787–789} In mechanoluminescence, external pressure stimuli can shift the emission wavelength by tuning crystal field effects. By applying stress stimuli, shifts in emission peaks and changes in emission ratios or lifetimes can be observed in different host materials.^{385,790,791} In 2020, Zhuang et al. reported stress sensing by force-induced charge carrier storage, using SrSi₂O₂N₂, BaSi₂O₂N₂, and (Sr_{0.5}Ba_{0.5})Si₂O₂N₂ materials doped with Eu²⁺, Yb²⁺, and Dy³⁺.⁷⁹² These stress-responsive materials are well suited for electronic signature documentation, fall monitoring, and traffic accident recording. It is also hoped that the stress-dependent color modulation of mechanoluminescent materials could be capitalized for biosensing applications, especially for detecting acute stress in cell membranes and living organisms. This would require the development of new synthetic

Table 4. Summary of Rare-Earth-Doped Nanomaterials for Biodetection

target	host	dopant	exc (nm)	em (nm)	sensitive indicator/ acceptor	range	LOD ^a	ref
					Amino Acid			
cysteine	NaYF ₄ @mSiO ₂	Yb, Tm	980	518,475	fluorescein-O,O'-diacrylate	20–200 μM	20 μM	815
cysteine	NaYF ₄	Yb, Er	980	540	rhodamine-oxaldehyde	10–100 μM	1.1 μM	816
tyrosine	NaYF ₄	Yb, Tm	980	490	tyrosine	0.8–100 μM	1.1 μM	817
cysteine/ homocysteine	NaLuF ₄ @yolk shell	Yb, Er, Tm	980	540,800	ANP	0–18 equiv	28.5 μM	818
tryptophane	Zn-Hbtc-BPY	Tb	300	546,370	/	3.92–100 ppm	3.1 ppm	819
L-lysine	[Dy(L)(H ₂ O)(DMF)] _n	Dy	290	372,584	rhodamine B	0–0.4 μM	0.024 μM	820
D-lysine							0.007 μM	
					Nucleic Acid			
complementary ssDNA2	NaYF ₄	Yb, Tm	980	530, 480	SYBR green I	/	3.2 nM	821
ssDNA2-M3							7.6 nM	
microRNA-21	NaYF ₄ @NaYF ₄ :Yb/Er @NaYF ₄	Yb, Er	980	543	BHQ1	0.1 fM–0.1 nM	0.036 fM	822
miR-195	NaYF ₄	Yb, Tm	980	470	5-carboxyvinyl-2'-deoxyuridine	20 fM–500 pM	20 fM	823
ss-DNA	NaYF ₄	Yb, Tm	975	450–500	[(ppy) ₂ Ir(dcbpy)]PF ₆ -AuNP	1 pM–100 μM	1 pM	824
ss-DNA	NaYF ₄	Yb, Er	980	549, 654	graphene oxide	/	5 pM	825
Ebola virus oligonucleotide	BaGdF ₅	Yb, Er	980	540	Au nanoparticle	50–700 fM	300 fM	826
BACE-1,PCA3	NaYF ₄	Yb, Er	980	545	graphene oxide	200 fM–5 nM	500 fM	827
					Peptide and Protein			
bovine hemoglobin	NaYF ₄	Yb, Er	980	543.5	bovine hemoglobin	0.1–0.6 mg/mL	0.062 mg/mL	828
glutathione	NaYF ₄	Yb, Er	980	550	dopamine–quinone	1–75 μM	0.29 μM	829
glutathione	NaYF ₄ :Yb/Er@NaYF ₄	Yb, Er	980	654	Au NP	0.05–2 μM	0.016 μM	830
glutathione	NaYF ₄	Yb, Er, Tm	980	540, 800	TCG	0–10 mM	0.83 mM	831
avidin	NaYF ₄	Yb, Tm	980	520, 480	FITC	0–4.5 nmol	48 pmol	832
alpha-fetoprotein	NaYF ₄	Yb, Tm	980	480	ZnO/Ag	0.05–100 ng/mL	40 pg/mL	833
cytochrome c	NaYF ₄	Yb, Er	980	543.5	cytochrome c	1–24 μM	0.73 μM	834
carcinoembryonic antigen	NaYF ₄	Yb, Tm	980	520, 480	FITC	0.1–100 ng/mL	0.89 ng/mL	835
prostate-specific antigen	NaYF ₄	Yb, Er	980	550	Au nanoparticle	0–500 pM	1 pM	836
CA-125 antibody	NaYF ₄	Yb, Tm	980	480	Ag nanoparticle	5–100 ng/mL	120 pg/mL	837
Caspase-9	NaYF ₄ : Yb/Er@NaGdF ₄	Yb, Er	980	655,541	Cy5	0.5–100 U/mL	0.068 U/mL	838
tyramine	NaGdF ₄ :Yb/Er@NaYF ₄	Yb, Er	980	541,655	/	0.167–33.3 μM	0.026 μM	839
tyrosinase						0.0033–1 U/mL	0.003 U/mL	
matrix metalloproteinase MMP-2	NaYF ₄ :Gd/Yb@NaYF ₄ : Yb/ Tm/Er	Yb, Er, Tm	980	450,655	TAMRA	0.001–0.2 μg/mL	2.2 ng/mL	840
MMP-7				541,655	FITC	0.01–1 μg/mL	13.9 ng/mL	
insulin	Gd(L)(H ₂ O)(DMF)	Gd	490	525	FAM-P	0–1.72 μM	0.0012 μM	820
creatine kinase	Eu-QPTCA	Eu	373	615	/	1.2–156.2 U/L	1 U/L	841
tyrosinase	NaYF ₄	Yb, Tm	980	475	dopamine–quinone	0.001–0.1 U/mL	/	842
alkaline phosphatase					o-phospho-L-tyrosine	0.5–50 U/mL	/	
lysozyme	NaLu/GdF ₄ :Tb@NaYF ₄	Gd, Tb	X-ray	546	BHQ1-DNA	3–200 nM	0.94 nM	843
					Small Molecule			
vitamin B12	NaYF ₄	Yb, Tm	980	345	vitamin B12	3–634 nM	3 nM	844
melamine	NaYF ₄	Yb, Er	980	550,650	melamine	5–100 nM	9.1 nM	845
ascorbic acid	NaYF ₄	Yb, Tm	980	360	cobalt oxyhydroxide	2–60 μM	0.2 μM	846
ascorbic acid	Eu _{0.07} Gd _{0.03} -MOF	Eu, Gd	UV	614,415	/	0–60 μM	0.184 μM	847
catecholamine	NaLuGdF ₄ -Fe ³⁺	Yb, Er	980	542	catecholamine	5–320 nM	2.8 nM	848
uric acid	NaYF ₄	Yb, Er, Mn	980	665	/	4 nM–10 μM	1.9 nM	849
uric acid	NaCeF ₄	Yb, Er	980	1530	/	0–900 μM	25.6 nM	574
glucose	NaYF ₄	Yb, Tm	980	450	MnO ₂	0–400 μM	3.7 μM	850
glucose	BaWO ₄ :Yb/Er@Au	Yb, Er	980	529	Au	0–0.1336 μM	3.1 nM	851
ATP	NaGdF ₄	Yb, Tm	980	360	DNA aptamer	1–10 nM	/	852

Table 4. continued

target	host	dopant	exc (nm)	em (nm)	sensitive indicator/ acceptor	range	LOD ^a	ref
			Small Molecule					
dopamine	NaYF ₄ : Yb@NaYF ₄ :Er@NaYF ₄ :Yb	Yb, Er	980	542	graphene oxide	1–10 pM	/	853
ppGpp	MoS ₂	Eu	254	616,410	/	50 nM –25 μM	44.4 nM	854
dipicolinic acid	Tb(BTC)(H ₂ O) ₆	Tb	290	545	/	1 nM–5 μM	0.04 nM	855
			Free Radical					
ONOO ⁻	NaYF ₄ @NaYF ₄ :Nd	Nd	808	1060	MY-1057	0–40 μM	/	856
ONOO ⁻	NaYF ₄	Yb, Tm	980	800	Cy7	3.5–17.5 μM	0.08 μM	857
·OH	NaYF ₄ @NaYF ₄ :Yb/Tm@NaYF ₄	Yb, Tm	980	480	mOG	1.2–194.6 fM	/	858
H ₂ O ₂	NaErF ₄ :Ho@NaYF ₄	Er, Ho	1530	980, 1180	IR1061	0–100 μM	/	189
H ₂ O ₂	NaYF ₄	Yb, Tm	980	450	MnO ₂	0–350 μM	0.9 μM	850
H ₂ O ₂	NaYF ₄ @ZIF-NiS _x	Yb, Er	980	660, 540	ZIF-NiS _x	0.05–20 μM	0.037 μM	859
ClO ⁻	NaGdF ₄	Yb, Tm	980	476	MoS ₂	0.5–15 μM	0.384 μM	860
ClO ⁻	NaYF ₄ :Yb,Nd,Er@NaYF ₄ :Nd	Nd, Yb, Er	808	540, 654	hCy3	0–80 μM	27 ppb	861
			Gas					
H ₂ S	NaLuF ₄ :Yb, Er,Tm@NaLuF ₄	Yb, Er, Tm	980	800/550, 654/550	Prussian Blue	0–150 μM	50 nM	862
H ₂ S	NaYF ₄	Yb, Er, Tm	980	540/800	merocyanines	0–115 μM	0.58 μM	863
H ₂ S	UiO-66-(COOH) ₂	Eu	305	615/393	/	0–625 μM	/	864
O ₂	NaYF ₄	Yb, Tm	980	613/477	[Ru(dpp) ₃] ²⁺ Cl ₂	0–39.16 mg/mL	/	865
O ₂	NaYF ₄	Yb, Er	980	645	PtOEP	0–100%	/	866
			Cation					
Cu ²⁺	NaGdF ₄ @NaYF ₄ :Ce/Tb	Ce, Tb	254	548	/	0–0.08 μM	0.35 nM	867
Cu ²⁺	NaYF ₄ @NaYF ₄ :Er/Yb@NaYF ₄	Yb, Er	980	543/658	rhodamine B hydrazide	0–360 μM	5.4 nM	868
Cu ²⁺	SrF ₂	Ce, Tb	290	544	/	1–10 μM	2 nM	869
Cu ²⁺	[Tb ₃ (L) ₂ (HCOO)(H ₂ O) ₅].DMF·4H ₂ O	Tb	327	550	/	1 μM–10 mM	/	870
Pb ²⁺	NaY(MoO ₄) ₂ :Tm/Ho/Yb	Yb, Tm, Ho	975	657	/	62.5–500 μM	/	871
Pb ²⁺	NaYF ₄ :Yb/Tm	Yb, Tm	980	545	CdTe	20–3600 nM	80 nM	872
Fe ³⁺	graphene quantum dots	Er	360	440	/	0.01–120 μM	2.8 nM	873
			730	442	/	0.1–200 μM	28 nM	
Fe ³⁺	NaYF ₄ :Gd/Yb/Ho	Gd, Yb, Ho	980	546/758	EPA	0.25–50 μM	0.65 nM	874
Fe ³⁺	NaYF ₄ :Yb/Er/Tm@NaGdF ₄	Yb, Er, Tm	980	540	Nile Red derivative	0–30 μM	89.6 nM	875
K ⁺ , Fe ³⁺	[LnK(BPDSDC)(DMF)(H ₂ O)]·x(solvent)	Eu	316	618	/	0.01–1 mM	/	876
Fe ³⁺	[Tb ₄ (OH) ₄ (DSOA) ₂ (H ₂ O) ₈].8H ₂ O	Tb	350	542	/	10 ⁻⁶ –10 ⁻¹ M	/	877
Cr ⁴⁺	carbon quantum dot	Eu, Tb	360	438	/	1–20 μM	0.175 μM	808
Hg ²⁺	ZnS	Ce	230	459/689	/	10–100 μM	0.82 μM	878
Hg ²⁺	NaYF ₄	Yb, Er, Tm	980	540/803	thiazole-derivative	0.8–5 mM	63 nM	879
Hg ²⁺	BA-Eu-MOF	Eu	275	620	/	0–240 μM	220 nM	880
CH ₃ Hg ⁺						0–200 μM	440 nM	
Ag ⁺	NaYF ₄	Yb, Er	980	543	graphene quantum dots	1–200 μM	60 pM	881
Ag ⁺	MIL-121	Sm	320	603	/	/	/	882
Zn ²⁺	NaYF ₄	Yb, Tm	980	475/654	compound 1	0–0.09 mM	/	883
Pb ²⁺	Tb(L)(H ₂ O) ₅	Tb	334	545	/	0.34–800 μM	0.34 μM	884
			Anion					
F ⁻	NaYF ₄	Yb, Er, Tm	980	546/758	curcumin	5–200 μM	5 μM	885
CN ⁻	NaYF ₄ :Yb/Er@NaYF ₄ :Yb	Yb, Er	980	655	Au nanoparticle	0–200 μM	1.53 μM	886
CN ⁻	NaYF ₄	Gd, Yb, Er	980	650/550	polydiacetylenes	10–25 mM	/	887

^aLimit of detection.

approaches for nanosized mechanoluminescent materials with well-controlled particle size, morphology, and surface modification.

4.2.3. pH Sensing. Since most rare-earth-doped nanophosphors are inert to pH changes, pH sensing based on these nanomaterials has been mainly accomplished by coupling pH-sensitive species such as molecular indicators (ETH 5418, pH-rodod red, bromothymol blue, etc.) and functional nanomaterials (graphene oxide, Ag₂S, etc.).^{793–795,797,798} The absorption of the pH indicators must overlap with the emission of the nanophosphors. Typically, pH changes can be identified by measuring variations in absorption wavelength, or absorption and emission intensities.⁸¹⁴

The 4f–4f transitions of rare-earth ions are relatively insensitive to environmental changes because the 4f electrons are shielded by filled 5s and 5p shells. Therefore, rare-earth emission can be employed as an internal reference for ratiometric pH measurement. For instance, Lei et al. proposed a new concept for rare-earth-based pH sensing by modulating an energy cascade from Ce³⁺ to the emitters.⁸⁰⁵ Ce³⁺ is a widely used sensitizer that absorbs ultraviolet light due to its 4f–5d transition facilitated by the electric dipole. In this sensor, citric acid was used as a pH-reactive ligand that combines with the nanoparticles. The electronegativity of citric acid decreases with increasing pH, which enhances the covalency between the ligand and Ce³⁺. This process disrupts the d–f transition and decreases the sensitization efficiency of Ce³⁺ toward the activators Tb³⁺, Eu³⁺, and Mn³⁺, leading to a decrease in emission intensity. Table 3 summarizes the recently reported pH sensors based on rare-earth-doped nanomaterials.

4.2.4. Molecular Detection. Rare-earth-doped nanomaterials have enabled the development of miniaturized, wearable molecular sensors with rapid signal responses. As these nanoparticles are largely inert to environmental changes, detection of molecules is mainly based on switching luminescence on and off by energy transfer, either by Förster resonance energy transfer (FRET) or by radiative reabsorption, between the nanoparticles and specific environmentally sensitive species (molecular biosensors and organic fluorophores).^{888,889} A number of species that provide detailed information about physiological state, including amino acids, nucleic acids, proteins, small molecules, free radicals, gases, and ions, have been detected with rare-earth-doped nanomaterials (Table 4).

To minimize background autofluorescence, NIR-to-visible UCNP are usually utilized. For instance, Tsang et al. combined BaGdF₅:Yb/Er UCNP and Au nanoparticles to construct a biodetection system for Ebola virus oligonucleotides.⁸²⁶ This detection was based on hybridization of Ebola virus oligonucleotides and complementary single-stranded oligonucleotides that brought UCNP and Au nanoparticles into close proximity to induce luminescence quenching. FRET-based molecular sensing normally requires high energy transfer efficiency to improve detection sensitivity. In this regard, Deng et al. utilized fluorescein NaGdF₄:Yb/Tm@NaGdF₄ nanoparticles to enhance FRET efficiency through Gd–Gd energy migration within the particles.⁷⁰⁵ Compared to conventional UCNP without energy migration within the particles, a >600-fold increase in acceptor emission was achieved in core–shell UCNP with an average size of 30 nm. By harnessing the effect of Tb–Tb energy migration within the NaYbF₄:Tb@NaTbF₄ nanoprobe, researchers have demonstrated quantitative anal-

ysis of photoreaction kinetics with single-molecule precision.⁸⁹⁰

In addition to upconversion from the NIR to the visible, Liu et al. recently designed H₂O₂ detection using NIR-to-NIR upconversion nanoprobes with both excitation and emission in the NIR-II window.¹⁸⁹ In that design, NaErF₄:Ho@NaYF₄ UCNP were employed as energy donors that generated upconverted NIR-II emission at 980 nm (⁴I_{11/2} → ⁴I_{15/2} transition of Er³⁺) and 1180 nm (⁵I₆ → ⁵I₈ transition of Ho³⁺) under 1530 nm excitation. Upconverted NIR-II emissions were quenched after conjugation with the organic chromophore IR1061. IR1061 decomposed in the presence of H₂O₂, leading to recovery in upconverted emission. Because of the low scattering and attenuation of NIR-II light in biological tissue, these nanoprobes enabled the detection of H₂O₂ with high spatial resolution (200 μm × 200 μm) in deep tissue.

The long lifetime of rare-earth emitters has enabled temporal imaging that avoids interference from short-lived autofluorescence. Zhang's group implemented luminescence lifetime-based *in situ* imaging of hepatocellular carcinoma using Nd³⁺-doped downshifting nanoparticles as energy donors.⁸⁵⁶ An ONOO⁻-sensitive dye (MY-1057) was coupled to these nanoparticles as an energy acceptor. The dye molecule absorbed the NIR-II emission and shortened the lifetime of Nd³⁺ emission. These dye-coupled nanoprobes distinguished lesions from normal liver tissue by imaging lifetime changes in response to ONOO⁻ in the tumor microenvironment. Compared to conventional imaging intensity-based biosensing, luminescence lifetime measurement provides much higher spatial resolution with clear pattern discrimination between tumor lesions (275 ± 49 μs) and normal tissue (205 ± 7 μs).

Another intriguing detection method is the use of rare-earth-doped nanoparticles as single-particle counters for the quantification of target molecules. As a typical example, Mendez-Gonzalez et al. constructed an ingenious DNA detection scaffold based on UCNP. The researchers employed two oligonucleotide probes, “UC-probe” and “c-probe” for detection.⁸²³ In the presence of target DNA, these oligonucleotide probes hybridized and captured UCNP in microwells. The number of target DNA sequences can be determined by counting the number of UCNP bound in the microwells. Indeed, single-particle/single-molecule imaging is an emerging technique with the advantage of high sensitivity and low detection limits, and its application in molecular sensing has gained increasing attention.^{32,564} Liu's group has developed a hedgehog-like core–shell nanostructure for upconversion, which can be used to detect dithiothreitol.⁸⁹¹ This nanostructure was first modified with an MnO₂ layer to attenuate upconversion luminescence. After addition of dithiothreitol, a “turn-on” process of luminescence was observed at the single-particle level.

Rare-earth-doped nanomaterials can be applied to gas sensing by monitoring changes in electrical conductivity. Rare-earth oxides (Sm₂O₃, CeO₂, Dy₂O₃), rare-earth perovskite oxides (REFeO₃ and REMnO₃), and rare-earth-doped semiconductor nanocrystals (ZnO, NiO, SnO₂) have attracted considerable attention for gas sensing.^{892–899} When rare-earth-doped nanoprobes are exposed to air, adsorbed oxygen on the surface withdraws electrons from the conduction band of the host material, resulting in negatively charged chemisorbed species such as O⁻, O²⁻, and O₂⁻. This leads to a layer with increased electron depletion. Binding gas molecules to nanoprobe surfaces leads to electron release into the

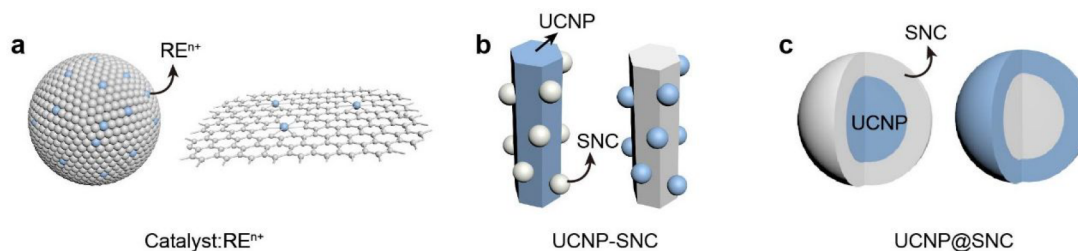


Figure 24. Schematic design of rare-earth-doped nanomaterials for catalysis. (a) Rare-earth-doped nanocatalysts. (b) Heterogeneous catalysts based on UCNP-semiconductor nanocrystal (SNC) hybrids. (c) UCNP@SNC core-shell catalysts.

conduction band, eliminating the electron depletion layer. For n-type semiconductors, the increased electrons enhance the electrical conductivity and decrease the resistance, while for p-type semiconductors, the increased electrons deplete hole density and increase the resistance. Gas molecules, including NO_x ,^{900,901} CO ,⁹⁰² CO_2 ,⁹⁰³ H_2 ,⁸⁹⁹ H_2S ,⁹⁰⁴ SO_2 ,⁹⁰⁵ NH_3 ,⁹⁰⁶ and volatile organic compounds such as acetone,⁹⁰⁷ ethanol,⁹⁰⁸ methanol,⁹⁰⁹ and formaldehyde,⁸⁹⁶ induce resistivity changes in rare-earth-based semiconductor nanopores.

Reactions with gas molecules can form an excited intermediate on material surfaces. This intermediate can emit photons when it returns to the ground state, a process known as cataluminescence.⁹¹⁰ Tang et al. developed a novel cataluminescent gas sensor based on $\text{NaYF}_4:\text{Er}$ nanocrystals.²⁰⁴ This gas sensor shows excellent selectivity for ketones, with detection limits of 1.7 and $0.7 \mu\text{g mL}^{-1}$ for acetone and butanone, respectively. The sensor exhibits negligible cataluminescence for alcohols, aldehydes, acetonitrile, dipropylmethane, and ethyl acetate. Moreover, $\text{NaYF}_4:\text{Er}$ nanocrystals have a short response time of 3 s at 250°C . Nevertheless, gas sensors based on resistance changes or cataluminescence generally require high working temperatures ($>100^\circ\text{C}$), which is unsuitable for daily use. There is still a huge need for the development of gas sensors based on nanomaterials that can operate at ambient temperature.

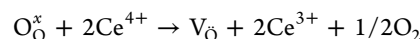
It is worth noting that optical materials are of great use in the development of wireless sensors for the internet of things (IoT).^{911,912} With the ability to measure multiple components simultaneously, IoT optical sensors can generate a wealth of data in various contexts, which can then be processed and leveraged remotely by users. Rare-earth-doped nanomaterials could impact the IoT sensor industry in the not-too-distant future.

4.3. Catalysis

Catalysis is essential for pollution control and all aspects of industry. Rare-earth elements are used as catalysts in various forms, such as alloys, rare-earth complexes, and photocatalysts.^{21,913,914} They are often combined with precious metals and semiconductor nanocrystals (Figure 24). The use of rare-earth nanomaterials could promote reactivity and facilitate solar energy harvesting.

4.3.1. Ceria-Based Catalysis. Catalysts based on ceria (CeO_2) have been widely used for water-gas reaction,^{915,916} steam reforming of methanol,⁹¹⁷ water splitting,^{918,919} and automobile exhaust treatment (e.g., CO oxidation^{920–922} and NO reduction^{923,924}). The catalytic property of CeO_2 is mainly due to the reversible valence change of $\text{Ce}^{4+}/\text{Ce}^{3+}$, which allows the simultaneous release/storage of oxygen to form CeO_x . Oxygen vacancies form in CeO_2 after the reduction of Ce^{4+} to Ce^{3+} . Oxygen vacancies can serve as active sites for

many reactions. Using Kröger–Vink notation, the reaction can be expressed as follows:



Since an oxygen vacancy can be generated and vanish in a short time, this reaction leads to a high oxygen storage capacity of CeO_2 .

Impurity doping can modify the catalytic performance of CeO_2 . A typical example is the doping of Zr^{4+} with CeO_2 , which strongly promotes the redox property of the catalyst.¹⁰ Esch and co-workers reported high-resolution scanning tunneling microscopy (STM) to study the (111) facet of CeO_2 with atomic resolution. They observed that oxygen vacancies tend to form linear clusters at high temperatures ($300\text{--}400^\circ\text{C}$).⁹²⁵ Zr^{4+} dopants can increase surface thermal stability and porosity, thus improving the catalytic performance of CeO_2 . Besides Zr^{4+} , other metals such as Au, Pt, Rh, Ti, Fe, and Cu have been incorporated into CeO_2 to form $(\text{Ce}_x\text{M}_{1-x})\text{O}_2$ solid solutions, which can be used to fine-tune the formation energy of oxygen vacancies in the oxides.^{922,926–930}

Apart from impurity doping, metal nanoparticles on nanocrystalline CeO_2 supports have attracted much attention for catalysis. Carretin et al. deposited Au nanoparticles on nanocrystalline CeO_2 .⁹²⁰ This hybrid structure increased the catalytic activity of Au/ CeO_2 nanocomposites by 2 orders of magnitude in low-temperature CO oxidation in the presence of H_2 . Cargnello et al. investigated the size effect of nanoparticles deposited on a CeO_2 support.⁹³¹ Ni, Pd, and Pt nanoparticles of various sizes were deposited on a CeO_2 support to catalyze CO oxidation. The metal atoms at the interface between the metal nanoparticles, the CeO_2 support, and the atmosphere were determined to be the catalytic sites. Due to a larger contact area with the CeO_2 support, smaller metal nanoparticles showed higher catalytic activity for CO oxidation.

The enhanced catalytic properties of metal nanoparticles on CeO_2 supports are mainly due to the charge transfer resulting from metal-support interactions. Besides the particle size, the structure of the nanoparticles and the chemical properties of the support can also influence the dynamics of the charge transfer.⁹³² Additionally, nanocrystalline CeO_2 can serve as a support for single-atom catalysis. Nie et al. treated atomically dispersed Pt atoms on CeO_2 with high-temperature steam (750°C) to promote the formation of active surface oxygen lattices in the vicinity of Pt sites.²¹ In this way, the oxidation of CO was dramatically accelerated at a much lower reaction temperature (lowered from 320 to 148°C).

Nanoceria has shown great promise for biological catalysis. CeO_2 exhibits activities that mimic various enzymes such as photolyases,⁹³³ phosphatases,⁹³⁴ oxidases,⁹³⁵ peroxidases,⁹³⁶

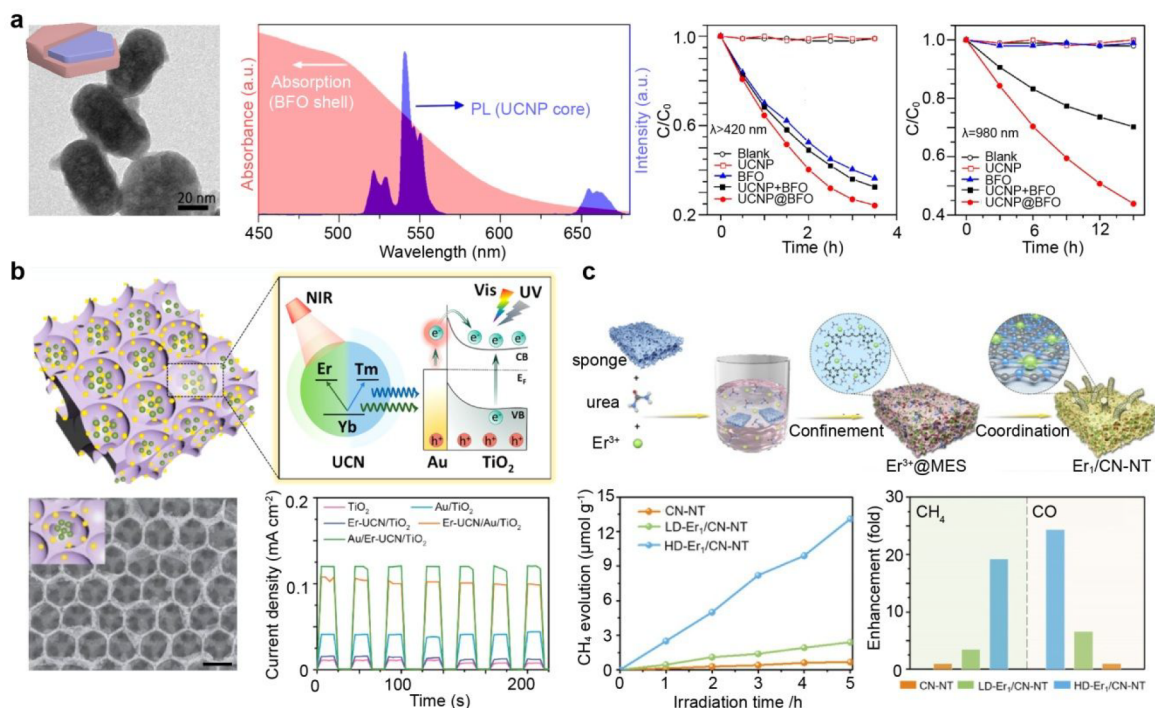


Figure 25. (a) Structure and catalytic properties of UCNP@BiFeO₃ (BFO) core-shell nanoparticles. (b) Schematic of the photoinduced catalysis process and photoelectrochemical properties of UCN/Au/TiO₂ nanohybrids with inverse opal structures. The scale bar is 500 nm. (c) Schematic of the synthetic process and photocatalytic performance of single-atom Er₁/CN-NT catalysts (Adapted with permission from refs 510, 942, and 943. Copyright 2017, 2019 American Chemical Society; Copyright 2020 Wiley-VCH Verlag GmbH & Co. KGaA, Weinheim).

catalases,⁹³⁷ and superoxide dismutases.⁹³⁸ Recently, Zhao et al. constructed enzyme surrogates for inflammatory bowel disease therapy based on enzyme-mimicking CeO₂@montmorillonite (MMT) materials.⁹³⁹ In that design, a negatively charged MMT layer facilitated transportation of positively charged CeO₂ to the inflamed colon. CeO₂ efficiently scavenged ROS to alleviate tissue inflammation. Moreover, CeO₂ catalyzed the degradation of H₂O₂, mimicking superoxide dismutase and catalase. After oral administration, CeO₂@MMT inhibited colonic inflammation, diarrhea, and rectal bleeding and improved the histological appearance in dextran sulfate sodium-induced rodents.

Phosphatase is an enzyme capable of hydrolyzing organic deleterious phosphorus compounds.⁹⁴⁰ Mugesh's group reported that vacancy-engineered nanoceria (VE CeO₂) efficiently promoted the hydrolysis of organophosphate triester such as paraoxon *in vivo*.⁹⁴¹ Enrichment of oxygen vacancies endowed the nanoceria with phosphotriesterase-mimetic hotspots. VE CeO₂ nanoparticles exhibited much higher catalytic activity than pristine CeO₂ nanoparticles, indicating the versatility of vacancy engineering in tuning catalytic properties.

Nanosized ceria powder has also proven useful as a photocatalyst for medical treatment, gas conversion, and pollutant removal.^{944–946} Unlike bulk cerium oxide, the bandgap of nanoceria can be tuned by controlling its size and morphology. Yao et al. synthesized mesoporous Yb³⁺/Tm³⁺-codoped CeO₂ UCNPs with a 2.89 eV bandgap.²⁵⁸ Under 980 nm excitation, UV emission from Tm³⁺ sensitized CeO₂ and converted O₂ and H₂O into cytotoxic ROS. Due to the catalase-like activity of CeO₂, the abundant H₂O₂ molecules in tumor cells were decomposed while synergistically providing O₂. In 2019, Wang et al. improved the

photocatalytic activity of CeO_{2-x} for CO₂ reduction by introducing Cu to stabilize oxygen vacancies.⁹⁴⁷ The combination of Cu and CeO_{2-x} improved CO production 26-fold compared to pure CeO_{2-x} catalysts.

4.3.2. Photocatalysis. To harvest NIR light for photocatalysis, rare-earth-doped UCNPs can be combined with semiconductor photocatalysts. For instance, Qin et al. demonstrated the combination of TiO₂ and UCNP transducers for photocatalysis. They coated a TiO₂ shell on YF₃:Yb/Tm nanoparticles and then investigated the photocatalytic performance by monitoring the degradation of methylene blue (MB).⁹⁴⁸ About 60% of MB was degraded after 30 h of laser irradiation at 980 nm. In a follow-up study, the researchers also confirmed that the degradation of MB was mainly due to the photocatalytic generation of ROS, rather than a thermal effect caused by NIR irradiation.²¹⁹ Yu et al. combined NaYF₄:Yb/Tm nanoparticles with CdS nanoparticles, which resulted in ~23% degradation of rhodamine B after 3 h of NIR irradiation.⁹⁴⁹

Zhang et al. designed NaGdF₄:Yb/Er@BiFeO₃ nanoparticles for photodegradation of methylene orange (Figure 25a).⁹⁵⁰ BiFeO₃ is a multiferroic material with a bandgap of ~2.0–2.6 eV. The corresponding absorption of BiFeO₃ well matches the upconverted emission of Er³⁺. Under monochromatic NIR irradiation for 15 h, 55% degradation of methylene orange was achieved. In addition to NaYF₄, CaF₂ is also a suitable host with low phonon energy for efficient photon upconversion. Huang et al. deposited CaF₂:Yb/Er/Tm nanoparticles on the surface of BiVO₄ with dendritic morphology. Bi³⁺ can tailor the local crystal field of lanthanide dopants at the UCNP–BiVO₄ interface and enhance upconversion luminescence, which improves the photocatalytic performance.⁹⁵¹

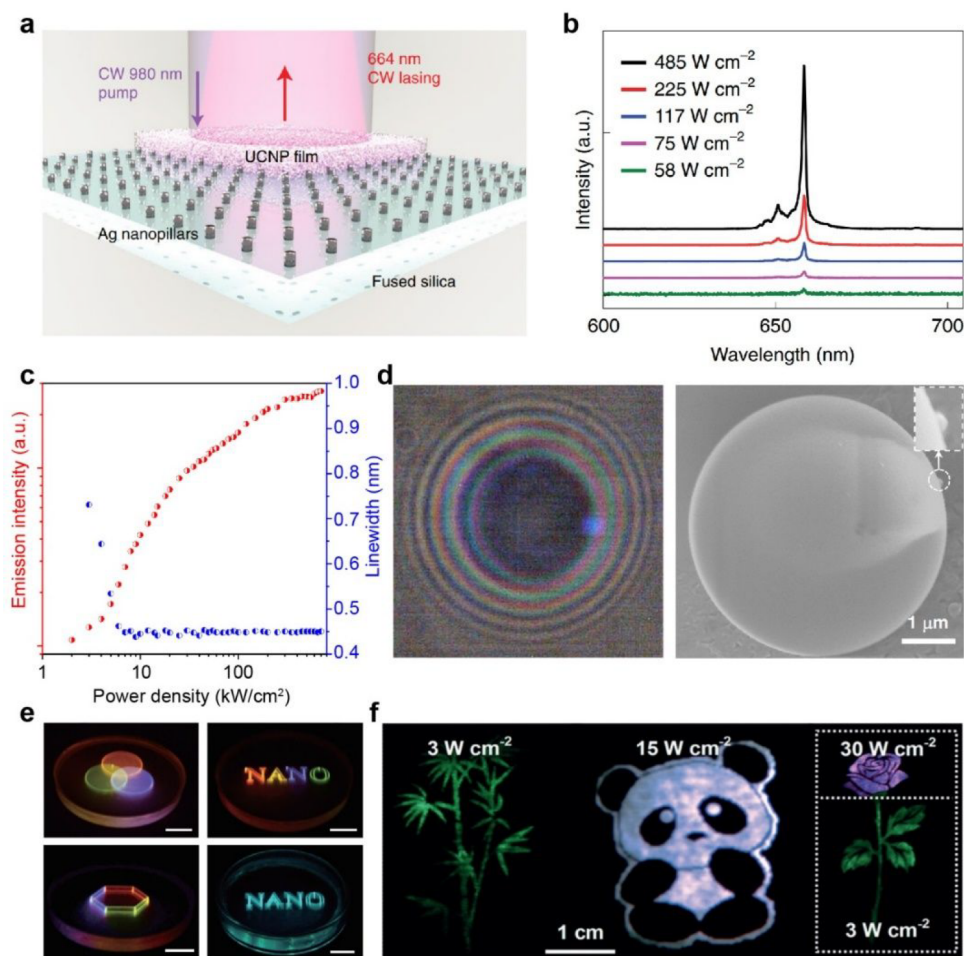


Figure 26. (a) Schematic of upconversion lasing based on UCNP-Ag arrays. (b) Power-dependent lasing spectra of UCNP-Ag arrays. (c) Excitation power-dependent emission intensities and spectral line width (peak@808 nm). (d) Wide-field image (left) and SEM image (right) of a single UCNP in a microcavity. (e) Luminescence color images generated in different nanocrystal/PDMS composite monoliths. Scale bars are 1 cm. (f) Images of bamboo, panda, and rose printed on a piece of A4 paper using the colloidal nanostructure as colorless ink (Adapted with permission from refs 33, 312, 965, and 973. Copyright 2015, 2019, 2020 Nature Publishing Group; Copyright 2015 Wiley-VCH Verlag GmbH & Co. KGaA, Weinheim).

Besides binary nanocomposites, Zhang et al. fabricated TiO₂ nanofibers in combination with a large amount of NaYF₄:Yb/Tm nanoparticles and CdS nanospheres to achieve full-spectrum absorption.⁹⁵² In 2019, Boppella et al. deposited UCNPs and Au nanoparticles on an inverse 3D TiO₂ opal (Figure 25b).⁹⁴³ Incorporation of Au nanoparticles not only enhanced light collection but also promoted energy transfer from UCNPs to TiO₂ via surface plasmon resonance.⁹⁵³ They prepared NaYF₄:Yb/Er and NaYF₄:Yb/Tm UCNPs whose emission overlapped the absorption of Au nanoparticles. This composite device achieved a 10-fold increase in photocurrent upon exposure to vis–NIR irradiation, compared to control devices using pristine TiO₂. In addition to Au nanoparticles, graphene and graphene oxides can act as energy acceptors for UCNPs. Wang et al. employed reduced graphene oxide (RGO) as the support to fabricate NaYF₄:Yb/Tm@TiO₂/RGO nanocomposites.⁹⁵⁴ This nanocomposite showed improved photocatalytic performance under NIR irradiation because it can scavenge photoinduced electrons from TiO₂ and prevent e⁻–h⁺ recombination by RGO.

Rare-earth-doped nanomaterials are viable catalysts for water splitting. They are amenable to photoelectrochemical hydrogen production. Chen et al. constructed a photoelectrochem-

ical cell using CdTe QD-decorated ZnO nanorods as the photoanode, a Pt plate as the counter electrode, and Au-modified UCNPs attached to ZnO nanorods for NIR harvesting.⁹⁵⁵ When this photoelectrochemical cell was exposed to sunlight, electrons generated in ZnO transferred to Pt via an external circuit and subsequently reduced hydrogen ions to hydrogen. Meanwhile, photogenerated holes reacted with water to generate oxygen molecules.

Beyond broadening the absorption spectrum, the introduction of Nd³⁺, Sm³⁺, and Eu³⁺ ions can reduce semiconductor bandgaps (e.g., Ag₃VO₄). Trivalent dopants can also inhibit the recombination of photogenerated electron–hole pairs, improving the photocatalytic performance.^{956,957} Moreover, Xie et al. found that surface Nd³⁺ dopants can serve as Lewis acid to form complexes with dyes. The dyes can capture visible light and inject electrons into the conduction band of TiO₂. Subsequently, Nd³⁺ ions scavenge electrons transferred from TiO₂ to generate superoxide radical anions.⁹⁵⁸ Nd³⁺ can harness visible light while facilitating electron–hole separation. A similar phenomenon was recently reported by Wang et al.,⁹⁵⁹ who demonstrated that Gd³⁺-rich nanoparticles can enhance adhesion of organic molecules on UCNPs–TiO₂ hybrid

catalysts, enhancing cycloreversion of organic chromophores during photocatalytic degradation.

4.3.3. Single-Atom Catalyst. Recently, rare-earths have drawn increasing attention to single-atom catalysis. In 2020, Liu et al. first demonstrated atomically dispersed Sc and Y as active sites for catalysis.¹⁶ Atomic Sc- and Y-doped C_3N_4 (Y_1/NC and Sc_1/NC) samples were synthesized by a simple solid-state reaction. Based on calculations and EXAFS analysis, rare-earth atoms preferred carbon defect sites where they were coordinated by six nitrogen and carbon atoms. The researchers also performed nitrogen and carbon dioxide reduction reactions to investigate the electrocatalytic performance of Y_1/NC and Sc_1/NC at room temperature. Both catalysts exhibited good stability and excellent catalytic properties.

Shortly afterward, Li's group employed Er atoms to fabricate single-atom photocatalysts supported by carbon nitride nanotubes ($Er_1/CN-NT$) using a strategy of atom confinement and coordination (ACC) (Figure 25c).⁵¹⁰ They demonstrated that the presence of Er atoms promoted absorption in the visible region. The production of CH_4 and CO was much faster with $Er_1/CN-NT$ than with pristine CN-NT. The researchers also used the ACC strategy to prepare single-atom catalysts other than Er. On a separate note, Dong's group reported La-doped carbon nitride single-atom catalysts with a La–N charge-transfer bridge as the active site, which exhibited high efficiency and selectivity in CO_2 reduction.²⁶⁰

4.4. Lighting and Displays

4.4.1. Nanoparticle Lasing. As a product of rapidly developing nanotechnology, nanolasers have recently received considerable attention for utilization in integrated circuits because they can be confined in cavities on the wavelength or subwavelength scale.⁹⁶⁰ Nanolasers consist of a gain medium and an optical cavity. Rare-earth-doped nanomaterials can act as the gain medium, while the optical cavities have different compositions and structures. Lowering the laser threshold has become the "holy grail" of the field, especially for upconversion lasers, since multiphoton upconversion emission usually requires a high energy input. Various methods have been explored to enhance light emission and lower the threshold. The most widely adopted technologies are plasmon amplification and whispering gallery mode (WGM).

Since surface plasmon resonance influences rare-earth luminescence in various settings,⁹⁶¹ this technique has been explored to develop rare-earth-doped nanolasers. By combining rare-earth-doped materials and noble metals, hybrid nanoparticle films and arrays have been prepared.^{962–964} Fernandez-Bravo et al. prepared Ag nanopillar arrays in a square lattice and subsequently coated $NaYF_4:Yb(20\%)/Er(20\%)@NaYF_4$ UCNP on the Ag nanopillar array (Figure 26a and b).⁹⁶⁵ The Ag nanopillar array has a lattice plasmon resonance that overlaps the red emission, arising from the $^4F_{9/2} \rightarrow ^4I_{15/2}$ transition of Er^{3+} . As a result, the red emission was greatly enhanced, and the pump threshold could decrease to $29 W cm^{-2}$. Moreover, the change in the lattice constant, a_0 , of the nanopillars modulated upconversion emission due to a change in the plasmon resonance, revealing the feasibility of determining the laser power directly using single-lattice plasmon cavities. Intriguingly, plasmonic array upconverting lasers provide directional beamlike emission with a small divergence angle of $\sim 0.5^\circ$, which is different from nanolasers with spherical and cylindrical cavity geometries based on WGM. Meanwhile, Wu et al. reported superburst upconversion

by coupling gap plasmon modes with nanoparticle emitters.⁶²² A three-layer structure, consisting of a silver nanocube, a $NaYF_4:Yb/Er$ UCNP layer, and a thin gold film was fabricated. This gap-mode nanocavity enabled an increase in upconversion emission by 4–5 orders of magnitude and a 166-fold increase in spontaneous emission with a lifetime of less than 2 μs .

Beyond the enhancement of surface plasmon resonance, WGM resonance has also received much attention. Under certain conditions, photons can be confined in a microscale or nanoscale cavity by total internal reflection. By preventing photons from losing energy, interactions between light and matter are efficiently enhanced. WGM is typically supported in spherical and cylindrical cavities, and many studies have focused on the coupling of WGM and rare-earth-doped nanoparticles.^{966–969} For example, Fernandez-Bravo et al. coated a layer (~ 100 nm thick) of Tm^{3+} -doped UCNP on 5- μm polystyrene microspheres.⁹⁷⁰ These microlasers exhibited upconverted lasing under excitation at 1064 nm with a low threshold of $14 kW cm^{-2}$. Recently, Jin's group succeeded in generating an ultralow threshold laser from single UCNP by modulating cross-relaxation.³³ They argued that appropriate cross-relaxation can accumulate energy in excited intermediate states, facilitating population inversion and lowering the pump threshold by precisely controlling the doping concentration of the emitter. Single-layer $NaYF_4:Yb/Tm$ UCNP were deposited on polystyrene microspheres to form WGM cavities. By measuring emission intensity, the full width at half-maximum (~ 0.45 nm) and laser threshold, optimal Tm^{3+} doping concentration and particle size were determined as 2% and 24 nm, respectively, at a pump power of $\sim 150 W cm^{-2}$. Furthermore, a single-particle laser with a peak at 808 nm was realized by depositing a single UCNP on the polystyrene microsphere (Figure 26c,d).

Hyperbolic metamaterials are electromagnetic materials developed to enhance emission and create other fascinating applications.⁹⁷¹ The most commonly used hyperbolic metamaterials include alternating metal–dielectric layer structures and hyperbolic dispersed nanowire arrays embedded in a dielectric medium. Haider et al. reported a white-emitting random nanolaser by coupling UCNP with multilayer hyperbolic Au/MoO_3 metamaterials.⁹⁷² According to their design, Au/MoO_3 hyperbolic metamaterials were deposited beneath a thick layer of $NaYF_4:Yb/Er/Tm@NaYF_4:Eu$ nanoparticles, and SiO_2/Si was employed as the substrate. At 980 nm excitation, UCNP emitted red (Eu^{3+}), green (Er^{3+}), and blue (Tm^{3+}) light, rendering integrated white light output. Notably, variations in the filling ratio of the Au/MoO_3 multilayers change the wavelength for hyperbolic dispersion. Consequently, the intensities and lifetimes of red, green, and blue emissions, as well as the emitting color are tunable. In the optimal case, emission intensity was increased 50-fold when the pump threshold was lowered from 0.5 to 0.1 $kW cm^{-2}$.

4.4.2. Displays. White, full-color emission is essential for displays and lighting. However, conventional rare-earth-doped nanomaterials emit light with limited wavelength ranges. In 2015, Deng et al. reported the use of multilayer core–shell UCNP for full-color volumetric displays by modulating the pulse width of laser excitation (Figure 26e).⁹⁷³ They found that the pulse width of laser beams significantly influences luminescence, which is governed by a transient upconversion process. When the pulse width of the 980 nm excitation varied from 200 μs to 6 ms, the emission color of Ho^{3+} changed from

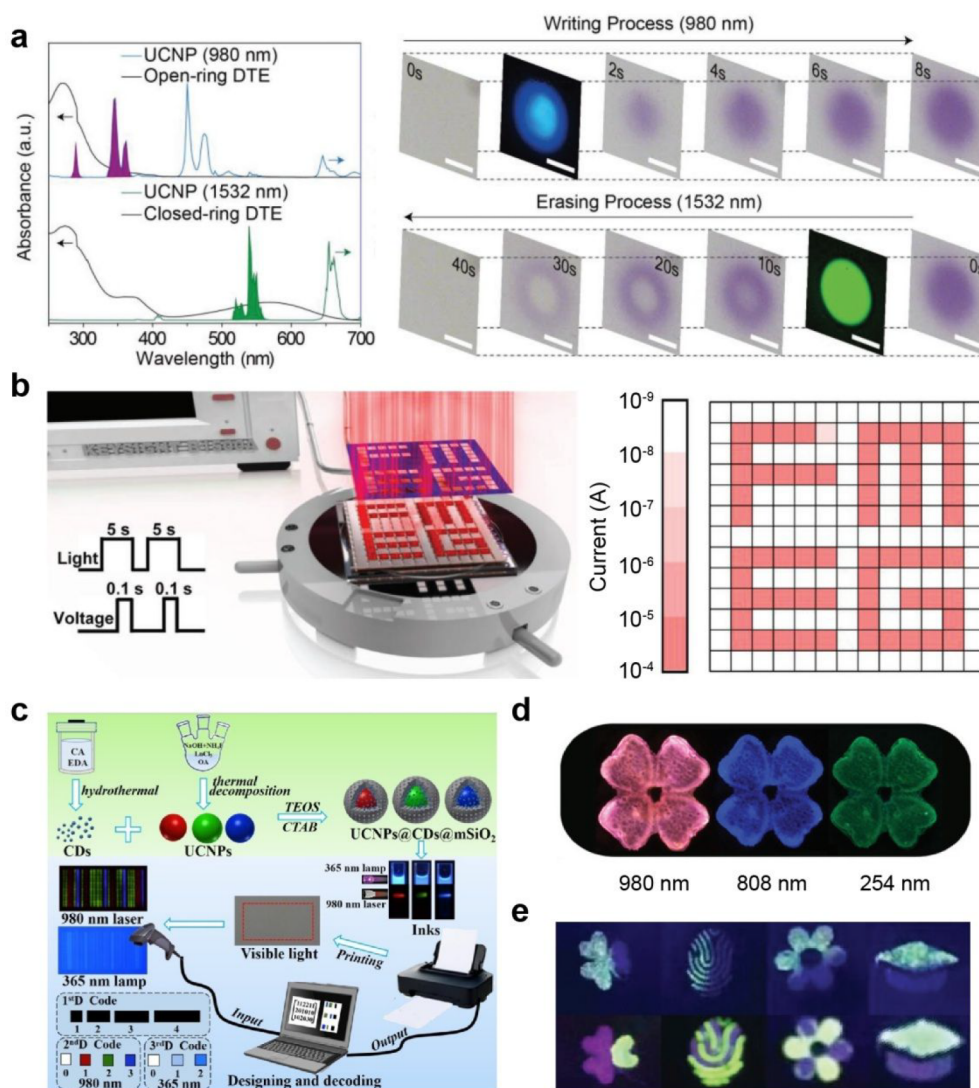


Figure 27. (a) Write and erase processes based on a PMMA film containing a UCNPs-DTE hybrid under excitation at 980 and 1532 nm, respectively. Scale bars are 50 μm . (b) Schematic of information storage using an RRAM device based on MoS_2 -UCNPs under light illumination. (c) Schematic of inkjet-printing of UCNPs for anticounterfeiting applications. (d) Optical microphotographs of the patterns under 980, 808, and 254 nm excitation, respectively. (e) Patterns of Ce/Eu-doped nanoparticles under irradiation with a 254 nm UV lamp and a 980 nm defocusing laser (top) and patterns of Ce/Tb- and Ce/Eu-doped nanoparticles under irradiation at 245 nm (bottom) (Adapted with permission from refs 976–980. Copyright 2019 American Chemical Society; Copyright 2018,2020 WILEY-VCH Verlag GmbH & Co. KGaA, Weinheim; Copyright 2017 The Royal Society of Chemistry).

green to red. Addition of a blue luminescence component under 808 nm laser excitation enabled a full-color display. In another work, Zhang et al. designed multilayer UCNPs with an emission spectrum spanning the entire visible range.³¹² These nanoparticles consist of $\text{NaGdF}_4\text{:Yb/Tm/Er}$ as the core for blue and green emission, $\text{NaGdF}_4\text{:Eu}$ as the first shell, and NaYF_4 as the inert outer shell to minimize surface quenching. With the help of energy migration through Gd^{3+} ions, the excitation energy can be transferred from Tm^{3+} to Eu^{3+} for red emission. These nanoparticles can emit adjustable light from green to white when irradiated at 980 nm with $3\text{--}30\text{ W cm}^{-2}$ (Figure 26f).

In addition to efforts to manipulate emission colors, factors that contribute to practical displays, such as display flexibility and speed, are also considered. Park et al. reported a flexible transparent display integrating UCNPs into a polymer waveguide that exhibited bright emission under 980 nm irradiation, irrespective of bending.⁹⁷⁴ In 2020, Gao et al.

reported a UCNPs-based video-rate display by temporally synchronizing the excitation sampling time with the emission rise time of individual nanoparticles.⁹⁷⁵

4.4.3. Information Storage. Information recording began in ancient times with the notation of nodes. However, the arrangement was sophisticated and the storage density was low. In the digital era, ultrafast reading or erasing of large amounts of data has become possible. The optical format seems promising in transferring information over distances and achieving higher data density among various storage formats.⁹⁸¹ Rare-earth-doped phosphors with various colors have been widely used in information storage through defect engineering.^{982,983} In this section, we focus on the examples involving rare-earth nanomaterials.

A typical strategy for using rare-earth-doped nanoparticles for optically rewritable memories is to combine nanoparticles with photoswitchable organic compounds.^{981,984,985} In those systems, nanoparticle emission is utilized to trigger the write

process, while the erase process can be performed with heat or light. For example, Zheng et al. combined $\text{NaYF}_4:\text{Er}@ \text{NaYF}_4@ \text{NaYF}_4:\text{Yb}/\text{Tm}@ \text{NaYF}_4$ nanoparticles with the photochromic molecule diarylethene (DTE). Under 980 nm laser excitation, the blue emission of nanoparticles well matches the absorption of DTE in the open-ring form. In contrast, under 1532 nm irradiation, their green emission matches the absorption of DTE in the closed-ring form, resulting in structural transformation and color change (Figure 27a).⁹⁷⁶ To ensure high spectral purity, they developed multilayer $\text{NaYF}_4:\text{Er}@ \text{NaYF}_4@ \text{NaYF}_4:\text{Yb}/\text{Tm}@ \text{NaYF}_4$ UCNP. The energy transfer from Yb^{3+} to Er^{3+} and cross-relaxation are efficiently hindered to avoid interference with DTE isomerization. The luminescence dynamics suggest that the energy transfer between UCNP and DTE is due to an internal filtering effect instead of FRET. To verify and simulate writing and erasing, they prepared a thin film from a UCNP-DTE array and PMMA. Each dot of the array could be “painted” or erased with NIR light, forming distinctive patterns to record different types of information. Similar photochromism was accomplished by Wang et al., who fabricated a two-dimensional hybrid system of $\text{Yb}^{3+}/\text{Er}^{3+}$ -codoped UCNP and $\{[\text{Fe}(\text{1,3-bpp})_2(\text{SCN})_2]_2\}_n$ nanosheets.⁹⁸⁶ These nanoparticles were hybridized with thiocyanate (SCN^-) ligands on both sides of the nanosheets. At 980 nm irradiation, upconversion luminescence weakened metal-to-ligand charge transfer (MLCT) and triggered the high-spin to low-spin transition. However, heating at 40 °C enhanced the MLCT, and the low-to-high spin transition occurred. This demonstrates that reversible molecular switching is possible by altering NIR irradiation and thermal stimulation.

The conversion of optical signals into electrical signals is important for photonic information storage. Zhai et al. integrated rare-earth-doped UCNP with 2D semiconducting MoS_2 to fabricate a NIR-sensitive memory device based on a MoS_2 -UCNP heterostructure.⁹⁷⁷ The memory device consisted of a three-layer Al/MoS_2 -UCNP/ITO structure supported on a substrate. MoS_2 -UCNP serves as the active material for the memory device. When irradiated at 980 nm, the light emitted from UCNP is absorbed by MoS_2 . The charge carriers generated are separated at the interface of MoS_2 and UCNP under an applied electric field. Trapping/detrapping processes result in a switch between high-impedance and low-impedance states, allowing data to be written and erased (Figure 27b).

4.4.4. Anticounterfeiting. Colloidal nanocrystals doped with rare-earths have been utilized as luminescent inks to print various patterns for encryption and protection against counterfeiting (Figure 27c). In particular, these nanomaterials have multiple encryption modes to meet the complex requirements of anticounterfeiting in business and document and copyright protection. Patterns printed with colloidal solutions containing rare-earths are colorless under ambient light. When irradiated under a specific condition, these patterns emit visible light in different colors. Rational design in rare-earth doping renders nanocrystals with increased sensitivity to excitations or external stimuli, allowing fine-tuning of luminescence.^{34,987,988} Variation in dopant composition is often combined with other strategies to construct materials with multimodal encryption. Rare-earth-doped nanoparticles with different emission colors can be printed to create polychromatic patterns by single wavelength excitation, as the emission color can be easily varied by tuning the dopant composition and concentration.^{283,989}

Multicolor encryption can be realized in microscopic views by spatially controlling the doping with different rare-earth ions. Zhang et al. reported two-color, spatially encoded RE-doped microrods that can produce red emission at the end of the rods and green emission in the middle.³²³ These spatially distributed colors can only be distinguished at high microscopic magnification, providing additional confidence for multicolor labeling. In 2016, Zhang et al. reported three-color microbarcodes using upconversion microrods and microdisks.³⁶ These barcodes can be resolved to the single-particle level and have the potential for multiplexed labeling.

Time-domain optical anticounterfeiting can provide different colors or pattern information on different time scales after laser irradiation is turned off.⁹⁹⁰ The lifetime of rare-earth-doped nanomaterials can be tuned by varying the doping composition and concentration.^{300,581,991} Liu et al. designed a multilayered structure, $\text{NaYF}_4@ \text{NaYF}_4:x\% \text{Yb}/1\% \text{Tm}@ \text{NaYF}_4:y\% \text{Yb}@ \text{NaYF}_4$, to modulate the emission intensity and lifetime independently by varying the doping concentration.⁹⁹² They also prepared two other types of UCNP with different lifetimes to produce green and red colors. The three types of upconversion nanoparticles were encapsulated in polydimethylsiloxane (PDMS) beads with a specific mixing ratio, producing a colorful array. This array exhibits random patterns under continuous laser irradiation. However, in time-delay mode, irradiation with different lasers revealed hidden letters. This orthogonal manipulation enables multimode encryption, which extends the realm of multiplex luminescence imaging.

Han et al. reported that in addition to pulse width, repetition frequency can also contribute to color manipulation.⁹⁹³ They demonstrated that by varying the pulse width at a fixed frequency from 100 μs to 6 ms, the emission color of $\text{NaYF}_4:\text{Er}/\text{Tm}(2/0.5\%)@ \text{NaYF}_4$ UCNP can be tuned from green to red. When the pulse duration was set to 100 μs , increasing the frequency also resulted in a color change from green to red. By manipulating the pulse width, labeled patterns of UCNP exhibited green, yellow, or red colors, allowing higher falsification reliability than single-mode emission. Intriguingly, Liu et al. reported multiplex coding by manipulating the luminescence kinetics of UCNP.⁹⁹⁴ They showed that UCNP exhibit a delayed luminescence maximum in the time trace in response to harmonic wave excitation (e.g., phase angle). By varying the phase angle of the materials, a kinetics-based optical encoding technique could be developed. UCNP with different luminescence colors and phase angles were encapsulated into polymer beads. The array arranged by these polymer beads showed only encrypted letters with harmonic 980 nm laser excitation after phase angle analysis.

Liu et al. utilized plasmonic nanostructures in combination with UCNP to provide a high degree of optical security.⁹⁹⁵ They constructed a sandwich metal-UCNP-metal nanostructure, in which a monolayer of UCNP was sandwiched between an array of aluminum nanodisks and an aluminum thin film. Due to the surface plasmon diffraction of aluminum, these nanocomposites displayed a nonluminescent plasmonic color under ambient light. The embedded UCNP emitted visible light only when excited by NIR irradiation. Both the nonluminescent and luminescent colors can be tuned by varying the diameter and spacing of the nanodisks. They designed a nonluminescent butterfly pattern with NaGdF_4 -containing plasmonic nanomaterials. The sandwich metal-UCNP-metal nanomaterials were filled into a reserved empty region of the butterfly pattern, forming hidden luminescent

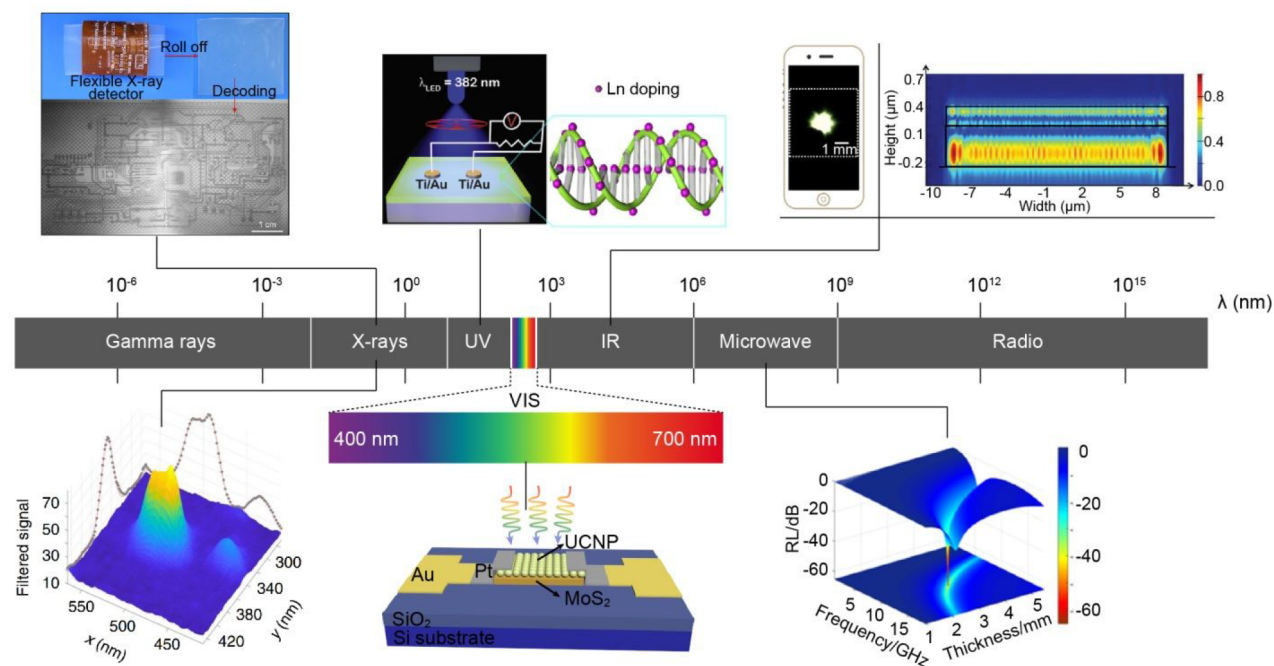


Figure 28. Schematic of the electromagnetic spectrum and examples of rare-earth-doped nanomaterials as photodetectors in various applications (Adapted from refs 595, 613, 1011, and 1014–1017. Copyright 2019, 2020 Nature Publishing Group; Copyright 2018 Elsevier B.V.; Copyright 2019 Elsevier Ltd.; Copyright 2016, 2017 WILEY-VCH Verlag GmbH & Co. KGaA, Weinheim; Copyright 2019 American Chemical Society).

patterns. This study provides a new way of optical security printing with different color patterns under white light and NIR irradiation.

By permutation and combination with different emitters, color groups of upconversion and downshift luminescence can be obtained under different excitation sources.^{996–1000} Sun et al. designed three types of rare-earth-doped nanoparticles ($\text{NaYF}_4@\text{NaYF}_4:\text{Yb}/\text{Er}@\text{NaYF}_4$, $\text{NaYF}_4:\text{Yb}/\text{Tm}@\text{NaYF}_4:\text{Yb}/\text{Nd}@\text{NaYF}_4$, and $\text{NaGdF}_4:\text{Ce}/\text{Tb}$) that emitted red, blue, and green under 980, 808, and 254 nm excitation, respectively.⁹⁷⁹ Mixtures of these nanoparticles can be used as security inks to print tamper-resistant patterns (Figure 27d). In addition to mixing multicomponent nanoparticles, Huang et al. combined upconversion and downshift luminescence in multilayer rare-earth-doped nanoparticles ($\text{NaYF}_4:\text{Nd}/\text{Yb}@\text{NaYF}_4:\text{Yb}/\text{Er}@\text{NaGdF}_4:\text{Yb}/\text{Tm}@\text{NaGdF}_4:\text{A}@\text{NaYF}_4$; A = Ce, Tb, Eu).⁹⁸⁰ Complex luminescence patterns can be obtained by modulating the excitation wavelength and power density (Figure 27e).

In 2013, Zhao et al. reported that bright upconversion luminescence of highly doped nanoparticles with suppressed concentration quenching can be achieved at ultrahigh excitation power density ($>10^6 \text{ W cm}^{-2}$).¹⁰⁰¹ When the nanocrystal solution was applied as a security ink to print a hidden pattern, the printed pattern remained dark at low excitation power (10^4 W cm^{-2}) but became visible at high excitation power (10^6 W cm^{-2}). Chen et al. demonstrated that color tuning from green to yellow and red in $\text{NaYF}_4@\text{NaYbF}_4:\text{Ho}(1\%)@\text{NaYF}_4$ nanoparticles can be accomplished by varying the excitation power ($1.25\text{--}46.25 \text{ W cm}^{-2}$).¹⁰⁰² Compared to UCNPs with lower Yb^{3+} content, $\text{NaYF}_4@\text{NaYbF}_4:\text{Ho}(1\%)@\text{NaYF}_4$ nanoparticles exhibited 5.6-fold enhanced power sensitivity, which is mainly due to the maximum utilization of incident energy. The improved power sensitivity is suitable for data decoding.

The temperature-dependent luminescence of rare-earth-doped nanomaterials has also been exploited for optical anticounterfeiting.¹⁰⁰³ For instance, Lei et al. demonstrated this concept using $\text{Na}_3\text{ZrF}_7:\text{Yb}/\text{Er}@\text{Na}_3\text{ZrF}_7$ nanocrystals with temperature-dependent emission profiles.⁷⁷⁷ After coating with poly(acrylic acid) (PAA) molecules, these nanocrystals were used as inks for pattern printing. The brightness of the pattern at 980 nm excitation increased as the temperature increased from room temperature to 413 K. Zou et al. reported a 29-fold increase in the green emission of $\text{Yb}_2\text{W}_3\text{O}_{12}:\text{Er}$ UCNPs by raising the temperature from 303 to 573 K.³⁸¹ At higher temperatures, there is contraction and distortion of the host lattice, resulting in altered crystal symmetry and enhanced energy extraction by the activator. They printed a two-color pattern using $\text{Yb}_2\text{W}_3\text{O}_{12}:\text{Er}$ as the green phosphor and $\text{Yb}_2\text{WO}_6:\text{Er}$ as the red phosphor. Of note, unlike $\text{Yb}_2\text{W}_3\text{O}_{12}$, the Yb_2WO_6 lattice expands at high temperatures. Hence, the sample showed enhanced green luminescence and decreased red luminescence at 573 K.

Quick response (QR) codes made of rare-earth inks can be smart labels for the IoT. Ramalho et al. designed multiplexed QR codes based on several lanthanide complexes and printed them on banknotes.¹⁰⁰⁴ They developed a mobile application to sort out multiplexed luminescent QR codes and provide an additional layer of security.

4.5. Photodetectors

Photodetectors have developed rapidly in recent decades because of their potential applications in research, military practice, medicine, and industry. Rare-earths have been incorporated into various nanomaterials to detect all types of electromagnetic radiation from microwaves to γ rays (Figure 28).

4.5.1. Microwaves. Microwave-absorbing materials are functional materials that can convert electromagnetic radiation into other forms of energy such as thermal energy or dissipate

electromagnetic radiation and reduce microwave reflection to a large extent. This unique property can be capitalized for applications in radar cloaking, communication security, and electromagnetic shielding. Microwave absorbing materials are mainly dielectric materials, which have two distinct loss mechanisms, namely dielectric loss and magnetic loss. To meet the critical requirements of microwave absorption, a combination of dielectric and magnetic materials is usually employed to achieve maximum absorption of electromagnetic energy.

In the last two decades, lanthanide doping techniques have also been applied to ferrite absorbers. The magnetic loss mechanisms of ferrites mainly include hysteresis loss and residual loss. Rare-earth ions possess relaxation characteristics that are likely to affect the electromagnetic properties of ferrites. Yang et al. synthesized cobalt ferrite (CoFe_2O_4) nanomaterials doped with La^{3+} , Ce^{3+} , or Y^{3+} ions and combined them with a conducting polymer, polyaniline, using a hydrothermal coordination oxidation method.¹⁰⁰⁵ Electromagnetic measurements showed that the microwave absorption capacity of La^{3+} -doped polyaniline- $\text{CoRE}_x\text{Fe}_{2-x}\text{O}_4$ composites was better than that of Ce^{3+} - and Y^{3+} -substituted counterparts. By varying the doping concentration of La^{3+} , an optimal microwave absorption performance was achieved at $x = 0.15$, and the conductivity of the nanocomposite was $\sim 0.833 \text{ S cm}^{-1}$. Under these conditions, the nanocomposites showed excellent performance with a maximum reflection loss of -42.65 dB at 15.91 GHz . In addition to the above-mentioned elements, Pr, Nd, Sm, Gd, Tb, Dy, Ho, Er, and Tm have been widely incorporated into ferrites and alloys for microwave absorption.^{1006–1012} Moreover, CeO_2 and $\text{Gd}(\text{OH})_3$ nanoparticles also exhibit efficient microwave absorption.^{1011,1013}

4.5.2. Infrared. All objects on Earth emit infrared radiation as heat.¹⁰¹⁸ Infrared waves have longer wavelengths than visible light and can penetrate dense tissue with less scattering and absorption. Nd^{3+} , Yb^{3+} , and Er^{3+} ions absorb infrared radiation at around 808, 908, and 1540 nm, respectively. The appropriately doped upconversion nanoparticles can convert infrared light into UV or visible emission, which can be observed directly with the naked eye or recorded by a camera or cell phone.^{1016,1017,1019} Au and Ag nanoparticles are often combined with rare-earth-doped nanoparticles to improve infrared detection.^{1016,1020} The detection result can be an optical or electrical signal, as photoelectric conversion materials such as perovskite nanocrystals, graphene, and semiconducting polymers are often combined with UCNPs.^{1021–1025} Excitation energy can be transferred to the photoelectric device nonradiatively, whereupon a photocurrent is generated. Since most photoelectric moieties absorb light in the UV or visible range, the hybrid material can also serve as a broadband photodetector.

4.5.3. Ultraviolet–Visible. For UV–vis detection, semiconductors such as CdS, ZnO, and TiO_2 are commonly doped with rare-earth ions to enhance the photodetection performance.^{1024–1027} Shkir et al. prepared Eu-doped CdS thin films by the spray pyrolysis method and investigated their optical and photoelectric properties.¹⁰²⁸ By varying the Eu doping concentration from 1 to 5 wt %, the direct bandgap could be tuned from 2.43 to 2.48 eV, which is attributed to electronic interactions between the 4f electrons of Eu and the s and p electrons of CdS. More importantly, at 5 wt % CdS:Eu, the photosensitivity increased almost 10-fold compared to undoped CdS. The external quantum efficiency was ~ 8 -fold

greater. Double-crossed DNA lattices formed by rare-earth doping can also increase the photocurrent and photovoltage under UV irradiation, due to enhanced charge carrier generation by both DNA and rare-earths.¹⁰¹⁴ Ghosh et al. designed a broadband (325–1064 nm) photodetector using $\text{NaGdF}_4:\text{Yb}/\text{Er}$ nanocrystals and MoS_2 flakes that were chemically exfoliated.¹⁰¹⁵ These nanocomposites were fabricated on a gold-patterned SiO_2/Si substrate and exhibited high sensitivity with a maximum value of 1254 A W^{-1} with $V_{\text{ds}} = 1 \text{ V}$ at 980 nm. They also showed excellent performance in normalized gain and detectivity with values of $7.12 \times 10^{-4} \text{ cm}^2 \text{ V}^{-1}$ and $1.05 \times 10^{15} \text{ Jones}$ (at 980 nm, 1 V), respectively.

4.5.4. X-rays and γ -rays. X-rays and γ -rays are high-energy waves that can travel great distances at the speed of light and completely penetrate the human body. Since the discovery of X-rays and γ -rays in the late 19th century, they have become indispensable in defense science, industry, and medical treatment and have created a great demand for the detection of high-energy waves. A scintillator is a material that can absorb high-energy waves and emit UV–vis light, which enables the detection of high-energy radiation. Rare-earth-based phosphors have been extensively researched for detection of X-rays and γ -rays because rare-earths are heavy atoms that favor high energy absorption.¹⁰²⁹ Rare-earth halides, oxides, oxyhalides, oxysulfides, oxyorthosilicates, and perovskites possess excellent scintillation performance.¹⁰³⁰ In particular, Y, La, Gd, and Lu have been extensively studied as host lattices for controlling radioluminescence.¹⁰³¹ Rare-earth-doped nanoscintillators with fast decay or persistent luminescence are being developed for specific applications. Recent studies show a research trend for high-energy beam imaging, and nanoscintillators are typically embedded in organic and inorganic substrates such as poly(methyl methacrylate) (PMMA),¹⁰³² diamond,¹⁰³³ and glass^{1034,1035} to form a transparent mass for radiography.

Ou et al. developed a flat-panel-free X-ray luminescence extension imaging (Xr-LEI) technology using persistent luminescent nanoscintillators.⁵⁹⁵ They synthesized $\text{NaLuF}_4:\text{Tb}(15 \text{ mol } \%)\text{@NaYF}_4$ nanocrystals using a coprecipitation method. After X-ray irradiation was terminated, an afterglow was observed that lasted for more than 30 days. When Lu was replaced by Y, the afterglow intensity weakened, mainly due to the lower absorption coefficient of Y. The mechanisms of the ultralong afterglow can be described as follows. First, the incident X-ray energy is absorbed by Lu atoms, and electrons are generated by the photoelectric effect. Then, fluoride ions are displaced by elastic collisions with X-ray photons with large momentum, forming anion-Frenkel defects. The photogenerated electrons are captured by fluoride vacancy traps, while holes are trapped in interstitial sites. Finally, the trapped charge carriers migrate to Tb ions and electron–hole recombination takes place, which simultaneously causes the Tb emitters to light up. To realize Xr-LEI, nanoscintillators were embedded in a PDMS substrate to form a flexible detector for 3D imaging. This imaging capability was not available for conventional flat-panel X-ray detectors. Prigozhin et al. reported single-particle imaging of rare-earth-doped NaGdF_4 under a specific electron excitation flux (cathodoluminescence) with a sub-20 nm resolution.⁶¹³ Various rare-earth ions (Eu^{3+} , Er^{3+} , Ho^{3+} , Tb^{3+} , Sm^{3+} , Dy^{3+} , Nd^{3+} , Tm^{3+} , and Yb^{3+}) were incorporated into NaGdF_4 , resulting in multicolor imaging with ultrahigh resolution.

Table 5. Summary of Rare-Earth-Doped Nanomaterials for Solar Cells

mode ^a (DS/ DC/UC)	sensitizer	emitter	host lattice	exc (nm)	em (nm)	solar cell	PLQY (%)	PCE (%)	ref	
DS	VO ₄ ³⁻	Eu ³⁺	YVO ₄	295	614	DSSC	/	8.11	1039	
	TiO ₂	Eu ³⁺	TiO ₂	325	489, 586, 614, 622	DSSC	/	8.8	1040	
	TiO ₂ , Eu	Eu ³⁺	TiO ₂	260–280, 384, 396, 415	578, 591, 614, 652, 700	PSC	/	15.79	1041	
	VO ₄ ³⁻ , Bi ³⁺	Eu ³⁺	YVO ₄	220–350	621	PSC	/	17.9	1042	
	VO ₄ ³⁻	Eu ³⁺	YVO ₄	300–350	619	DSSC	/	/	1043	
DC	Ce	Nd, Yb	NaGdF ₄	254	600–750, 850–900, 1064	c-Si	/	0.8 (254 nm)	1044	
	AIEE dye(Tb)	Yb	NaYF ₄	405	980	c-Si	/	8% increase	1045	
	Tm	Yb	Lu ₂ O ₃	463	~1000	/	148.2	/	1046	
	CsPbCl ₃	Yb	CsPbCl ₃	365	990	c-Si	/	/	456	
	CsPb(Cl _{1-x} Br _x) ₃	Yb	CsPb(Cl _{1-x} Br _x) ₃	375, 405	980	/	120 (AM1.5)	/	1047	
	CsPbCl ₃	Yb	CsPbCl ₃	380	990	/	170	/	454	
	CsPb(Cl _{1-x} Br _x) ₃	Yb	CsPb(Cl _{1-x} Br _x) ₃	375	979	/	200	/	455	
	Pr ³⁺ , Ce ³⁺ , CsPbClBr ₂	Yb	CsPbClBr ₂	365	988	CIGS	173	19.1	38	
	Ce, CsPbCl _{1.5} Br _{1.5}	Yb	CsPbCl _{1.5} Br _{1.5}	365	988	c-Si	146	21.5	40	
	Pr	Pr	NaLaF ₄	180	~410, 480, 605	/	/	/	1048	
	UC	mCu _{2x} S	Er	Er ₂ O ₃	980	~550, 660	PSC	/	17.8	1049
		Er	Er	Y ₂ O ₃	980	525, 560, 660	DSSC	/	8.62	1050
		Yb	Er	NaYF ₄	980	522, 542, 655	PSC	/	19.7	1051
						525, 541, 654	PSC	/	20.19	1052
						408, 523, 543, 655	PSC	/	16	1053
					408, 523, 542, 655	PSC	/	17.8	1054	
					522, 542, 655	DSSC	/	7.79 (980 nm)	1055	
					543, 655	DSSC	/	6.34	1056	
Yb		Er	LiYF ₄	980	547, 556, 674	PSC	/	11.87	1057	
Yb		Er	CeO ₂	980	525, 550, 562	DSSC	/	6.66	1058	
Yb		Er	CeO ₂	980	517–532, 532–551, 659–679	DSSC	/	7.3	1059	
Ni ²⁺		Er	CaZrO ₃	1490, 1300	980	c-Si	/	/	1060	
IR-783, Nd		Er	NaYF ₄	808	414, 526, 546, 660	PSC	1.2 (UC)	20.5	1061	
IR783		Er	NaYF ₄	800	525, 540	DSSC	/	8.568	1062	
Nd		Er	NaYF ₄	808	525, 540, 654	DSSC	/	5.87	1037	
Yb	Ho	YbF ₃	980	545, 650, 750	DSSC	/	8	1063		
Yb	Ho	NaYbF ₄	980	540, 644, 750	PSC	/	14.32	1064		
UC/DS	Yb/Er	Er/Er	NaYF ₄	968, 400	660, 540, 520, 500	c-Si	/	12.8	1065	
UC/DC	Tb/Er	Yb/Er	NaYF ₄	488, 1523	990	/	173 (DC)	/	1066	

^aDS downshifting; DC downconversion; UC upconversion.

4.6. Photovoltaics

Rare-earth-doped nanomaterials have shown promise in improving the performance of photovoltaics by fully utilizing the solar spectrum for energy conversion. When integrated into photovoltaic devices, these nanomaterials have been employed as spectral converters to minimize energy losses.^{1018,1038} This has been achieved mainly by using downconversion (also known as quantum-cutting), upconversion, and downshifting nanophosphors (Table 5).

For instance, rare-earth-doped downconversion phosphors can convert one high-energy photon into two low-energy photons and thus increase the photocurrent of solar cells.^{1067,1068} Efficient downconversion from UV to NIR has been realized in various hosts using Pr³⁺, Gd³⁺, Tm³⁺, Er³⁺, Ho³⁺, Nd³⁺, and Yb³⁺ as dopants.^{1069–1074} A major challenge for the use of downconversion in photovoltaic applications is the low absorption cross-section of rare-earths. In this regard, Wang and co-workers demonstrated the use of broadband Ce³⁺-sensitized quantum cutting to enhance the power

conversion efficiency of hybrid crystalline silicon (c-Si) solar cells.¹⁰⁷⁵ The researchers synthesized NaGdF₄:Ce@NaGdF₄:Nd@NaYF₄ nanoparticles that exhibited parity-allowed 4f → 5d Ce³⁺ absorption and Ce³⁺-sensitized quantum cutting in Nd³⁺ ions. These nanoparticles enhanced the power conversion of c-Si in the UV range, resulting in a 1.2-fold increase in short-circuit current and a 1.4-fold increase (from 0.57 to 0.80%) in power conversion efficiency.

Recent investigations have shown that Yb³⁺-doped CsPbCl₃ and CsPbCl_xBr_{3-x} perovskite nanocrystals are promising spectral converters for downconversion.^{38,40,454,456} These nanocrystals display high luminescence quantum yields (>100%) and large absorption coefficients, which are ideal for practical photovoltaic applications. For instance, Song and co-workers have demonstrated a total emission quantum yield of 173% in Yb³⁺-Pr³⁺-Ce³⁺-tridoped CsPbClBr₂ perovskite nanocrystals.³⁸ Given this high quantum yield, these nanocrystals have been developed as efficient downconversion layers that have enhanced power conversion efficiency by a

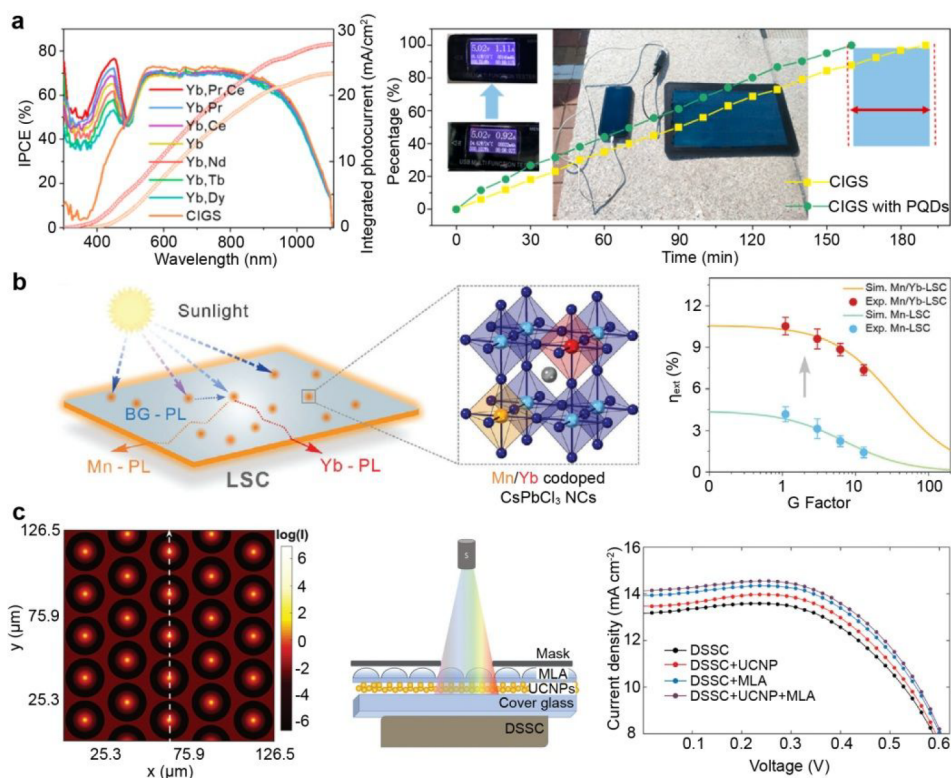


Figure 29. (a) Properties of CIGS solar cells coated with a rare-earth-doped perovskite film. (b) Mn²⁺/Yb³⁺-encoded CsPbCl₃ perovskite nanocrystals as luminescent solar concentrators. (c) MLA- and UCNP-coated DSSCs with enhanced photovoltaic performance (Adapted with permission from refs 38, 1036, and 1037. Copyright 2019 American Chemical Society; Copyright 2020 WILEY-VCH Verlag GmbH & Co. KGaA, Weinheim; Copyright 2019 The Royal Society of Chemistry).

factor of ~20% in c-Si and CuIn_{1-x}Ga_xSe₂ solar cells (Figure 29a). It would be even more attractive if rare-earth-doped perovskite nanocrystals could help break the Shockley–Quiesser barrier of single-junction c-Si solar cells. Perhaps this will be achieved through a combination of multiple doping and device engineering.

As with downconversion nanophosphors, downshifting nanomaterials have also been used to increase the efficiency of photovoltaic devices that have a poor spectral response to short-wavelength radiation.^{1039,1042,1043,1076–1078} For example, Jin et al. incorporated YVO₄:Eu/Bi nanophosphors into a mesoporous TiO₂ layer of CH₃NH₃PbI₃ perovskite solar cells (PSCs).¹⁰⁴² Compared with the control device, these downshifting nanophosphors enhanced the power conversion efficiency from 16.3 to 17.9%. Meanwhile, these nanophosphors significantly prevented device degradation caused by UV light. In 2019, Alexandre et al. performed theoretical calculations and their study suggested that optimized downshifting materials can increase the photocurrent of PSCs by ~2% while reducing harmful UV photocarrier generation in TiO₂ and perovskite layers.¹⁰⁷⁹ In addition to absorbing harmful UV light, rare-earth dopants can be incorporated into perovskite structures to increase the durability of photovoltaic devices. A typical example is the incorporation of Eu³⁺ into MAPbI₃ and CsPbI₂Br to stabilize the perovskite phase at room temperature and thus significantly improve the operating lifetime of the corresponding PSCs.^{450,465} On the other hand, downshifting nanophosphors have been widely implemented as solar converters in luminescent solar concentrators.¹⁰⁸⁰ For example, Cai et al. demonstrated the use of Mn²⁺/Yb³⁺-encoded CsPbCl₃ perovskite nanocrystals as spectral con-

verters to achieve both downconversion and downshifting luminescence.¹⁰³⁶ These perovskite nanocrystals proved as efficient luminescent solar concentrators for photovoltaic applications due to their strong light-concentrating effect when embedded in a polydimethylsiloxane matrix (Figure 29b).

In addition, UCNPs are widely used to reduce the nonabsorption energy losses of photovoltaics by converting sub-bandgap radiation into visible emission.¹⁰⁶⁸ In an early experiment, Shalav et al. investigated the enhancement of the sub-bandgap NIR response of silicon solar cells by coupling NaYF₄:Er nanophosphors.¹⁰⁸¹ Under NIR excitation at 1532 nm, an external power conversion efficiency of ~2.5% was recorded, corresponding to an internal upconversion efficiency of 3.8% for the upconverted silicon solar cell. The power conversion efficiency can be further improved by increasing the luminescence quantum yield of upconversion phosphors. The highest quantum yield to date for Gd₂O₂S:10%Er phosphors is ~12%, reported by Martín-Rodríguez et al.¹⁰⁸² While Er³⁺-doped upconversion phosphors can be used for narrow bandgap c-Si solar cells ($E_g = 1.1$ eV), UCNPs codoped with Yb³⁺/Ln³⁺ (Ln = Er, Tm, Ho) are more suitable for wide bandgap photovoltaics, such as dye-sensitized solar cells (DSSCs) and PSCs.^{1054,1083} For instance, Demopoulos and co-workers reported the use of a backside layer of β-NaYF₄:Er/Yb nanoplates to improve the performance of DSSCs with a transparent TiO₂ layer.¹⁰⁸⁴ In their device, the nanoplate functioned as an external light-reflecting and NIR harvesting bifunctional layer, which enhanced the overall power conversion efficiency of DSSCs by approximately 10%. In 2016, He et al. demonstrated incorporation of NaYF₄:Yb/Er

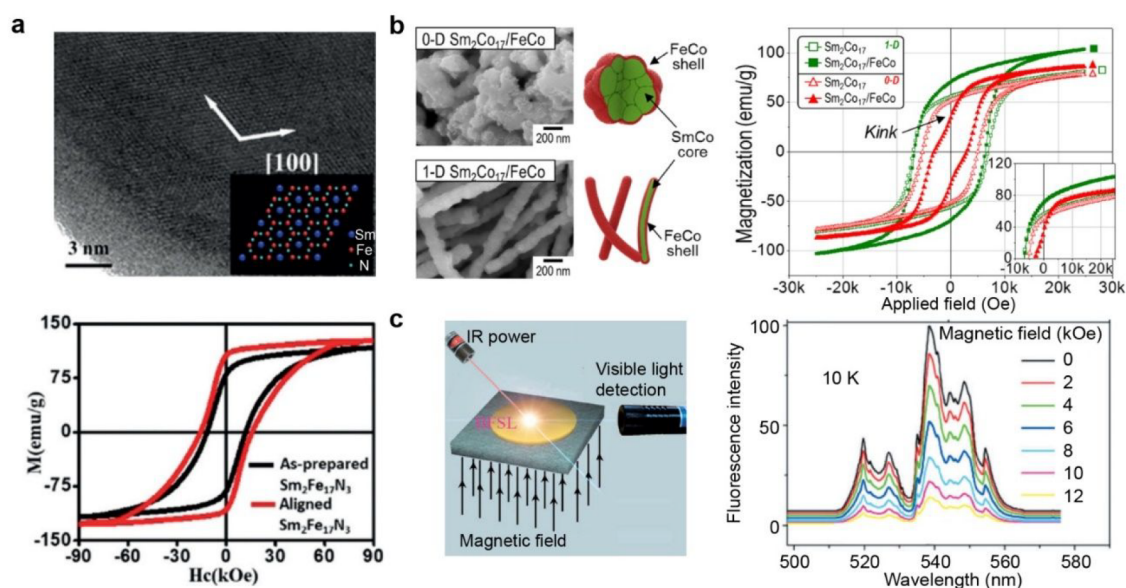


Figure 30. (a) HRTEM image of a $\text{Sm}_2\text{Fe}_{17}\text{N}_3$ nanoparticle. (inset) Atomic model of $\text{Sm}_2\text{Fe}_{17}\text{N}_3$ structure projected along the c -axis and hysteresis loops of synthesized and aligned $\text{Sm}_2\text{Fe}_{17}\text{N}_3$ nanoparticles at 300 K. (b) Structures of 0 and 1D $\text{Sm}_2\text{Co}_{17}/\text{FeCo}$ core-shell nanomaterials and magnetic properties of core and core-shell samples. (c) Effect of external magnetic field on fluorescence intensity of UCNPs (Adapted with permission from refs 1086–1088. Copyright 2013, 2019 Wiley-VCH Verlag GmbH & Co. KGaA, Weinheim; Copyright 2019 American Chemical Society).

UCNPs as a mesoporous electrode in $\text{CH}_3\text{NH}_3\text{PbI}_3$ -based PSCs, achieving a power conversion efficiency of 0.35%.¹⁰⁵⁴

A significant limitation of upconversion photovoltaics is that efficient upconversion luminescence generally requires concentrated irradiation, such as high-power laser excitation. To overcome this drawback, attempts have been made to improve the conversion efficiency of upconversion and to enable upconversion photovoltaics even at low irradiation power. For example, Zhou et al. reported the enhancement of broadband upconversion in $\text{mCu}_{2-x}\text{S}@\text{SiO}_2@\text{Er}_2\text{O}_3$ nanocomposites by using the broadband (800–1600 nm) plasmonic semiconductor mCu_{2-x}S .¹⁰⁴⁹ An internal quantum yield of 14.3% was achieved for Er_2O_3 using mCu_{2-x}S as an antenna to sensitize upconversion. These nanocomposites were used to enhance the power conversion efficiency of PSCs under irradiation of 15 suns. Besides plasmonic enhancement, dye-sensitized photon upconversion may be an effective way to improve upconversion photovoltaics.^{621,624,1085} In 2017, Hao et al. demonstrated the use of $\text{NaYF}_4:\text{Yb}/\text{Er}@\text{NaYF}_4:\text{Nd}$ nanocrystals functionalized with the dye IR783 to enhance broadband NIR harvesting in DSSC devices.¹⁰⁶² The dye modification increased upconversion luminescence by 9-fold. An increase of 13.1% was obtained in DSSCs coupled with dye-sensitized UCNPs. In 2019, Liu et al. developed a strategy to enhance upconversion luminescence by placing a polymer microlens array on UCNPs.¹⁰³⁷ They fabricated a photovoltaic device with a layered structure containing DSSCs, upconversion nanoparticles, and microlens arrays. This structure improved the performance of the DSSCs by a factor of 3.17% under one-sun irradiation (Figure 29c).

4.7. Nanomagnets and Magneto-optic Devices

Magnetism at the nanoscale has important implications for biomedicine, data storage, catalysis, and the development of permanent nanomagnets.^{100,1089,1090} Beyond controlling size, magnetocrystalline phases, and surface state, doping magnetic nanoparticles with impurities provides an alternative means of

controlling magnetic properties. Doping with magnetically susceptible elements can greatly affect the magnetism of nanoparticles.

Rare-earth doping of magnetic nanoparticles has been intensively investigated for magnetite (Fe_3O_4 or FeFe_2O_4) nanocrystals with a spinel structure, in which Fe^{3+} sites can be occupied by trivalent rare-earths (La, Ce, Sm, Eu, and Gd).^{1091,1092} In this crystal structure, O^{2-} forms a tight fcc packing, and Fe^{2+} or Fe^{3+} occupy either tetrahedral (T_d) or octahedral (O_h) interstitial sites. When these nanocrystals are exposed to an external magnetic field, the magnetic spins at the O_h sites align parallel to the external magnetic field, while the spins at the T_d sites align antiparallel. The antiferromagnetic interactions between T_d and O_h cannot fully compensate for this because the number of O_h sites is twice that of the T_d sites. The resulting uncompensated magnetic moments from dominant T_d – O_h interactions can then be modulated as a function of the doping ions occupying either T_d or O_h sites. Rare-earth-doped magnetite nanoparticles can be used as T_2 contrast agents for MRI. These nanoparticles are known to be effective adsorbents for the removal of antimony from aqueous solutions.^{1093,1094}

Rare-earth-based hard nanomagnets, such as NdFeB , SmCo , and SmFeN , have attracted much attention due to their potential utility in energy and sensing applications. However, the fabrication of monodisperse colloidal nanomagnets remains challenging due to the low chemical stability of rare-earths to oxidation. Currently, SmCo_5 nanomagnets with controllable size and morphology are mainly fabricated by a two-step approach involving high-temperature annealing in a CaO matrix.^{1095–1097} This method can produce uniform SmCo_5 nanoparticles with a high coercivity of up to 49.2 kOe. The two-step approach can also be used to synthesize hard magnetic $\text{Sm}_2\text{Fe}_{17}\text{N}_3$ nanoparticles with controllable size and morphology (Figure 30a).¹⁰⁸⁶ It is possible to integrate rare-earth-based hard nanomagnets into soft magnetic nano-

composites to construct exchange-coupled SmCo@FeCo nanocomposites (Figure 30b).¹⁰⁸⁷ After dispersion as colloidal suspensions in a solution, these nanomagnets can serve as magnetic ink to build flexible and printable magnets, or they can be assembled with other components to construct powerful permanent magnets.

Paramagnetic hosts containing rare-earth luminescent dopants can exhibit a dual optical-magnetic function. This was first demonstrated by Li, Peng, and co-workers using NaGdF₄:Nd/Yb/Er nanoplatelets.¹⁰⁸⁸ In that study, the upconversion luminescence of the paramagnetic nanoplatelets decreased monotonically when the external magnetic field increased from 0 to 12 kOe (Figure 30c). The researchers attributed the magnetic tuning to the magnetic splitting of the ⁴S_{3/2} level of Er³⁺, which decreased the excitation population of that level. Recently, Dai et al. investigated the magnetic tuning of upconversion luminescence in Au-NaGdF₄:Yb/Er nanocomposites.¹⁰⁹⁸ They found that the luminescence of Au-coupled UCNPs was independent of a magnetic field below 6 T due to the surface plasmon resonance of Au, whereas the luminescence intensity of pristine NaGdF₄:Yb/Er nanoparticles decreased monotonically with increasing external magnetic field from 0 to 37.1 T.

5. SUMMARY AND OUTLOOK

In the past decade, research in rare-earth-doped inorganic nanomaterials has grown faster than ever. Nanomaterial design provides an added dimension to control both physical and chemical interactions of rare-earths at the nanoscopic scale, enabling the development of diverse functional nanomaterials. These newly developed nanomaterials have created a kaleidoscopic toolbox that can be used to realize multidisciplinary applications, including bioimaging, therapy, drug delivery, neuroscience, sensing and detection, catalysis, light emission, information storage and encryption, nanolasing, and optical communication. In this review, we have summarized recent advances in rare-earth-doped inorganic nanomaterials in the context of material designs and new applications.

Further progress in this field will hinge upon the precise control of nanostructured architectures over an extended range of compositions. Although current methods have enabled structural engineering in rare-earth fluorides and semiconductors, it remains a formidable challenge to modulate the crystal size, morphology, and surface functionality of nanomaterials such as yttrium aluminum garnet, silicate glass, and magnetic rare-earth alloys, particularly in the fabrication of well-defined heterostructures. Successful implementation of sophisticated structural designs for these materials can lead to exotic optical and magnetic phenomena.

Nanostructured substrates can critically affect the physicochemical behavior of rare-earth ions. It is therefore crucial to continue the exploration of novel host materials, unconventional architectures, and associated properties. Along this line of effort, nanoscale engineering and hybridization may be a viable way to control rare-earth emission by various means such as light, electricity, mechanical force, and biological stimuli in unprecedented formats. In this context, quantum mechanical simulations and artificial intelligence based on machine learning can be adopted as complementary tools for screening new material substrates. For example, first-principles calculations based on density functional theory (DFT) have proven powerful in identifying and characterizing defects and corresponding defect levels in given materials.^{1099–1101} More-

over, the variation of DFT-calculated orbital energies can be considered as a descriptor for the change in optical transition energies of rare-earth ions.^{1102–1104} In addition, quantum mechanical calculations can be used to correlate substrate materials with the chemical/physical properties of rare-earth ions, enabling high-throughput computational structure design.¹¹⁰⁵ Apart from quantum simulations, machine learning has been applied in a variety of disciplines in recent years, including molecular design and photonics.^{1106–1110} Expanding the library of nanostructured hosts is likely to significantly advance basic research in rare-earth luminescence and facilitate many technological applications.

Another trend for future investigations is to open up new areas for rare-earth-doped inorganic nanomaterials. For instance, current applied research on how the luminescence properties of these nanomaterials affect the design of photodetectors with improved sensitivity needs to be refined. With recent advances in spectroscopy and imaging techniques, it is also useful to reconsider rare-earth-doped nanophosphors for practical bioimaging and clinical applications where biocompatible optical probes with high photostability and specific targeting are critical. Such research directions require interdisciplinary knowledge or close collaboration between different fields. Given advances in information technology, one may look for ways to integrate earlier rare-earth technologies into new smart gadgets. The development of biometric sensors or devices that monitor environmental conditions such as the concentration of metal ions or acidity can benefit significantly from rare-earth-doped nanomaterials. At the same time, it is worth exploring new data processing protocols for nanomaterial applications that facilitate material design and device integration. For applications in catalysts, the potential contribution of the surface charge of rare-earth ions to catalytic substrates could increase interest in surface-mediated catalysis. Moreover, doping of nanomaterials with rare-earths in a single-atom format could provide more reactive sites for catalytic conversion, which clearly requires more research attention.

The future will envision the integration of multidisciplinary knowledge and technologies to explore new functions of rare-earth-doped nanomaterials in rapidly growing research areas. This development will further drive the discovery of optical nanomaterials for breakthrough applications in diverse fields, such as photodetectors, optogenetics, immunotherapy, super-resolution imaging, optoelectronics, and many others.^{562,1111}

AUTHOR INFORMATION

Corresponding Authors

Juan Wang – Institute of Environmental Health, MOE Key Laboratory of Environmental Remediation and Ecosystem Health, College of Environmental & Resource Sciences, Zhejiang University, Hangzhou 310058, China; orcid.org/0000-0002-1340-9011; Email: wjuan@zju.edu.cn

Feng Wang – Department of Materials Science and Engineering, City University of Hong Kong, Hong Kong SAR 999077, China; orcid.org/0000-0001-9471-4386; Email: fwang24@cityu.edu.hk

Renren Deng – State Key Laboratory of Silicon Materials, Institute for Composites Science Innovation, School of Materials Science and Engineering, Zhejiang University,

Hangzhou 310027, China; orcid.org/0000-0001-8213-6304; Email: rdeng@zju.edu.cn

Xiaogang Liu – Department of Chemistry, National University of Singapore, Singapore 117543, Singapore; orcid.org/0000-0003-2517-5790; Email: chmlx@nus.edu.sg

Authors

Bingzhu Zheng – State Key Laboratory of Silicon Materials, Institute for Composites Science Innovation, School of Materials Science and Engineering, Zhejiang University, Hangzhou 310027, China

Jingyue Fan – Department of Chemistry, National University of Singapore, Singapore 117543, Singapore; orcid.org/0000-0003-4987-7025

Bing Chen – Department of Materials Science and Engineering, City University of Hong Kong, Hong Kong SAR 999077, China; orcid.org/0000-0002-0663-1343

Xian Qin – Department of Chemistry, National University of Singapore, Singapore 117543, Singapore

Complete contact information is available at:

<https://pubs.acs.org/10.1021/acs.chemrev.1c00644>

Notes

The authors declare no competing financial interest.

Biographies

Bingzhu Zheng earned her B.S. degree in Materials Science from Central South University in China in 2017. She is currently a Ph.D. student at the School of Material Science and Engineering, Zhejiang University, under the supervision of Prof. Renren Deng. Her research interests include energy transfer processes between organic molecules and inorganic rare-earth-doped nanocrystals and exploring potential applications of hybrid nanomaterials for catalysis, drug delivery, and therapy.

Jingyue Fan received her B.S. degree in Chemistry (Hons) from the National University of Singapore in 2017, and she is currently a Ph.D. student in the group of Prof. Xiaogang Liu. Her research focuses on the fundamental study of rare-earth-doped luminescent nanomaterials and their surface interaction properties.

Bing Chen was born in Zhejiang, China. He received his B.E. (2012) and Ph.D. (2017) degrees in Materials Science and Engineering from Zhejiang University. Currently, he is a postdoctoral researcher in Prof. Feng Wang's group at City University of Hong Kong. His research interest is on the development of luminescent micro/nanomaterials containing lanthanide ions.

Xian Qin earned her B.S. degree (2007) in Mechanical Engineering from Sichuan University. She received her Ph.D. degree from Harbin Institute of Technology, P. R. China, in 2013 under the supervision of Prof. Qingyuan Meng. She subsequently carried out postdoctoral training in the Chemistry Department of National University of Singapore and also the Institute of Materials Research and Engineering (IMRE) of A*STAR, Singapore. Her current research focuses on molecular optoelectronics, energy conversion, and nanocatalysis, as well as developing quantum and classical methodologies to understand the photophysical processes of luminescent nanomaterials.

Juan Wang is a professor at the College of Environment and Resources Science, Zhejiang University. She received her Ph.D. from the National University of Singapore in 2012. She then worked as a consultant at EnviroSolutions. Pte. Ltd. followed by postdoctoral studies at Nanyang Technological University between 2013 and 2016.

Her research interests include photocatalysis, photothermal catalysis, photothermal conversion materials, and devices for wastewater and seawater treatment.

Feng Wang is a professor in the Department of Materials Science and Engineering at the City University of Hong Kong. He obtained his B.E. and Ph.D. degrees in Materials Science and Engineering from Zhejiang University, China. He then carried out postdoctoral research at the National University of Singapore and the Institute of Materials Research and Engineering of A*STAR. His current research focuses on the synthesis, spectroscopic investigation, and application of micro/nanostructured luminescent materials.

Renren Deng is a professor at the School of Materials Science and Engineering, Zhejiang University, China. He received his B.S. degree in Chemistry from Zhejiang University, China, in 2009 and his Ph.D. in Chemistry from the National University of Singapore (NUS) in 2014. From 2014–2016, he worked as a postdoctoral researcher at NUS and Cavendish Laboratory at Cambridge University. His research interests focus on developing luminescent nanomaterials for applications in photovoltaics and biomedicine and understanding energy transfer through organic molecule–inorganic nanocrystal hybrid systems.

Xiaogang Liu received his B.E. degree in Chemical Engineering from Beijing Technology and Business University, China. He received his M.S. degree in Chemistry from East Carolina University and his Ph.D. degree from Northwestern University. He then worked as a postdoctoral researcher at the Massachusetts Institute of Technology for two years before moving to the National University of Singapore in 2006. He is currently an associate editor of *Nanoscale* and serves on the editorial boards of *Research*, *Nanoscale Horizons*, *Chemistry: An Asian Journal*, *Advanced Optical Materials*, *Analysis and Sensing*, *Journal of Luminescence*, and *Journal of Physical Chemistry Letters*. His research areas include catalysis, molecular sensing, and biomedicine, as well as the development of luminescent nanomaterials for optogenetic neuromodulation, cancer immunotherapy, assistive technologies, and X-ray imaging.

ACKNOWLEDGMENTS

We gratefully acknowledge financial support from the Singapore Ministry of Education (MOE2017-T2-2-110), the Agency for Science, Technology and Research (A*STAR) under its AME programme (grant nos. A1883c0011 and A1983c0038), National Research Foundation, the Prime Minister's Office of Singapore under its NRF Investigatorship Programme (award no. NRF-NRFIO5-2019-0003), the King Abdullah University of Science and Technology (KAUST) Office of Sponsored Research (OSR) under award no. OSR-2018-CRG7-3736, the National Natural Science Foundation of China (51872256, 21801222, 21976152, 21773200), the Zhejiang Provincial National Natural Science Foundation of China (LR19B010002, LR21B070002), the Fundamental Research Funds for the Central Universities, and the Research Grants Council of Hong Kong under a Research Fellowship Scheme (Grant No. RFS2021-1S03).

ABBREVIATIONS AND LIST OF ACRONYMS

ACC	atom confinement and coordination
BDC	1,4-benzendicarboxylate
BPDC	biphenyl dicarboxylate
BTB	1,3,5-tris(4-carboxyphenyl)benzene
BTc	1,3,5-benzenetricarboxylic acid
CB	conduction band

ChR	channelrhodopsins	PLQY	photoluminescence quantum yield
CN	coordination numbers	PMMA	poly(methyl methacrylate)
CR	cross-relaxation	PSC	perovskite solar cell
CRISPR-Cas9	clustered regularly interspaced short palindromic repeats-associated protein 9	PTT	photothermal therapy
CRR	carbon dioxide reduction reaction	QD	quantum dot
CT	computed tomography	RBS	Roussin's black salt
CVD	chemical vapor deposition	RGO	reduced graphene oxide
DEF	<i>N,N'</i> -diethylformamide	ROS	reactive oxygen species
DFT	density functional theory	RRAM	resistive random-access memory
DMA	dimethylammonium	SEM	scanning electron microscopy
DMBDC	2,5-dimethoxy-1,4-benzenedicarboxylate	SPECT	single-photon emission computed tomography
DMF	<i>N,N</i> -dimethylformamide	SPR	surface plasmon resonance
DMSO	dimethyl sulfoxide	STED	stimulated-emission depletion
DOX	doxorubicin	STEM	scanning transmission electron microscopy
DSSC	dye-sensitized solar cell	STM	scanning tunneling microscopy
DTE	diarylethene	TEM	transmission electron microscopy
DTT	dithiothreitol	TMS-Br	trimethylbromosilane
EDS	energy dispersive spectroscopy	TMS-Cl	trimethylchlorosilane
EDTA	ethylenedinitrilo-tetraacetic acid	UCNP	upconversion nanoparticle
EELS	electron energy loss spectroscopy	UV	ultraviolet
eNpHR	enhanced Natronomonas halorhodopsin	VB	valence band
FA	formamidinium	VE	vacancy-engineered
FIR	fluorescence intensity ratio	VIS	visible
FRET	Förster resonance energy transfer	VOC	volatile organic compounds
FT-EXAFS	Fourier-transformed extended X-ray absorption fine structure	WGM	whispering gallery mode
fwhm	full width at half-maximum	XAFS	X-ray absorption fine structure
GO	graphene oxide	XPS	X-ray photoelectron spectroscopy
HAADF-STEM	high-angle annular dark-field image scanning transmission electron microscopy	XRD	X-ray diffraction
HCR	hybridization chain reaction	Xr-LEI	X-ray luminescence extension imaging
hfa	hexafluoro acetylacetonato		
HHTP	2,3,6,7,10,11-hexahydroxytriphenylene		
HMM	hyperbolic meta-material		
HRTEM	high-resolution transmission electron microscope		
ICP-AES	inductively coupled plasma–atomic emission spectroscopy		
ICP-OES	inductively coupled plasma–optical emission spectroscopy		
IoT	internet of things		
LMCT	ligand-to-metal charge transfer		
LRH	layered rare-earth hydroxide		
MA	methylammonium		
MASR-CVD	matrix-assisted sustained-release chemical vapor deposition		
MB	Methylene Blue		
MMT	montmorillonite		
MN	motor neuron		
MOF	metal–organic framework		
MRI	magnetic resonance imaging		
NIR	near-infrared		
NP	nanoparticle		
OA	oleic acid		
ODE	1-octadecene		
OM	oleylamine		
OSC	oxygen storage capacity		
PAA	polyacrylic acid		
PCE	power conversion efficiency		
PDMS	polydimethylsiloxane		
PDT	photodynamic therapy		
PET	positron emission tomography		

REFERENCES

- (1) Pigué, C. Extricate Erbium. *Nat. Chem.* **2014**, *6*, 370–370.
- (2) McCoy, H. N. The Separation of Europium from Other Rare Earths. *J. Am. Chem. Soc.* **1935**, *57*, 1756–1756.
- (3) Werts, M. H. V. Making Sense of Lanthanide Luminescence. *Sci. Prog. (St. Albans, U. K.)* **2005**, *88*, 101–131.
- (4) Dabbousi, B. O.; Rodriguez-Viejo, J.; Mikulec, F. V.; Heine, J. R.; Mattoussi, H.; Ober, R.; Jensen, K. F.; Bawendi, M. G. (CdSe)ZnS Core–Shell Quantum Dots: Synthesis and Characterization of A Size Series of Highly Luminescent Nanocrystallites. *J. Phys. Chem. B* **1997**, *101*, 9463–9475.
- (5) Grundmann, M.; Christen, J.; Ledentsov, N. N.; Böhrer, J.; Bimberg, D.; Ruvimov, S. S.; Werner, P.; Richter, U.; Gösele, U.; Heydenreich, J.; et al. Ultranarrow Luminescence Lines from Single Quantum Dots. *Phys. Rev. Lett.* **1995**, *74*, 4043–4046.
- (6) Dhanaraj, J.; Jagannathan, R.; Kutty, T. R. N.; Lu, C.-H. Photoluminescence Characteristics of Y₂O₃:Eu³⁺ Nanophosphors Prepared Using Sol–Gel Thermolysis. *J. Phys. Chem. B* **2001**, *105*, 11098–11105.
- (7) Ye, T.; Guiwen, Z.; Weiping, Z.; Shangda, X. Combustion Synthesis and Photoluminescence of Nanocrystalline Y₂O₃:Eu Phosphors. *Mater. Res. Bull.* **1997**, *32*, 501–506.
- (8) Beverloo, H. B.; van Schadewijk, A.; van Gelderen-Boele, S.; Tanke, H. J. Inorganic Phosphors as New Luminescent Labels for Immunocytochemistry and Time-Resolved Microscopy. *Cytometry* **1990**, *11*, 784–792.
- (9) Zijlmans, H. J. M. A. A.; Bonnet, J.; Burton, J.; Kardos, K.; Vail, T.; Niedbal, R. S.; Tanke, H. J. Detection of Cell and Tissue Surface Antigens Using Up-Converting Phosphors: A New Reporter Technology. *Anal. Biochem.* **1999**, *267*, 30–36.
- (10) Auzel, F. History of Upconversion Discovery and Its Evolution. *J. Lumin.* **2020**, *223*, 116900.
- (11) Auzel, F. Upconversion and Anti-Stokes Processes with f and d Ions in Solids. *Chem. Rev.* **2004**, *104*, 139–174.

- (12) Mai, H.-X.; Zhang, Y.-W.; Si, R.; Yan, Z.-G.; Sun, L.-d.; You, L.-P.; Yan, C.-H. High-Quality Sodium Rare-Earth Fluoride Nanocrystals: Controlled Synthesis and Optical Properties. *J. Am. Chem. Soc.* **2006**, *128*, 6426–6436.
- (13) Boyer, J.-C.; Cuccia, L. A.; Capobianco, J. A. Synthesis of Colloidal Upconverting NaYF₄: Er³⁺/Yb³⁺ and Tm³⁺/Yb³⁺ Monodisperse Nanocrystals. *Nano Lett.* **2007**, *7*, 847–852.
- (14) Chatterjee, D. K.; Yong, Z. Upconverting Nanoparticles as Nanotransducers for Photodynamic Therapy in Cancer Cells. *Nanomedicine* **2008**, *3*, 73–82.
- (15) Wang, L.; Li, Y. Na(Y_{1.5}Na_{0.5})F₆ Single-Crystal Nanorods as Multicolor Luminescent Materials. *Nano Lett.* **2006**, *6*, 1645–1649.
- (16) Liu, J.; Kong, X.; Zheng, L.; Guo, X.; Liu, X.; Shui, J. Rare Earth Single-Atom Catalysts for Nitrogen and Carbon Dioxide Reduction. *ACS Nano* **2020**, *14*, 1093–1101.
- (17) Du, J.; Xia, C.; Xiong, W.; Zhao, X.; Wang, T.; Jia, Y. Tuning the Electronic Structures and Magnetism of Two-Dimensional Porous C 2 N via Transition Metal Embedding. *Phys. Chem. Chem. Phys.* **2016**, *18*, 22678–22686.
- (18) Yuan, Z.; Li, N. Manipulating the Magnetic Moment in Phosphorene by Lanthanide Atom Doping: a First-Principle Study. *RSC Adv.* **2016**, *6*, 92048–92056.
- (19) Lyu, Y.; Wu, Z.; Io, W. F.; Hao, J. Observation and Theoretical Analysis of Near-Infrared Luminescence from CVD Grown Lanthanide Er Doped Monolayer MoS₂ Triangles. *Appl. Phys. Lett.* **2019**, *115*, 153105.
- (20) Xu, Z.; Quintanilla, M.; Vetrone, F.; Govorov, A. O.; Chaker, M.; Ma, D. Harvesting Lost Photons: Plasmon and Upconversion Enhanced Broadband Photocatalytic Activity in Core@ Shell Microspheres Based on Lanthanide-Doped NaYF₄, TiO₂, and Au. *Adv. Funct. Mater.* **2015**, *25*, 2950–2960.
- (21) Nie, L.; Mei, D.; Xiong, H.; Peng, B.; Ren, Z.; Hernandez, X. I. P.; DeLaRiva, A.; Wang, M.; Engelhard, M. H.; Kovarik, L.; et al. Activation of Surface Lattice Oxygen in Single-Atom Pt/CeO₂ for Low-Temperature CO Oxidation. *Science* **2017**, *358*, 1419–1423.
- (22) Shao, Y.; Liu, B.; Di, Z.; Zhang, G.; Sun, L.-D.; Li, L.; Yan, C.-H. Engineering of Upconverted Metal–Organic Frameworks for Near-Infrared Light-Triggered Combinational Photodynamic/Chemo-/Immunotherapy against Hypoxic Tumors. *J. Am. Chem. Soc.* **2020**, *142*, 3939–3946.
- (23) Li, Y.; Di, Z.; Gao, J.; Cheng, P.; Di, C.; Zhang, G.; Liu, B.; Shi, X.; Sun, L. D.; Li, L.; Yan, C. H. Heterodimers Made of Upconversion Nanoparticles and Metal–Organic Frameworks. *J. Am. Chem. Soc.* **2017**, *139*, 13804–13810.
- (24) Zhang, Y.; Wang, Y.; Liu, L.; Wei, N.; Gao, M.-L.; Zhao, D.; Han, Z.-B. Robust Bifunctional Lanthanide Cluster Based Metal–Organic Frameworks (MOFs) for Tandem Deacetalization–Knoevenagel Reaction. *Inorg. Chem.* **2018**, *57*, 2193–2198.
- (25) Idris, N. M.; Gnanasammandhan, M. K.; Zhang, J.; Ho, P. C.; Mahendran, R.; Zhang, Y. *In Vivo* Photodynamic Therapy Using Upconversion Nanoparticles as Remote-Controlled Nanotransducers. *Nat. Med.* **2012**, *18*, 1580–1585.
- (26) Yuan, P.; Lee, Y. H.; Gnanasammandhan, M. K.; Guan, Z.; Zhang, Y.; Xu, Q. H. Plasmon Enhanced Upconversion Luminescence of NaYF₄:Yb, Er@SiO₂@Ag Core–Shell Nanocomposites for Cell Imaging. *Nanoscale* **2012**, *4*, 5132–5137.
- (27) Lim, S. F.; Riehn, R.; Ryu, W. S.; Khanarian, N.; Tung, C. K.; Tank, D.; Austin, R. H. *In Vivo* and Scanning Electron Microscopy Imaging of Upconverting Nanophosphors in *Caenorhabditis Elegans*. *Nano Lett.* **2006**, *6*, 169–174.
- (28) Ma, J.; Huang, P.; He, M.; Pan, L.; Zhou, Z.; Feng, L.; Gao, G.; Cui, D. Folic Acid-Conjugated LaF₃:Yb, Tm@SiO₂ Nanoprobes for Targeting Dual-Modality Imaging of Upconversion Luminescence and X-ray Computed Tomography. *J. Phys. Chem. B* **2012**, *116*, 14062–14070.
- (29) Zhan, Q.; Liu, H.; Wang, B.; Wu, Q.; Pu, R.; Zhou, C.; Huang, B.; Peng, X.; Ågren, H.; He, S. Achieving High-Efficiency Emission Depletion Nanoscopy by Employing Cross Relaxation in Upconversion Nanoparticles. *Nat. Commun.* **2017**, *8*, 1058.
- (30) Li, X.; Shen, D.; Yang, J.; Yao, C.; Che, R.; Zhang, F.; Zhao, D. Successive Layer-by-Layer Strategy for Multi-Shell Epitaxial Growth: Shell Thickness and Doping Position Dependence in Upconverting Optical Properties. *Chem. Mater.* **2013**, *25*, 106–112.
- (31) Xie, X.; Gao, N.; Deng, R.; Sun, Q.; Xu, Q.-H.; Liu, X. Mechanistic Investigation of Photon Upconversion in Nd³⁺-Sensitized Core–Shell Nanoparticles. *J. Am. Chem. Soc.* **2013**, *135*, 12608–12611.
- (32) Liu, Q.; Zhang, Y.; Peng, C. S.; Yang, T.; Joubert, L.-M.; Chu, S. Single Upconversion Nanoparticle Imaging at Sub-10 W cm⁻² Irradiance. *Nat. Photonics* **2018**, *12*, 548–553.
- (33) Shang, Y.; Zhou, J.; Cai, Y.; Wang, F.; Fernandez-Bravo, A.; Yang, C.; Jiang, L.; Jin, D. Low Threshold Lasing Emissions from a Single Upconversion Nanocrystal. *Nat. Commun.* **2020**, *11*, 6156.
- (34) Liu, X.; Wang, Y.; Li, X.; Yi, Z.; Deng, R.; Liang, L.; Xie, X.; Loong, D. T. B.; Song, S.; Fan, D.; et al. Binary Temporal Upconversion Codes of Mn²⁺-Activated Nanoparticles for Multilevel Anti-Counterfeiting. *Nat. Commun.* **2017**, *8*, 899.
- (35) Buisette, V.; Giaume, D.; Gacoin, T.; Boilot, J. P. Aqueous Routes to Lanthanide-Doped Oxide Nanophosphors. *J. Mater. Chem.* **2006**, *16*, 529–539.
- (36) Zhang, Y.; Huang, L.; Liu, X. Unraveling Epitaxial Habits in the NaLnF₄ System for Color Multiplexing at the Single-Particle Level. *Angew. Chem.* **2016**, *128*, 5812–5816.
- (37) Wang, M.; Huang, Q. L.; Hong, J. M.; Wu, W. H.; Yu, Z.; Chen, X. T.; Xue, Z. L. Room Temperature Synthesis and Characterization of NaEuF₄ Nanorods and Na₃Eu₃F₃₂ Nanospheres. *Solid State Commun.* **2005**, *136*, 210–214.
- (38) Zhou, D.; Sun, R.; Xu, W.; Ding, N.; Li, D.; Chen, X.; Pan, G.; Bai, X.; Song, H. Impact of Host Composition, Codoping, or Tridoping on Quantum-Cutting Emission of Ytterbium in Halide Perovskite Quantum Dots and Solar Cell Applications. *Nano Lett.* **2019**, *19*, 6904–6913.
- (39) Cheng, Y.; Shen, C.; Shen, L.; Xiang, W.; Liang, X. Tb³⁺, Eu³⁺ Co-doped CsPbBr₃ QDs Glass with Highly Stable and Luminous Adjustable for White LEDs. *ACS Appl. Mater. Interfaces* **2018**, *10*, 21434–21444.
- (40) Zhou, D.; Liu, D.; Pan, G.; Chen, X.; Li, D.; Xu, W.; Bai, X.; Song, H. Cerium and Ytterbium Codoped Halide Perovskite Quantum Dots: A Novel and Efficient Downconverter for Improving the Performance of Silicon Solar Cells. *Adv. Mater.* **2017**, *29*, 1704149.
- (41) Du, Y.; Jiang, Y.; Sun, T.; Zhao, J.; Huang, B.; Peng, D.; Wang, F. Mechanically Excited Multicolor Luminescence in Lanthanide Ions. *Adv. Mater.* **2019**, *31*, 1807062.
- (42) Yi, Z.; Li, X.; Lu, W.; Liu, H.; Zeng, S.; Hao, J. Hybrid Lanthanide Nanoparticles as a New Class of Binary Contrast Agents for *In Vivo* T₁/T₂ Dual-Weighted MRI and Synergistic Tumor Diagnosis. *J. Mater. Chem. B* **2016**, *4*, 2715–2722.
- (43) Liu, X.; Wang, L. S.; Ma, Y.; Zheng, H.; Lin, L.; Zhang, Q.; Chen, Y.; Qiu, Y.; Peng, D. L. Enhanced Microwave Absorption Properties by Tuning Cation Deficiency of Perovskite Oxides of Two-Dimensional LaFeO₃/C Composite in X-Band. *ACS Appl. Mater. Interfaces* **2017**, *9*, 7601–7610.
- (44) Lee, J.; Lee, G.; Hwang, T. Y.; Lim, H. R.; Cho, H. B.; Kim, J.; Choa, Y. H. Phase-and Composition-Tunable Hard/Soft Magnetic Nanofibers for High-Performance Permanent Magnet. *ACS Appl. Nano Mater.* **2020**, *3*, 3244–3251.
- (45) Xu, J.; Zhu, K.; Gao, S.; Hou, Y. Rare Earth Permanent Magnetic Nanostructures: Chemical Design and Microstructure Control to Optimize Magnetic Properties. *Inorg. Chem. Front.* **2021**, *8*, 383–395.
- (46) Fischbacher, J.; Kovacs, A.; Gusenbauer, M.; Oezelt, H.; Exl, L.; Bance, S.; Schrefl, T. Micromagnetics of Rare-earth Efficient Permanent Magnets. *J. Phys. D: Appl. Phys.* **2018**, *51*, 193002.
- (47) Malta, O. L. Mechanisms of Non-radiative Energy Transfer Involving Lanthanide Ions Revisited. *J. Non-Cryst. Solids* **2008**, *354*, 4770–4776.

- (48) Ward, M. *The Rare Earth Elements: Fundamentals and Applications*; Atwood, D. A., Ed.; Wiley-VCH, 2012; Vol. 27, p 436; ISBN: 978-1-1199-5097-4.
- (49) Beaudry, B. J.; Gschneidner, K. A. *In Handbook on the Physics and Chemistry of Rare Earths*; Elsevier, 1978; Vol. 1.
- (50) Shannon, R. Revised Effective Ionic Radii and Systematic Studies of Interatomic Distances in Halides and Chalcogenides. *Acta Crystallogr., Sect. A: Cryst. Phys., Diffr., Theor. Gen. Crystallogr.* **1976**, *32*, 751–767.
- (51) Li, L.; Wang, X.; Zhang, Y. Enhanced Visible Light-Responsive Photocatalytic Activity of LnFeO₃ (Ln = La, Sm) Nanoparticles by Synergistic Catalysis. *Mater. Res. Bull.* **2014**, *50*, 18–22.
- (52) Liu, J.; Zhao, Z.; Xu, C.-m.; Duan, A.-j. Simultaneous Removal of NO_x and Diesel Soot over Nanometer Ln-Na-Cu-O Perovskite-Like Complex Oxide Catalysts. *Appl. Catal., B* **2008**, *78*, 61–72.
- (53) Malecka, M. A.; Kępiński, L.; Miśta, W. Structure Evolution of Nanocrystalline CeO₂ and CeLnO_x Mixed Oxides (Ln = Pr, Tb, Lu) in O₂ and H₂ Atmosphere and Their Catalytic Activity in Soot Combustion. *Appl. Catal., B* **2007**, *74*, 290–298.
- (54) Yao, M.; Liu, B.; Zou, Y.; Wang, L.; Cui, T.; Zou, G.; Li, J.; Sundqvist, B. Effect of Rare-Earth Component of the RE/Ni Catalyst on the Formation and Nanostructure of Single-Walled Carbon Nanotubes. *J. Phys. Chem. B* **2006**, *110*, 15284–15290.
- (55) Riwootzki, K.; Meyssamy, H.; Schnablegger, H.; Kornowski, A.; Haase, M. Liquid-Phase Synthesis of Colloids and Redispersible Powders of Strongly Luminescing LaPO₄:Ce,Tb Nanocrystals. *Angew. Chem., Int. Ed.* **2001**, *40*, 573–576.
- (56) Buissette, V.; Moreau, M.; Gacoin, T.; Boilot, J.-P.; Chane-Ching, J.-Y.; Le Mercier, T. Colloidal Synthesis of Luminescent Rhabdophane LaPO₄:Ln³⁺·xH₂O (Ln = Ce, Tb, Eu; x ≈ 0.7) Nanocrystals. *Chem. Mater.* **2004**, *16*, 3767–3773.
- (57) Liu, C.; Wang, H.; Zhang, X.; Chen, D. Morphology- and Phase-Controlled Synthesis of Monodisperse Lanthanide-Doped NaGdF₄ Nanocrystals with Multicolor Photoluminescence. *J. Mater. Chem.* **2009**, *19*, 489–496.
- (58) Wang, F.; Fan, X.; Wang, M.; Zhang, Y. Multicolour PEI/NaGdF₄: Ce³⁺, Ln³⁺ Nanocrystals by Single-Wavelength Excitation. *Nanotechnology* **2007**, *18*, 025701.
- (59) Yang, H.; Kim, Y.-S. Energy Transfer-Based Spectral Properties of Tb-, Pr-, or Sm-Codoped YAG: Ce Nanocrystalline Phosphors. *J. Lumin.* **2008**, *128*, 1570–1576.
- (60) Meng, F.; Zhang, C.; Fan, Z.; Gong, J.; Li, A.; Ding, Z.; Tang, H.; Zhang, M.; Wu, G. Hydrothermal Synthesis of Hexagonal CeO₂ Nanosheets and Their Room Temperature Ferromagnetism. *J. Alloys Compd.* **2015**, *647*, 1013–1021.
- (61) Li, M.; Gao, X.; Wu, Y.; Li, H. Simple and Effective Hydrothermal Synthesis and Magnetic Properties of Large-Scale Monodisperse Fish-Like CeO₂ Nanostructures. *J. Mater. Sci.: Mater. El.* **2017**, *28*, 16798–16801.
- (62) Li, G.-R.; Qu, D.-L.; Yu, X.-L.; Tong, Y.-X. Microstructural Evolution of CeO₂ from Porous Structures to Clusters of Nanosheet Arrays Assisted by Gas Bubbles via Electrodeposition. *Langmuir* **2008**, *24*, 4254–4259.
- (63) Kang, Y.; Leng, Q.; Guo, D.; Yang, D.; Pu, Y.; Hu, C. Room-Temperature Magnetism of Ceria Nanocubes by Inductively Transferring Electrons to Ce Atoms from Nearby Oxygen Vacancy. *Nano-Micro Lett.* **2016**, *8*, 13–19.
- (64) Arora, M.; Kumar, M. Structural, Magnetic and Optical Properties of Ce Substituted BiFeO₃ Nanoparticles. *Ceram. Int.* **2015**, *41*, 5705–5712.
- (65) Mohanapriya, P.; Pradeepkumar, R.; Victor Jaya, N.; Natarajan, T. S. Magnetic and Optical Properties of Electrospun Hollow Nanofibers of SnO₂ Doped with Ce-Ion. *Appl. Phys. Lett.* **2014**, *105*, 022406.
- (66) Liu, J.; Zhao, Z.; Xu, C.; Duan, A.; Wang, L.; Zhang, S. Synthesis of Nanopowder Ce–Zr–Pr Oxide Solid Solutions and Their Catalytic Performances for Soot Combustion. *Catal. Commun.* **2007**, *8*, 220–224.
- (67) Sudarsanam, P.; Kuntaiah, K.; Reddy, B. M. Promising Ceria-Samarium-Based Nano-Oxides for Low Temperature Soot Oxidation: A Combined Study of Structure-Activity Properties. *New J. Chem.* **2014**, *38*, 5991–6001.
- (68) Kašpar, J.; Fornasiero, P.; Graziani, M. Use of CeO₂-Based Oxides in the Three-Way Catalysis. *Catal. Today* **1999**, *50*, 285–298.
- (69) Wang, Z.; Wang, Q.; Liao, Y.; Shen, G.; Gong, X.; Han, N.; Liu, H.; Chen, Y. Comparative Study of CeO₂ and Doped CeO₂ with Tailored Oxygen Vacancies for CO Oxidation. *ChemPhysChem* **2011**, *12*, 2763–2770.
- (70) Bharali, P.; Saikia, P.; Reddy, B. M. Large-Scale Synthesis of Ceria-Based Nano-Oxides with High CO Oxidation Activity. *Catal. Sci. Technol.* **2012**, *2*, 931–933.
- (71) Laosiripojana, N.; Charojrochkul, S.; Kim-Lohsoontorn, P.; Assabumrungrat, S. Role and Advantages of H₂S in Catalytic Steam Reforming Over Nanoscale CeO₂-Based Catalysts. *J. Catal.* **2010**, *276*, 6–15.
- (72) Sudarsanam, P.; Rangaswamy, A.; Reddy, B. M. An Efficient Noble Metal-Free Ce-Sm/SiO₂ Nano-Oxide Catalyst for Oxidation of Benzylamines under Ecofriendly Conditions. *RSC Adv.* **2014**, *4*, 46378–46382.
- (73) Sutradhar, N.; Sinhamahapatra, A.; Pahari, S.; Jayachandran, M.; Subramanian, B.; Bajaj, H. C.; Panda, A. B. Facile Low-Temperature Synthesis of Ceria and Samarium-Doped Ceria Nanoparticles and Catalytic Allylic Oxidation of Cyclohexene. *J. Phys. Chem. C* **2011**, *115*, 7628–7637.
- (74) Yao, S. Y.; Xu, W. Q.; Johnston-Peck, A. C.; Zhao, F. Z.; Liu, Z. Y.; Luo, S.; Senanayake, S. D.; Martinez-Arias, A.; Liu, W. J.; Rodriguez, J. A. Morphological Effects of the Nanostructured Ceria Support on the Activity and Stability of CuO/CeO₂ Catalysts for the Water-Gas Shift Reaction. *Phys. Chem. Chem. Phys.* **2014**, *16*, 17183–17195.
- (75) Celardo, I.; Pedersen, J. Z.; Traversa, E.; Ghibelli, L. Pharmacological Potential of Cerium Oxide Nanoparticles. *Nanoscale* **2011**, *3*, 1411–1420.
- (76) Zhou, X.; Deng, Y.; Jiang, S.; Xiang, G.; Li, L.; Tang, X.; Luo, X.; Pang, Y.; Huang, Y. Investigation of Energy Transfer in Pr³⁺, Yb³⁺ Co-Doped Phosphate Phosphor: The Role of ³P₀ and ¹D₂. *J. Lumin.* **2019**, *209*, 45–51.
- (77) Pelle, F.; Dhaouadi, M.; Michely, L.; Aschehoug, P.; Toncelli, A.; Veronesi, S.; Tonelli, M. Spectroscopic Properties and Upconversion in Pr³⁺: YF₃ Nanoparticles. *Phys. Chem. Chem. Phys.* **2011**, *13*, 17453–17460.
- (78) Pan, Y.; Su, Q.; Xu, H.; Chen, T.; Ge, W.; Yang, C.; Wu, M. Synthesis and Red Luminescence of Pr³⁺-Doped CaTiO₃ Nanophosphor from Polymer Precursor. *J. Solid State Chem.* **2003**, *174*, 69–73.
- (79) Yang, X.; Zhou, Y.; Yu, X.; Demir, H. V.; Sun, X. W. Bifunctional Highly Fluorescent Hollow Porous Microspheres Made of BaMoO₄: Pr³⁺ Nanocrystals via a Template-Free Synthesis. *J. Mater. Chem.* **2011**, *21*, 9009–9013.
- (80) Lemański, K.; Dereń, P. J. Luminescent Properties of LaAlO₃ Nanocrystals, Doped with Pr³⁺ and Yb³⁺ Ions. *J. Lumin.* **2014**, *146*, 239–242.
- (81) Gusowski, M. A.; Swart, H. C.; Karlsson, L. S.; Trzebiatowska-Gusowska, M. NaYF₄: Pr³⁺ Nanocrystals Displaying Photon Cascade Emission. *Nanoscale* **2012**, *4*, 541–546.
- (82) Xiang, G.; Zhang, J.; Hao, Z.; Zhang, X.; Pan, G.; Luo, Y.; Lu, S.; Zhao, H. The Energy Transfer Mechanism in Pr³⁺ and Yb³⁺ Codoped [small beta]-NaLuF₄ Nanocrystals. *Phys. Chem. Chem. Phys.* **2014**, *16*, 9289–9293.
- (83) Wang, Z.; Meijerink, A. Dye-Sensitized Downconversion. *J. Phys. Chem. Lett.* **2018**, *9*, 1522–1526.
- (84) Bharathkumar, S.; Sakar, M.; Ponpandian, N.; Balakumar, S. Dual Oxidation State Induced Oxygen Vacancies in Pr Substituted BiFeO₃ Compounds: An Effective Material Activation Strategy to Enhance the Magnetic and Visible Light-Driven Photocatalytic Properties. *Mater. Res. Bull.* **2018**, *101*, 107–115.

- (85) Das, R.; Khan, G. G.; Varma, S.; Mukherjee, G. D.; Mandal, K. Effect of Quantum Confinement on Optical and Magnetic Properties of Pr–Cr-Codoped Bismuth Ferrite Nanowires. *J. Phys. Chem. C* **2013**, *117*, 20209–20216.
- (86) Ouyang, X.; Yuan, S.; Qiu, Q.; Zeng, W.; Hope, G. A.; Li, H. Facile Synthesis of Porous Pr(OH)₃ Nanowire Bundles and Their Magnetic Properties. *Inorg. Chem. Commun.* **2014**, *46*, 21–23.
- (87) Wang, Y.; Nguyen, T. S.; Wang, C.; Wang, X. Ethanol Electrooxidation on Pt/C Catalysts Promoted with Praseodymium Oxide Nanorods. *Dalton T.* **2009**, 7606–7609.
- (88) Reddy, B. M.; Thrimurthulu, G.; Katta, L.; Yamada, Y.; Park, S.-E. Structural Characteristics and Catalytic Activity of Nanocrystalline Ceria–Praseodymia Solid Solutions. *J. Phys. Chem. C* **2009**, *113*, 15882–15890.
- (89) Khataee, A.; Khataee, A.; Fathinia, M.; Hanifehpour, Y.; Joo, S. W. Kinetics and Mechanism of Enhanced Photocatalytic Activity under Visible Light Using Synthesized Pr_xCd_{1-x}Se Nanoparticles. *Ind. Eng. Chem. Res.* **2013**, *52*, 13357–13369.
- (90) Chiou, C.-H.; Juang, R.-S. Photocatalytic Degradation of Phenol in Aqueous Solutions by Pr-Doped TiO₂ Nanoparticles. *J. Hazard. Mater.* **2007**, *149*, 1–7.
- (91) Yu, X. F.; Chen, L. D.; Li, M.; Xie, M. Y.; Zhou, L.; Li, Y.; Wang, Q. Q. Highly Efficient Fluorescence of NdF₃/SiO₂ Core/Shell Nanoparticles and the Applications for *In Vivo* NIR Detection. *Adv. Mater.* **2008**, *20*, 4118–4123.
- (92) Chen, G.; Ohulchanskyy, T. Y.; Liu, S.; Law, W.-C.; Wu, F.; Swihart, M. T.; Ågren, H.; Prasad, P. N. Core/Shell NaGdF₄:Nd³⁺/NaGdF₄ Nanocrystals with Efficient Near-Infrared to Near-Infrared Downconversion Photoluminescence for Bioimaging Applications. *ACS Nano* **2012**, *6*, 2969–2977.
- (93) Wei, W.; Chen, G.; Baev, A.; He, G. S.; Shao, W.; Damasco, J.; Prasad, P. N. Alleviating Luminescence Concentration Quenching in Upconversion Nanoparticles through Organic Dye Sensitization. *J. Am. Chem. Soc.* **2016**, *138*, 15130–15133.
- (94) Chen, D.; Yu, Y.; Huang, F.; Lin, H.; Huang, P.; Yang, A.; Wang, Z.; Wang, Y. Lanthanide Dopant-Induced Formation of Uniform Sub-10 nm Active-Core/Active-Shell Nanocrystals with Near-Infrared to Near-Infrared Dual-Modal Luminescence. *J. Mater. Chem.* **2012**, *22*, 2632–2640.
- (95) Wang, Y.-F.; Liu, G.-Y.; Sun, L.-D.; Xiao, J.-W.; Zhou, J.-C.; Yan, C.-H. Nd³⁺-Sensitized Upconversion Nanophosphors: Efficient *In Vivo* Bioimaging Probes with Minimized Heating Effect. *ACS Nano* **2013**, *7*, 7200–7206.
- (96) Zhong, Y.; Tian, G.; Gu, Z.; Yang, Y.; Gu, L.; Zhao, Y.; Ma, Y.; Yao, J. Elimination of Photon Quenching by a Transition Layer to Fabricate a Quenching-Shield Sandwich Structure for 800 nm Excited Upconversion Luminescence of Nd³⁺-Sensitized Nanoparticles. *Adv. Mater.* **2014**, *26*, 2831–2837.
- (97) Zhu, Q.; Sun, T.; Chung, M. N.; Sun, X.; Xiao, Y.; Qiao, X.; Wang, F. Yb³⁺-Sensitized Upconversion and Downshifting Luminescence in Nd³⁺ Ions Through Energy Migration. *Dalton T.* **2018**, *47*, 8581–8584.
- (98) Gutfleisch, O.; Willard, M. A.; Brück, E.; Chen, C. H.; Sankar, S. G.; Liu, J. P. Magnetic Materials and Devices for the 21st Century: Stronger, Lighter, and More Energy Efficient. *Adv. Mater.* **2011**, *23*, 821–842.
- (99) Deheri, P. K.; Swaminathan, V.; Bhame, S. D.; Liu, Z.; Ramanujan, R. V. Sol–Gel Based Chemical Synthesis of Nd₂Fe₁₄B Hard Magnetic Nanoparticles. *Chem. Mater.* **2010**, *22*, 6509–6517.
- (100) Poudyal, N.; Ping Liu, J. Advances in Nanostructured Permanent Magnets Research. *J. Phys. D: Appl. Phys.* **2013**, *46*, 043001.
- (101) Du, J.; Chen, H.; Yang, H.; Sang, R.; Qian, Y.; Li, Y.; Zhu, G.; Mao, Y.; He, W.; Kang, D. J. A Facile Sol–Gel Method for Synthesis of Porous Nd-Doped TiO₂ Monolith with Enhanced Photocatalytic Activity under UV–Vis Irradiation. *Microporous Mesoporous Mater.* **2013**, *182*, 87–94.
- (102) Yayapao, O.; Thongtem, T.; Phuruangrat, A.; Thongtem, S. Ultrasonic-Assisted Synthesis of Nd-Doped ZnO for Photocatalysis. *Mater. Lett.* **2013**, *90*, 83–86.
- (103) Hwang, D. W.; Lee, J. S.; Li, W.; Oh, S. H. Electronic Band Structure and Photocatalytic Activity of Ln₂Ti₂O₇ (Ln = La, Pr, Nd). *J. Phys. Chem. B* **2003**, *107*, 4963–4970.
- (104) Du, J.; Wang, Z.; Zhao, G.; Qian, Y.; Chen, H.; Yang, J.; Liu, X.; Li, K.; He, C.; Du, W.; et al. Facile Synthesis and Enhanced Photocatalytic Activity of Porous Sn/Nd-codoped TiO₂ Monoliths. *Microporous Mesoporous Mater.* **2014**, *195*, 167–173.
- (105) Álvarez-Rodríguez, J.; Rodríguez-Ramos, I.; Guerrero-Ruiz, A.; Arcoya, A. Selective Hydrogenation of Citral Over Pt/KL Type Catalysts Doped With Sr, La, Nd and Sm. *Appl. Catal., A* **2011**, *401*, 56–64.
- (106) Kim, S. H.; Choi, J.; Yun, J.; Jeong, E.-w. Bimodal NdNiAl and NdFeB Hybrid Catalytic and Magnetic Nanoparticles Laminated on Fe Foam: Catalytic Conversion of CO + 3H₂ to CH₄. *RSC Adv.* **2017**, *7*, 16709–16720.
- (107) Sureshkumar, D.; Hashimoto, K.; Kumagai, N.; Shibasaki, M. A Modified Preparation Procedure for Carbon Nanotube-Confined Nd/Na Heterobimetallic Catalyst for Anti-Selective Catalytic Asymmetric Nitroaldol Reactions. *J. Org. Chem.* **2013**, *78*, 11494–11500.
- (108) Ogawa, T.; Kumagai, N.; Shibasaki, M. Self-Assembling Neodymium/Sodium Heterobimetallic Asymmetric Catalyst Confined in a Carbon Nanotube Network. *Angew. Chem., Int. Ed.* **2013**, *52* (24), 6196–6201.
- (109) Hou, Z.; Yang, P.; Li, C.; Wang, L.; Lian, H.; Quan, Z.; Lin, J. Preparation and Luminescence Properties of YVO₄:Ln and Y(V,P)O₄:Ln (Ln = Eu³⁺, Sm³⁺, Dy³⁺) Nanofibers and Microbelts by Sol–Gel/Electrospinning Process. *Chem. Mater.* **2008**, *20* (21), 6686–6696.
- (110) Huang, X. Realizing Efficient Upconversion and Downshifting Dual-mode Luminescence in Lanthanide-doped NaGdF₄ Core–shell–shell Nanoparticles Through Gadolinium Sublattice-mediated Energy Migration. *Dyes Pigm.* **2016**, *130*, 99–105.
- (111) Chang, M.; Song, Y.; Chen, J.; Zhang, X.; Meng, D.; Zhu, H.; Shi, Z.; Zou, H.; Sheng, Y. Multisite Luminescence and Photocatalytic Properties of TiO₂:Sm³⁺ and TiO₂:Sm³⁺@TiO₂/TiO₂:Sm³⁺@SiO₂ Luminescent Enhancement Materials. *J. Alloys Compd.* **2017**, *725*, 724–738.
- (112) Poornaprakash, B.; Poojitha, P. T.; Chalapathi, U.; Subramanyam, K.; Park, S.-H. Synthesis, Structural, Optical, and Magnetic Properties of Co Doped, Sm Doped and Co+Sm Co-doped ZnS Nanoparticles. *Phys. E* **2016**, *83*, 180–185.
- (113) Wang, Y.; Li, Y.; Rong, C.; Liu, J. P. Sm–Co Hard Magnetic Nanoparticles Prepared by Surfactant-assisted Ball Milling. *Nanotechnology* **2007**, *18* (46), 465701.
- (114) Rashmi, S. K.; Naik, H. S. B.; Jayadevappa, H.; Sudhamani, C. N.; Patil, S. B.; Naik, M. M. Influence of Sm³⁺ Ions on Structural, Optical and Solar Light Driven Photocatalytic Activity of Spinel MnFe₂O₄ Nanoparticles. *J. Solid State Chem.* **2017**, *255*, 178–192.
- (115) Rashmi, S. K.; Bhojya Naik, H. S.; Jayadevappa, H.; Viswanath, R.; Patil, S. B.; Madhukara Naik, M. Solar Light Responsive Sm-Zn Ferrite Nanoparticle as Efficient Photocatalyst. *Mater. Sci. Eng., B* **2017**, *225*, 86–97.
- (116) Hu, Z.; Chen, D.; Wang, S.; Zhang, N.; Qin, L.; Huang, Y. Facile Synthesis of Sm-doped BiFeO₃ Nanoparticles for Enhanced Visible Light Photocatalytic Performance. *Mater. Sci. Eng., B* **2017**, *220*, 1–12.
- (117) Wang, X.; Jiang, H.; Liu, Y.; Gao, M. Rapid Microwave-assisted Hydrothermal Synthesis of Sm, N, and P Tridoped Anatase-TiO₂ Nanosheets From TiCl₄ Hydrolysis. *Mater. Lett.* **2015**, *147*, 72–74.
- (118) Jianfeng, H.; Dan, W.; Lixiong, Y.; Liyun, C.; Haibo, O.; Jiayin, L.; Wei, H. Influence of DETA on the Structure and Photocatalytic Activity of Sm(OH)₃ Nanocrystallites Prepared by Hydrothermal Process. *J. Alloys Compd.* **2014**, *612*, 233–238.

- (119) Back, M.; Marin, R.; Franceschin, M.; Sfar Hancha, N.; Enrichi, F.; Trave, E.; Polizzi, S. Energy Transfer in Color-tunable Water-dispersible Tb-Eu Codoped CaF₂ Nanocrystals. *J. Mater. Chem. C* **2016**, *4*, 1906–1913.
- (120) Liu, Y.; Tu, D.; Zhu, H.; Li, R.; Luo, W.; Chen, X. A Strategy to Achieve Efficient Dual-Mode Luminescence of Eu³⁺ in Lanthanides Doped Multifunctional NaGdF₄ Nanocrystals. *Adv. Mater.* **2010**, *22*, 3266–3271.
- (121) Zafar, A.; ur Rahman, A.; Shahzada, S.; Anwar, S.; Khan, M.; Nisar, A.; Ahmad, M.; Karim, S. Electrical and Magnetic Properties of Nano-sized Eu Doped Barium Hexaferrites. *J. Alloys Compd.* **2017**, *727*, 683–690.
- (122) Gu, H.; Yu, L.; Wang, J.; Ni, M.; Liu, T.; Chen, F. Tunable Luminescence and Enhanced Photocatalytic Activity for Eu(III) Doped Bi₂WO₆ Nanoparticles. *Spectrochim. Acta, Part A* **2017**, *177*, 58–62.
- (123) Trandafilović, L. V.; Jovanović, D. J.; Zhang, X.; Ptasinska, S.; Dramićanin, M. D. Enhanced Photocatalytic Degradation of Methylene Blue and Methyl Orange by ZnO:Eu Nanoparticles. *Appl. Catal., B* **2017**, *203*, 740–752.
- (124) Phuruangrat, A.; Cheed-Im, U.; Thongtem, T.; Thongtem, S. High Visible Light Photocatalytic Activity of Eu-doped MoO₃ Nanobelts Synthesized by Hydrothermal Method. *Mater. Lett.* **2016**, *172*, 166–170.
- (125) Shiraishi, Y.; Takeshita, S.; Isobe, T. Two Photoenergy Conversion Modes of YVO₄:Eu³⁺ Nanoparticles: Photoluminescence and Photocatalytic Activity. *J. Phys. Chem. C* **2015**, *119*, 13502–13508.
- (126) Sarkar, A.; Ghosh, A. B.; Saha, N.; Dutta, A. K.; Srivastava, D. N.; Paul, P.; Adhikary, B. Enhanced Photocatalytic Activity of Eu-doped Bi₂S₃ Nanoflowers for Degradation of Organic Pollutants Under Visible Light Illumination. *Catal. Sci. Technol.* **2015**, *5*, 4055–4063.
- (127) Zhang, C.; Uchikoshi, T.; Li, J.-G.; Watanabe, T.; Ishigaki, T. Photocatalytic Activities of Europium (III) and Niobium (V) Codoped TiO₂ Nanopowders Synthesized in Ar/O₂ Radio-frequency Thermal Plasmas. *J. Alloys Compd.* **2014**, *606*, 37–43.
- (128) Dorenbos, P. Energy of the First 4f⁷→4f⁶5d Transition of Eu²⁺ in Inorganic Compounds. *J. Lumin.* **2003**, *104*, 239–260.
- (129) Peng, T.; Yang, H.; Pu, X.; Hu, B.; Jiang, Z.; Yan, C. Combustion Synthesis and Photoluminescence of SrAl₂O₄:Eu,Dy Phosphor Nanoparticles. *Mater. Lett.* **2004**, *58*, 352–356.
- (130) Kshatri, D. S.; Khare, A. Comparative Study of Optical and Structural Properties of Micro- and Nanocrystalline SrAl₂O₄:Eu²⁺, Dy³⁺ Phosphors. *J. Lumin.* **2014**, *155*, 257–268.
- (131) Rodríguez Burbano, D. C.; Rodríguez, E. M.; Dorenbos, P.; Bettinelli, M.; Capobianco, J. A. The Near-IR Photo-stimulated Luminescence of CaS:Eu²⁺/Dy³⁺ Nanophosphors. *J. Mater. Chem. C* **2014**, *2*, 228–231.
- (132) Pan, Y.; Xie, X.; Huang, Q.; Gao, C.; Wang, Y.; Wang, L.; Yang, B.; Su, H.; Huang, L.; Huang, W. Inherently Eu²⁺/Eu³⁺ Codoped Sc₂O₃ Nanoparticles as High-Performance Nanothermometers. *Adv. Mater.* **2018**, *30*, 1705256.
- (133) Du, J.; Poelman, D. Red-Light-Activated Red-Emitting Persistent Luminescence for Multicycle Bioimaging: A Case Study of CaS:Eu²⁺,Dy³⁺. *J. Phys. Chem. C* **2020**, *124*, 16586–16595.
- (134) Li, Z.; Huang, L.; Zhang, Y.; Zhao, Y.; Yang, H.; Han, G. Near-infrared Light Activated Persistent Luminescence Nanoparticles via Upconversion. *Nano Res.* **2017**, *10*, 1840–1846.
- (135) Tu, L.; Liu, X.; Wu, F.; Zhang, H. Excitation Energy Migration Dynamics in Upconversion Nanomaterials. *Chem. Soc. Rev.* **2015**, *44*, 1331–1345.
- (136) Cao, C.; Qin, W.; Zhang, J.; Wang, Y.; Zhu, P.; Wei, G.; Wang, G.; Kim, R.; Wang, L. Ultraviolet Upconversion Emissions of Gd³⁺. *Opt. Lett.* **2008**, *33*, 857–859.
- (137) Qin, W.; Cao, C.; Wang, L.; Zhang, J.; Zhang, D.; Zheng, K.; Wang, Y.; Wei, G.; Wang, G.; Zhu, P.; et al. Ultraviolet Upconversion Fluorescence From ⁶D₁ of Gd³⁺ Induced by 980 nm Excitation. *Opt. Lett.* **2008**, *33*, 2167–2169.
- (138) Zhang, Y.; Das, G. K.; Vijayaragavan, V.; Xu, Q. C.; Padmanabhan, P.; Bhakoo, K. K.; Tamil Selvan, S.; Tan, T. T. Y. "Smart" Theranostic Lanthanide Nanoprobes With Simultaneous Upconversion Fluorescence and Tunable T₁-T₂ Magnetic Resonance Imaging Contrast and Near-infrared Activated Photodynamic Therapy. *Nanoscale* **2014**, *6*, 12609–12617.
- (139) Li, J.; You, J.; Dai, Y.; Shi, M.; Han, C.; Xu, K. Gadolinium Oxide Nanoparticles and Aptamer-Functionalized Silver Nanoclusters-Based Multimodal Molecular Imaging Nanoprobe for Optical/Magnetic Resonance Cancer Cell Imaging. *Anal. Chem.* **2014**, *86*, 11306–11311.
- (140) Evanics, F.; Diamente, P. R.; van Veggel, F. C. J. M.; Stanisz, G. J.; Prosser, R. S. Water-Soluble GdF₃ and GdF₃/LaF₃ Nanoparticles Physical Characterization and NMR Relaxation Properties. *Chem. Mater.* **2006**, *18*, 2499–2505.
- (141) Hifumi, H.; Yamaoka, S.; Tanimoto, A.; Akatsu, T.; Shindo, Y.; Honda, A.; Citterio, D.; Oka, K.; Kuribayashi, S.; Suzuki, K. Dextran Coated Gadolinium Phosphate Nanoparticles for Magnetic Resonance Tumor Imaging. *J. Mater. Chem.* **2009**, *19*, 6393–6399.
- (142) Bridot, J.-L.; Faure, A.-C.; Laurent, S.; Rivière, C.; Billotey, C.; Hiba, B.; Janier, M.; Jossierand, V.; Coll, J.-L.; Vander Elst, L.; et al. Hybrid Gadolinium Oxide Nanoparticles: Multimodal Contrast Agents for *In Vivo* Imaging. *J. Am. Chem. Soc.* **2007**, *129*, 5076–5084.
- (143) Ruan, M. Y.; Ouyang, Z. W.; Wang, Z. X.; Xia, Z. C.; Rao, G. H. Magnetization, ESR, and Giant Magnetocaloric Effects in Nanocrystals of Haldane-chain Compound Gd₂BaNiO₅. *Appl. Phys. Lett.* **2017**, *111*, 122403.
- (144) Yang, D.; Li, G.; Kang, X.; Cheng, Z.; Ma, P. a.; Peng, C.; Lian, H.; Li, C.; Lin, J. Room Temperature Synthesis of Hydrophilic Ln³⁺-doped KGdF₄ (Ln = Ce, Eu, Tb, Dy) Nanoparticles With Controllable Size: Energy Transfer, Size-dependent and Color-tunable Luminescence Properties. *Nanoscale* **2012**, *4*, 3450–3459.
- (145) Zhao, D.; Guo, X.; Wang, L.; Zheng, Y.; Yang, Q. Amine-Assisted Synthesis and Characterization of Lanthanide Hydroxide Nanorods and Derived Oxides. *Nano LIFE* **2014**, *04*, 1441005.
- (146) Lu, D.; Fang, P.; Ding, J.; Yang, M.; Cao, Y.; Zhou, Y.; Peng, K.; Kondamareddy, K. K.; Liu, M. Two-dimensional TiO₂-based Nanosheets Co-modified by Surface-enriched Carbon Dots and Gd₂O₃ Nanoparticles for Efficient Visible-light-driven Photocatalysis. *Appl. Surf. Sci.* **2017**, *396*, 185–201.
- (147) Khataee, A.; Karimi, A.; Hasanzadeh, A.; Joo, S. W. Kinetic Modeling of Sonocatalytic Performance of Gd-doped CdSe Nanoparticles for Degradation of Acid Blue 5. *Ultrason. Sonochem.* **2017**, *39*, 344–353.
- (148) Li, H.; Li, W.; Wang, F.; Liu, X.; Ren, C.; Miao, X. Fabrication of Pt Nanoparticles Decorated Gd-doped Bi₂MoO₆ Nanosheets: Design, Radicals Regulating and Mechanism of Gd/Pt-Bi₂MoO₆ Photocatalyst. *Appl. Surf. Sci.* **2018**, *427*, 1046–1053.
- (149) Ullah, N.; Imran, M.; Liang, K.; Yuan, C.-Z.; Zeb, A.; Jiang, N.; Qazi, U. Y.; Sahar, S.; Xu, A.-W. Highly Dispersed Ultra-small Pd Nanoparticles on Gadolinium Hydroxide Nanorods for Efficient Hydrogenation Reactions. *Nanoscale* **2017**, *9*, 13800–13807.
- (150) Padhi, D. k.; Pradhan, G. K.; Parida, K. M.; Singh, S. K. Facile Fabrication of Gd(OH)₃ Nanorod/RGO Composite: Synthesis, Characterisation and Photocatalytic Reduction of Cr(VI). *Chem. Eng. J.* **2014**, *255*, 78–88.
- (151) Kim, S.; Park, G.; Kim, S. K.; Kim, Y. T.; Jun, K.-W.; Kwak, G. Gd/HZSM-5 Catalyst for Conversion of Methanol to Hydrocarbons: Effects of Amounts of the Gd Loading and Catalyst Preparation Method. *Appl. Catal., B* **2018**, *220*, 191–201.
- (152) Kim, S.; Kim Yong, T.; Hwang, A.; Jun, K. W.; Kwak, G. Coke-Tolerant Gadolinium-Promoted HZSM-5 Catalyst for Methanol Conversion Into Hydrocarbons. *Chem. Catal. Chem.* **2017**, *9*, 1569–1573.
- (153) Sarkar, B.; Goyal, R.; Pendem, C.; Sasaki, T.; Bal, R. Highly Nanodispersed Gd-doped Ni/ZSM-5 Catalyst for Enhanced Carbon-resistant Dry Reforming of Methane. *J. Mol. Catal. A: Chem.* **2016**, *424*, 17–26.

- (154) Singh, M.; Weerathunge, P.; Liyanage, P. D.; Mayes, E.; Ramanathan, R.; Bansal, V. Competitive Inhibition of the Enzyme-Mimic Activity of Gd-Based Nanorods Toward Highly Specific Colorimetric Sensing of L-Cysteine. *Langmuir* **2017**, *33*, 10006–10015.
- (155) Behnamfar, M. T.; Hadadzadeh, H.; Akbarnejad, E.; Allafchian, A. R.; Assefi, M.; Khedri, N. Electrocatalytic Reduction of CO₂ to CO by Gd(III) and Dy(III) Complexes; and M₂O₃ Nanoparticles (M = Gd and Dy). *J. CO₂ Util.* **2016**, *13*, 61–70.
- (156) Xue, M.; Zhu, X.; Qiu, X.; Gu, Y.; Feng, W.; Li, F. Highly Enhanced Cooperative Upconversion Luminescence Through Energy Transfer Optimization and Quenching Protection. *ACS Appl. Mater. Interfaces* **2016**, *8*, 17894–17901.
- (157) Patzke, G. R.; Krumeich, F.; Nesper, R. Oxidic Nanotubes and Nanorods—Anisotropic Modules for a Future Nanotechnology. *Angew. Chem., Int. Ed.* **2002**, *41*, 2446–2461.
- (158) Kim, S. Y.; Jeong, J. S.; Mkhoyan, K. A.; Jang, H. S. Direct Observation of the Core/double-shell Architecture of Intense Dual-mode Luminescent Tetragonal Bipyramidal Nanophosphors. *Nanoscale* **2016**, *8*, 10049–10058.
- (159) Zhang, Q. Y.; Yang, C. H.; Pan, Y. X. Cooperative Quantum Cutting in One-dimensional (Yb₃Gd_{1-x})Al₃(BO₃)₄:Tb³⁺ Nanorods. *Appl. Phys. Lett.* **2007**, *90*, 021107.
- (160) Ramu, S.; Vijayalakshmi, R. P. Effect of Terbium Doping on the Structural and Magnetic Properties of ZnS Nanoparticles. *J. Supercond. Novel Magn.* **2017**, *30*, 1921–1925.
- (161) Li, G.-R.; Lu, X.-H.; Su, C.-Y.; Tong, Y.-X. Facile Synthesis of Hierarchical ZnO:Tb³⁺ Nanorod Bundles and Their Optical and Magnetic Properties. *J. Phys. Chem. C* **2008**, *112*, 2927–2933.
- (162) Lotey, G. S.; Singh, J.; Verma, N. K. Room Temperature Ferromagnetism in Tb-doped ZnO Dilute Magnetic Semiconducting Nanoparticles. *J. Mater. Sci.: Mater. El.* **2013**, *24*, 3611–3616.
- (163) Lotey, G. S.; Verma, N. K. Magnetolectric Coupling in Multiferroic Tb-doped BiFeO₃ Nanoparticles. *Mater. Lett.* **2013**, *111*, 55–58.
- (164) Hoque, S. M.; Hakim, M. A.; Khan, F. A.; Dan, N. H. Effect of Tb Substitution on the Magnetic Properties of Exchange-biased Nd₂Fe₁₄B/Fe₃B. *J. Mater. Sci.* **2007**, *42*, 9415–9420.
- (165) Qu, D.; Xie, F.; Meng, H.; Gong, L.; Zhang, W.; Chen, J.; Li, G.; Liu, P.; Tong, Y. Preparation and Characterization of Nanocrystalline CeO₂-Tb₂O₃ Films Obtained by Electrochemical Deposition Method. *J. Phys. Chem. C* **2010**, *114*, 1424–1429.
- (166) Wang, L.; Wang, Y.; Li, A.; Yang, Y.; Tang, Q.; Cao, H.; Qi, T.; Li, C. Electrocatalysis of Carbon Black- or Poly-(diallyldimethylammonium Chloride)-functionalized Activated Carbon Nanotubes-supported Pd–Tb Towards Methanol Oxidation in Alkaline Media. *J. Power Sources* **2014**, *257*, 138–146.
- (167) Nguyen, S. T.; Ling Tan, D. S.; Lee, J.-M.; Chan, S. H.; Wang, J. Y.; Wang, X. Tb Promoted Pd/C Catalysts for the Electrooxidation of Ethanol in Alkaline Media. *Int. J. Hydrogen Energy* **2011**, *36*, 9645–9652.
- (168) Ida, S.; Koga, S.; Daio, T.; Hagiwara, H.; Ishihara, T. Direct Imaging of Light Emission Centers in Two-Dimensional Crystals and Their Luminescence and Photocatalytic Properties. *Angew. Chem., Int. Ed.* **2014**, *53*, 13078–13082.
- (169) Vidya, Y. S.; Gurusantha, K.; Nagabhushana, H.; Sharma, S. C.; Anantharaju, K. S.; Shivakumara, C.; Suresh, D.; Nagaswarupa, H. P.; Prashantha, S. C.; Anilkumar, M. R. Phase Transformation of ZrO₂:Tb³⁺ Nanophosphor: Color Tunable Photoluminescence and Photocatalytic Activities. *J. Alloys Compd.* **2015**, *622*, 86–96.
- (170) Li, D.; Ma, Q.; Song, Y.; Xi, X.; Dong, X.; Yu, W.; Wang, J.; Liu, G. NaGdF₄:Dy³⁺ Nanofibers and Nanobelts: Facile Construction Technique, Structure and Bifunctionality of Luminescence and Enhanced Paramagnetic Performances. *Phys. Chem. Chem. Phys.* **2016**, *18*, 27536–27544.
- (171) Rodriguez Burbano, D. C.; Rodriguez, E. M.; Dorenbos, P.; Bettinelli, M.; Capobianco, J. A. The Near-IR Photo-stimulated Luminescence of CaS:Eu²⁺/Dy³⁺ Nanophosphors. *J. Mater. Chem. C* **2014**, *2*, 228–231.
- (172) Lü, W.; Zhou, H.; Chen, G.; Li, J.; Zhu, Z.; You, Z.; Tu, C. Photoluminescence Properties of Neat and Dy³⁺-Doped Gd₃Ga₅O₁₂ Nanocrystals. *J. Phys. Chem. C* **2009**, *113*, 3844–3849.
- (173) Poornaprakash, B.; Chalapathi, U.; Kumar, M.; Poojitha, P. T. Achieving Room Temperature Ferromagnetism in ZnO Nanoparticles via Dy Doping. *J. Mater. Sci.: Mater. Electron.* **2018**, *29*, 2316–2321.
- (174) Gonzalez-Mancebo, D.; Becerro, A. I.; Rojas, T. C.; Garcia-Martin, M. L.; de la Fuente, J. M.; Ocana, M. HoF₃ and DyF₃ Nanoparticles as Contrast Agents for High-Field Magnetic Resonance Imaging. *Part. Part. Syst. Char.* **2017**, *34*, 1700116.
- (175) Zhang, X.; Blasiak, B.; Marenco, A. J.; Trudel, S.; Tomanek, B.; van Veggel, F. C. J. M. Design and Regulation of NaHoF₄ and NaDyF₄ Nanoparticles for High-Field Magnetic Resonance Imaging. *Chem. Mater.* **2016**, *28*, 3060–3072.
- (176) Tegafaw, T.; Xu, W.; Ahmad, M. W.; Baeck, J. S.; Chang, Y.; Bae, J. E.; Chae, K. S.; Kim, T. J.; Lee, G. H. Dual-mode T₁ and T₂ Magnetic Resonance imaging Contrast Agent Based on Ultrasmall Mixed Gadolinium-dysprosium Oxide Nanoparticles: Synthesis, Characterization, and In Vivo Application. *Nanotechnology* **2015**, *26*, 365102.
- (177) Dumrongrojthanath, P.; Thongtem, T.; Phuruangrat, A.; Thongtem, S. Glycothermal Synthesis of Dy-doped Bi₂MoO₆ Nanoplates and Their Photocatalytic Performance. *Res. Chem. Intermed.* **2016**, *42*, 5087–5097.
- (178) Khataee, A.; Darvishi Cheshmeh Soltani, R.; Hanifehpour, Y.; Safarpour, M.; Gholipour Ranjbar, H.; Joo, S. W. Synthesis and Characterization of Dysprosium-Doped ZnO Nanoparticles for Photocatalysis of a Textile Dye Under Visible Light Irradiation. *Ind. Eng. Chem. Res.* **2014**, *53*, 1924–1932.
- (179) Yayapao, O.; Thongtem, T.; Phuruangrat, A.; Thongtem, S. Sonochemical Synthesis of Dy-doped ZnO Nanostructures and Their Photocatalytic Properties. *J. Alloys Compd.* **2013**, *576*, 72–79.
- (180) Ahmed, N.; Tarannum, S.; Siddiqui, Z. N. Dy/chitosan: a Highly Efficient and Recyclable Heterogeneous Nano Catalyst for the Synthesis of Hexahydropyrimidines in Aqueous Media. *RSC Adv.* **2015**, *5*, 50691–50700.
- (181) Kamimura, M.; Matsumoto, T.; Suyari, S.; Umezawa, M.; Soga, K. Ratiometric Near-infrared Fluorescence Nanothermometry in the OTN-NIR (NIR II/III) Biological Window Based on Rare-earth Doped Beta-NaYF₄ Nanoparticles. *J. Mater. Chem. B* **2017**, *5*, 1917–1925.
- (182) Feng, Y.; Xiao, Q.; Zhang, Y.; Li, F.; Li, Y.; Li, C.; Wang, Q.; Shi, L.; Lin, H. Neodymium-doped NaHoF₄ Nanoparticles as Near-infrared Luminescent/T₂-weighted MR Dual-modal Imaging Agents. *In Vivo. J. Mater. Chem. B* **2017**, *5*, 504–510.
- (183) Liu, X.; Fang, P.; Liu, Y.; Liu, Z.; Lu, D.; Gao, Y.; Chen, F.; Wang, D.; Dai, Y. Effect of Holmium Doping on the Structure and Photocatalytic Behavior of TiO₂-based Nanosheets. *J. Mater. Sci.* **2014**, *49*, 8063–8073.
- (184) Phuruangrat, A.; Yayapao, O.; Thongtem, T.; Thongtem, S. Preparation, Characterization and Photocatalytic Properties of Ho Doped ZnO Nanostructures Synthesized by Sonochemical Method. *Superlattices Microstruct.* **2014**, *67*, 118–126.
- (185) Xu, X.; Zhou, S.; Long, J.; Wu, T.; Fan, Z. The Synthesis of a Core-Shell Photocatalyst Material YF₃:Ho³⁺@TiO₂ and Investigation of Its Photocatalytic Properties. *Materials* **2017**, *10*, 302.
- (186) Yao, M.; Liu, B.; Zou, Y.; Wang, L.; Li, D.; Cui, T.; Zou, G.; Sundqvist, B. Synthesis of Single-wall Carbon Nanotubes and Long Nanotube Ribbons With Ho/Ni as Catalyst by arc Discharge. *Carbon* **2005**, *43*, 2894–2901.
- (187) Su, X.; Sun, X.; Wu, S.; Zhang, S. Manipulating the Emission Intensity and Lifetime of NaYF₄:Yb³⁺,Er³⁺ Simultaneously by Embedding it Into CdS Photonic Crystals. *Nanoscale* **2017**, *9*, 7666–7673.
- (188) Moran, C. E.; Hale, G. D.; Halas, N. J. Synthesis and Characterization of Lanthanide-Doped Silica Microspheres. *Langmuir* **2001**, *17*, 8376–8379.
- (189) Liu, L.; Wang, S.; Zhao, B.; Pei, P.; Fan, Y.; Li, X.; Zhang, F. Er³⁺ Sensitized 1530 to 1180 nm Second Near-Infrared Window

Upconversion Nanocrystals for *In Vivo* Biosensing. *Angew. Chem., Int. Ed.* **2018**, *57*, 7518–7522.

(190) Zhou, B.; Yan, L.; Huang, J.; Liu, X.; Tao, L.; Zhang, Q. NIR II-responsive Photon Upconversion Through Energy Migration in an Ytterbium Sublattice. *Nat. Photonics* **2020**, *14*, 760–766.

(191) Chen, Q.; Xie, X.; Huang, B.; Liang, L.; Han, S.; Yi, Z.; Wang, Y.; Li, Y.; Fan, D.; Huang, L.; et al. Confining Excitation Energy in Er³⁺-Sensitized Upconversion Nanocrystals Through Tm³⁺-Mediated Transient Energy Trapping. *Angew. Chem., Int. Ed.* **2017**, *56*, 7605–7609.

(192) Yao, B.; Wang, P.; Wang, S.; Zhang, M. Ce Doping Influence on the Magnetic Phase Transition in In₂S₃:Ce Nanoparticles. *CrystEngComm* **2014**, *16*, 2584–2588.

(193) Sharma, D. K.; Sharma, K. K.; Kumar, V.; Sharma, A. Synthesis of Er Doped ZnO Cone-like Nanostructures With Enhanced Structural, Optical and Magnetic Properties. *J. Mater. Sci.: Mater. Electron.* **2018**, *29*, 3840–3849.

(194) Wang, H.; Yi, Z.; Rao, L.; Liu, H.; Zeng, S. High Quality Multi-functional NaErF₄ Nanocrystals: Structure-controlled Synthesis, Phase-induced Multi-color Emissions and Tunable Magnetic Properties. *J. Mater. Chem. C* **2013**, *1*, 5520–5526.

(195) Zhou, H. F.; Hou, Z. L.; Kong, L. B.; Jin, H. B.; Cao, M. S.; Qi, X. Enhanced Magnetization and Improved Leakage in Er-doped BiFeO₃ Nanoparticles. *Phys. Status Solidi A* **2013**, *210*, 809–813.

(196) Prakash, N.; Karthikeyan, R.; Thangaraju, D.; Navaneethan, M.; Arivanandhan, M.; Koyama, T.; Hayakawa, Y. Effect of Erbium on the Photocatalytic Activity of TiO₂/Ag Nanocomposites Under Visible Light Irradiation. *ChemPhysChem* **2015**, *16*, 3084–3092.

(197) Lemos, S. C. S.; Romeiro, F. C.; de Paula, L. F.; Gonçalves, R. F.; de Moura, A. P.; Ferrer, M. M.; Longo, E.; Patrocínio, A. O. T.; Lima, R. C. Effect of Er³⁺ Ions on the Phase Formation and Properties of In₂O₃ Nanostructures Crystallized Upon Microwave Heating. *J. Solid State Chem.* **2017**, *249*, 58–63.

(198) Zhang, W.; Yu, N.; Zhang, L.; Jiang, K.; Chen, Y.; Chen, Z. Synthesis of Yb³⁺/Er³⁺ Co-doped Bi₂WO₆ Nanosheets With Enhanced Photocatalytic Activity. *Mater. Lett.* **2016**, *163*, 16–19.

(199) Zhang, X.; Dong, S.; Zhou, X.; Yan, L.; Chen, G.; Dong, S.; Zhou, D. A Facile One-pot Synthesis of Er–Al Co-doped ZnO Nanoparticles With Enhanced Photocatalytic Performance Under Visible Light. *Mater. Lett.* **2015**, *143*, 312–314.

(200) Khataee, A.; Arefi-Oskoui, S.; Fathinia, M.; Esmaeili, A.; Hanifehpour, Y.; Joo, S. W.; Hammabard, N. Synthesis, Characterization and Photocatalytic Properties of Er-doped PbSe Nanoparticles as a Visible Light-activated Photocatalyst. *J. Mol. Catal. A: Chem.* **2015**, *398*, 255–267.

(201) Tong, Y.; Cao, F.; Yang, J.; Xu, M.; Zheng, C.; Zhu, X.; Chen, D.; Zhang, M.; Huang, F.; Zhou, J.; et al. Urchinlike Pristine and Er-doped ZnS Hierarchical Nanostructures: Controllable Synthesis, Photoluminescence and Enhanced Photocatalytic Performance. *Mater. Chem. Phys.* **2015**, *151*, 357–363.

(202) Kim, M.-J.; Choi, Y. I.; Joo, S. W.; Kang, M.; Sohn, Y. Synthesis of Er and Yb-doped Cubic and Hexagonal Phase ZnSe Nano-assembled Microspheres and Their Photocatalytic Activities. *Ceram. Int.* **2014**, *40*, 16051–16059.

(203) Adhikari, R.; Gyawali, G.; Cho, S. H.; Narro-García, R.; Sekino, T.; Lee, S. W. Er³⁺/Yb³⁺ co-doped Bismuth Molybdate Nanosheets Upconversion Photocatalyst With Enhanced Photocatalytic Activity. *J. Solid State Chem.* **2014**, *209*, 74–81.

(204) Tang, J.; Song, H.; Zeng, B.; Zhang, L.; Lv, Y. Cataluminescence Gas Sensor for Ketones Based on Nanosized NaYF₄:Er. *Sens. Actuators, B* **2016**, *222*, 300–306.

(205) Malkhasian, A. Y. S.; Mohamed, R. M. Environmental Remediation of Cr(VI) Solutions by Photocatalytic Reduction Using Ag–Er(OH)₃ Nanocomposite. *J. Alloys Compd.* **2015**, *632*, 735–740.

(206) Li, L.; Yang, Y.; Fan, R.; Chen, S.; Wang, P.; Yang, B.; Cao, W. Conductive Upconversion Er,Yb-FTO Nanoparticle Coating To Replace Pt as a Low-Cost and High-Performance Counter Electrode for Dye-Sensitized Solar Cells. *ACS Appl. Mater. Interfaces* **2014**, *6*, 8223–8229.

(207) Sato, F.; Yamada, Y.; Sato, S. Preparation of Er₂O₃ Nanorod Catalyst Without Using Organic Additive and Its Application to Catalytic Dehydration of 1,4-Butanediol. *Chem. Lett.* **2012**, *41*, 593–594.

(208) Sekhar, P. K.; Wilkinson, A. R.; Elliman, R. G.; Kim, T. H.; Bhansali, S. Erbium Emission From Nanoengineered Silicon Surface. *J. Phys. Chem. C* **2008**, *112*, 20109–20113.

(209) Hazra, C.; Ullah, S.; Serge Correales, Y. E.; Caetano, L. G.; Ribeiro, S. J. L. Enhanced NIR-I Emission From Water-dispersible NIR-II Dye-sensitized Core/active Shell Upconverting Nanoparticles. *J. Mater. Chem. C* **2018**, *6*, 4777–4785.

(210) Yin, A.; Zhang, Y.; Sun, L.; Yan, C. Colloidal Synthesis and Blue Based Multicolor Upconversion Emissions of Size and Composition Controlled Monodisperse Hexagonal NaYF₄: Yb, Tm Nanocrystals. *Nanoscale* **2010**, *2*, 953–959.

(211) Thakuria, P.; Joy, P. A. High Room Temperature Ferromagnetic Moment of Ho Substituted Nanocrystalline BiFeO₃. *Appl. Phys. Lett.* **2010**, *97*, 162504.

(212) Su, W.; Zheng, M.; Li, L.; Wang, K.; Qiao, R.; Zhong, Y.; Hu, Y.; Li, Z. Directly Coat TiO₂ on Hydrophobic NaYF₄:Yb, Tm Nanoplates and Regulate Their Photocatalytic Activities With the Core Size. *J. Mater. Chem. A* **2014**, *2*, 13486–13491.

(213) Ma, Y.; Liu, H.; Han, Z.; Yang, L.; Liu, J. Non-ultraviolet Photocatalytic Kinetics of NaYF₄:Yb, Tm@TiO₂/Ag Core@comby Shell Nanostructures. *J. Mater. Chem. A* **2015**, *3*, 14642–14650.

(214) Ye, Q.-L.; Yang, X.; Li, C.; Li, Z. Synthesis of UV/NIR Photocatalysts by Coating TiO₂ Shell on Peanut-like YF₃:Yb, Tm Upconversion Nanocrystals. *Mater. Lett.* **2013**, *106*, 238–241.

(215) Wang, C.; Song, K.; Feng, Y.; Yin, D.; Ouyang, J.; Liu, B.; Cao, X.; Zhang, L.; Han, Y.; Wu, M. Preparation of NaLuF₄:Gd, Yb, Tm-TiO₂ Nanocomposite With High Catalytic activity for Solar Light Assisted Photocatalytic Degradation of Dyes and Wastewater. *RSC Adv.* **2014**, *4*, 39118–39125.

(216) Yin, D.; Zhang, L.; Cao, X.; Chen, Z.; Tang, J.; Liu, Y.; Zhang, T.; Wu, M. Preparation of a Novel Nanocomposite NaLuF₄:Gd, Yb, Tm@SiO₂@Ag@TiO₂ With High Photocatalytic Activity Driven by Simulated Solar Light. *Dalton T.* **2016**, *45*, 1467–1475.

(217) Ganguli, S.; Hazra, C.; Chatti, M.; Samanta, T.; Mahalingam, V. A Highly Efficient UV–Vis–NIR Active Ln³⁺-Doped BiPO₄/BiVO₄ Nanocomposite for Photocatalysis Application. *Langmuir* **2016**, *32*, 247–253.

(218) Cheng, E.; Yin, W.; Bai, S.; Qiao, R.; Zhong, Y.; Li, Z. Synthesis of VIS/NIR-driven Hybrid Photocatalysts by Electrostatic Assembly of NaYF₄:Yb, Tm Nanocrystals on g-C₃N₄ Nanosheets. *Mater. Lett.* **2015**, *146*, 87–90.

(219) Tang, Y.; Di, W.; Zhai, X.; Yang, R.; Qin, W. NIR-Responsive Photocatalytic Activity and Mechanism of NaYF₄:Yb, Tm@TiO₂ Core–Shell Nanoparticles. *ACS Catal.* **2013**, *3*, 405–412.

(220) Lv, Y.; Yue, L.; Li, Q.; Shao, B.; Zhao, S.; Wang, H.; Wu, S.; Wang, Z. Recyclable (Fe₃O₄-NaYF₄:Yb, Tm)@TiO₂ Nanocomposites With Near-infrared Enhanced Photocatalytic Activity. *Dalton T.* **2018**, *47*, 1666–1673.

(221) Cheng, E.; Zhou, S.; Li, M.; Li, Z. Synthesis of g-C₃N₄-based NaYF₄:Yb, Tm@TiO₂ Ternary Composite With Enhanced Vis/NIR-driven Photocatalytic activities. *Appl. Surf. Sci.* **2017**, *410*, 383–392.

(222) Stouwdam, J. W.; Hebbink, G. A.; Huskens, J.; van Veggel, F. C. J. M. Lanthanide-Doped Nanoparticles With Excellent Luminescent Properties in Organic Media. *Chem. Mater.* **2003**, *15*, 4604–4616.

(223) Zhang, Q. Y.; Yang, G. F.; Jiang, Z. H. Cooperative Downconversion in GdAl₃(BO₃)₄:RE³⁺, Yb³⁺ (RE = Pr, Tb, and Tm). *Appl. Phys. Lett.* **2007**, *91*, 051903.

(224) Chen, X.; Zhu, Y.; Zhou, D.; Xu, W.; Zhu, J.; Pan, G.; Yin, Z.; Wang, H.; Cui, S.; Song, H. Size-dependent Downconversion Near-infrared Emission of NaYF₄:Yb³⁺, Er³⁺ Nanoparticles. *J. Mater. Chem. C* **2017**, *5*, 2451–2458.

(225) Ni, D.; Bu, W.; Zhang, S.; Zheng, X.; Li, M.; Xing, H.; Xiao, Q.; Liu, Y.; Hua, Y.; Zhou, L.; et al. Single Ho³⁺-Doped Upconversion Nanoparticles for High-Performance T₂-Weighted Brain Tumor

- Diagnosis and MR/UCL/CT Multimodal Imaging. *Adv. Funct. Mater.* **2014**, *24*, 6613–6620.
- (226) Shannon, R. D.; Prewitt, C. T. Effective Ionic Radii in Oxides and Fluorides. *Acta Crystallogr., Sect. B: Struct. Crystallogr. Cryst. Chem.* **1969**, *25*, 925–946.
- (227) Riwozki, K.; Meysamy, H.; Schnablegger, H.; Kornowski, A.; Haase, M. Liquid-Phase Synthesis of Colloids and Redispersible Powders of Strongly Luminescing LaPO₄:Ce,Tb Nanocrystals. *Angew. Chem., Int. Ed.* **2001**, *40*, 573–576.
- (228) Wang, F.; Deng, R.; Wang, J.; Wang, Q.; Han, Y.; Zhu, H.; Chen, X.; Liu, X. Tuning Upconversion Through Energy Migration in Core-shell Nanoparticles. *Nat. Mater.* **2011**, *10*, 968–973.
- (229) Wen, S.; Zhou, J.; Zheng, K.; Bednarkiewicz, A.; Liu, X.; Jin, D. Advances in Highly Doped Upconversion Nanoparticles. *Nat. Commun.* **2018**, *9*, 2415.
- (230) Wang, F.; Liu, X. Multicolor Tuning of Lanthanide-Doped Nanoparticles by Single Wavelength Excitation. *Acc. Chem. Res.* **2014**, *47*, 1378–1385.
- (231) Yi, Z.; Luo, Z.; Qin, X.; Chen, Q.; Liu, X. Lanthanide-Activated Nanoparticles: A Toolbox for Bioimaging, Therapeutics, and Neuromodulation. *Acc. Chem. Res.* **2020**, *53*, 2692–2704.
- (232) Dong, C.; Raudsepp, M.; van Veggel, F. C. J. M. Kinetically Determined Crystal Structures of Undoped and La³⁺-Doped LnF₃. *J. Phys. Chem. C* **2009**, *113*, 472–478.
- (233) Wang, F.; Han, Y.; Lim, C. S.; Lu, Y.; Wang, J.; Xu, J.; Chen, H.; Zhang, C.; Hong, M.; Liu, X. Simultaneous Phase and Size Control of Upconversion Nanocrystals Through Lanthanide Doping. *Nature* **2010**, *463*, 1061–1065.
- (234) Wang, T.; Yu, Y.; Ji, X.; Xu, W.; Fu, Y.; Cao, H.; He, Q.; Cheng, J. A New Method to Synthesize Sub-10 nm CaF₂:Nd³⁺ Nanoparticles and Fluorescent Enhancement via Li⁺ Ions or Ce³⁺ Ions Doping. *Dyes Pigm.* **2020**, *175*, 108129.
- (235) Yin, W.; Tian, G.; Ren, W.; Yan, L.; Jin, S.; Gu, Z.; Zhou, L.; Li, J.; Zhao, Y. Design of Multifunctional Alkali Ion Doped CaF₂ Upconversion Nanoparticles for Simultaneous Bioimaging and Therapy. *Dalton T.* **2014**, *43*, 3861–3870.
- (236) Wang, J.; Song, H.; Xu, W.; Dong, B.; Xu, S.; Chen, B.; Yu, W.; Zhang, S. Phase Transition, Size Control and Color Tuning of NaREF₄:Yb³⁺, Er³⁺ (RE = Y, Lu) Nanocrystals. *Nanoscale* **2013**, *5*, 3412–3420.
- (237) Xiang, G.; Zhang, J.; Hao, Z.; Zhang, X.; Pan, G.-H.; Luo, Y.; Zhao, H. Decrease in Particle Size and Enhancement of Upconversion Emission Through Y³⁺ Ions Doping in Hexagonal NaLuF₄:Yb³⁺/Er³⁺ Nanocrystals. *CrystEngComm* **2015**, *17*, 3103–3109.
- (238) Zeng, S.; Ren, G.; Xu, C.; Yang, Q. Modifying Crystal Phase, Shape, Size, Optical and Magnetic Properties of Monodispersed Multifunctional NaYbF₄ Nanocrystals Through Lanthanide Doping. *CrystEngComm* **2011**, *13*, 4276–4281.
- (239) Zhang, W.-H.; Wang, F.; Zhang, W.-D. Phase Transformation of Ultrathin Nanowires Through Lanthanide Doping: From InOOH to rh-In₂O₃. *Dalton T.* **2013**, *42*, 4361–4364.
- (240) Zhao, B.; Xie, X.; Xu, S.; Pan, Y.; Yang, B.; Guo, S.; Wei, T.; Su, H.; Wang, H.; Chen, X.; et al. From ScOOH to Sc₂O₃: Phase Control, Luminescent Properties, and Applications. *Adv. Mater.* **2016**, *28*, 6665–6671.
- (241) Chen, Y.; Yan, X.; Liu, Q.; Wang, X. Morphology and Upconversion Luminescence of NaYbF₄:Tm³⁺ Nanocrystals Modified by Gd³⁺ Ions. *J. Alloys Compd.* **2013**, *562*, 99–105.
- (242) Mukherjee, P.; Shade, C. M.; Yingling, A. M.; Lamont, D. N.; Waldeck, D. H.; Petoud, S. Lanthanide Sensitization in II–VI Semiconductor Materials: A Case Study With Terbium(III) and Europium(III) in Zinc Sulfide Nanoparticles. *J. Phys. Chem. A* **2011**, *115*, 4031–4041.
- (243) Planelles-Aragó, J.; Cordoncillo, E.; Ferreira, R. A. S.; Carlos, L. D.; Escribano, P. Synthesis, Characterization and Optical Studies on Lanthanide-doped CdS Quantum Dots: New Insights on CdS → Lanthanide Energy Transfer Mechanisms. *J. Mater. Chem.* **2011**, *21*, 1162–1170.
- (244) Martín-Rodríguez, R.; Geitenbeek, R.; Meijerink, A. Incorporation and Luminescence of Yb³⁺ in CdSe Nanocrystals. *J. Am. Chem. Soc.* **2013**, *135*, 13668–13671.
- (245) Fung, K. Z.; Chen, J.; Virkar, A. V. Effect of Aliovalent Dopants on the Kinetics of Phase Transformation and Ordering in RE₂O₃-Bi₂O₃ (RE = Yb, Er, Y, or Dy) Solid Solutions. *J. Am. Ceram. Soc.* **1993**, *76*, 2403–2418.
- (246) Cortelletti, P.; Pedroni, M.; Boschi, F.; Pin, S.; Ghigna, P.; Canton, P.; Vetrone, F.; Speghini, A. Luminescence of Eu³⁺ Activated CaF₂ and SrF₂ Nanoparticles: Effect of the Particle Size and Codoping With Alkaline Ions. *Cryst. Growth Des.* **2018**, *18*, 686–694.
- (247) Quintanilla, M.; Zhang, Y.; Liz-Marzán, L. M. Subtissue Plasmonic Heating Monitored With CaF₂:Nd³⁺,Y³⁺ Nanothermometers in the Second Biological Window. *Chem. Mater.* **2018**, *30*, 2819–2828.
- (248) Li, Z.; Liu, H.; Wang, R.; Ji, C.; Wei, Y.; Shi, M.; Wang, Y.; Du, Y.; Zhang, Y.; Yuan, Q.; et al. Bioactive Core-Shell CaF₂ Upconversion Nanostructure for Promotion and Visualization of Engineered Bone Reconstruction. *ACS Nano* **2020**, *14*, 16085–16095.
- (249) Wang, F.; Fan, X.; Pi, D.; Wang, M. Synthesis and Luminescence Behavior of Eu³⁺-doped CaF₂ Nanoparticles. *Solid State Commun.* **2005**, *133*, 775–779.
- (250) Misiak, M.; Skowicki, M.; Lipiński, T.; Kowalczyk, A.; Prorok, K.; Arabasz, S.; Bednarkiewicz, A. Biofunctionalized Upconverting CaF₂:Yb,Tm Nanoparticles for Candida Albicans Detection and Imaging. *Nano Res.* **2017**, *10*, 3333–3345.
- (251) Yao, J.-S.; Ge, J.; Han, B.-N.; Wang, K.-H.; Yao, H.-B.; Yu, H.-L.; Li, J.-H.; Zhu, B.-S.; Song, J.-Z.; Chen, C.; et al. Ce³⁺-Doping to Modulate Photoluminescence Kinetics for Efficient CsPbBr₃ Nanocrystals Based Light-Emitting Diodes. *J. Am. Chem. Soc.* **2018**, *140*, 3626–3634.
- (252) Miodyńska, M.; Mikolajczyk, A.; Bajorowicz, B.; Zwara, J.; Klimczuk, T.; Lisowski, W.; Trykowski, G.; Pinto, H. P.; Zaleska-Medynska, A. Urchin-like TiO₂ Structures Decorated With Lanthanide-doped Bi₂S₃ Quantum Dots to Boost Hydrogen Photogeneration Performance. *Appl. Catal., B* **2020**, *272*, 118962.
- (253) Wang, F.; Wang, J.; Liu, X. Direct Evidence of a Surface Quenching Effect on Size-Dependent Luminescence of Upconversion Nanoparticles. *Angew. Chem., Int. Ed.* **2010**, *49*, 7456–7460.
- (254) Yi, G.-S.; Chow, G.-M. Water-Soluble NaYF₄:Yb,Er(Tm)/NaYF₄/Polymer Core/Shell/Shell Nanoparticles With Significant Enhancement of Upconversion Fluorescence. *Chem. Mater.* **2007**, *19*, 341.
- (255) Zheng, L.; Cui, B.; Zhao, L.; Li, W.; Zhu, M.; Hadjipanayis, G. C. Core/shell SmCo₅/Sm₂O₃ Magnetic Composite Nanoparticles. *J. Nanopart. Res.* **2012**, *14*, 1129.
- (256) Tian, G.; Gu, Z.; Liu, X.; Zhou, L.; Yin, W.; Yan, L.; Jin, S.; Ren, W.; Xing, G.; Li, S.; et al. Facile Fabrication of Rare-Earth-Doped Gd₂O₃ Hollow Spheres With Upconversion Luminescence, Magnetic Resonance, and Drug Delivery Properties. *J. Phys. Chem. C* **2011**, *115*, 23790–23796.
- (257) Li, Z.; Tao, Y.; Huang, S.; Gao, N.; Ren, J.; Qu, X. Lanthanide-based Hollow Mesoporous Nanoparticles: a Novel Multifunctional Platform for Simultaneous Gene Delivery and Cell Imaging. *Chem. Commun.* **2013**, *49*, 7129–7131.
- (258) Yao, C.; Wang, W.; Wang, P.; Zhao, M.; Li, X.; Zhang, F. Near-Infrared Upconversion Mesoporous Cerium Oxide Hollow Biophotocatalyst for Concurrent pH-/H₂O₂-Responsive O₂-Evolving Synergetic Cancer Therapy. *Adv. Mater.* **2018**, *30*, 1704833.
- (259) Liu, D.; Xu, X.; Du, Y.; Qin, X.; Zhang, Y.; Ma, C.; Wen, S.; Ren, W.; Goldys, E. M.; Piper, J. A.; et al. Three-dimensional Controlled Growth of Monodisperse Sub-50 nm Heterogeneous Nanocrystals. *Nat. Commun.* **2016**, *7*, 10254.
- (260) Chen, P.; Lei, B.; Dong, X. a.; Wang, H.; Sheng, J.; Cui, W.; Li, J.; Sun, Y.; Wang, Z.; Dong, F. Rare-Earth Single-Atom La–N Charge-Transfer Bridge on Carbon Nitride for Highly Efficient and Selective Photocatalytic CO₂ Reduction. *ACS Nano* **2020**, *14*, 15841–15852.

- (261) Cui, Y.; Yue, Y.; Qian, G.; Chen, B. Luminescent Functional Metal–Organic Frameworks. *Chem. Rev.* **2012**, *112*, 1126–1162.
- (262) Stouwdam, J. W.; van Veggel, F. C. J. M. Near-infrared Emission of Redispersible Er^{3+} , Nd^{3+} , and Ho^{3+} Doped LaF_3 Nanoparticles. *Nano Lett.* **2002**, *2*, 733–737.
- (263) Wong, H.-T.; Chan, H. L. W.; Hao, J. H. Magnetic and Luminescent Properties of Multifunctional $\text{GdF}_3:\text{Eu}^{3+}$ Nanoparticles. *Appl. Phys. Lett.* **2009**, *95*, 022512.
- (264) Teng, X.; Zhu, Y.; Wei, W.; Wang, S.; Huang, J.; Naccache, R.; Hu, W.; Tok, A. I. Y.; Han, Y.; Zhang, Q.; et al. Lanthanide-Doped $\text{Na}_x\text{ScF}_{3+x}$ Nanocrystals: Crystal Structure Evolution and Multicolor Tuning. *J. Am. Chem. Soc.* **2012**, *134*, 8340–8343.
- (265) Ding, Y.; Zhang, X.; Zhu, H.; Zhu, J.-J. A Lanthanide-doping Route to aspect-ratio-controlled KScF_7 Nanocrystals for Upconversion, Downconversion and Magnetism. *J. Mater. Chem. C* **2014**, *2*, 946–952.
- (266) Vetrone, F.; Mahalingam, V.; Capobianco, J. A. Near-Infrared-to-Blue Upconversion in Colloidal $\text{BaYF}_5:\text{Tm}^{3+}$, Yb^{3+} Nanocrystals. *Chem. Mater.* **2009**, *21*, 1847–1851.
- (267) Zeng, S.; Tsang, M.-K.; Chan, C.-F.; Wong, K.-L.; Hao, J. PEG Modified $\text{BaGdF}_5:\text{Yb}/\text{Er}$ Nanoprobes for Multi-modal Upconversion Fluorescent, *In Vivo* X-ray Computed Tomography and Biomagnetic Imaging. *Biomaterials* **2012**, *33*, 9232–9238.
- (268) Wang, J.; Deng, R.; MacDonald, M. A.; Chen, B.; Yuan, J.; Wang, F.; Chi, D.; Andy Hor, T. S.; Zhang, P.; Liu, G.; et al. Enhancing Multiphoton Upconversion Through Energy Clustering at Sublattice Level. *Nat. Mater.* **2014**, *13*, 157–162.
- (269) Lee, T.-J.; Luo, L.-Y.; Diao, E. W.-G.; Chen, T.-M.; Cheng, B.-M.; Tung, C.-Y. Visible Quantum Cutting Through Downconversion in Green-emitting $\text{K}_2\text{GdF}_5:\text{Tb}^{3+}$ Phosphors. *Appl. Phys. Lett.* **2006**, *89*, 131121.
- (270) Wang, L.; Li, P.; Li, Y. Down- and Up-Conversion Luminescent Nanorods. *Adv. Mater.* **2007**, *19*, 3304–3307.
- (271) Heer, S.; Kömpe, K.; Güdel, H. U.; Haase, M. Highly Efficient Multicolour Upconversion Emission in Transparent Colloids of Lanthanide-Doped NaYF_4 Nanocrystals. *Adv. Mater.* **2004**, *16*, 2102–2105.
- (272) Liu, Q.; Sun, Y.; Yang, T.; Feng, W.; Li, C.; Li, F. Sub-10 nm Hexagonal Lanthanide-Doped NaLuF_4 Upconversion Nanocrystals for Sensitive Bioimaging *In Vivo*. *J. Am. Chem. Soc.* **2011**, *133*, 17122–17125.
- (273) Liu, Y.; Tu, D.; Zhu, H.; Li, R.; Luo, W.; Chen, X. A Strategy to Achieve Efficient Dual-Mode Luminescence of Eu^{3+} in Lanthanides Doped Multifunctional NaGdF_4 Nanocrystals. *Adv. Mater.* **2010**, *22*, 3266–3271.
- (274) Mahalingam, V.; Vetrone, F.; Naccache, R.; Speghini, A.; Capobianco, J. A. Colloidal $\text{Tm}^{3+}/\text{Yb}^{3+}$ -Doped LiYF_4 Nanocrystals: Multiple Luminescence Spanning the UV to NIR Regions via Low-Energy Excitation. *Adv. Mater.* **2009**, *21*, 4025–4028.
- (275) Chen, G.; Ohulchanskyy, T. Y.; Kachynski, A.; Ågren, H.; Prasad, P. N. Intense Visible and Near-Infrared Upconversion Photoluminescence in Colloidal $\text{LiYF}_4:\text{Er}^{3+}$ Nanocrystals Under Excitation at 1490 nm. *ACS Nano* **2011**, *5*, 4981–4986.
- (276) Jalani, G.; Naccache, R.; Rosenzweig, D. H.; Haglund, L.; Vetrone, F.; Cerruti, M. Photocleavable Hydrogel-Coated Upconverting Nanoparticles: A Multifunctional Theranostic Platform for NIR Imaging and On-Demand Macromolecular Delivery. *J. Am. Chem. Soc.* **2016**, *138*, 1078–1083.
- (277) Huang, P.; Zheng, W.; Zhou, S.; Tu, D.; Chen, Z.; Zhu, H.; Li, R.; Ma, E.; Huang, M.; Chen, X. Lanthanide-Doped LiLuF_4 Upconversion Nanoprobes for the Detection of Disease Biomarkers. *Angew. Chem., Int. Ed.* **2014**, *53*, 1252–1257.
- (278) Schäfer, H.; Ptacek, P.; Zerzouf, O.; Haase, M. Synthesis and Optical Properties of KYF_4/Yb , Er Nanocrystals, and Their Surface Modification With Undoped KYF_4 . *Adv. Funct. Mater.* **2008**, *18*, 2913–2918.
- (279) Wong, H.-T.; Vetrone, F.; Naccache, R.; Chan, H. L. W.; Hao, J.; Capobianco, J. A. Water Dispersible Ultra-small Multifunctional $\text{KGdF}_4:\text{Tm}^{3+}$, Yb^{3+} Nanoparticles With Near-infrared to Near-infrared Upconversion. *J. Mater. Chem.* **2011**, *21*, 16589–16596.
- (280) Jiao, J.; Li, Y.; Shen, W.; Gai, S.; Tang, J.; Wang, Y.; Huang, L.; Liu, J.; Wang, W.; Belfiore, L. A. Fabrication and Luminescence of $\text{KGdF}_4:\text{Yb}^{3+}/\text{Er}^{3+}$ Nanoplates and Their Improving Performance for Polymer Solar Cells. *Sci. Bull.* **2018**, *63*, 216–218.
- (281) Wang, F.; Deng, R.; Liu, X. Preparation of Core-shell NaGdF_4 Nanoparticles Doped With Luminescent Lanthanide Ions to Be Used as Upconversion-based Probes. *Nat. Protoc.* **2014**, *9*, 1634–1644.
- (282) Liu, X.; Deng, R.; Zhang, Y.; Wang, Y.; Chang, H.; Huang, L.; Liu, X. Probing the Nature of Upconversion Nanocrystals: Instrumentation Matters. *Chem. Soc. Rev.* **2015**, *44*, 1479–1508.
- (283) Wang, F.; Liu, X. Upconversion Multicolor Fine-Tuning: Visible to Near-Infrared Emission From Lanthanide-Doped NaYF_4 Nanoparticles. *J. Am. Chem. Soc.* **2008**, *130*, 5642–5643.
- (284) Wilhelm, S.; Kaiser, M.; Würth, C.; Heiland, J.; Carrillo-Carrion, C.; Muhr, V.; Wolfbeis, O. S.; Parak, W. J.; Resch-Genger, U.; Hirsch, T. Water Dispersible Upconverting Nanoparticles: Effects of Surface Modification on Their Luminescence and Colloidal Stability. *Nanoscale* **2015**, *7*, 1403–1410.
- (285) Dong, C.; van Veggel, F. C. J. M. Cation Exchange in Lanthanide Fluoride Nanoparticles. *ACS Nano* **2009**, *3*, 123–130.
- (286) Dong, C.; Korinek, A.; Blasiak, B.; Tomanek, B.; van Veggel, F. C. J. M. Cation Exchange: A Facile Method To Make $\text{NaYF}_4:\text{Yb}/\text{Tm}-\text{NaGdF}_4$ Core–Shell Nanoparticles With a Thin, Tunable, and Uniform Shell. *Chem. Mater.* **2012**, *24*, 1297–1305.
- (287) Guan, M.; Zhou, Z.; Mei, L.; Zheng, H.; Ren, W.; Wang, L.; Du, Y.; Jin, D.; Zhou, J. Direct Cation Exchange of Surface Ligand Capped Upconversion Nanocrystals to Produce Strong Luminescence. *Chem. Commun.* **2018**, *54*, 9587–9590.
- (288) Han, S.; Qin, X.; An, Z.; Zhu, Y.; Liang, L.; Han, Y.; Huang, W.; Liu, X. Multicolour Synthesis in Lanthanide-doped Nanocrystals Through Cation Exchange in Water. *Nat. Commun.* **2016**, *7*, 13059.
- (289) Chen, H.; Zhang, P.; Cui, H.; Qin, W.; Zhao, D. Synthesis and Luminescence Properties of Water Soluble $\alpha\text{-NaGdF}_4/\beta\text{-NaYF}_4:\text{Yb}/\text{Er}$ Core–Shell Nanoparticles. *Nanoscale Res. Lett.* **2017**, *12*, 548.
- (290) Zhao, Q.; Lü, W.; Guo, N.; Jia, Y.; Lv, W.; Shao, B.; Jiao, M.; You, H. Inorganic-salt-induced Morphological Transformation and Luminescent Performance of GdF_3 Nanostructures. *Dalton T.* **2013**, *42*, 6902–6908.
- (291) Chen, G.; Ågren, H.; Ohulchanskyy, T. Y.; Prasad, P. N. Light Upconverting Core–shell Nanostructures: Nanophotonic Control for Emerging applications. *Chem. Soc. Rev.* **2015**, *44*, 1680–1713.
- (292) Fischer, S.; Bronstein, N. D.; Swabeck, J. K.; Chan, E. M.; Alivisatos, A. P. Precise Tuning of Surface Quenching for Luminescence Enhancement in Core–Shell Lanthanide-Doped Nanocrystals. *Nano Lett.* **2016**, *16*, 7241–7247.
- (293) Skripka, A.; Benayas, A.; Brites, C. D.; Martín, I. R.; Carlos, L. D.; Vetrone, F. Inert Shell Effect on the Quantum Yield of Neodymium-doped Near-infrared Nanoparticles: The Necessary Shield in an aqueous Dispersion. *Nano Lett.* **2020**, *20*, 7648–7654.
- (294) Chen, B.; Wang, F. Combating Concentration Quenching in Upconversion Nanoparticles. *Acc. Chem. Res.* **2020**, *53*, 358–367.
- (295) Wang, Z.; Meijerink, A. Concentration Quenching in Upconversion Nanocrystals. *J. Phys. Chem. C* **2018**, *122*, 26298–26306.
- (296) Shen, B.; Cheng, S.; Gu, Y.; Ni, D.; Gao, Y.; Su, Q.; Feng, W.; Li, F. Revisiting the Optimized Doping Ratio in Core/shell Nanostructured Upconversion Particles. *Nanoscale* **2017**, *9*, 1964–1971.
- (297) Johnson, N. J. J.; He, S.; Diao, S.; Chan, E. M.; Dai, H.; Almutairi, A. Direct Evidence for Coupled Surface and Concentration Quenching Dynamics in Lanthanide-Doped Nanocrystals. *J. Am. Chem. Soc.* **2017**, *139*, 3275–3282.
- (298) Li, D.; Liu, X.; Qiu, J. Probing Interaction Distance of Surface Quenchers in Lanthanide-Doped Upconversion Core–Shell Nanoparticles. *J. Phys. Chem. C* **2018**, *122*, 10278–10283.
- (299) Homann, C.; Krukewitt, L.; Frenzel, F.; Grauel, B.; Würth, C.; Resch-Genger, U.; Haase, M. $\text{NaYF}_4:\text{Yb}/\text{Er}/\text{NaYF}_4$ Core/Shell

Nanocrystals With High Upconversion Luminescence Quantum Yield. *Angew. Chem., Int. Ed.* **2018**, *57*, 8765–8769.

(300) Chen, F.; Bu, W.; Zhang, S.; Liu, X.; Xing, H.; Xiao, Q.; Zhou, L.; Peng, W.; Wang, L.; et al. Positive and Negative Lattice Shielding Effects Co-existing in Gd (III) Ion Doped Bifunctional Upconversion Nanoparticles. *Adv. Funct. Mater.* **2011**, *21*, 4285–4294.

(301) Xu, J.; Yang, P.; Sun, M.; Bi, H.; Liu, B.; Yang, D.; Gai, S.; He, F.; Lin, J. Highly Emissive Dye-Sensitized Upconversion Nanostructure for Dual-Photosensitizer Photodynamic Therapy and Bioimaging. *ACS Nano* **2017**, *11*, 4133–4144.

(302) Liu, Y.; Kang, N.; Lv, J.; Zhou, Z.; Zhao, Q.; Ma, L.; Chen, Z.; Ren, L.; Nie, L. Deep Photoacoustic/Luminescence/Magnetic Resonance Multimodal Imaging in Living Subjects Using High-Efficiency Upconversion Nanocomposites. *Adv. Mater.* **2016**, *28*, 6411–6419.

(303) Zhou, L.; Zheng, X.; Gu, Z.; Yin, W.; Zhang, X.; Ruan, L.; Yang, Y.; Hu, Z.; Zhao, Y. Mesoporous NaYbF₄@NaGdF₄ Core-shell Up-conversion Nanoparticles for Targeted Drug Delivery and Multimodal Imaging. *Biomaterials* **2014**, *35*, 7666–7678.

(304) Vetrone, F.; Naccache, R.; Mahalingam, V.; Morgan, C. G.; Capobianco, J. A. The Active-Core/Active-Shell Approach: A Strategy to Enhance the Upconversion Luminescence in Lanthanide-Doped Nanoparticles. *Adv. Funct. Mater.* **2009**, *19*, 2924–2929.

(305) Zhu, W.; Chen, D.; Lei, L.; Xu, J.; Wang, Y. An Active-core/active-shell Structure With Enhanced Quantum-cutting Luminescence in Pr–Yb Co-doped Monodisperse Nanoparticles. *Nanoscale* **2014**, *6*, 10500–10504.

(306) Bhuckory, S.; Hemmer, E.; Wu, Y.-T.; Yahia, A.; Vetrone, F.; Hildebrandt, N. Core or Shell? Er³⁺ FRET Donors in Upconversion Nanoparticles. *Eur. J. Inorg. Chem.* **2017**, *2017*, 5186–5195.

(307) DiMaio, J. R.; Sabatier, C.; Kokuoz, B.; Ballato, J. Controlling Energy Transfer Between Multiple Dopants Within a Single Nanoparticle. *Proc. Natl. Acad. Sci. U. S. A.* **2008**, *105*, 1809–1813.

(308) Li, X.; Guo, Z.; Zhao, T.; Lu, Y.; Zhou, L.; Zhao, D.; Zhang, F. Filtration Shell Mediated Power Density Independent Orthogonal Excitations–Emissions Upconversion Luminescence. *Angew. Chem., Int. Ed.* **2016**, *55*, 2464–2469.

(309) Mei, Q.; Bansal, A.; Jayakumar, M. K. G.; Zhang, Z.; Zhang, J.; Huang, H.; Yu, D.; Ramachandra, C. J. A.; Hausenloy, D. J.; Soong, T. W.; Zhang, Y. Manipulating Energy Migration Within Single Lanthanide Activator for Switchable Upconversion Emissions Towards Bidirectional Photoactivation. *Nat. Commun.* **2019**, *10*, 4416.

(310) Dong, H.; Sun, L.-D.; Feng, W.; Gu, Y.; Li, F.; Yan, C.-H. Versatile Spectral and Lifetime Multiplexing Nanoplatform With Excitation Orthogonalized Upconversion Luminescence. *ACS Nano* **2017**, *11*, 3289–3297.

(311) Zhou, B.; Tao, L.; Chai, Y.; Lau, S. P.; Zhang, Q.; Tsang, Y. H. Constructing Interfacial Energy Transfer for Photon Up- and Down-conversion From Lanthanides in a Core–Shell Nanostructure. *Angew. Chem., Int. Ed.* **2016**, *55*, 12356–12360.

(312) Zhang, C.; Yang, L.; Zhao, J.; Liu, B.; Han, M.-Y.; Zhang, Z. White-Light Emission From an Integrated Upconversion Nanostructure: Toward Multicolor Displays Modulated by Laser Power. *Angew. Chem., Int. Ed.* **2015**, *54*, 11531–11535.

(313) Quintanilla, M.; Ren, F.; Ma, D.; Vetrone, F. Light Management in Upconverting Nanoparticles: Ultrasmall Core/Shell Architectures to Tune the Emission Color. *ACS Photonics* **2014**, *1*, 662–669.

(314) Wen, H.; Zhu, H.; Chen, X.; Hung, T. F.; Wang, B.; Zhu, G.; Yu, S. F.; Wang, F. Upconverting Near-Infrared Light Through Energy Management in Core–Shell Nanoparticles. *Angew. Chem., Int. Ed.* **2013**, *52*, 13419–13423.

(315) Lin, C.; Xia, Z.; Zhang, L.; Chen, X.; Sun, Q.; Lu, M.; Yuan, Z.; Xie, X.; Huang, L. Organic Linkers Enable Tunable Transfer of Migrated Energy From Upconversion Nanoparticles. *ACS Appl. Mater. Interfaces* **2020**, *12*, 31783–31792.

(316) Su, Q.; Han, S.; Xie, X.; Zhu, H.; Chen, H.; Chen, C.-K.; Liu, R.-S.; Chen, X.; Wang, F.; Liu, X. The Effect of Surface Coating on

Energy Migration-Mediated Upconversion. *J. Am. Chem. Soc.* **2012**, *134*, 20849–20857.

(317) Zhou, B.; Yan, L.; Tao, L.; Song, N.; Wu, M.; Wang, T.; Zhang, Q. Enabling Photon Upconversion and Precise Control of Donor–Acceptor Interaction Through Interfacial Energy Transfer. *Adv. Sci.* **2018**, *5*, 1700667.

(318) Peng, D.; Ju, Q.; Chen, X.; Ma, R.; Chen, B.; Bai, G.; Hao, J.; Qiao, X.; Fan, X.; Wang, F. Lanthanide-Doped Energy Cascade Nanoparticles: Full Spectrum Emission by Single Wavelength Excitation. *Chem. Mater.* **2015**, *27*, 3115–3120.

(319) Prorok, K.; Pawlyta, M.; Stręk, W.; Bednarkiewicz, A. Energy Migration Up-conversion of Tb³⁺ in Yb³⁺ and Nd³⁺ Codoped Active-Core/Active-Shell Colloidal Nanoparticles. *Chem. Mater.* **2016**, *28*, 2295–2300.

(320) Zhao, J.; Chen, X.; Chen, B.; Luo, X.; Sun, T.; Zhang, W.; Wang, C.; Lin, J.; Su, D.; Qiao, X.; et al. Accurate Control of Core–Shell Upconversion Nanoparticles Through Anisotropic Strain Engineering. *Adv. Funct. Mater.* **2019**, *29*, 1903295.

(321) Fischer, S.; Swabeck, J. K.; Alivisatos, A. P. Controlled Isotropic and Anisotropic Shell Growth in β-NaLnF₄ Nanocrystals Induced by Precursor Injection Rate. *J. Am. Chem. Soc.* **2017**, *139*, 12325–12332.

(322) Xu, B.; Zhang, X.; Huang, W.; Yang, Y.; Ma, Y.; Gu, Z.; Zhai, T.; Zhao, Y. Nd³⁺ Sensitized Dumbbell-like Upconversion Nanoparticles for Photodynamic Therapy application. *J. Mater. Chem. B* **2016**, *4*, 2776–2784.

(323) Zhang, Y.; Zhang, L.; Deng, R.; Tian, J.; Zong, Y.; Jin, D.; Liu, X. Multicolor Barcoding in a Single Upconversion Crystal. *J. Am. Chem. Soc.* **2014**, *136*, 4893–4896.

(324) Chen, B.; Kong, W.; Liu, Y.; Lu, Y.; Li, M.; Qiao, X.; Fan, X.; Wang, F. Crystalline Hollow Microrods for Site-Selective Enhancement of Nonlinear Photoluminescence. *Angew. Chem., Int. Ed.* **2017**, *56*, 10383–10387.

(325) Wang, P.; Wang, C.; Lu, L.; Li, X.; Wang, W.; Zhao, M.; Hu, L.; El-Toni, A. M.; Li, Q.; Zhang, F. Kinetics-mediate Fabrication of Multi-model Bioimaging Lanthanide Nanoplates With Controllable Surface Roughness for Blood Brain Barrier Transportation. *Biomaterials* **2017**, *141*, 223–232.

(326) Shang, M.; Geng, D.; Kang, X.; Yang, D.; Zhang, Y.; Lin, J. Hydrothermal Derived LaOF:Ln³⁺ (Ln = Eu, Tb, Sm, Dy, Tm, and/or Ho) Nanocrystals With Multicolor-Tunable Emission Properties. *Inorg. Chem.* **2012**, *51*, 11106–11116.

(327) Li, R.; Liu, Y.; Zhang, N.; Li, L.; Liu, L.; Liang, Y.; Gan, S. Shape Controllable Synthesis and Multicolour Fluorescence of Lanthanide Doped Vernier Yttrium Oxyfluoride. *J. Mater. Chem. C* **2015**, *3*, 3928–3934.

(328) Liu, D.; Chen, X.; Yuan, Z.; Lu, M.; Yin, L.; Xie, X.; Huang, L. Coating and Transforming the Y(OH)CO₃ Shell on Upconversion Nanoparticles. *Wuli Huaxue Xuebao* **2020**, *36*, 1907011.

(329) Du, Y.-P.; Zhang, Y.-W.; Yan, Z.-G.; Sun, L.-D.; Yan, C.-H. Highly Luminescent Self-Organized Sub-2-nm EuOF Nanowires. *J. Am. Chem. Soc.* **2009**, *131*, 16364–16365.

(330) Grzyb, T.; Węclawiak, M.; Rozowska, J.; Lis, S. Structural and Spectroscopic Properties of YOF:Eu³⁺ Nanocrystals. *J. Alloys Compd.* **2013**, *576*, 345–349.

(331) Wang, H.; Tu, D.; Xu, J.; Shang, X.; Hu, P.; Li, R.; Zheng, W.; Chen, Z.; Chen, X. Lanthanide-doped LaOBr Nanocrystals: Controlled Synthesis, Optical Spectroscopy and Bioimaging. *J. Mater. Chem. B* **2017**, *5*, 4827–4834.

(332) Du, Y.; Wang, Y.; Deng, Z.; Chen, X.; Yang, X.; Sun, T.; Zhang, X.; Zhu, G.; Yu, S. F.; Wang, F. Blue-Pumped Deep Ultraviolet Lasing From Lanthanide-Doped Lu₆O₅F₈ Upconversion Nanocrystals. *Adv. Opt. Mater.* **2020**, *8*, 1900968.

(333) Wen, T.; Luo, W.; Wang, Y.; Zhang, M.; Guo, Y.; Yuan, J.; Ju, J.; Wang, Y.; Liao, F.; Yang, B. Multicolour and Up-conversion Fluorescence of Lanthanide Doped Vernier Phase Yttrium Oxyfluoride Nanocrystals. *J. Mater. Chem. C* **2013**, *1*, 1995–2001.

(334) Wen, T.; Zhou, Y.; Guo, Y.; Zhao, C.; Yang, B.; Wang, Y. Color-tunable and Single-band Red Upconversion Luminescence

From Rare-earth Doped Vernier Phase Ytterbium Oxyfluoride Nanoparticles. *J. Mater. Chem. C* **2016**, *4*, 684–690.

(335) Xu, J.; Zhou, S.; Tu, D.; Zheng, W.; Huang, P.; Li, R.; Chen, Z.; Huang, M.; Chen, X. Sub-5 nm Lanthanide-doped Lutetium Oxyfluoride Nanoprobes for Ultrasensitive Detection of Prostate Specific antigen. *Chem. Sci.* **2016**, *7*, 2572–2578.

(336) Shao, B.; Feng, Y.; Jiao, M.; Lü, W.; You, H. A Two-step Synthetic Route to GdOF:Ln³⁺ Nanocrystals With Multicolor Luminescence Properties. *Dalton T.* **2016**, *45*, 2485–2491.

(337) Zhao, S.; Shao, B.; Feng, Y.; Yuan, S.; Huo, J.; Lü, W.; Liu, K.; You, H. Facile Synthesis of Lanthanide (Ce, Eu, Tb, Ce/Tb, Yb/Er, Yb/Ho, and Yb/Tm)-Doped LnF₃ and LnOF Porous Sub-Microspheres With Multicolor Emissions. *Chem. - Asian J.* **2017**, *12*, 3046–3052.

(338) Yi, G.; Peng, Y.; Gao, Z. Strong Red-Emitting Near-Infrared-to-Visible Upconversion Fluorescent Nanoparticles. *Chem. Mater.* **2011**, *23*, 2729–2734.

(339) Yan, J.; He, W.; Li, N.; Yu, M.; Du, Y.; Lei, B.; Ma, P. X. Simultaneously Targeted Imaging Cytoplasm and Nucleus in Living Cell by Biomolecules Capped Ultra-small GdOF Nanocrystals. *Biomaterials* **2015**, *59*, 21–29.

(340) Lv, R.; Yang, P.; He, F.; Gai, S.; Li, C.; Dai, Y.; Yang, G.; Lin, J. A Yolk-like Multifunctional Platform for Multimodal Imaging and Synergistic Therapy Triggered by a Single Near-Infrared Light. *ACS Nano* **2015**, *9*, 1630–1647.

(341) Zong, L.; Xu, J.; Jiang, S.; Zhao, K.; Wang, Z.; Liu, P.; Zhao, H.; Chen, J.; Xing, X.; Yu, R. Composite Yttrium-Carbonaceous Spheres Templated Multi-Shell YVO₄ Hollow Spheres With Superior Upconversion Photoluminescence. *Adv. Mater.* **2017**, *29*, 1604377.

(342) Amurisana, B.; Bao, L.; Bao, L.; Tegus, O. Fabrication and Photoluminescence Properties of Color-tunable Light Emitting Lanthanide Doped GdVO₄ Hierarchitectures. *J. Lumin.* **2017**, *184*, 150–159.

(343) Chen, H.; Moore, T.; Qi, B.; Colvin, D. C.; Jelen, E. K.; Hitchcock, D. A.; He, J.; Mefford, O. T.; Gore, J. C.; Alexis, F.; et al. Monitoring pH-Triggered Drug Release From Radioluminescent Nanocapsules With X-ray Excited Optical Luminescence. *ACS Nano* **2013**, *7*, 1178–1187.

(344) Song, Y.; You, H.; Huang, Y.; Yang, M.; Zheng, Y.; Zhang, L.; Guo, N. Highly Uniform and Monodisperse Gd₂O₂S:Ln³⁺ (Ln = Eu, Tb) Submicrospheres: Solvothermal Synthesis and Luminescence Properties. *Inorg. Chem.* **2010**, *49*, 11499–11504.

(345) Dhanaraj, J.; Jagannathan, R.; Trivedi, D. C. Y₂O₂S:Eu³⁺ Nanocrystals—synthesis and Luminescence Properties. *J. Mater. Chem.* **2003**, *13*, 1778–1782.

(346) Som, S.; Mitra, P.; Kumar, V.; Kumar, V.; Terblans, J. J.; Swart, H. C.; Sharma, S. K. The Energy Transfer Phenomena and Colour Tunability in Y₂O₂S:Eu³⁺/Dy³⁺ Micro-fibers for White Emission in Solid State Lighting applications. *Dalton T.* **2014**, *43*, 9860–9871.

(347) Tian, Y.; Lu, F.; Xing, M.; Ran, J.; Fu, Y.; Peng, Y.; Luo, X. Upconversion Luminescence Properties of Y₂O₂S:Er³⁺@Y₂O₂S:Yb³⁺,Tm³⁺ Core-shell Nanoparticles Prepared via Homogeneous Co-precipitation. *Opt. Mater.* **2017**, *64*, 58–63.

(348) Lin, S.-L.; Liu, T.-Y.; Lo, C.-L.; Wang, B.-S.; Lee, Y.-J.; Lin, K.-Y.; Chang, C. A. Synthesis, Surface Modification, and Photophysical Studies of Ln₂O₂S:Ln'³⁺ (Ln = Gd, Tb, Eu; Ln' = Tb and/or Eu) Nanoparticles for Luminescence Bioimaging. *J. Lumin.* **2016**, *175*, 165–175.

(349) Dai, Q.; Song, H.; Wang, M.; Bai, X.; Dong, B.; Qin, R.; Qu, X.; Zhang, H. Size and Concentration Effects on the Photoluminescence of La₂O₂S:Eu³⁺ Nanocrystals. *J. Phys. Chem. C* **2008**, *112*, 19399–19404.

(350) Pokhrel, M.; Kumar, G. A.; Sardar, D. K. Highly Efficient NIR to NIR and VIS Upconversion in Er³⁺ and Yb³⁺ Doped in M₂O₂S (M = Gd, La, Y). *J. Mater. Chem. A* **2013**, *1*, 11595–11606.

(351) Zhao, F.; Yuan, M.; Zhang, W.; Gao, S. Monodisperse Lanthanide Oxysulfide Nanocrystals. *J. Am. Chem. Soc.* **2006**, *128*, 11758–11759.

(352) Ledoux, G.; Amans, D.; Dujardin, C.; Masenelli-Varlot, K. Facile and Rapid Synthesis of Highly Luminescent Nanoparticles via Pulsed Laser Ablation in Liquid. *Nanotechnology* **2009**, *20*, 445605.

(353) Zhang, B.; Zou, H.; Guan, H.; Dai, Y.; Song, Y.; Zhou, X.; Sheng, Y. Lu₂O₂S:Tb³⁺, Eu³⁺ Nanorods: Luminescence, Energy Transfer, and Multicolour Tuneable Emission. *CrystEngComm* **2016**, *18*, 7620–7628.

(354) Jiang, Y.; Wu, Y.; Xie, Y.; Qian, Y.-T. Synthesis and Characterization of Nanocrystalline Lanthanide Oxysulfide via a La(OH)₃ Gel Solvothermal Route. *J. Am. Ceram. Soc.* **2000**, *83*, 2628–2630.

(355) Qiao, Y.; Lin, Y.; Zhang, S.; Huang, J. Lanthanide-Containing Photoluminescent Materials: From Hybrid Hydrogel to Inorganic Nanotubes. *Chem. - Eur. J.* **2011**, *17*, 5180–5187.

(356) Ding, Y.; Gu, J.; Ke, J.; Zhang, Y.-W.; Yan, C.-H. Sodium Doping Controlled Synthesis of Monodisperse Lanthanide Oxysulfide Ultrathin Nanoplates Guided by Density Functional Calculations. *Angew. Chem., Int. Ed.* **2011**, *50*, 12330–12334.

(357) Fang, Y.-P.; Xu, A.-W.; Song, R.-Q.; Zhang, H.-X.; You, L.-P.; Yu, J. C.; Liu, H.-Q. Systematic Synthesis and Characterization of Single-Crystal Lanthanide Orthophosphate Nanowires. *J. Am. Chem. Soc.* **2003**, *125*, 16025–16034.

(358) Ren, W.; Tian, G.; Zhou, L.; Yin, W.; Yan, L.; Jin, S.; Zu, Y.; Li, S.; Gu, Z.; Zhao, Y. Lanthanide Ion-doped GdPO₄ Nanorods With Dual-modal Bio-optical and Magnetic Resonance Imaging Properties. *Nanoscale* **2012**, *4*, 3754–3760.

(359) Wang, M.; Li, M.; Yu, A.; Wu, J.; Mao, C. Rare Earth Fluorescent Nanomaterials for Enhanced Development of Latent Fingerprints. *ACS Appl. Mater. Interfaces* **2015**, *7*, 28110–28115.

(360) Zhang, L.; Yin, M.; You, H.; Yang, M.; Song, Y.; Huang, Y. Multifunctional GdPO₄:Eu³⁺ Hollow Spheres: Synthesis and Magnetic and Luminescent Properties. *Inorg. Chem.* **2011**, *50*, 10608–10613.

(361) Pan, B.; Luo, S.; Su, W.; Wang, X. Photocatalytic CO₂ Reduction With H₂O Over LaPO₄ Nanorods Deposited With Pt Cocatalyst. *Appl. Catal., B* **2015**, *168*, 458–464.

(362) Runowski, M.; Shyichuk, A.; Tyimiński, A.; Grzyb, T.; Lavín, V.; Lis, S. Multifunctional Optical Sensors for Nanomanometry and Nanothermometry: High-Pressure and High-Temperature Upconversion Luminescence of Lanthanide-Doped Phosphates—LaPO₄/YPO₄:Yb³⁺–Tm³⁺. *ACS Appl. Mater. Interfaces* **2018**, *10*, 17269–17279.

(363) Meyssamy, H.; Riwozki, K.; Kornowski, A.; Nased, S.; Haase, M. Wet-Chemical Synthesis of Doped Colloidal Nanomaterials: Particles and Fibers of LaPO₄:Eu, LaPO₄:Ce, and LaPO₄:Ce,Tb. *Adv. Mater.* **1999**, *11*, 840–844.

(364) Kömpe, K.; Borchert, H.; Storz, J.; Lobo, A.; Adam, S.; Möller, T.; Haase, M. Green-Emitting CePO₄:Tb/LaPO₄ Core-Shell Nanoparticles With 70% Photoluminescence Quantum Yield. *Angew. Chem., Int. Ed.* **2003**, *42*, 5513–5516.

(365) Shao, B.; Feng, Y.; Zhao, S.; Yuan, S.; Huo, J.; Lü, W.; You, H. Phase-Tunable Synthesis of Monodisperse YPO₄:Ln³⁺ (Ln = Ce, Eu, Tb) Micro/Nanocrystals via Topotactic Transformation Route With Multicolor Luminescence Properties. *Inorg. Chem.* **2017**, *56*, 6114–6121.

(366) Jia, Y.; Sun, T.-Y.; Wang, J.-H.; Huang, H.; Li, P.; Yu, X.-F.; Chu, P. K. Synthesis of Hollow Rare-earth Compound Nanoparticles by a Universal Sacrificial Template Method. *CrystEngComm* **2014**, *16*, 6141–6148.

(367) Yu, M.; Lin, J.; Wang, Z.; Fu, J.; Wang, S.; Zhang, H. J.; Han, Y. C. Fabrication, Patterning, and Optical Properties of Nanocrystalline YVO₄:A (A = Eu³⁺, Dy³⁺, Sm³⁺, Er³⁺) Phosphor Films via Sol-Gel Soft Lithography. *Chem. Mater.* **2002**, *14*, 2224–2231.

(368) Wang, F.; Xue, X.; Liu, X. Multicolor Tuning of (Ln, P)-Doped YVO₄ Nanoparticles by Single-Wavelength Excitation. *Angew. Chem., Int. Ed.* **2008**, *47*, 906–909.

(369) Huignard, A.; Buisette, V.; Franville, A.-C.; Gacoin, T.; Boilot, J.-P. Emission Processes in YVO₄:Eu Nanoparticles. *J. Phys. Chem. B* **2003**, *107*, 6754–6759.

- (370) Mahata, M. K.; Kumar, K.; Rai, V. K. Er³⁺–Yb³⁺ Doped Vanadate Nanocrystals: A Highly Sensitive Thermographic Phosphor and Its Optical Nanoheater Behavior. *Sens. Actuators, B* **2015**, *209*, 775–780.
- (371) Yin, W.; Zhou, L.; Gu, Z.; Tian, G.; Jin, S.; Yan, L.; Liu, X.; Xing, G.; Ren, W.; Liu, F.; et al. Lanthanide-doped GdVO₄ Upconversion Nanophosphors With Tunable Emissions and Their applications for Biomedical Imaging. *J. Mater. Chem.* **2012**, *22*, 6974–6981.
- (372) Xu, Y.; Liu, J.; Xie, M.; Jing, L.; Xu, H.; She, X.; Li, H.; Xie, J. Construction of Novel CNT/LaVO₄ Nanostructures for Efficient antibiotic Photodegradation. *Chem. Eng. J.* **2019**, *357*, 487–497.
- (373) Gavrilović, T. V.; Jovanović, D. J.; Lojpur, V.; Dramićanin, M. D. Multifunctional Eu³⁺- and Er³⁺/Yb³⁺-doped GdVO₄ Nanoparticles Synthesized by Reverse Micelle Method. *Sci. Rep.* **2015**, *4*, 4209.
- (374) Fan, W.; Song, X.; Bu, Y.; Sun, S.; Zhao, X. Selected-Control Hydrothermal Synthesis and Formation Mechanism of Monazite- and Zircon-Type LaVO₄ Nanocrystals. *J. Phys. Chem. B* **2006**, *110*, 23247–23254.
- (375) Antić, Ž.; Dramićanin, M. D.; Prashanthi, K.; Jovanović, D.; Kuzman, S.; Thundat, T. Pulsed Laser Deposited Dysprosium-Doped Gadolinium–Vanadate Thin Films for Noncontact, Self-Referencing Luminescence Thermometry. *Adv. Mater.* **2016**, *28*, 7745–7752.
- (376) Weng, X.; Yang, Q.; Wang, L.; Xu, L.; Sun, X.; Liu, J. General Synthesis and Self-assembly of Lanthanide orthovanadate Nanorod arrays. *CrystEngComm* **2013**, *15*, 10230–10237.
- (377) Wei, Z.; Sun, L.; Liao, C.; Yin, J.; Jiang, X.; Yan, C.; Lü, S. Size-Dependent Chromaticity in YBO₃:Eu Nanocrystals: Correlation With Microstructure and Site Symmetry. *J. Phys. Chem. B* **2002**, *106*, 10610–10617.
- (378) Li, Z.; Zeng, J.; Li, Y. Solvothermal Route to Synthesize Well-Dispersed YBO₃:Eu Nanocrystals. *Small* **2007**, *3*, 438–443.
- (379) Szczeszak, A.; Grzyb, T.; Barszcz, B.; Nagirnyi, V.; Kotlov, A.; Lis, S. Hydrothermal Synthesis and Structural and Spectroscopic Properties of the New Triclinic Form of GdBO₃:Eu³⁺ Nanocrystals. *Inorg. Chem.* **2013**, *52*, 4934–4940.
- (380) Zou, H.; Chen, B.; Hu, Y.; Zhang, Q.; Wang, X.; Wang, F. Simultaneous Enhancement and Modulation of Upconversion by Thermal Stimulation in Sc₂Mo₃O₁₂ Crystals. *J. Phys. Chem. Lett.* **2020**, *11*, 3020–3024.
- (381) Zou, H.; Yang, X.; Chen, B.; Du, Y.; Ren, B.; Sun, X.; Qiao, X.; Zhang, Q.; Wang, F. Thermal Enhancement of Upconversion by Negative Lattice Expansion in Orthorhombic Yb₂W₃O₁₂. *Angew. Chem., Int. Ed.* **2019**, *58*, 17255–17259.
- (382) Wang, Z. J.; Zhang, Y. L.; Zhong, J. P.; Yao, H. H.; Wang, J.; Wu, M. M.; Meijerink, A. One-step Synthesis and Luminescence Properties of Tetragonal Double Tungstates Nanocrystals. *Nanoscale* **2016**, *8*, 15486–15489.
- (383) Andrade, A. B.; Ferreira, N. S.; Valerio, M. E. G. Particle Size Effects on Structural and Optical Properties of BaF₂ Nanoparticles. *RSC Adv.* **2017**, *7*, 26839–26848.
- (384) Du, Y.-P.; Sun, X.; Zhang, Y.-W.; Yan, Z.-G.; Sun, L.-D.; Yan, C.-H. Uniform Alkaline Earth Fluoride Nanocrystals With Diverse Shapes Grown From Thermolysis of Metal Trifluoroacetates in Hot Surfactant Solutions. *Cryst. Growth Des.* **2009**, *9*, 2013–2019.
- (385) Runowski, M.; Marciniak, J.; Grzyb, T.; Przybylska, D.; Shyichuk, A.; Barszcz, B.; Katrusiak, A.; Lis, S. Lifetime Nanomanometry – High-pressure Luminescence of Up-converting Lanthanide Nanocrystals – SrF₂:Yb³⁺,Er³⁺. *Nanoscale* **2017**, *9*, 16030–16037.
- (386) Dong, N.-N.; Pedroni, M.; Piccinelli, F.; Conti, G.; Sbarbati, A.; Ramírez-Hernández, J. E.; Maestro, L. M.; Iglesias-de la Cruz, M. C.; Sanz-Rodríguez, F.; Juarranz, A.; et al. NIR-to-NIR Two-Photon Excited CaF₂:Tm³⁺,Yb³⁺ Nanoparticles: Multifunctional Nanoprobes for Highly Penetrating Fluorescence Bio-Imaging. *ACS Nano* **2011**, *5*, 8665–8671.
- (387) Zheng, W.; Zhou, S.; Chen, Z.; Hu, P.; Liu, Y.; Tu, D.; Zhu, H.; Li, R.; Huang, M.; Chen, X. Sub-10 nm Lanthanide-Doped CaF₂ Nanoprobes for Time-Resolved Luminescent Biodetection. *Angew. Chem.* **2013**, *125*, 6803–6808.
- (388) Ritter, B.; Haida, P.; Fink, F.; Krahl, T.; Gawlitza, K.; Rurack, K.; Scholz, G.; Kemnitz, E. Novel and Easy Access to Highly Luminescent Eu and Tb Doped Ultra-small CaF₂, SrF₂ and BaF₂ Nanoparticles – Structure and Luminescence. *Dalton T.* **2017**, *46*, 2925–2936.
- (389) Chen, D.; Yu, Y.; Huang, F.; Wang, Y. Phase Transition From Hexagonal LnF₃ (Ln = La, Ce, Pr) to Cubic Ln_{0.8}M_{0.2}F_{2.8} (M = Ca, Sr, Ba) Nanocrystals With Enhanced Upconversion Induced by Alkaline-earth Doping. *Chem. Commun.* **2011**, *47*, 2601–2603.
- (390) Chen, D.; Yu, Y.; Huang, F.; Huang, P.; Yang, A.; Wang, Y. Modifying the Size and Shape of Monodisperse Bifunctional Alkaline-Earth Fluoride Nanocrystals Through Lanthanide Doping. *J. Am. Chem. Soc.* **2010**, *132*, 9976–9978.
- (391) Xu, B.; He, H.; Gu, Z.; Jin, S.; Ma, Y.; Zhai, T. Improving 800 nm Triggered Upconversion Emission for Lanthanide-Doped CaF₂ Nanoparticles Through Sodium Ion Doping. *J. Phys. Chem. C* **2017**, *121*, 18280–18287.
- (392) Hong, B.-C.; Kawano, K. Syntheses of CaF₂:Eu Nanoparticles and the Modified Reducing TCRA Treatment to Divalent Eu Ion. *Opt. Mater.* **2008**, *30*, 952–956.
- (393) Terraschke, H.; Olchowka, J.; Geringer, E.; Rodrigues, A. V.; Wickleder, C. Facile Ionic Liquid-Assisted Strategy for Direct Precipitation of Eu²⁺-Activated Nanophosphors Under Ambient Conditions. *Small* **2018**, *14*, 1703707.
- (394) Chen, G.; Shen, J.; Ohulchanskyy, T. Y.; Patel, N. J.; Kutikov, A.; Li, Z.; Song, J.; Pandey, R. K.; Ågren, H.; Prasad, P. N.; et al. (α-NaYbF₄:Tm³⁺)/CaF₂ Core/Shell Nanoparticles With Efficient Near-Infrared to Near-Infrared Upconversion for High-Contrast Deep Tissue Bioimaging. *ACS Nano* **2012**, *6*, 8280–8287.
- (395) Hao, S.; Chen, G.; Yang, C.; Shao, W.; Wei, W.; Liu, Y.; Prasad, P. N. Nd³⁺-Sensitized Multicolor Upconversion Luminescence From a Sandwiched Core/shell/shell Nanostructure. *Nanoscale* **2017**, *9*, 10633–10638.
- (396) Li, Y.; Gu, Y.; Yuan, W.; Cao, T.; Li, K.; Yang, S.; Zhou, Z.; Li, F. Core–Shell–Shell NaYbF₄:Tm@CaF₂@NaDyF₄ Nanocomposites for Upconversion/T₂-Weighted MRI/Computed Tomography Lymphatic Imaging. *ACS Appl. Mater. Interfaces* **2016**, *8*, 19208–19216.
- (397) Chen, B.; Wang, F. NaYbF₄@CaF₂ Core–satellite Upconversion Nanoparticles: One-pot Synthesis and Sensitive Detection of Glutathione. *Nanoscale* **2018**, *10*, 19898–19905.
- (398) Hao, S.; Yang, L.; Qiu, H.; Fan, R.; Yang, C.; Chen, G. Heterogeneous Core/shell Fluoride Nanocrystals With Enhanced Upconversion Photoluminescence for *In Vivo* Bioimaging. *Nanoscale* **2015**, *7*, 10775–10780.
- (399) Dong, H.; Sun, L.-D.; Li, L.-D.; Si, R.; Liu, R.; Yan, C.-H. Selective Cation Exchange Enabled Growth of Lanthanide Core/Shell Nanoparticles With Dissimilar Structure. *J. Am. Chem. Soc.* **2017**, *139*, 18492–18495.
- (400) Wang, Y.-F.; Sun, L.-D.; Xiao, J.-W.; Feng, W.; Zhou, J.-C.; Shen, J.; Yan, C.-H. Rare-Earth Nanoparticles With Enhanced Upconversion Emission and Suppressed Rare-Earth-Ion Leakage. *Chem. - Eur. J.* **2012**, *18*, 5558–5564.
- (401) Zhao, Y.; Rabouw, F. T.; Puffelen, T. v.; Walree, C. A. v.; Gamelin, D. R.; de Mello Donegá, C.; Meijerink, A. Lanthanide-Doped CaS and SrS Luminescent Nanocrystals: A Single-Source Precursor Approach for Doping. *J. Am. Chem. Soc.* **2014**, *136*, 16533–16543.
- (402) Wang, J.; Zhu, Y.; Grimes, C. A.; Cai, Q. Multicolor Lanthanide-doped CaS and SrS Near-infrared Stimulated Luminescent Nanoparticles With Bright Emission: application in Broad-spectrum Lighting, Information Coding, and Bio-imaging. *Nanoscale* **2019**, *11*, 12497–12501.
- (403) Rodríguez Burbano, D. C.; Sharma, S. K.; Dorenbos, P.; Viana, B.; Capobianco, J. A. Nanophosphors: Persistent and Photostimulated Red Emission in CaS:Eu²⁺,Dy³⁺ Nanophosphors (Advanced Opt. Mater. 4/2015). *Adv. Opt. Mater.* **2015**, *3*, 551–557.

- (404) Gao, Y.; Li, R.; Zheng, W.; Shang, X.; Wei, J.; Zhang, M.; Xu, J.; You, W.; Chen, Z.; Chen, X. Broadband NIR Photostimulated Luminescence Nanoprobes Based on CaS:Eu²⁺,Sm³⁺ Nanocrystals. *Chem. Sci.* **2019**, *10*, 5452–5460.
- (405) Zhang, M.; Zheng, W.; Liu, Y.; Huang, P.; Gong, Z.; Wei, J.; Gao, Y.; Zhou, S.; Li, X.; Chen, X. A New Class of Blue-LED-Excitable NIR-II Luminescent Nanoprobes Based on Lanthanide-Doped CaS Nanoparticles. *Angew. Chem., Int. Ed.* **2019**, *58*, 9556–9560.
- (406) Bünzli, J.-C. G.; Wong, K.-L. Lanthanide Mechanoluminescence. *J. Rare Earths* **2018**, *36*, 1–41.
- (407) Yu, X.; Zhou, C.; He, X.; Peng, Z.; Yang, S.-P. The Influence of Some Processing Conditions on Luminescence of SrAl₂O₄:Eu²⁺ Nanoparticles Produced by Combustion Method. *Mater. Lett.* **2004**, *58*, 1087–1091.
- (408) Thompson, N.; Murugaraj, P.; Rix, C.; Mainwaring, D. E. Role of Oxidative Pre-calcination in Extending Blue Emission of Sr₄Al₁₄O₂₅ Nanophosphors Formed With Microemulsions. *J. Alloys Compd.* **2012**, *537*, 147–153.
- (409) Chen, Z.; Yan, Y.; Liu, J.; Yin, Y.; Wen, H.; Zao, J.; Liu, D.; Tian, H.; Zhang, C.; Li, S. Microwave Induced Solution Combustion Synthesis of Nano-sized Phosphors. *J. Alloys Compd.* **2009**, *473*, L13–16.
- (410) Jeet, S.; Pandey, O. P. Template Free Synthesis Route to Monophasic BaMgAl₁₀O₁₇:Eu²⁺ With High Luminescence Efficiency. *J. Alloys Compd.* **2018**, *750*, 85–91.
- (411) Fan, J.; Gou, J.; Chen, Y.; Yu, B.; Liu, S. F. Enhanced Luminescence and Tunable Color of Sr₈CaSc(PO₄)₇:Eu²⁺, Ce³⁺, Mn²⁺ Phosphor by Energy Transfer Between Ce³⁺-Eu²⁺-Mn²⁺. *J. Alloys Compd.* **2018**, *731*, 796–804.
- (412) Zeuner, M.; Schmidt, P. J.; Schnick, W. One-Pot Synthesis of Single-Source Precursors for Nanocrystalline LED Phosphors M₂Si₅N₈:Eu²⁺ (M = Sr, Ba). *Chem. Mater.* **2009**, *21*, 2467–2473.
- (413) Zhang, H.; Qiao, J.; Li, G.; Li, S.; Wang, G.; Wang, J.; Song, Y. Preparation of Ce⁴⁺-doped BaZrO₃ by Hydrothermal Method and application in Dual-frequent Sonocatalytic Degradation of Norfloxacin in aqueous Solution. *Ultrason. Sonochem.* **2018**, *42*, 356–367.
- (414) Artiglia, L.; Agnoli, S.; Paganini, M. C.; Cattelan, M.; Granozzi, G. TiO₂@CeO_x Core–Shell Nanoparticles as Artificial Enzymes With Peroxidase-Like Activity. *ACS Appl. Mater. Interfaces* **2014**, *6*, 20130–20136.
- (415) Xiong, Z.; Zhao, Y.; Zhang, J.; Zheng, C. Efficient Photocatalytic Reduction of CO₂ Into Liquid Products Over Cerium Doped Titania Nanoparticles Synthesized by a Sol–gel auto-ignited Method. *Fuel Process. Technol.* **2015**, *135*, 6–13.
- (416) Si, R.; Zhang, Y.-W.; Li, S.-J.; Lin, B.-X.; Yan, C.-H. Urea-Based Hydrothermally Derived Homogeneous Nanostructured Ce_{1-x}Zr_xO₂ (x = 0–0.8) Solid Solutions: A Strong Correlation Between Oxygen Storage Capacity and Lattice Strain. *J. Phys. Chem. B* **2004**, *108*, 12481–12488.
- (417) Katta, L.; Sudarsanam, P.; Thrimurthulu, G.; Reddy, B. M. Doped Nanosized Ceria Solid Solutions for Low Temperature Soot Oxidation: Zirconium Versus Lanthanum Promoters. *Appl. Catal., B* **2010**, *101*, 101–108.
- (418) Hernández, S.; Gionco, C.; Husak, T.; Castellino, M.; Muñoz-Tabares, J. A.; Tolod, K. R.; Giamello, E.; Paganini, M. C.; Russo, N. Insights Into the Sunlight-Driven Water Oxidation by Ce and Er-Doped ZrO₂. *Front. Chem.* **2018**, *6*, 368.
- (419) Liu, Y.; Fang, P.; Cheng, Y.; Gao, Y.; Chen, F.; Liu, Z.; Dai, Y. Study on Enhanced Photocatalytic Performance of Cerium Doped TiO₂-based Nanosheets. *Chem. Eng. J.* **2013**, *219*, 478–485.
- (420) Charbonnière, L. J.; Hildebrandt, N. Lanthanide Complexes and Quantum Dots: a Bright Wedding For resonance Energy Transfer. *Eur. J. Inorg. Chem.* **2008**, *2008*, 3241–3251.
- (421) Wu, P.; Yan, X.-P. Doped Quantum Dots for Chemo/biosensing and Bioimaging. *Chem. Soc. Rev.* **2013**, *42*, 5489–5521.
- (422) Dethlefsen, J. R.; Mikhailovsky, A. A.; Burks, P. T.; Døssing, A.; Ford, P. C. Lanthanide Modification of CdSe/ZnS Core/Shell Quantum Dots. *J. Phys. Chem. C* **2012**, *116*, 23713–23720.
- (423) Mukherjee, P.; Sloan, R. F.; Shade, C. M.; Waldeck, D. H.; Petoud, S. A Postsynthetic Modification of II–VI Semiconductor Nanoparticles to Create Tb³⁺ and Eu³⁺ Luminophores. *J. Phys. Chem. C* **2013**, *117*, 14451–14460.
- (424) Chen, L.; Zhang, J.; Lu, S.; Ren, X.; Wang, X. On the Energy Transfer From Nanocrystalline ZnS to Tb³⁺ Ions Confined in Reverse Micelles. *Chem. Phys. Lett.* **2005**, *409*, 144.
- (425) Wang, Y.; Liang, X.; Liu, E.; Hu, X.; Fan, J. Incorporation of Lanthanide (Eu³⁺) Ions in ZnS Semiconductor Quantum Dots With a Trapped-dopant Model and Their Photoluminescence Spectroscopy Study. *Nanotechnology* **2015**, *26*, 375601.
- (426) Brandt, R. E.; Poindexter, J. R.; Gorai, P.; Kurchin, R. C.; Hoye, R. L. Z.; Nienhaus, L.; Wilson, M. W. B.; Polizzotti, J. A.; Sereika, R.; Zaltauskas, R.; et al. Searching for “Defect-Tolerant” Photovoltaic Materials: Combined Theoretical and Experimental Screening. *Chem. Mater.* **2017**, *29*, 4667–4674.
- (427) Buchtelova, H.; Strmiska, V.; Skubalova, Z.; Dostalova, S.; Michalek, P.; Krizkova, S.; Hynek, D.; Kalina, L.; Richtera, L.; Moullick, A.; et al. Improving Cytocompatibility of CdTe Quantum Dots by Schiff-base-coordinated Lanthanides Surface Doping. *J. Nanobiotechnol.* **2018**, *16*, 43.
- (428) Chen, W.; Malm, J.-O.; Zwiler, V.; Huang, Y.; Liu, S.; Wallenberg, R.; Bovin, J.-O.; Samuelson, L. Energy Structure and Fluorescence of Eu²⁺ in ZnS:Eu Nanoparticles. *Phys. Rev. B: Condens. Matter Mater. Phys.* **2000**, *61*, 11021.
- (429) Horoz, S. Effect of Eu²⁺ Doping on Structural, optical, Magnetic and Photovoltaic Properties of ZnS Quantum Dots. *Superlattices Microstruct.* **2017**, *111*, 1043–1049.
- (430) Marin, R.; Jaque, D. Doping Lanthanide Ions in Colloidal Semiconductor Nanocrystals for Brighter Photoluminescence. *Chem. Rev.* **2021**, *121*, 1425–1462.
- (431) Tan, H.; Che, F.; Wei, M.; Zhao, Y.; Saidaminov, M. I.; Todorović, P.; Broberg, D.; Walters, G.; Tan, F.; Zhuang, T.; et al. Dipolar Cations Confer Defect Tolerance in Wide-bandgap Metal Halide Perovskites. *Nat. Commun.* **2018**, *9*, 3100.
- (432) Huang, H.; Bodnarchuk, M. I.; Kershaw, S. V.; Kovalenko, M. V.; Rogach, A. L. Lead Halide Perovskite Nanocrystals in the Research Spotlight: Stability and Defect Tolerance. *ACS Energy Lett.* **2017**, *2*, 2071–2083.
- (433) Akkerman, Q. A.; Rainò, G.; Kovalenko, M. V.; Manna, L. Genesis, Challenges and Opportunities for Colloidal Lead Halide Perovskite Nanocrystals. *Nat. Mater.* **2018**, *17*, 394–405.
- (434) Swarnkar, A.; Ravi, V. K.; Nag, A. Beyond Colloidal Cesium Lead Halide Perovskite Nanocrystals: Analogous Metal Halides and Doping. *ACS Energy Lett.* **2017**, *2*, 1089–1098.
- (435) Kang, J.; Wang, L.-W. High Defect Tolerance in Lead Halide Perovskite CsPbBr₃. *J. Phys. Chem. Lett.* **2017**, *8*, 489–493.
- (436) Ma, J.-P.; Chen, Y.-M.; Zhang, L.-M.; Guo, S.-Q.; Liu, J.-D.; Li, H.; Ye, B.-J.; Li, Z.-Y.; Zhou, Y.; Zhang, B.-B.; et al. Insights Into the Local Structure of Dopants, Doping Efficiency, and Luminescence Properties of Lanthanide-doped CsPbCl₃ Perovskite Nanocrystals. *J. Mater. Chem. C* **2019**, *7*, 3037–3048.
- (437) Mir, W. J.; Sheikh, T.; Arfin, H.; Xia, Z.; Nag, A. Lanthanide Doping in Metal Halide Perovskite Nanocrystals: Spectral Shifting, Quantum Cutting and Optoelectronic applications. *NPG Asia Mater.* **2020**, *12*, 9.
- (438) Locardi, F.; Cirignano, M.; Baranov, D.; Dang, Z.; Prato, M.; Drago, F.; Ferretti, M.; Pinchetti, V.; Fanciulli, M.; Brovelli, S.; et al. Colloidal Synthesis of Double Perovskite Cs₂AgInCl₆ and Mn-Doped Cs₂AgInCl₆ Nanocrystals. *J. Am. Chem. Soc.* **2018**, *140*, 12989–12995.
- (439) Luo, J.; Wang, X.; Li, S.; Liu, J.; Guo, Y.; Niu, G.; Yao, L.; Fu, Y.; Gao, L.; Dong, Q.; et al. Efficient and Stable Emission of Warm-white Light From Lead-free Halide Double Perovskites. *Nature* **2018**, *563*, 541–545.
- (440) Slavney, A. H.; Leppert, L.; Saldívar Valdes, A.; Bartesaghi, D.; Savenije, T. J.; Neaton, J. B.; Karunadasa, H. I. *Angew. Chem., Int. Ed.* **2018**, *57*, 12765–12770.
- (441) Yang, B.; Chen, J.; Yang, S.; Hong, F.; Sun, L.; Han, P.; Pullerits, T.; Deng, W.; Han, K. Lead-Free Silver-Bismuth Halide

- Double Perovskite Nanocrystals. *Angew. Chem., Int. Ed.* **2018**, *57*, 5359–5363.
- (442) Yang, B.; Pan, W.; Wu, H.; Niu, G.; Yuan, J.-H.; Xue, K.-H.; Yin, L.; Du, X.; Miao, X.-S.; Yang, X.; et al. Heteroepitaxial Passivation of $\text{Cs}_2\text{AgBiBr}_6$ Wafers With Suppressed Ionic Migration for X-ray Imaging. *Nat. Commun.* **2019**, *10*, 1989.
- (443) Hu, Q.; Li, Z.; Tan, Z.; Song, H.; Ge, C.; Niu, G.; Han, J.; Tang, J. Rare Earth Ion-Doped CsPbBr_3 Nanocrystals. *Adv. Opt. Mater.* **2018**, *6*, 1700864.
- (444) Pan, G.; Bai, X.; Yang, D.; Chen, X.; Jing, P.; Qu, S.; Zhang, L.; Zhou, D.; Zhu, J.; Xu, W.; et al. Doping Lanthanide Into Perovskite Nanocrystals: Highly Improved and Expanded Optical Properties. *Nano Lett.* **2017**, *17*, 8005–8011.
- (445) Mir, W. J.; Mahor, Y.; Lohar, A.; Jagadeeswararao, M.; Das, S.; Mahamuni, S.; Nag, A. Postsynthesis Doping of Mn and Yb Into CsPbX_3 ($X = \text{Cl, Br, or I}$) Perovskite Nanocrystals for Down-conversion Emission. *Chem. Mater.* **2018**, *30*, 8170–8178.
- (446) Cao, Q.; Ilyas, A.; Zhang, S.; Ju, Z.; Sun, F.; Liu, T.; Yang, Y.; Lu, Y.; Liu, X.; Deng, R. Lanthanide-doping Enables Kinetic Control Growth of Deep-blue Two-monolayer Halide Perovskite Nanoplatelets. *Nanoscale* **2021**, *13*, 11552–11560.
- (447) Yuan, R.; Shen, L.; Shen, C.; Liu, J.; Zhou, L.; Xiang, W.; Liang, X. $\text{CsPbBr}_3:\text{xEu}^{3+}$ Perovskite QD Borosilicate Glass: a New Member of the Luminescent Material Family. *Chem. Commun.* **2018**, *54*, 3395–3398.
- (448) Li, X.; Yu, Y.; Hong, J.; Feng, Z.; Guan, X.; Chen, D.; Zheng, Z. Optical Temperature Sensing of Eu^{3+} -doped Oxyhalide Glasses Containing CsPbBr_3 Perovskite Quantum Dots. *J. Lumin.* **2020**, *219*, 116897.
- (449) Huang, J.; Lei, T.; Siron, M.; Zhang, Y.; Yu, S.; Seeler, F.; Dehestani, A.; Quan, L. N.; Schierle-Arndt, K.; Yang, P. Lead-free Cesium Europium Halide Perovskite Nanocrystals. *Nano Lett.* **2020**, *20*, 3734–3739.
- (450) Wang, L.; Zhou, H.; Hu, J.; Huang, B.; Sun, M.; Dong, B.; Zheng, G.; Huang, Y.; Chen, Y.; Li, L.; et al. A Eu^{3+} - Eu^{2+} Ion Redox Shuttle Imparts Operational Durability to Pb-I Perovskite Solar Cells. *Science* **2019**, *363*, 265–270.
- (451) Crane, M. J.; Kroupa, D. M.; Roh, J. Y.; Anderson, R. T.; Smith, M. D.; Gamelin, D. R. Single-Source Vapor Deposition of Quantum-Cutting $\text{Yb}^{3+}:\text{CsPb}(\text{Cl}_{1-x}\text{Br}_x)_3$ and Other Complex Metal-Halide Perovskites. *ACS Appl. Energy Mater.* **2019**, *2*, 4560–4565.
- (452) Shannon, R. Revised Effective Ionic Radii and Systematic Studies of Interatomic Distances in Halides and Chalcogenides. *Acta Crystallogr., Sect. A: Cryst. Phys., Diffraction, Theor. Gen. Crystallogr.* **1976**, *32*, 751–767.
- (453) Moon, B. J.; Kim, S. J.; Lee, S.; Lee, A.; Lee, H.; Lee, D. S.; Kim, T.-W.; Lee, S.-K.; Bae, S.; Lee, S. H. Rare-Earth-Element-Ytterbium-Substituted Lead-Free Inorganic Perovskite Nanocrystals for Optoelectronic Applications. *Adv. Mater.* **2019**, *31*, 1901716.
- (454) Milstein, T. J.; Kroupa, D. M.; Gamelin, D. R. Picosecond Quantum Cutting Generates Photoluminescence Quantum Yields Over 100% in Ytterbium-Doped CsPbCl_3 Nanocrystals. *Nano Lett.* **2018**, *18*, 3792–3799.
- (455) Milstein, T. J.; Kluherz, K. T.; Kroupa, D. M.; Erickson, C. S.; De Yoreo, J. J.; Gamelin, D. R. Anion Exchange and the Quantum-Cutting Energy Threshold in Ytterbium-Doped $\text{CsPb}(\text{Cl}_{1-x}\text{Br}_x)_3$ Perovskite Nanocrystals. *Nano Lett.* **2019**, *19*, 1931–1937.
- (456) Luo, X.; Ding, T.; Liu, X.; Liu, Y.; Wu, K. Quantum-Cutting Luminescent Solar Concentrators Using Ytterbium-Doped Perovskite Nanocrystals. *Nano Lett.* **2019**, *19*, 338–341.
- (457) Zeng, M.; Artizzu, F.; Liu, J.; Singh, S.; Locardi, F.; Mara, D.; Hens, Z.; Van Deun, R. Boosting the Er^{3+} 1.5 μm Luminescence in CsPbCl_3 Perovskite Nanocrystals for Photonic Devices Operating at Telecommunication Wavelengths. *ACS Appl. Nano Mater.* **2020**, *3*, 4699–4707.
- (458) Lee, W.; Hong, S.; Kim, S. Colloidal Synthesis of Lead-Free Silver–Indium Double-Perovskite $\text{Cs}_2\text{AgInCl}_6$ Nanocrystals and Their Doping With Lanthanide Ions. *J. Phys. Chem. C* **2019**, *123*, 2665–2672.
- (459) Chen, N.; Cai, T.; Li, W.; Hills-Kimball, K.; Yang, H.; Que, M.; Nagaoka, Y.; Liu, Z.; Yang, D.; Dong, A.; et al. Yb- and Mn-Doped Lead-Free Double Perovskite $\text{Cs}_2\text{AgBiX}_6$ ($X = \text{Cl}^-$ and Br^-) Nanocrystals. *ACS Appl. Mater. Interfaces* **2019**, *11*, 16855–16863.
- (460) Liu, Y.; Rong, X.; Li, M.; Molokeev, M. S.; Zhao, J.; Xia, Z. Incorporating Rare-Earth Terbium(III) Ions Into $\text{Cs}_2\text{AgInCl}_6:\text{Bi}$ Nanocrystals Toward Tunable Photoluminescence. *Angew. Chem., Int. Ed.* **2020**, *59*, 11634–11640.
- (461) Duan, J.; Zhao, Y.; Yang, X.; Wang, Y.; He, B.; Tang, Q. Lanthanide Ions Doped CsPbBr_3 Halides for HTM-Free 10.14%-Efficiency Inorganic Perovskite Solar Cell With an Ultrahigh Open-Circuit Voltage of 1.594 V. *Adv. Energy Mater.* **2018**, *8*, 1802346.
- (462) Wu, X.; Li, H.; Wang, K.; Sun, X.; Wang, L. $\text{CH}_3\text{NH}_3\text{Pb}_{1-x}\text{Eu}_x\text{I}_3$ Mixed Halide Perovskite for Hybrid Solar Cells: the Impact of Divalent Europium Doping on Efficiency and Stability. *RSC Adv.* **2018**, *8*, 11095–11101.
- (463) Wang, K.; Zheng, L.; Zhu, T.; Yao, X.; Yi, C.; Zhang, X.; Cao, Y.; Liu, L.; Hu, W.; Gong, X. Efficient Perovskite Solar Cells by Hybrid Perovskites Incorporated With Heterovalent Neodymium Cations. *Nano Energy* **2019**, *61*, 352–360.
- (464) Jena, A. K.; Kulkarni, A.; Sanehira, Y.; Ikegami, M.; Miyasaka, T. Stabilization of α - CsPbI_3 in Ambient Room Temperature Conditions by Incorporating Eu Into CsPbI_3 . *Chem. Mater.* **2018**, *30*, 6668–6674.
- (465) Xiang, W.; Wang, Z.; Kubicki, D. J.; Tress, W.; Luo, J.; Prochowicz, D.; Akin, S.; Emsley, L.; Zhou, J.; Dietler, G.; et al. Europium-Doped CsPbI_2Br for Stable and Highly Efficient Inorganic Perovskite Solar Cells. *Joule* **2019**, *3*, 205–214.
- (466) Sahli, F.; Werner, J.; Kamino, B. A.; Bräuninger, M.; Monnard, R.; Paviet-Salomon, B.; Barraud, L.; Ding, L.; Diaz Leon, J. J.; Sacchetto, D.; et al. Fully Textured Monolithic Perovskite/silicon Tandem Solar Cells With 25.2% Power Conversion Efficiency. *Nat. Mater.* **2018**, *17*, 820–826.
- (467) Werner, J.; Sahli, F.; Fu, F.; Diaz Leon, J. J.; Walter, A.; Kamino, B. A.; Niesen, B.; Nicolay, S.; Jeangros, Q.; Ballif, C. Perovskite/Perovskite/Silicon Monolithic Triple-Junction Solar Cells With a Fully Textured Design. *ACS Energy Lett.* **2018**, *3*, 2052–2058.
- (468) Abednatanzi, S.; Gohari Derakhshandeh, P.; Depauw, H.; Coudert, F.-X.; Vrielinck, H.; Van Der Voort, P.; Leus, K. Mixed-metal Metal–organic Frameworks. *Chem. Soc. Rev.* **2019**, *48*, 2535–2565.
- (469) Rice, A. M.; Martin, C. R.; Galitskiy, V. A.; Berseneva, A. A.; Leith, G. A.; Shustova, N. B. Photophysics Modulation in Photo-switchable Metal–Organic Frameworks. *Chem. Rev.* **2020**, *120*, 8790–8813.
- (470) Wu, S.; Min, H.; Shi, W.; Cheng, P. Multicenter Metal–Organic Framework-Based Ratiometric Fluorescent Sensors. *Adv. Mater.* **2020**, *32*, 1805871.
- (471) Cui, Y.; Li, B.; He, H.; Zhou, W.; Chen, B.; Qian, G. Metal–Organic Frameworks as Platforms for Functional Materials. *Acc. Chem. Res.* **2016**, *49*, 483–493.
- (472) Howarth, A. J.; Liu, Y.; Li, P.; Li, Z.; Wang, T. C.; Hupp, J. T.; Farha, O. K. Chemical, Thermal and Mechanical Stabilities of Metal–organic Frameworks. *Nat. Rev. Mater.* **2016**, *1*, 15018.
- (473) Allendorf, M. D.; Bauer, C. A.; Bhakta, R. K.; Houk, R. J. T. Luminescent Metal–organic Frameworks. *Chem. Soc. Rev.* **2009**, *38*, 1330–1352.
- (474) Rocha, J.; Carlos, L. D.; Paz, F. A. A.; Ananias, D. Luminescent Multifunctional Lanthanides-based Metal–organic Frameworks. *Chem. Soc. Rev.* **2011**, *40*, 926–940.
- (475) An, J.; Rosi, N. L. Tuning MOF CO_2 Adsorption Properties via Cation Exchange. *J. Am. Chem. Soc.* **2010**, *132*, 5578–5579.
- (476) Zhu, M.; Song, X.-Z.; Song, S.-Y.; Zhao, S.-N.; Meng, X.; Wu, L.-L.; Wang, C.; Zhang, H.-J. A Temperature-Responsive Smart Europium Metal–Organic Framework Switch for Reversible Capture and Release of Intrinsic Eu^{3+} Ions. *Adv. Sci.* **2015**, *2*, 1500012.
- (477) Yang, X.; Lin, X.; Zhao, Y.; Zhao, Y. S.; Yan, D. Lanthanide Metal–Organic Framework Microrods: Colored Optical Waveguides

- and Chiral Polarized Emission. *Angew. Chem., Int. Ed.* **2017**, *56*, 7853–7857.
- (478) Skorupskii, G.; Trump, B. A.; Kasel, T. W.; Brown, C. M.; Hendon, C. H.; Dinca, M. Efficient and Tunable One-dimensional Charge Transport in Layered Lanthanide Metal–organic Frameworks. *Nat. Chem.* **2020**, *12*, 131–136.
- (479) Zhou, Y.; Chen, H.-H.; Yan, B. An Eu³⁺ Post-functionalized Nanosized Metal–organic Framework for Cation Exchange-based Fe³⁺-sensing in an aqueous Environment. *J. Mater. Chem. A* **2014**, *2*, 13691–13697.
- (480) Dou, Z.; Yu, J.; Cui, Y.; Yang, Y.; Wang, Z.; Yang, D.; Qian, G. Luminescent Metal–Organic Framework Films As Highly Sensitive and Fast-Response Oxygen Sensors. *J. Am. Chem. Soc.* **2014**, *136*, 5527–5530.
- (481) Das, S.; Kim, H.; Kim, K. Metathesis in Single Crystal: Complete and Reversible Exchange of Metal Ions Constituting the Frameworks of Metal–Organic Frameworks. *J. Am. Chem. Soc.* **2009**, *131*, 3814–3815.
- (482) Hendrickx, K.; Joos, J. J.; De Vos, A.; Poelman, D.; Smet, P. F.; Van Speybroeck, V.; Van Der Voort, P.; Lejaeghere, K. Exploring Lanthanide Doping in UiO-66: A Combined Experimental and Computational Study of the Electronic Structure. *Inorg. Chem.* **2018**, *57*, 5463–5474.
- (483) Falcaro, P.; Furukawa, S. Doping Light Emitters Into Metal–Organic Frameworks. *Angew. Chem., Int. Ed.* **2012**, *51*, 8431–8433.
- (484) Pagis, C.; Ferbinteanu, M.; Rothenberg, G.; Tanase, S. Lanthanide-Based Metal Organic Frameworks: Synthetic Strategies and Catalytic Applications. *ACS Catal.* **2016**, *6*, 6063–6072.
- (485) Cui, Y.; Chen, B.; Qian, G. Lanthanide Metal-organic Frameworks for Luminescent Sensing and Light-emitting applications. *Coord. Chem. Rev.* **2014**, *273*, 76–86.
- (486) Sava, D. F.; Rohwer, L. E. S.; Rodriguez, M. A.; Nenoff, T. M. Intrinsic Broad-Band White-Light Emission by a Tuned, Corrugated Metal–Organic Framework. *J. Am. Chem. Soc.* **2012**, *134*, 3983–3986.
- (487) Li, Z.; Wang, G.; Ye, Y.; Li, B.; Li, H.; Chen, B. Loading Photochromic Molecules Into a Luminescent Metal–Organic Framework for Information Anticounterfeiting. *Angew. Chem., Int. Ed.* **2019**, *58*, 18025–18031.
- (488) Troyano, J.; Carné-Sánchez, A.; Avci, C.; Imaz, I.; Maspoch, D. Colloidal Metal–organic Framework Particles: the Pioneering Case of ZIF-8. *Chem. Soc. Rev.* **2019**, *48*, 5534–5546.
- (489) Luo, T.-Y.; Liu, C.; Eliseeva, S. V.; Muldoon, P. F.; Petoud, S.; Rosi, N. L. Rare Earth pcu Metal–Organic Framework Platform Based on RE₄(μ₃-OH)₄(COO)₆²⁺ Clusters: Rational Design, Directed Synthesis, and Deliberate Tuning of Excitation Wavelengths. *J. Am. Chem. Soc.* **2017**, *139*, 9333–9340.
- (490) Zhang, L.; Yuan, S.; Feng, L.; Guo, B.; Qin, J.-S.; Xu, B.; Lollar, C.; Sun, D.; Zhou, H.-C. Pore-Environment Engineering With Multiple Metal Sites in Rare-Earth Porphyrinic Metal–Organic Frameworks. *Angew. Chem., Int. Ed.* **2018**, *57*, S095–S099.
- (491) Feng, L.; Wang, Y.; Zhang, K.; Wang, K.-Y.; Fan, W.; Wang, X.; Powell, J. A.; Guo, B.; Dai, F.; Zhang, L.; et al. Molecular Pivot-Hinge Installation to Evolve Topology in Rare-Earth Metal–Organic Frameworks. *Angew. Chem., Int. Ed.* **2019**, *58*, 16682–16690.
- (492) Yao, Q.; Bermejo Gómez, A.; Su, J.; Pascanu, V.; Yun, Y.; Zheng, H.; Chen, H.; Liu, L.; Abdelhamid, H. N.; Martín-Matute, B.; et al. Series of Highly Stable Isorecticular Lanthanide Metal–Organic Frameworks With Expanding Pore Size and Tunable Luminescent Properties. *Chem. Mater.* **2015**, *27*, 5332–5339.
- (493) Duan, T.-W.; Yan, B. Hybrids Based on Lanthanide Ions Activated Yttrium Metal–organic Frameworks: Functional assembly, Polymer Film Preparation and Luminescence Tuning. *J. Mater. Chem. C* **2014**, *2*, S098–S104.
- (494) Xue, D.-X.; Belmabkhout, Y.; Shekhah, O.; Jiang, H.; Adil, K.; Cairns, A. J.; Eddaoudi, M. Tunable Rare Earth fcu-MOF Platform: Access to Adsorption Kinetics Driven Gas/Vapor Separations via Pore Size Contraction. *J. Am. Chem. Soc.* **2015**, *137*, 5034–5040.
- (495) Assen, A. H.; Yassine, O.; Shekhah, O.; Eddaoudi, M.; Salama, K. N. MOFs for the Sensitive Detection of Ammonia: Development of fcu-MOF Thin Films as Effective Chemical Capacitive Sensors. *ACS Sensors* **2017**, *2*, 1294–1301.
- (496) Cui, Y.; Xu, H.; Yue, Y.; Guo, Z.; Yu, J.; Chen, Z.; Gao, J.; Yang, Y.; Qian, G.; Chen, B. A Luminescent Mixed-Lanthanide Metal–Organic Framework Thermometer. *J. Am. Chem. Soc.* **2012**, *134*, 3979–3982.
- (497) Cadiou, A.; Brites, C. D. S.; Costa, P. M. F. J.; Ferreira, R. A. S.; Rocha, J.; Carlos, L. D. Ratiometric Nanothermometer Based on an Emissive Ln³⁺-Organic Framework. *ACS Nano* **2013**, *7*, 7213–7218.
- (498) D’Vries, R. F.; Álvarez-García, S.; Sneško, N.; Bausá, L. E.; Gutiérrez-Puebla, E.; de Andrés, A.; Monge, M. A. Multimetal Rare Earth MOFs for Lighting and Thermometry: Tailoring Color and Optimal Temperature Range Through Enhanced Disulfobenzoic Triplet Phosphorescence. *J. Mater. Chem. C* **2013**, *1*, 6316–6324.
- (499) Zhao, S.-N.; Li, L.-J.; Song, X.-Z.; Zhu, M.; Hao, Z.-M.; Meng, X.; Wu, L.-L.; Feng, J.; Song, S.-Y.; Wang, C.; et al. Lanthanide Ion Codoped Emitters for Tailoring Emission Trajectory and Temperature Sensing. *Adv. Funct. Mater.* **2015**, *25*, 1463–1469.
- (500) Miyata, K.; Konno, Y.; Nakanishi, T.; Kobayashi, A.; Kato, M.; Fushimi, K.; Hasegawa, Y. Chameleon Luminophore for Sensing Temperatures: Control of Metal-to-Metal and Energy Back Transfer in Lanthanide Coordination Polymers. *Angew. Chem., Int. Ed.* **2013**, *52*, 6413–6416.
- (501) Chen, D.-H.; Haldar, R.; Neumeier, B. L.; Fu, Z.-H.; Feldmann, C.; Wöll, C.; Redel, E. Tunable Emission in Heteroepitaxial Ln-SURMOFs. *Adv. Funct. Mater.* **2019**, *29*, 1903086.
- (502) Yao, Y.; Gao, Z.; Lv, Y.; Lin, X.; Liu, Y.; Du, Y.; Hu, F.; Zhao, Y. S. Heteroepitaxial Growth of Multiblock Ln-MOF Microrods for Photonic Barcodes. *Angew. Chem., Int. Ed.* **2019**, *58*, 13803–13807.
- (503) Usman, M.; Mendiratta, S.; Lu, K.-L. Semiconductor Metal–Organic Frameworks: Future Low-Bandgap Materials. *Adv. Mater.* **2017**, *29*, 1605071.
- (504) Sun, L.; Campbell, M. G.; Dinca, M. Electrically Conductive Porous Metal–Organic Frameworks. *Angew. Chem., Int. Ed.* **2016**, *55*, 3566–3579.
- (505) Xie, L. S.; Skorupskii, G.; Dinca, M. Electrically Conductive Metal–Organic Frameworks. *Chem. Rev.* **2020**, *120*, 8536–8580.
- (506) Zhang, S.-Y.; Wang, Z.-Y.; Gao, J.; Wang, K.; Gianolio, E.; Aime, S.; Shi, W.; Zhou, Z.; Cheng, P.; Zaworotko, M. J. A Gadolinium(III) Zeolite-like Metal–Organic-Framework-Based Magnetic Resonance Thermometer. *Chem.* **2019**, *5*, 1609–1618.
- (507) Novoselov, K. S.; Geim, A. K.; Morozov, S. V.; Jiang, D.; Zhang, Y.; Dubonos, S. V.; Grigorieva, I. V.; Firsov, A. A. Electric Field Effect in Atomically Thin Carbon Films. *Science* **2004**, *306*, 666–669.
- (508) Shinde, S. S.; Sami, A.; Lee, J.-H. Lanthanides-based Graphene Catalysts for High Performance Hydrogen Evolution and Oxygen Reduction. *Electrochim. Acta* **2016**, *214*, 173–181.
- (509) Feng, X.; Chen, H.; Jiang, F.; Wang, X. In-situ Self-sacrificial Fabrication of Lanthanide Hydroxycarbonates/graphitic Carbon Nitride Heterojunctions: Nitrogen Photofixation Under Simulated Solar Light Irradiation. *Chem. Eng. J.* **2018**, *347*, 849–859.
- (510) Ji, S.; Qu, Y.; Wang, T.; Chen, Y.; Wang, G.; Li, X.; Dong, J.; Chen, Q.; Zhang, W.; Zhang, Z.; et al. Rare-Earth Single Erbium Atoms for Enhanced Photocatalytic CO₂ Reduction. *Angew. Chem., Int. Ed.* **2020**, *59*, 10651–10744.
- (511) Zhu, Z.; Ma, C.; Yu, K.; Lu, Z.; Liu, Z.; Huo, P.; Tang, X.; Yan, Y. Synthesis Ce-doped Biomass Carbon-based g-C₃N₄ via Plant Growing Guide and Temperature-programmed Technique for Degrading 2-Mercaptobenzothiazole. *Appl. Catal., B* **2020**, *268*, 118432.
- (512) Zhao, Q.; Lu, Q.; Liu, Y.; Zhang, M. Two-dimensional Dy Doped MoS₂ Ferromagnetic Sheets. *Appl. Surf. Sci.* **2019**, *471*, 118–123.
- (513) Liu, J.; Van Deun, R.; Kaczmarek, A. M. Optical Thermometry of MoS₂:Eu³⁺ 2D Luminescent Nanosheets. *J. Mater. Chem. C* **2016**, *4*, 9937–9941.

- (514) Bai, G.; Yang, Z.; Lin, H.; Jie, W.; Hao, J. Lanthanide Yb/Er Co-doped Semiconductor Layered WSe₂ Nanosheets With Near-infrared Luminescence at Telecommunication Wavelengths. *Nanoscale* **2018**, *10*, 9261–9267.
- (515) Bai, G.; Yuan, S.; Zhao, Y.; Yang, Z.; Choi, S. Y.; Chai, Y.; Yu, S. F.; Lau, S. P.; Hao, J. 2D Layered Materials of Rare-Earth Er-Doped MoS₂ With NIR-to-NIR Down- and Up-Conversion Photoluminescence. *Adv. Mater.* **2016**, *28*, 7472–7477.
- (516) Xu, J.; Chen, X.; Xu, Y.; Du, Y.; Yan, C. Ultrathin 2D Rare-Earth Nanomaterials: Compositions, Syntheses, and Applications. *Adv. Mater.* **2020**, *32*, 1806461.
- (517) Zhang, L.; Kang, W.; Ma, Q.; Xie, Y.; Jia, Y.; Deng, N.; Zhang, Y.; Ju, J.; Cheng, B. Two-dimensional Acetate-based Light Lanthanide Fluoride Nanomaterials (F–Ln, Ln = La, Ce, Pr, and Nd): Morphology, Structure, Growth Mechanism, and Stability. *J. Am. Chem. Soc.* **2019**, *141*, 13134–13142.
- (518) Sun, Y.; Wang, Q.; Chen, C.; Tan, X.; Wang, X. Interaction Between Eu(III) and Graphene Oxide Nanosheets Investigated by Batch and Extended X-ray Absorption Fine Structure Spectroscopy and by Modeling Techniques. *Environ. Sci. Technol.* **2012**, *46*, 6020–6027.
- (519) Xu, D.; Chen, W.; Zeng, M.; Xue, H.; Chen, Y.; Sang, X.; Xiao, Y.; Zhang, T.; Unocic, R. R.; Xiao, K.; et al. Crystal-Field Tuning of Photoluminescence in Two-Dimensional Materials With Embedded Lanthanide Ions. *Angew. Chem., Int. Ed.* **2018**, *57*, 755–759.
- (520) Meng, M.; Ma, X. Improving the Photoelectric Characteristics of MoS₂ Thin Films by Doping Rare Earth Element Erbium. *Nanoscale Res. Lett.* **2016**, *11*, 513.
- (521) Maddi, C.; Aswin, J. R.; Scott, A.; Aslam, Z.; Willneff, E.; Adarsh, K. N. V. D.; Jha, A. Structural, Spectroscopic, and Excitonic Dynamic Characterization in Atomically Thin Yb³⁺-Doped MoS₂, Fabricated by Femtosecond Pulsed Laser Deposition. *Adv. Opt. Mater.* **2019**, *7*, 1900753.
- (522) Zhao, Q.; Zhang, H.; Liu, Y.; Zhu, M.; Zhang, M. Magnetic and Optical Properties of Two-dimensional SnS₂ Nanosheets Doped With Ho Ions. *Appl. Surf. Sci.* **2019**, *481*, 1370–1376.
- (523) Gándara, F.; Perles, J.; Snejko, N.; Iglesias, M.; Gómez-Lor, B.; Gutiérrez-Puebla, E.; Monge, M. A. Layered Rare-Earth Hydroxides: A Class of Pillared Crystalline Compounds for Intercalation Chemistry. *Angew. Chem., Int. Ed.* **2006**, *45*, 7998–8001.
- (524) Lee, B.-I.; Lee, K. S.; Lee, J. H.; Lee, I. S.; Byeon, S.-H. Synthesis of Colloidal aqueous Suspensions of a Layered Gadolinium Hydroxide: a Potential MRI Contrast Agent. *Dalton T.* **2009**, 2490–2495.
- (525) Hu, L.; Ma, R.; Ozawa, T. C.; Sasaki, T. Exfoliation of Layered Europium Hydroxide Into Unilamellar Nanosheets. *Chem. - Asian J.* **2010**, *5*, 248–251.
- (526) Lee, B.-I.; Lee, E.-s.; Byeon, S.-H. Assembly of Layered Rare-Earth Hydroxide Nanosheets and SiO₂ Nanoparticles to Fabricate Multifunctional Transparent Films Capable of Combinatorial Color Generation. *Adv. Funct. Mater.* **2012**, *22*, 3562–3569.
- (527) Su, F.; Guo, R.; Yu, Z.; Li, J.; Liang, Z.; Shi, K.; Ma, S.; Sun, G.; Li, H. Layered Rare-earth Hydroxide (LRH, R = Tb, Y) Composites With Fluorescein: Delamination, Tunable Luminescence and application in Chemosensing for Detecting Fe(III) Ions. *Dalton T.* **2018**, *47*, 5380–5389.
- (528) Yang, W.; Li, Q.; Zheng, X.; Li, X.; Li, X. Luminescent Sensing Film Based on Sulfosalicylic Acid Modified Tb(III)-doped Yttrium Hydroxide Nanosheets. *J. Adv. Ceram.* **2018**, *7*, 352–361.
- (529) Zhao, Y.; Li, J.-G.; Guo, M.; Yang, X. Structural and Photoluminescent Investigation of LTbH/LEuH Nanosheets and Their Color-tunable Colloidal Hybrids. *J. Mater. Chem. C* **2013**, *1*, 3584–3592.
- (530) Liu, L.; Yu, M.; Zhang, J.; Wang, B.; Liu, W.; Tang, Y. Facile Fabrication of Color-tunable and White Light Emitting Nanocomposite Films Based on Layered Rare-earth Hydroxides. *J. Mater. Chem. C* **2015**, *3*, 2326–2333.
- (531) Lee, S. W.; Park, S. K.; Min, B.-K.; Kang, J.-G.; Sohn, Y. Structural/spectroscopic analyses and H₂/O₂/CO Responses of Thulium(III) Oxide Nanosquare Sheets. *Appl. Surf. Sci.* **2014**, *307*, 736–743.
- (532) Wang, Z.; Li, J.-G.; Zhu, Q.; Li, X.; Sun, X. Sacrificial Conversion of Layered Rare-earth Hydroxide (LRH) Nanosheets Into (Y_{1-x}Eu_x)PO₄ Nanophosphors and Investigation of Photoluminescence. *Dalton T.* **2016**, *45*, 5290–5299.
- (533) Li, H.; Tan, M.; Wang, X.; Li, F.; Zhang, Y.; Zhao, L.; Yang, C.; Chen, G. Temporal Multiplexed *In Vivo* Upconversion Imaging. *J. Am. Chem. Soc.* **2020**, *142*, 2023–2030.
- (534) Li, Y.; Zeng, S.; Hao, J. Non-Invasive Optical Guided Tumor Metastasis/Vessel Imaging by Using Lanthanide Nanoprobe With Enhanced Down-Shifting Emission Beyond 1500 nm. *ACS Nano* **2019**, *13*, 248–259.
- (535) Gu, Y.; Guo, Z.; Yuan, W.; Kong, M.; Liu, Y.; Liu, Y.; Gao, Y.; Feng, W.; Wang, F.; Zhou, J.; et al. High-sensitivity Imaging of Time-domain Near-infrared Light Transducer. *Nat. Photonics* **2019**, *13*, 525–531.
- (536) Maldiney, T.; Lecointre, A.; Viana, B.; Bessière, A.; Bessodes, M.; Gourier, D.; Richard, C.; Scherman, D. Controlling Electron Trap Depth To Enhance Optical Properties of Persistent Luminescence Nanoparticles for *In Vivo* Imaging. *J. Am. Chem. Soc.* **2011**, *133*, 11810–11815.
- (537) Sun, M.; Xu, L.; Ma, W.; Wu, X.; Kuang, H.; Wang, L.; Xu, C. Hierarchical Plasmonic Nanorods and Upconversion Core–Satellite Nanoassemblies for Multimodal Imaging-Guided Combination Phototherapy. *Adv. Mater.* **2016**, *28*, 898–904.
- (538) Sun, Y.; Peng, J.; Feng, W.; Li, F. Upconversion Nanophosphors NaLuF₄:Yb,Tm for Lymphatic Imaging *In Vivo* by Real-time Upconversion Luminescence Imaging Under Ambient Light and High-resolution X-ray CT. *Theranostics* **2013**, *3*, 346.
- (539) Yang, Y.; Sun, Y.; Cao, T.; Peng, J.; Liu, Y.; Wu, Y.; Feng, W.; Zhang, Y.; Li, F. Hydrothermal Synthesis of NaLuF₄:¹⁵³Sm,Yb,Tm Nanoparticles and Their application in Dual-modality Upconversion Luminescence and SPECT Bioimaging. *Biomaterials* **2013**, *34*, 774–783.
- (540) Ai, X.; Wang, Z.; Cheong, H.; Wang, Y.; Zhang, R.; Lin, J.; Zheng, Y.; Gao, M.; Xing, B. Multispectral Optoacoustic Imaging of Dynamic Redox Correlation and Pathophysiological Progression Utilizing Upconversion Nanoprobes. *Nat. Commun.* **2019**, *10*, 1087.
- (541) Jaque, D.; Richard, C.; Viana, B.; Soga, K.; Liu, X.; García Solé, J. Inorganic Nanoparticles for Optical Bioimaging. *Adv. Opt. Photonics* **2016**, *8*, 1–103.
- (542) Chen, G.; Yang, C.; Prasad, P. N. Nanophotonics and Nanochemistry: Controlling the Excitation Dynamics for Frequency Up- and Down-conversion in Lanthanide-doped Nanoparticles. *Acc. Chem. Res.* **2013**, *46*, 1474–1486.
- (543) Liu, Y.; Lu, Y.; Yang, X.; Zheng, X.; Wen, S.; Wang, F.; Vidal, X.; Zhao, J.; Liu, D.; Zhou, Z.; et al. Amplified Stimulated Emission in Upconversion Nanoparticles for Super-resolution Nanoscopy. *Nature* **2017**, *543*, 229–233.
- (544) Lee, C.; Xu, E. Z.; Liu, Y.; Teitelboim, A.; Yao, K.; Fernandez-Bravo, A.; Kotulska, A. M.; Nam, S. H.; Suh, Y. D.; Bednarkiewicz, A.; et al. Giant Nonlinear Optical Responses From Photon-avalanching Nanoparticles. *Nature* **2021**, *589*, 230–235.
- (545) Wen, S.; Liu, Y.; Wang, F.; Lin, G.; Zhou, J.; Shi, B.; Suh, Y. D.; Jin, D. Nanorods With Multidimensional Optical Information Beyond the Diffraction Limit. *Nat. Commun.* **2020**, *11*, 6047.
- (546) Liang, L.; Feng, Z.; Zhang, Q.; Cong, T. D.; Wang, Y.; Qin, X.; Yi, Z.; Ang, M. J. Y.; Zhou, L.; Feng, H.; et al. Continuous-wave Near-infrared Stimulated-emission Depletion Microscopy Using Down-shifting Lanthanide Nanoparticles. *Nat. Nanotechnol.* **2021**, *16*, 975–980.
- (547) Haase, M.; Schäfer, H. Upconverting Nanoparticles. *Angew. Chem., Int. Ed.* **2011**, *50*, S808–S829.
- (548) Dong, H.; Du, S.-R.; Zheng, X.-Y.; Lyu, G.-M.; Sun, L.-D.; Li, L.-D.; Zhang, P.-Z.; Zhang, C.; Yan, C.-H. Lanthanide Nanoparticles:

- From Design Toward Bioimaging and Therapy. *Chem. Rev.* **2015**, *115*, 10725–10815.
- (549) Chen, G.; Qiu, H.; Prasad, P. N.; Chen, X. Upconversion Nanoparticles: Design, Nanochemistry, and Applications in Theranostics. *Chem. Rev.* **2014**, *114*, 5161–5214.
- (550) Zhou, J.; Liu, Z.; Li, F. Upconversion Nanophosphors for Small-animal Imaging. *Chem. Soc. Rev.* **2012**, *41*, 1323–1349.
- (551) Zhou, J.; Liu, Q.; Feng, W.; Sun, Y.; Li, F. Upconversion Luminescent Materials: Advances and Applications. *Chem. Rev.* **2015**, *115*, 395–465.
- (552) Park, Y. I.; Lee, K. T.; Suh, Y. D.; Hyeon, T. Upconverting Nanoparticles: a Versatile Platform for Wide-field Two-photon Microscopy and Multi-modal *In Vivo* Imaging. *Chem. Soc. Rev.* **2015**, *44*, 1302–1317.
- (553) Zhou, J.; Chizhik, A. I.; Chu, S.; Jin, D. Single-particle Spectroscopy for Functional Nanomaterials. *Nature* **2020**, *579*, 41–50.
- (554) Bednarkiewicz, A.; Chan, E. M.; Kotulska, A.; Marciniak, L.; Prorok, K. Photon avalanche in Lanthanide Doped Nanoparticles for Biomedical applications: Super-resolution Imaging. *Nanoscale Horiz.* **2019**, *4*, 881–889.
- (555) Kolesov, R.; Lasse, S.; Rothfuchs, C.; Wieck, A. D.; Xia, K.; Kornher, T.; Wrachtrup, J. Superresolution Microscopy of Single Rare-Earth Emitters in YAG and H3 Centers in Diamond. *Phys. Rev. Lett.* **2018**, *120*, 033903.
- (556) Nam, S. H.; Bae, Y. M.; Park, Y. I.; Kim, J. H.; Kim, H. M.; Choi, J. S.; Lee, K. T.; Hyeon, T.; Suh, Y. D. Long-Term Real-Time Tracking of Lanthanide Ion Doped Upconverting Nanoparticles in Living Cells. *Angew. Chem., Int. Ed.* **2011**, *50*, 6093–6097.
- (557) Drees, C.; Raj, A. N.; Kurre, R.; Busch, K. B.; Haase, M.; Piehler, J. Engineered Upconversion Nanoparticles for Resolving Protein Interactions Inside Living Cells. *Angew. Chem., Int. Ed.* **2016**, *55*, 11668–11672.
- (558) Wang, F.; Wen, S.; He, H.; Wang, B.; Zhou, Z.; Shimoni, O.; Jin, D. Microscopic Inspection and Tracking of Single Upconversion Nanoparticles in Living Cells. *Light: Sci. Appl.* **2018**, *7*, 18007.
- (559) Xu, C. T.; Svenmarker, P.; Liu, H.; Wu, X.; Messing, M. E.; Wallenberg, L. R.; Andersson-Engels, S. High-Resolution Fluorescence Diffuse Optical Tomography Developed With Nonlinear Upconverting Nanoparticles. *ACS Nano* **2012**, *6* (6), 4788–4795.
- (560) Zeng, X.; Chen, S.; Weitemier, A.; Han, S.; Blasiak, A.; Prasad, A.; Zheng, K.; Yi, Z.; Luo, B.; Yang, L.-H.; et al. Visualization of Intra-neuronal Motor Protein Transport Through Upconversion Microscopy. *Angew. Chem., Int. Ed.* **2019**, *58*, 9262–9268.
- (561) Park, H. S.; Kim, J.; Cho, M. Y.; Cho, Y.-J.; Suh, Y. D.; Nam, S. H.; Hong, K. S. Effectual Labeling of Natural Killer Cells With Upconverting Nanoparticles by Electroporation for *In Vivo* Tracking and Biodistribution Assessment. *ACS Appl. Mater. Interfaces* **2020**, *12*, 49362–49370.
- (562) Ma, Y.; Bao, J.; Zhang, Y.; Li, Z.; Zhou, X.; Wan, C.; Huang, L.; Zhao, Y.; Han, G.; Xue, T. Mammalian Near-Infrared Image Vision Through Injectable and Self-Powered Retinal Nanoantennae. *Cell* **2019**, *177*, 243–255.
- (563) Tian, B.; Fernandez-Bravo, A.; Najafiaghdam, H.; Torquato, N. A.; Altoe, M. V. P.; Teitelboim, A.; Tajon, C. A.; Tian, Y.; Borys, N. J.; Barnard, E. S.; et al. Low Irradiance Multiphoton Imaging With Alloyed Lanthanide Nanocrystals. *Nat. Commun.* **2018**, *9*, 3082.
- (564) Gargas, D. J.; Chan, E. M.; Ostrowski, A. D.; Aloni, S.; Altoe, M. V. P.; Barnard, E. S.; Sanii, B.; Urban, J. J.; Milliron, D. J.; Cohen, B. E.; et al. Engineering Bright Sub-10-nm Upconverting Nanocrystals for Single-molecule Imaging. *Nat. Nanotechnol.* **2014**, *9*, 300–305.
- (565) Smith, A. M.; Mancini, M. C.; Nie, S. Second Window for *In Vivo* Imaging. *Nat. Nanotechnol.* **2009**, *4*, 710–711.
- (566) Naczynski, D. J.; Tan, M. C.; Zevon, M.; Wall, B.; Kohl, J.; Kulesa, A.; Chen, S.; Roth, C. M.; Riman, R. E.; Moghe, P. V. Rare-earth-doped Biological Composites as *In Vivo* Shortwave Infrared Reporters. *Nat. Commun.* **2013**, *4*, 2199.
- (567) del Rosal, B.; Ortgies, D. H.; Fernández, N.; Sanz-Rodríguez, F.; Jaque, D.; Rodríguez, E. M. Overcoming Autofluorescence: Long-Lifetime Infrared Nanoparticles for Time-Gated *In Vivo* Imaging. *Adv. Mater.* **2016**, *28*, 10188–10193.
- (568) Binnemans, K. Lanthanide-Based Luminescent Hybrid Materials. *Chem. Rev.* **2009**, *109*, 4283–4374.
- (569) Wang, D.; Wang, D.; Kuzmin, A.; Pliss, A.; Shao, W.; Xia, J.; Qu, J.; Prasad, P. N. ICG-Sensitized NaYF₄:Er Nanostructure for Theranostics. *Adv. Opt. Mater.* **2018**, *6*, 1701142.
- (570) Song, X.; Li, S.; Guo, H.; You, W.; Shang, X.; Li, R.; Tu, D.; Zheng, W.; Chen, Z.; Yang, H.; et al. Graphene-Oxide-Modified Lanthanide Nanoprobes for Tumor-Targeted Visible/NIR-II Luminescence Imaging. *Angew. Chem., Int. Ed.* **2019**, *58*, 18981–18986.
- (571) Zhao, M.; Wang, R.; Li, B.; Fan, Y.; Wu, Y.; Zhu, X.; Zhang, F. Precise *In Vivo* Inflammation Imaging Using *In Situ* Responsive Cross-linking of Glutathione-Modified Ultra-Small NIR-II Lanthanide Nanoparticles. *Angew. Chem., Int. Ed.* **2019**, *58*, 2050–2054.
- (572) Shao, W.; Chen, G.; Kuzmin, A.; Kutscher, H. L.; Pliss, A.; Ohulchanskyy, T. Y.; Prasad, P. N. Tunable Narrow Band Emissions From Dye-Sensitized Core/Shell/Shell Nanocrystals in the Second Near-Infrared Biological Window. *J. Am. Chem. Soc.* **2016**, *138*, 16192–16195.
- (573) Zhong, Y.; Ma, Z.; Zhu, S.; Yue, J.; Zhang, M.; Antaris, A. L.; Yuan, J.; Cui, R.; Wan, H.; Zhou, Y.; et al. Boosting the Down-shifting Luminescence of Rare-earth Nanocrystals for Biological Imaging Beyond 1500 nm. *Nat. Commun.* **2017**, *8*, 737.
- (574) Lei, X.; Li, R.; Tu, D.; Shang, X.; Liu, Y.; You, W.; Sun, C.; Zhang, F.; Chen, X. Intense Near-infrared-II Luminescence From NaCeF₄:Er/Yb Nanoprobes for *In Vitro* Bioassay and *In Vivo* Bioimaging. *Chem. Sci.* **2018**, *9*, 4682–4688.
- (575) Zhong, Y.; Ma, Z.; Wang, F.; Wang, X.; Yang, Y.; Liu, Y.; Zhao, X.; Li, J.; Du, H.; Zhang, M.; et al. *In Vivo* Molecular Imaging for Immunotherapy Using Ultra-bright Near-infrared-IIb Rare-earth Nanoparticles. *Nat. Biotechnol.* **2019**, *37*, 1322–1331.
- (576) Lu, L.; Li, B.; Ding, S.; Fan, Y.; Wang, S.; Sun, C.; Zhao, M.; Zhao, C.-X.; Zhang, F. NIR-II Bioluminescence for *In Vivo* High Contrast Imaging and *In Situ* ATP-mediated Metastases Tracing. *Nat. Commun.* **2020**, *11*, 4192.
- (577) Zhang, K. Y.; Yu, Q.; Wei, H.; Liu, S.; Zhao, Q.; Huang, W. Long-Lived Emissive Probes for Time-Resolved Photoluminescence Bioimaging and Biosensing. *Chem. Rev.* **2018**, *118*, 1770–1839.
- (578) Tu, D.; Liu, L.; Ju, Q.; Liu, Y.; Zhu, H.; Li, R.; Chen, X. Time-Resolved FRET Biosensor Based on Amine-Functionalized Lanthanide-Doped NaYF₄ Nanocrystals. *Angew. Chem., Int. Ed.* **2011**, *50*, 6306–6310.
- (579) Ma, Q.; Wang, J.; Li, Z.; Lv, X.; Liang, L.; Yuan, Q. Recent Progress in Time-Resolved Biosensing and Bioimaging Based on Lanthanide-Doped Nanoparticles. *Small* **2019**, *15*, 1804969.
- (580) Tan, M.; Del Rosal, B.; Zhang, Y.; Martín Rodríguez, E.; Hu, J.; Zhou, Z.; Fan, R.; Ortgies, D. H.; Fernández, N.; Chaves-Coira, I.; et al. Rare-earth-doped Fluoride Nanoparticles With Engineered Long Luminescence Lifetime for Time-gated *In Vivo* Optical Imaging in the Second Biological Window. *Nanoscale* **2018**, *10*, 17771–17780.
- (581) Lu, Y.; Zhao, J.; Zhang, R.; Liu, Y.; Liu, D.; Goldys, E. M.; Yang, X.; Xi, P.; Sunna, A.; Lu, J.; et al. Tunable Lifetime Multiplexing Using Luminescent Nanocrystals. *Nat. Photonics* **2014**, *8*, 32–36.
- (582) Tessitore, G.; Maurizio, S. L.; Sabri, T.; Capobianco, J. A. Intrinsic Time-Tunable Emissions in Core–Shell Upconverting Nanoparticle Systems. *Angew. Chem., Int. Ed.* **2019**, *58*, 9742.
- (583) Ortgies, D. H.; Tan, M.; Ximenes, E. C.; del Rosal, B.; Hu, J.; Xu, L.; Wang, X.; Martín Rodríguez, E.; Jacinto, C.; Fernandez, N.; et al. Lifetime-Encoded Infrared-Emitting Nanoparticles for *In Vivo* Multiplexed Imaging. *ACS Nano* **2018**, *12*, 4362.
- (584) Deng, R.; Liu, X. Tunable Lifetime Nanocrystals. *Nat. Photonics* **2014**, *8*, 10–12.
- (585) Fan, Y.; Wang, P.; Lu, Y.; Wang, R.; Zhou, L.; Zheng, X.; Li, X.; Piper, J. A.; Zhang, F. Lifetime-engineered NIR-II Nanoparticles Unlock Multiplexed *In Vivo* Imaging. *Nat. Nanotechnol.* **2018**, *13*, 941–946.

- (586) Li, Y.; Gecevicius, M.; Qiu, J. Long Persistent Phosphors— from Fundamentals to applications. *Chem. Soc. Rev.* **2016**, *45*, 2090–2136.
- (587) le Masne de Chermont, Q.; Chanéac, C.; Seguin, J.; Pellé, F.; Maitrejean, S.; Jolivet, J.-P.; Gourier, D.; Bessodes, M.; Scherman, D. Nanoprobes With Near-infrared Persistent Luminescence for *In Vivo* Imaging. *Proc. Natl. Acad. Sci. U. S. A.* **2007**, *104*, 9266–9271.
- (588) Abdulkayum, A.; Chen, J.-T.; Zhao, Q.; Yan, X.-P. Functional Near Infrared-Emitting Cr³⁺/Pr³⁺ Co-Doped Zinc Gallogermanate Persistent Luminescent Nanoparticles With Superlong Afterglow for *In Vivo* Targeted Bioimaging. *J. Am. Chem. Soc.* **2013**, *135*, 14125–14133.
- (589) Xue, Z.; Li, X.; Li, Y.; Jiang, M.; Ren, G.; Liu, H.; Zeng, S.; Hao, J. A 980 nm Laser-activated Upconverted Persistent Probe for NIR-to-NIR Rechargeable *In Vivo* Bioimaging. *Nanoscale* **2017**, *9*, 7276–7283.
- (590) Zheng, B.; Bai, Y.; Chen, H.; Pan, H.; Ji, W.; Gong, X.; Wu, X.; Wang, H.; Chang, J. Near-Infrared Light-Excited Upconverting Persistent Nanophosphors *In Vivo* for Imaging-Guided Cell Therapy. *ACS Appl. Mater. Interfaces* **2018**, *10*, 19514–19522.
- (591) Song, L.; Lin, X.-H.; Song, X.-R.; Chen, S.; Chen, X.-F.; Li, J.; Yang, H.-H. Repeatable Deep-tissue Activation of Persistent Luminescent Nanoparticles by Soft X-ray for High Sensitivity Long-term *In Vivo* Bioimaging. *Nanoscale* **2017**, *9*, 2718–2722.
- (592) Zheng, S.; Shi, J.; Fu, X.; Wang, C.; Sun, X.; Chen, C.; Zhuang, Y.; Zou, X.; Li, Y.; Zhang, H. X-ray Recharged Long Afterglow Luminescent Nanoparticles MgGeO₃:Mn²⁺, Yb³⁺, Li⁺ in the First and Second Biological Windows for Long-term Bioimaging. *Nanoscale* **2020**, *12*, 14037–14046.
- (593) Huang, K.; Dou, X.; Zhang, Y.; Gao, X.; Lin, J.; Qu, J.; Li, Y.; Huang, P.; Han, G. Enhancing Light and X-Ray Charging in Persistent Luminescence Nanocrystals for Orthogonal Afterglow Anti-Counterfeiting. *Adv. Funct. Mater.* **2021**, *31*, 2009920.
- (594) Xue, Z.; Li, X.; Li, Y.; Jiang, M.; Liu, H.; Zeng, S.; Hao, J. X-ray-Activated Near-Infrared Persistent Luminescent Probe for Deep-Tissue and Renewable *In Vivo* Bioimaging. *ACS Appl. Mater. Interfaces* **2017**, *9*, 22132–22142.
- (595) Ou, X.; Qin, X.; Huang, B.; Zan, J.; Wu, Q.; Hong, Z.; Xie, L.; Bian, H.; Yi, Z.; Chen, X.; et al. High-resolution X-ray Luminescence Extension Imaging. *Nature* **2021**, *590*, 410–415.
- (596) Pei, P.; Chen, Y.; Sun, C.; Fan, Y.; Yang, Y.; Liu, X.; Lu, L.; Zhao, M.; Zhang, H.; Zhao, D.; et al. X-ray-activated Persistent Luminescence Nanomaterials for NIR-II Imaging. *Nat. Nanotechnol.* **2021**, *16*, 1011–1018.
- (597) Wahsner, J.; Gale, E. M.; Rodríguez-Rodríguez, A.; Caravan, P. Chemistry of MRI Contrast Agents: Current Challenges and New Frontiers. *Chem. Rev.* **2019**, *119*, 957–1057.
- (598) Ni, D.; Bu, W.; Ehlerding, E. B.; Cai, W.; Shi, J. Engineering of Inorganic Nanoparticles as Magnetic Resonance Imaging Contrast Agents. *Chem. Soc. Rev.* **2017**, *46*, 7438–7468.
- (599) Johnson, N. J. J.; Oakden, W.; Stanis, G. J.; Scott Prosser, R.; van Veggel, F. C. J. M. Size-Tunable, Ultrasmall NaGdF₄ Nanoparticles: Insights Into Their T₁ MRI Contrast Enhancement. *Chem. Mater.* **2011**, *23*, 3714–3722.
- (600) Yi, Z.; Luo, Z.; Barth, N. D.; Meng, X.; Liu, H.; Bu, W.; All, A.; Vendrell, M.; Liu, X. *In Vivo* Tumor Visualization Through MRI Off-On Switching of NaGdF₄–CaCO₃ Nanoconjugates. *Adv. Mater.* **2019**, *31*, 1901851.
- (601) Xu, J.; Han, W.; Yang, P.; Jia, T.; Dong, S.; Bi, H.; Gulzar, A.; Yang, D.; Gai, S.; He, F.; et al. Tumor Microenvironment-Responsive Mesoporous MnO₂-Coated Upconversion Nanoplatfor for Self-Enhanced Tumor Theranostics. *Adv. Funct. Mater.* **2018**, *28*, 1803804.
- (602) Cheung, E. N. M.; Alvares, R. D. A.; Oakden, W.; Chaudhary, R.; Hill, M. L.; Pichaandi, J.; Mo, G. C. H.; Yip, C.; Macdonald, P. M.; Stanis, G. J.; et al. Polymer-Stabilized Lanthanide Fluoride Nanoparticle Aggregates as Contrast Agents for Magnetic Resonance Imaging and Computed Tomography. *Chem. Mater.* **2010**, *22*, 4728–4739.
- (603) Wu, M.; Xue, Y.; Li, N.; Zhao, H.; Lei, B.; Wang, M.; Wang, J.; Luo, M.; Zhang, C.; Du, Y.; et al. Tumor-Microenvironment-Induced Degradation of Ultrathin Gadolinium Oxide Nanoscrolls for Magnetic-Resonance-Imaging-Monitored, Activatable Cancer Chemotherapy. *Angew. Chem., Int. Ed.* **2019**, *58*, 6880–6885.
- (604) Ni, D.; Zhang, J.; Bu, W.; Zhang, C.; Yao, Z.; Xing, H.; Wang, J.; Duan, F.; Liu, Y.; Fan, W.; et al. PEGylated NaHoF₄ Nanoparticles as Contrast Agents for Both X-ray Computed Tomography and Ultrahigh field Magnetic Resonance Imaging. *Biomaterials* **2016**, *76*, 218–225.
- (605) Das, G. K.; Johnson, N. J. J.; Cramen, J.; Blasiak, B.; Latta, P.; Tomanek, B.; van Veggel, F. C. J. M. NaDyF₄ Nanoparticles as T₂ Contrast Agents for Ultrahigh Field Magnetic Resonance Imaging. *J. Phys. Chem. Lett.* **2012**, *3*, 524–529.
- (606) Liu, M.; Shi, Z.; Wang, X.; Zhang, Y.; Mo, X.; Jiang, R.; Liu, Z.; Fan, L.; Ma, C.-g.; Shi, F. Simultaneous Enhancement of Red Upconversion Luminescence and CT Contrast of NaGdF₄:Yb,Er Nanoparticles via Lu³⁺ Doping. *Nanoscale* **2018**, *10*, 20279–20288.
- (607) Sun, Y.; Zhu, X.; Peng, J.; Li, F. Core–Shell Lanthanide Upconversion Nanophosphors as Four-Modal Probes for Tumor Angiogenesis Imaging. *ACS Nano* **2013**, *7*, 11290–11300.
- (608) He, S.; Johnson, N. J. J.; Nguyen Huu, V. A.; Cory, E.; Huang, Y.; Sah, R. L.; Jokerst, J. V.; Almutairi, A. Simultaneous Enhancement of Photoluminescence, MRI Relaxivity, and CT Contrast by Tuning the Interfacial Layer of Lanthanide Heteroepitaxial Nanoparticles. *Nano Lett.* **2017**, *17*, 4873–4880.
- (609) Xia, A.; Chen, M.; Gao, Y.; Wu, D.; Feng, W.; Li, F. Gd³⁺ Complex-modified NaLuF₄-based Upconversion Nanophosphors for Trimodality Imaging of NIR-to-NIR Upconversion Luminescence, X-Ray Computed Tomography and Magnetic Resonance. *Biomaterials* **2012**, *33*, 5394–5405.
- (610) Maji, S. K.; Sreejith, S.; Joseph, J.; Lin, M.; He, T.; Tong, Y.; Sun, H.; Yu, S. W.-K.; Zhao, Y. Upconversion Nanoparticles as a Contrast Agent for Photoacoustic Imaging in Live Mice. *Adv. Mater.* **2014**, *26*, 5633–5638.
- (611) Sheng, Y.; Liao, L.-D.; Bandla, A.; Liu, Y.-H.; Thakor, N.; Tan, M. C. Size and Shell Effects on the Photoacoustic and Luminescence Properties of Dual Modal Rare-Earth-Doped Nanoparticles for Infrared Photoacoustic Imaging. *ACS Biomater. Sci. Eng.* **2016**, *2*, 809–817.
- (612) Adams, S. R.; Mackey, M. R.; Ramachandra, R.; Palida Lemieux, S. F.; Steinbach, P.; Bushong, E. A.; Butko, M. T.; Giepmans, B. N.G.; Ellisman, M. H.; Tsien, R. Y. Multicolor Electron Microscopy for Simultaneous Visualization of Multiple Molecular Species. *Cell Chem. Biol.* **2016**, *23*, 1417–1427.
- (613) Prigozhin, M. B.; Maurer, P. C.; Curtis, A. M.; Liu, N.; Wisser, M. D.; Siefe, C.; Tian, B.; Chan, E.; Song, G.; Fischer, S.; et al. Bright Sub-20-nm Cathodoluminescent Nanoprobes for Electron Microscopy. *Nat. Nanotechnol.* **2019**, *14*, 420–425.
- (614) Prodi, L.; Rampazzo, E.; Rastrelli, F.; Speghini, A.; Zaccheroni, N. Imaging Agents Based on Lanthanide Doped Nanoparticles. *Chem. Soc. Rev.* **2015**, *44*, 4922–4952.
- (615) Guan, G.; Wu, M.; Han, M.-Y. Stimuli-Responsive Hybridized Nanostructures. *Adv. Funct. Mater.* **2020**, *30*, 1903439.
- (616) Ovais, M.; Mukherjee, S.; Pramanik, A.; Das, D.; Mukherjee, A.; Raza, A.; Chen, C. Designing Stimuli-Responsive Upconversion Nanoparticles That Exploit the Tumor Microenvironment. *Adv. Mater.* **2020**, *32*, 2000055.
- (617) Brennecke, B.; Wang, Q.; Zhang, Q.; Hu, H.-Y.; Nazaré, M. An Activatable Lanthanide Luminescent Probe for Time-Gated Detection of Nitroreductase in Live Bacteria. *Angew. Chem., Int. Ed.* **2020**, *59*, 8512–8516.
- (618) Li, M.; Zhao, J.; Chu, H.; Mi, Y.; Zhou, Z.; Di, Z.; Zhao, M.; Li, L. Light-Activated Nanoprobes for Biosensing and Imaging. *Adv. Mater.* **2019**, *31*, 1804745.
- (619) Peng, J.; Sun, Y.; Zhao, L.; Wu, Y.; Feng, W.; Gao, Y.; Li, F. Polyphosphoric Acid Capping Radioactive/upconverting NaLuF₄:Yb,Tm,¹⁵³Sm Nanoparticles for Blood Pool Imaging *In Vivo*. *Biomaterials* **2013**, *34*, 9535–9544.

- (620) Rao, L.; Bu, L.-L.; Cai, B.; Xu, J.-H.; Li, A.; Zhang, W.-F.; Sun, Z.-J.; Guo, S.-S.; Liu, W.; Wang, T.-H.; et al. Cancer Cell Membrane-Coated Upconversion Nanoprobes for Highly Specific Tumor Imaging. *Adv. Mater.* **2016**, *28*, 3460–3466.
- (621) Garfield, D. J.; Borys, N. J.; Hamed, S. M.; Torquato, N. A.; Tajon, C. A.; Tian, B.; Shevitski, B.; Barnard, E. S.; Suh, Y. D.; Aloni, S.; et al. Enrichment of Molecular Antenna Triplets Amplifies Upconverting Nanoparticle Emission. *Nat. Photonics* **2018**, *12*, 402–407.
- (622) Wu, Y.; Xu, J.; Poh, E. T.; Liang, L.; Liu, H.; Yang, J. K. W.; Qiu, C.-W.; Vallée, R. A. L.; Liu, X. Upconversion Superburst With Sub-2 μ s Lifetime. *Nat. Nanotechnol.* **2019**, *14*, 1110–1115.
- (623) Yanai, N.; Kimizuka, N. Stimuli-Responsive Molecular Photon Upconversion. *Angew. Chem., Int. Ed.* **2020**, *59*, 10252–10264.
- (624) Chen, G.; Damasco, J.; Qiu, H.; Shao, W.; Ohulchanskyy, T. Y.; Valiev, R. R.; Wu, X.; Han, G.; Wang, Y.; Yang, C.; et al. Energy-Cascaded Upconversion in an Organic Dye-Sensitized Core/Shell Fluoride Nanocrystal. *Nano Lett.* **2015**, *15*, 7400–7407.
- (625) Wang, J.; Deng, R. Energy Transfer in Dye-Coupled Lanthanide-Doped Nanoparticles: From Design to Application. *Chem. - Asian J.* **2018**, *13*, 614–625.
- (626) Liang, T.; Wang, Q.; Li, Z.; Wang, P.; Wu, J.; Zuo, M.; Liu, Z. Removing the Obstacle of Dye-Sensitized Upconversion Luminescence in Aqueous Phase to Achieve High-Contrast Deep Imaging *In Vivo*. *Adv. Funct. Mater.* **2020**, *30*, 1910765.
- (627) Wang, D.; Liu, B.; Quan, Z.; Li, C.; Hou, Z.; Xing, B.; Lin, J. New Advances on the Marrying of UCNPs and Photothermal Agents for Imaging-guided Diagnosis and the Therapy of Tumors. *J. Mater. Chem. B* **2017**, *5*, 2209–2230.
- (628) Ge, X.; Song, Z.-M.; Sun, L.; Yang, Y.-F.; Shi, L.; Si, R.; Ren, W.; Qiu, X.; Wang, H. Lanthanide (Gd^{3+} and Yb^{3+}) Functionalized Gold Nanoparticles for *In Vivo* Imaging and Therapy. *Biomaterials* **2016**, *108*, 35–43.
- (629) Yang, J.; Shen, D.; Zhou, L.; Li, W.; Fan, J.; El-Toni, A. M.; Zhang, W.-x.; Zhang, F.; Zhao, D. Mesoporous Silica-Coated Plasmonic Nanostructures for Surface-Enhanced Raman Scattering Detection and Photothermal Therapy. *Adv. Healthcare Mater.* **2014**, *3*, 1620–1628.
- (630) He, J.; Zheng, W.; Ligmajer, F.; Chan, C.-F.; Bao, Z.; Wong, K.-L.; Chen, X.; Hao, J.; Dai, J.; Yu, S.-F.; et al. Plasmonic Enhancement and Polarization Dependence of Nonlinear Upconversion Emissions From Single Gold Nanorod@ SiO_2 @ $CaF_2:Yb^{3+},Er^{3+}$ Hybrid Core-shell-satellite Nanostructures. *Light: Sci. Appl.* **2017**, *6*, No. e16217.
- (631) Huang, Y.; Skripka, A.; Labrador-Páez, L.; Sanz-Rodríguez, F.; Haro-González, P.; Jaque, D.; Rosei, F.; Vetrone, F. Upconverting Nanocomposites With Combined Photothermal and Photodynamic Effects. *Nanoscale* **2018**, *10*, 791–799.
- (632) Zhao, H.; Zhao, L.; Wang, Z.; Xi, W.; Dibaba, S. T.; Wang, S.; Shi, L.; Sun, L. Heterogeneous Growth of Palladium Nanocrystals on Upconversion Nanoparticles for Multimodal Imaging and Photothermal Therapy. *J. Mater. Chem. B* **2019**, *7*, 3652–3660.
- (633) Wang, C.; Xue, R.; Gulzar, A.; Kuang, Y.; Shao, H.; Gai, S.; Yang, D.; He, F.; Yang, P. Targeted and Imaging-guided Chemo-photothermal Ablation Achieved by Combining Upconversion Nanoparticles and Protein-capped Gold Nanodots. *Chem. Eng. J.* **2019**, *370*, 1239–1250.
- (634) Cheng, L.; Yang, K.; Li, Y.; Chen, J.; Wang, C.; Shao, M.; Lee, S.-T.; Liu, Z. Facile Preparation of Multifunctional Upconversion Nanoprobes for Multimodal Imaging and Dual-Targeted Photothermal Therapy. *Angew. Chem., Int. Ed.* **2011**, *50*, 7385–7390.
- (635) Chan, M.-H.; Chen, S.-P.; Chen, C.-W.; Chan, Y.-C.; Lin, R. J.; Tsai, D. P.; Hsiao, M.; Chung, R.-J.; Chen, X.; Liu, R.-S. Single 808 nm Laser Treatment Comprising Photothermal and Photodynamic Therapies by Using Gold Nanorods Hybrid Upconversion Particles. *J. Phys. Chem. C* **2018**, *122*, 2402–2412.
- (636) Chen, Q.; Wang, C.; Cheng, L.; He, W.; Cheng, Z.; Liu, Z. Protein Modified Upconversion Nanoparticles for Imaging-guided Combined Photothermal and Photodynamic Therapy. *Biomaterials* **2014**, *35*, 2915–2923.
- (637) Feng, L.; He, F.; Liu, B.; Yang, G.; Gai, S.; Yang, P.; Li, C.; Dai, Y.; Lv, R.; Lin, J. g- C_3N_4 Coated Upconversion Nanoparticles for 808 nm Near-Infrared Light Triggered Phototherapy and Multiple Imaging. *Chem. Mater.* **2016**, *28*, 7935–7946.
- (638) Wang, L.; Gao, C.; Liu, K.; Liu, Y.; Ma, L.; Liu, L.; Du, X.; Zhou, J. Cypate-Conjugated Porous Upconversion Nanocomposites for Programmed Delivery of Heat Shock Protein 70 Small Interfering RNA for Gene Silencing and Photothermal Ablation. *Adv. Funct. Mater.* **2016**, *26*, 3480–3489.
- (639) Ding, X.; Liu, J.; Liu, D.; Li, J.; Wang, F.; Li, L.; Wang, Y.; Song, S.; Zhang, H. Multifunctional Core/satellite Polydopamine@ Nd^{3+} -sensitized Upconversion nanocomposite: A Single 808 nm Near-infrared Light-triggered Theranostic Platform for *In Vivo* Imaging-guided Photothermal Therapy. *Nano Res.* **2017**, *10*, 3434–3446.
- (640) Li, P.; Yan, Y.; Chen, B.; Zhang, P.; Wang, S.; Zhou, J.; Fan, H.; Wang, Y.; Huang, X. Lanthanide-doped Upconversion Nanoparticles Complexed With Nano-oxide Graphene Used for Upconversion Fluorescence Imaging and Photothermal Therapy. *Biomater. Sci.* **2018**, *6*, 877–884.
- (641) Suo, H.; Zhao, X.; Zhang, Z.; Wu, Y.; Guo, C. Upconverting $LuVO_4:Nd^{3+}/Yb^{3+}/Er^{3+}@SiO_2@Cu_2S$ Hollow Nanoplatforms for Self-monitored Photothermal Ablation. *ACS Appl. Mater. Interfaces* **2018**, *10*, 39912–39920.
- (642) Sun, J.; Song, L.; Fan, Y.; Tian, L.; Luan, S.; Niu, S.; Ren, L.; Ming, W.; Zhao, J. Synergistic Photodynamic and Photothermal Antibacterial Nanocomposite Membrane Triggered by Single NIR Light Source. *ACS Appl. Mater. Interfaces* **2019**, *11*, 26581–26589.
- (643) Wang, Y.; Wang, H.; Liu, D.; Song, S.; Wang, X.; Zhang, H. Graphene Oxide Covalently Grafted Upconversion Nanoparticles for Combined NIR Mediated Imaging and Photothermal/photodynamic Cancer Therapy. *Biomaterials* **2013**, *34*, 7715–7724.
- (644) Lv, R.; Yang, P.; He, F.; Gai, S.; Yang, G.; Lin, J. Hollow Structured $Y_2O_3:Yb/Er-Cu_2S$ Nanospheres With Controllable Size for Simultaneous Chemo/Photothermal Therapy and Bioimaging. *Chem. Mater.* **2015**, *27*, 483–496.
- (645) Xu, M.; Yang, G.; Bi, H.; Xu, J.; Feng, L.; Yang, D.; Sun, Q.; Gai, S.; He, F.; Dai, Y.; et al. Combination of CuS and g- C_3N_4 QDs on Upconversion Nanoparticles for Targeted Photothermal and Photodynamic Cancer Therapy. *Chem. Eng. J.* **2019**, *360*, 866–878.
- (646) Zhou, K.; Qiu, X.; Xu, L.; Li, G.; Rao, B.; Guo, B.; Pei, D.; Li, A.; He, G. Poly(selenoviologen)-Assembled Upconversion Nanoparticles for Low-Power Single-NIR Light-Triggered Synergistic Photodynamic and Photothermal Antibacterial Therapy. *ACS Appl. Mater. Interfaces* **2020**, *12*, 26432–26443.
- (647) Zhu, X.; Feng, W.; Chang, J.; Tan, Y.-W.; Li, J.; Chen, M.; Sun, Y.; Li, F. Temperature-feedback Upconversion Nanocomposite for Accurate Photothermal Therapy at Facile Temperature. *Nat. Commun.* **2016**, *7*, 10437.
- (648) Zhu, X.; Li, J.; Qiu, X.; Liu, Y.; Feng, W.; Li, F. Upconversion Nanocomposite for Programming Combination Cancer Therapy by Precise Control of Microscopic Temperature. *Nat. Commun.* **2018**, *9*, 2176.
- (649) Wang, M.; Song, J.; Zhou, F.; Hoover, A. R.; Murray, C.; Zhou, B.; Wang, L.; Qu, J.; Chen, W. R. NIR-Triggered Phototherapy and Immunotherapy via an Antigen-Capturing Nanoplatform for Metastatic Cancer Treatment. *Adv. Sci.* **2019**, *6*, 1802157.
- (650) Agostinis, P.; Berg, K.; Cengel, K. A.; Foster, T. H.; Girotti, A. W.; Gollnick, S. O.; Hahn, S. M.; Hamblin, M. R.; Juzeniene, A.; Kessel, D.; et al. Photodynamic Therapy of Cancer: An Update. *Cancer J. Clin.* **2011**, *61*, 250–281.
- (651) Lucky, S. S.; Soo, K. C.; Zhang, Y. Nanoparticles in Photodynamic Therapy. *Chem. Rev.* **2015**, *115*, 1990.
- (652) Shanmugam, V.; Selvakumar, S.; Yeh, C.-S. Near-infrared Light-responsive Nanomaterials in Cancer Therapeutics. *Chem. Soc. Rev.* **2014**, *43*, 6254–6287.

- (653) Liu, Y.; Meng, X.; Bu, W. Upconversion-based Photodynamic Cancer Therapy. *Coord. Chem. Rev.* **2019**, *379*, 82–98.
- (654) Fan, W.; Tang, W.; Lau, J.; Shen, Z.; Xie, J.; Shi, J.; Chen, X. Breaking the Depth Dependence by Nanotechnology-Enhanced X-Ray-Excited Deep Cancer Theranostics. *Adv. Mater.* **2019**, *31*, 1806381.
- (655) Chen, H.; Wang, G. D.; Chuang, Y.-J.; Zhen, Z.; Chen, X.; Biddinger, P.; Hao, Z.; Liu, F.; Shen, B.; Pan, Z.; et al. Nanoscintillator-Mediated X-ray Inducible Photodynamic Therapy for *In Vivo* Cancer Treatment. *Nano Lett.* **2015**, *15*, 2249–2256.
- (656) Kamkaew, A.; Chen, F.; Zhan, Y.; Majewski, R. L.; Cai, W. Scintillating Nanoparticles as Energy Mediators for Enhanced Photodynamic Therapy. *ACS Nano* **2016**, *10*, 3918–3935.
- (657) Clement, S.; Campbell, J. M.; Deng, W.; Guller, A.; Nisar, S.; Liu, G.; Wilson, B. C.; Goldys, E. M. Mechanisms for Tuning Engineered Nanomaterials to Enhance Radiation Therapy of Cancer. *Adv. Sci.* **2020**, *7*, 2003584.
- (658) Chen, W.; Zhang, J. Using Nanoparticles to Enable Simultaneous Radiation and Photodynamic Therapies for Cancer Treatment. *J. Nanosci. Nanotechnol.* **2006**, *6*, 1159–1166.
- (659) Bulin, A.-L.; Truillet, C.; Chouikrat, R.; Lux, F.; Frochet, C.; Amans, D.; Ledoux, G.; Tillement, O.; Perriat, P.; Barberi-Heyob, M.; et al. X-ray-Induced Singlet Oxygen Activation With Nanoscintillator-Coupled Porphyrins. *J. Phys. Chem. C* **2013**, *117*, 21583–21589.
- (660) Zou, X.; Yao, M.; Ma, L.; Hossu, M.; Han, X.; Juzenas, P.; Chen, W. X-ray-induced Nanoparticle-based Photodynamic Therapy of Cancer. *Nanomedicine* **2014**, *9*, 2339–2351.
- (661) Zhong, X.; Wang, X.; Zhan, G.; Tang, Y. a.; Yao, Y.; Dong, Z.; Hou, L.; Zhao, H.; Zeng, S.; Hu, J.; et al. NaCeF₄:Gd,Tb Scintillator as an X-ray Responsive Photosensitizer for Multimodal Imaging-Guided Synchronous Radio/Radiodynamic Therapy. *Nano Lett.* **2019**, *19*, 8234–8244.
- (662) Ren, Y.; Rosch, J. G.; Landry, M. R.; Winter, H.; Khan, S.; Pratz, G.; Sun, C. Tb-Doped Core–shell–shell Nanophosphors for Enhanced X-ray Induced Luminescence and Sensitization of Radiodynamic Therapy. *Biomater. Sci.* **2021**, *9*, 496–505.
- (663) Yu, X.; Liu, X.; Wu, W.; Yang, K.; Mao, R.; Ahmad, F.; Chen, X.; Li, W. CT/MRI-Guided Synergistic Radiotherapy and X-ray Inducible Photodynamic Therapy Using Tb-Doped Gd-W-Nanoscintillators. *Angew. Chem., Int. Ed.* **2019**, *58*, 2017–2022.
- (664) Bulin, A.-L.; Broekgaarden, M.; Chaput, F.; Baisamy, V.; Garrevoet, J.; Busser, B.; Brueckner, D.; Youssef, A.; Ravanat, J.-L.; Dujardin, C.; et al. Radiation Dose-Enhancement Is a Potent Radiotherapeutic Effect of Rare-Earth Composite Nanoscintillators in Preclinical Models of Glioblastoma. *Adv. Sci.* **2020**, *7*, 2001675.
- (665) Ai, X.; Ho, C. J. H.; Aw, J.; Attia, A. B. E.; Mu, J.; Wang, Y.; Wang, X.; Wang, Y.; Liu, X.; Chen, H.; et al. *In Vivo* Covalent Cross-linking of Photon-converted Rare-earth Nanostructures for Tumour Localization and Theranostics. *Nat. Commun.* **2016**, *7*, 10432.
- (666) Li, S.; Liu, R.; Jiang, X.; Qiu, Y.; Song, X.; Huang, G.; Fu, N.; Lin, L.; Song, J.; Chen, X.; Yang, H.; et al. Near-Infrared Light-Triggered Sulfur Dioxide Gas Therapy of Cancer. *ACS Nano* **2019**, *13*, 2103–2113.
- (667) Zheng, B.; Zhong, D.; Xie, T.; Zhou, J.; Li, W.; Ilyas, A.; Lu, Y.; Zhou, M.; Deng, R. Near-infrared Photosensitization via Direct Triplet Energy Transfer From Lanthanide Nanoparticles. *Chem.* **2021**, *7*, 1615–1625.
- (668) Zhang, C.; Zhao, K.; Bu, W.; Ni, D.; Liu, Y.; Feng, J.; Shi, J. Marriage of Scintillator and Semiconductor for Synchronous Radiotherapy and Deep Photodynamic Therapy With Diminished Oxygen Dependence. *Angew. Chem., Int. Ed.* **2015**, *54*, 1770–1774.
- (669) Hsu, C.-C.; Lin, S.-L.; Chang, C. A. Lanthanide-Doped Core–Shell–Shell Nanocomposite for Dual Photodynamic Therapy and Luminescence Imaging by a Single X-ray Excitation Source. *ACS Appl. Mater. Interfaces* **2018**, *10*, 7859–7870.
- (670) Du, Z.; Zhang, X.; Guo, Z.; Xie, J.; Dong, X.; Zhu, S.; Du, J.; Gu, Z.; Zhao, Y. X-Ray-Controlled Generation of Peroxynitrite Based on Nanosized LiLuF₄:Ce³⁺ Scintillators and Their Applications for Radiosensitization. *Adv. Mater.* **2018**, *30*, 1804046.
- (671) Wang, C.; Tao, H.; Cheng, L.; Liu, Z. Near-infrared Light Induced *In Vivo* Photodynamic Therapy of Cancer Based on Upconversion Nanoparticles. *Biomaterials* **2011**, *32*, 6145–6154.
- (672) Cui, S.; Yin, D.; Chen, Y.; Di, Y.; Chen, H.; Ma, Y.; Achilefu, S.; Gu, Y. *In Vivo* Targeted Deep-Tissue Photodynamic Therapy Based on Near-Infrared Light Triggered Upconversion Nanoconstruct. *ACS Nano* **2013**, *7*, 676–688.
- (673) Hou, Z.; Zhang, Y.; Deng, K.; Chen, Y.; Li, X.; Deng, X.; Cheng, Z.; Lian, H.; Li, C.; Lin, J. UV-Emitting Upconversion-Based TiO₂ Photosensitizing Nanopatform: Near-Infrared Light Mediated *In Vivo* Photodynamic Therapy via Mitochondria-Involved Apoptosis Pathway. *ACS Nano* **2015**, *9*, 2584–2599.
- (674) Fan, W.; Bu, W.; Shen, B.; He, Q.; Cui, Z.; Liu, Y.; Zheng, X.; Zhao, K.; Shi, J. Intelligent MnO₂ Nanosheets Anchored With Upconversion Nanoprobes for Concurrent pH-/H₂O₂-Responsive UCL Imaging and Oxygen-Elevated Synergetic Therapy. *Adv. Mater.* **2015**, *27*, 4155–4161.
- (675) Zhang, Z.; Jayakumar, M. K. G.; Zheng, X.; Shikha, S.; Zhang, Y.; Bansal, A.; Poon, D. J. J.; Chu, P. L.; Yeo, E. L. L.; Chua, M. L. K.; et al. Upconversion Superballs for Programmable Photoactivation of Therapeutics. *Nat. Commun.* **2019**, *10*, 4586.
- (676) Zhang, J.; Liu, C.-L.; Liu, J.-J.; Bai, X.-H.; Cao, Z.-K.; Yang, J.; Yu, M.; Ramakrishna, S.; Long, Y.-Z. Eluting Mode of Photodynamic Nanofibers Without Photosensitizer Leakage for One-stop Treatment of Outdoor Hemostasis and Sterilizing Superbacteria. *Nanoscale* **2021**, *13*, 6105–6116.
- (677) Chan, M.-H.; Pan, Y.-T.; Lee, I. J.; Chen, C.-W.; Chan, Y.-C.; Hsiao, M.; Wang, F.; Sun, L.; Chen, X.; Liu, R.-S. Minimizing the Heat Effect of Photodynamic Therapy Based on Inorganic Nanocomposites Mediated by 808 nm Near-Infrared Light. *Small* **2017**, *13*, 1700038.
- (678) Xu, J.; Shi, R.; Chen, G.; Dong, S.; Yang, P.; Zhang, Z.; Niu, N.; Gai, S.; He, F.; Fu, Y.; et al. All-in-One Theranostic Nanomedicine With Ultrabright Second Near-Infrared Emission for Tumor-Modulated Bioimaging and Chemodynamic/Photodynamic Therapy. *ACS Nano* **2020**, *14*, 9613–9625.
- (679) Hu, P.; Wu, T.; Fan, W.; Chen, L.; Liu, Y.; Ni, D.; Bu, W.; Shi, J. Near Infrared-assisted Fenton Reaction for Tumor-specific and Mitochondrial DNA-targeted Photochemotherapy. *Biomaterials* **2017**, *141*, 86–95.
- (680) Liu, C.; Liu, B.; Zhao, J.; Di, Z.; Chen, D.; Gu, Z.; Li, L.; Zhao, Y. Nd³⁺-Sensitized Upconversion Metal–Organic Frameworks for Mitochondria-Targeted Amplified Photodynamic Therapy. *Angew. Chem., Int. Ed.* **2020**, *59*, 2634–2638.
- (681) Gu, T.; Cheng, L.; Gong, F.; Xu, J.; Li, X.; Han, G.; Liu, Z. Upconversion Composite Nanoparticles for Tumor Hypoxia Modulation and Enhanced Near-Infrared-Triggered Photodynamic Therapy. *ACS Appl. Mater. Interfaces* **2018**, *10*, 15494–15503.
- (682) Xu, S.; Zhu, X.; Zhang, C.; Huang, W.; Zhou, Y.; Yan, D. Oxygen and Pt(II) Self-generating Conjugate for Synergistic Photochemo Therapy of Hypoxic Tumor. *Nat. Commun.* **2018**, *9*, 2053.
- (683) Wu, X.; Yan, P.; Ren, Z.; Wang, Y.; Cai, X.; Li, X.; Deng, R.; Han, G. Ferric Hydroxide-Modified Upconversion Nanoparticles for 808 nm NIR-Triggered Synergetic Tumor Therapy With Hypoxia Modulation. *ACS Appl. Mater. Interfaces* **2019**, *11*, 385–393.
- (684) Liu, Y.; Liu, Y.; Bu, W.; Cheng, C.; Zuo, C.; Xiao, Q.; Sun, Y.; Ni, D.; Zhang, C.; Liu, J.; et al. Hypoxia Induced by Upconversion-Based Photodynamic Therapy: Towards Highly Effective Synergistic Bioreductive Therapy in Tumors. *Angew. Chem., Int. Ed.* **2015**, *54*, 8105–8109.
- (685) Xu, J.; Xu, L.; Wang, C.; Yang, R.; Zhuang, Q.; Han, X.; Dong, Z.; Zhu, W.; Peng, R.; Liu, Z. Near-Infrared-Triggered Photodynamic Therapy With Multitasking Upconversion Nanoparticles in Combination With Checkpoint Blockade for Immunotherapy of Colorectal Cancer. *ACS Nano* **2017**, *11*, 4463–4474.
- (686) Yan, S.; Zeng, X.; Tang, Y. a.; Liu, B.-F.; Wang, Y.; Liu, X. Activating Antitumor Immunity and Antimetastatic Effect Through Polydopamine-Encapsulated Core–Shell Upconversion Nanoparticles. *Adv. Mater.* **2019**, *31*, 1905825.

- (687) Guan, M.; Jin, D. Dark Bridge at the Interface of Hybrid Nanosystem: Lanthanide-triplet NIR Photosensitization. *Chem.* **2021**, *7*, 1412–1414.
- (688) Burks, P. T.; Garcia, J. V.; GonzalezIrias, R.; Tillman, J. T.; Niu, M.; Mikhailovsky, A. A.; Zhang, J.; Zhang, F.; Ford, P. C. Nitric Oxide Releasing Materials Triggered by Near-Infrared Excitation Through Tissue Filters. *J. Am. Chem. Soc.* **2013**, *135*, 18145–18152.
- (689) Garcia, J. V.; Yang, J.; Shen, D.; Yao, C.; Li, X.; Wang, R.; Stucky, G. D.; Zhao, D.; Ford, P. C.; Zhang, F. NIR-Triggered Release of Caged Nitric Oxide Using Upconverting Nanostructured Materials. *Small* **2012**, *8*, 3800–3805.
- (690) Zhang, X.; Tian, G.; Yin, W.; Wang, L.; Zheng, X.; Yan, L.; Li, J.; Su, H.; Chen, C.; Gu, Z.; et al. Controllable Generation of Nitric Oxide by Near-Infrared-Sensitized Upconversion Nanoparticles for Tumor Therapy. *Adv. Funct. Mater.* **2015**, *25*, 3049–3056.
- (691) Lan, Y.; Zhu, X.; Tang, M.; Wu, Y.; Zhang, J.; Liu, J.; Zhang, Y. Construction of a Near-infrared Responsive Upconversion Nanoplatfrom Against Hypoxic Tumors via NO-enhanced Photodynamic Therapy. *Nanoscale* **2020**, *12*, 7875–7887.
- (692) Zhang, X.; Guo, Z.; Liu, J.; Tian, G.; Chen, K.; Yu, S.; Gu, Z. Near Infrared Light Triggered Nitric Oxide Releasing Platform Based on Upconversion Nanoparticles for Synergistic Therapy of Cancer Stem-like Cells. *Sci. Bull.* **2017**, *62*, 985–996.
- (693) Zhang, Y.; Zhang, Y.; Song, G.; He, Y.; Zhang, X.; Liu, Y.; Ju, H. A DNA–Azobenzene Nanopump Fueled by Upconversion Luminescence for Controllable Intracellular Drug Release. *Angew. Chem.* **2019**, *131*, 18375–18379.
- (694) Yao, C.; Wang, P.; Li, X.; Hu, X.; Hou, J.; Wang, L.; Zhang, F. Near-Infrared-Triggered Azobenzene-Liposome/Upconversion Nanoparticle Hybrid Vesicles for Remotely Controlled Drug Delivery to Overcome Cancer Multidrug Resistance. *Adv. Mater.* **2016**, *28*, 9341–9348.
- (695) Sun, Y.; Feng, W.; Yang, P.; Huang, C.; Li, F. The Biosafety of Lanthanide Upconversion Nanomaterials. *Chem. Soc. Rev.* **2015**, *44*, 1509–1525.
- (696) Zhang, Y.; Zheng, F.; Yang, T.; Zhou, W.; Liu, Y.; Man, N.; Zhang, L.; Jin, N.; Dou, Q.; Zhang, Y.; et al. Tuning the autophagy-inducing Activity of Lanthanide-based Nanocrystals Through Specific Surface-coating Peptides. *Nat. Mater.* **2012**, *11*, 817–826.
- (697) Yang, D.; Ma, P. a.; Hou, Z.; Cheng, Z.; Li, C.; Lin, J. Current Advances in Lanthanide Ion (Ln³⁺)-based Upconversion Nanomaterials for Drug Delivery. *Chem. Soc. Rev.* **2015**, *44*, 1416–1448.
- (698) Yan, J.; He, W.; Yan, S.; Niu, F.; Liu, T.; Ma, B.; Shao, Y.; Yan, Y.; Yang, G.; Lu, W.; et al. Self-Assembled Peptide–Lanthanide Nanoclusters for Safe Tumor Therapy: Overcoming and Utilizing Biological Barriers to Peptide Drug Delivery. *ACS Nano* **2018**, *12*, 2017–2026.
- (699) Bagheri, A.; Arandiyani, H.; Boyer, C.; Lim, M. Lanthanide-Doped Upconversion Nanoparticles: Emerging Intelligent Light-Activated Drug Delivery Systems. *Adv. Sci.* **2016**, *3*, 1500437.
- (700) Yang, B.; Chen, H.; Zheng, Z.; Li, G. Application of Upconversion Rare Earth Fluorescent Nanoparticles in Biomedical Drug Delivery System. *J. Lumin.* **2020**, *223*, 117226.
- (701) Carling, C.-J.; Boyer, J.-C.; Branda, N. R. Remote-Control Photoswitching Using NIR Light. *J. Am. Chem. Soc.* **2009**, *131*, 10838.
- (702) Jayakumar, M. K. G.; Idris, N. M.; Zhang, Y. Remote Activation of Biomolecules in Deep Tissues Using Near-infrared-to-UV Upconversion Nanotransducers. *Proc. Natl. Acad. Sci. U. S. A.* **2012**, *109*, 8483–8488.
- (703) Yang, Y.; Shao, Q.; Deng, R.; Wang, C.; Teng, X.; Cheng, K.; Cheng, Z.; Huang, L.; Liu, Z.; Liu, X.; et al. *In Vitro* and *In Vivo* Uncaging and Bioluminescence Imaging by Using Photocaged Upconversion Nanoparticles. *Angew. Chem.* **2012**, *124*, 3179–3183.
- (704) Zhao, L.; Peng, J.; Huang, Q.; Li, C.; Chen, M.; Sun, Y.; Lin, Q.; Zhu, L.; Li, F. Near-Infrared Photoregulated Drug Release in Living Tumor Tissue via Yolk-Shell Upconversion Nanocages. *Adv. Funct. Mater.* **2014**, *24*, 363–371.
- (705) Deng, R.; Wang, J.; Chen, R.; Huang, W.; Liu, X. Enabling Förster Resonance Energy Transfer From Large Nanocrystals Through Energy Migration. *J. Am. Chem. Soc.* **2016**, *138*, 15972–15979.
- (706) Xiang, J.; Zhou, S.; Lin, J.; Wen, J.; Xie, Y.; Yan, B.; Yan, Q.; Zhao, Y.; Shi, F.; Fan, H. Low-Power Near-Infrared-Responsive Upconversion Nanovectors. *ACS Appl. Mater. Interfaces* **2021**, *13*, 7094–7101.
- (707) Chen, Z.; Thiramanas, R.; Schwendy, M.; Xie, C.; Parekh, S. H.; Mailänder, V.; Wu, S. Upconversion Nanocarriers Encapsulated With Photoactivatable Ru Complexes for Near-Infrared Light-Regulated Enzyme Activity. *Small* **2017**, *13*, 1700997.
- (708) Chu, H.; Zhao, J.; Mi, Y.; Zhao, Y.; Li, L. Near-Infrared Light-Initiated Hybridization Chain Reaction for Spatially and Temporally Resolved Signal Amplification. *Angew. Chem., Int. Ed.* **2019**, *58*, 14877–14881.
- (709) Qu, A.; Wu, X.; Li, S.; Sun, M.; Xu, L.; Kuang, H.; Xu, C. An NIR-Responsive DNA-Mediated Nanotetrahedron Enhances the Clearance of Senescent Cells. *Adv. Mater.* **2020**, *32*, 2000184.
- (710) Yan, Z.; Qin, H.; Ren, J.; Qu, X. Photocontrolled Multidirectional Differentiation of Mesenchymal Stem Cells on an Upconversion Substrate. *Angew. Chem., Int. Ed.* **2018**, *57*, 11182.
- (711) Chu, H.; Zhao, J.; Mi, Y.; Di, Z.; Li, L. NIR-light-mediated Spatially Selective Triggering of anti-tumor Immunity via Upconversion Nanoparticle-based Immunodevices. *Nat. Commun.* **2019**, *10*, 2839.
- (712) Zhang, Y.; Chen, W.; Zhang, Y.; Zhang, X.; Liu, Y.; Ju, H. A Near-Infrared Photo-Switched MicroRNA Amplifier for Precise Photodynamic Therapy of Early-Stage Cancers. *Angew. Chem.* **2020**, *132*, 21638–21643.
- (713) He, Y.; Guo, S.; Zhang, Y.; Liu, Y.; Ju, H. Near-Infrared Photo-controlled Permeability of a Biomimetic Polymersome With Sustained Drug Release and Efficient Tumor Therapy. *ACS Appl. Mater. Interfaces* **2021**, *13*, 14951–14963.
- (714) Pan, Y.; Yang, J.; Luan, X.; Liu, X.; Li, X.; Yang, J.; Huang, T.; Sun, L.; Wang, Y.; Lin, Y.; Song, Y. Near-infrared Upconversion-activated CRISPR-Cas9 System: A Remote-controlled Gene Editing Platform. *Sci. Adv.* **2019**, *5*, No. eaav7199.
- (715) Ao, Y.; Zeng, K.; Yu, B.; Miao, Y.; Hung, W.; Yu, Z.; Xue, Y.; Tan, T. T. Y.; Xu, T.; Zhen, M.; et al. An Upconversion Nanoparticle Enables Near Infrared-Optogenetic Manipulation of the *Caenorhabditis Elegans* Motor Circuit. *ACS Nano* **2019**, *13*, 3373–3386.
- (716) Ai, X.; Lyu, L.; Zhang, Y.; Tang, Y.; Mu, J.; Liu, F.; Zhou, Y.; Zuo, Z.; Liu, G.; Xing, B. Remote Regulation of Membrane Channel Activity by Site-Specific Localization of Lanthanide-Doped Upconversion Nanocrystals. *Angew. Chem., Int. Ed.* **2017**, *56*, 3031–3035.
- (717) Chen, S.; Weitmier, A. Z.; Zeng, X.; He, L.; Wang, X.; Tao, Y.; Huang, A. J. Y.; Hashimoto, Y.; Kano, M.; Iwasaki, H.; et al. Near-infrared Deep Brain Stimulation via Upconversion Nanoparticle-mediated Optogenetics. *Science* **2018**, *359*, 679–684.
- (718) Zhao, T.; Wang, P.; Li, Q.; Al-Khalaf, A. A.; Hozzein, W. N.; Zhang, F.; Li, X.; Zhao, D. Near-Infrared Triggered Decomposition of Nanocapsules With High Tumor Accumulation and Stimuli Responsive Fast Elimination. *Angew. Chem., Int. Ed.* **2018**, *57*, 2611–2645.
- (719) Han, S.; Samanta, A.; Xie, X.; Huang, L.; Peng, J.; Park, S. J.; Teh, D. B. L.; Choi, Y.; Chang, Y.-T.; All, A. H.; et al. Gold and Hairpin DNA Functionalization of Upconversion Nanocrystals for Imaging and *In Vivo* Drug Delivery. *Adv. Mater.* **2017**, *29*, 1700244.
- (720) Ruiyi, L.; Zaijun, L.; Xiulan, S.; Jan, J.; Lin, L.; Zhiguo, G.; Guangli, W. Graphene Quantum Dot-rare Earth Upconversion Nanocages With Extremely High Efficiency of Upconversion Luminescence, Stability and Drug Loading Towards Controlled Delivery and Cancer Theranostics. *Chem. Eng. J.* **2020**, *382*, 122992.
- (721) Kramer, R. H.; Mourrot, A.; Adesnik, H. Optogenetic Pharmacology for Control of Native Neuronal Signaling Proteins. *Nat. Neurosci.* **2013**, *16*, 816–823.
- (722) Deisseroth, K. Optogenetics: 10 Years of Microbial Opsins in Neuroscience. *Nat. Neurosci.* **2015**, *18*, 1213–1225.

- (723) Yu, N.; Huang, L.; Zhou, Y.; Xue, T.; Chen, Z.; Han, G. Near-Infrared-Light Activatable Nanoparticles for Deep-Tissue-Penetrating Wireless Optogenetics. *Adv. Healthcare Mater.* **2019**, *8*, 1801132.
- (724) All, A. H.; Zeng, X.; Teh, D. B. L.; Yi, Z.; Prasad, A.; Ishizuka, T.; Thakor, N.; Hiromu, Y.; Liu, X. Expanding the Toolbox of Upconversion Nanoparticles for *In Vivo* Optogenetics and Neuromodulation. *Adv. Mater.* **2019**, *31*, 1803474.
- (725) Hososhima, S.; Yuasa, H.; Ishizuka, T.; Hoque, M. R.; Yamashita, T.; Yamanaka, A.; Sugano, E.; Tomita, H.; Yawo, H. Near-infrared (NIR) Up-conversion Optogenetics. *Sci. Rep.* **2015**, *5*, 16533.
- (726) Shah, S.; Liu, J.-J.; Pasquale, N.; Lai, J.; McGowan, H.; Pang, Z. P.; Lee, K.-B. Hybrid Upconversion Nanomaterials for Optogenetic Neuronal Control. *Nanoscale* **2015**, *7*, 16571–16577.
- (727) Wu, X.; Zhang, Y.; Takle, K.; Bilsel, O.; Li, Z.; Lee, H.; Zhang, Z.; Li, D.; Fan, W.; Duan, C.; et al. Dye-Sensitized Core/Active Shell Upconversion Nanoparticles for Optogenetics and Bioimaging Applications. *ACS Nano* **2016**, *10*, 1060–1066.
- (728) Bansal, A.; Liu, H.; Jayakumar, M. K. G.; Andersson-Engels, S.; Zhang, Y. Quasi-Continuous Wave Near-Infrared Excitation of Upconversion Nanoparticles for Optogenetic Manipulation of C. *Small* **2016**, *12*, 1732–1743.
- (729) Lin, X.; Wang, Y.; Chen, X.; Yang, R.; Wang, Z.; Feng, J.; Wang, H.; Lai, K. W. C.; He, J.; Wang, F.; et al. Multiplexed Optogenetic Stimulation of Neurons With Spectrum-Selective Upconversion Nanoparticles. *Adv. Healthcare Mater.* **2017**, *6*, 1700446.
- (730) Brites, C. D. S.; Balabhadra, S.; Carlos, L. D. Lanthanide-Based Thermometers: At the Cutting-Edge of Luminescence Thermometry. *Adv. Opt. Mater.* **2019**, *7*, 1801239.
- (731) Su, X.; Wen, Y.; Yuan, W.; Xu, M.; Liu, Q.; Huang, C.; Li, F. Lifetime-based Nanothermometry *In Vivo* With Ultra-long-lived Luminescence. *Chem. Commun.* **2020**, *56*, 10694–10697.
- (732) Goderski, S.; Runowski, M.; Woźny, P.; Lavin, V.; Lis, S. Lanthanide Upconverted Luminescence for Simultaneous Contactless Optical Thermometry and Manometry—Sensing Under Extreme Conditions of Pressure and Temperature. *ACS Appl. Mater. Interfaces* **2020**, *12*, 40475–40485.
- (733) de Sousa Filho, P. C.; Alain, J.; Leménager, G.; Larquet, E.; Fick, J.; Osvaldo, A. S.; Gacoin, T. Colloidal Rare Earth Vanadate Single Crystalline Particles as Ratiometric Luminescent Thermometers. *J. Phys. Chem. C* **2019**, *123*, 2441–2450.
- (734) Fernandez-Bravo, A.; Yao, K.; Barnard, E. S.; Borys, N. J.; Levy, E. S.; Tian, B.; Tajon, C. A.; Moretti, L.; Altoe, M. V.; Aloni, S.; et al. Continuous-wave Upconverting Nanoparticle Microlasers. *Nat. Nanotechnol.* **2018**, *13*, 572–577.
- (735) Siaï, A.; Haro-González, P.; Horchani-Naifer, K.; Férid, M. La₂O₃: Tm, Yb, Er Upconverting Nano-oxides for Sub-tissue Lifetime Thermal Sensing. *Sens. Actuators, B* **2016**, *234*, 541–548.
- (736) Suo, H.; Guo, C.; Zheng, J.; Zhou, B.; Ma, C.; Zhao, X.; Li, T.; Guo, P.; Goldys, E. M. Sensitivity Modulation of Upconverting Thermometry Through Engineering Phonon Energy of a Matrix. *ACS Appl. Mater. Interfaces* **2016**, *8*, 30312–30319.
- (737) Brites, C. D. S.; Xie, X.; Debasu, M. L.; Qin, X.; Chen, R.; Huang, W.; Rocha, J.; Liu, X.; Carlos, L. D. Instantaneous Ballistic velocity of Suspended Brownian Nanocrystals Measured by Upconversion Nanothermometry. *Nat. Nanotechnol.* **2016**, *11*, 851–856.
- (738) Guo, J.; Zhou, B.; Yang, C.; Dai, Q.; Kong, L. Stretchable and Temperature-Sensitive Polymer Optical Fibers for Wearable Health Monitoring. *Adv. Funct. Mater.* **2019**, *29*, 1902898.
- (739) Li, X.; Yang, L.; Zhu, Y.; Zhong, J.; Chen, D. Upconversion of Transparent Glass Ceramics Containing β -NaYF₄:Yb³⁺, Er³⁺ Nanocrystals for Optical Thermometry. *RSC Adv.* **2019**, *9*, 7948–7954.
- (740) Baziulyte-Paulaviciene, D.; Traskina, N.; Vargalis, R.; Katelnikovas, A.; Sakirzanovas, S. Thermal Decomposition Synthesis of Er³⁺-activated NaYbF₄ Upconverting Microparticles for Optical Temperature Sensing. *J. Lumin.* **2019**, *215*, 116672.
- (741) Runowski, M.; Stopikowska, N.; Szeremeta, D.; Goderski, S.; Skwierczyńska, M.; Lis, S. Upconverting Lanthanide Fluoride Core@Shell Nanorods for Luminescent Thermometry in the First and Second Biological Windows: β -NaYF₄:Yb³⁺–Er³⁺@SiO₂ Temperature Sensor. *ACS Appl. Mater. Interfaces* **2019**, *11*, 13389–13396.
- (742) Luo, L.; Ran, W.; Du, P.; Li, W.; Wang, D. Photocatalytic and Thermometric Characteristics of Er³⁺-Activated Bi₅IO₇ Upconverting Microparticles. *Adv. Mater. Interfaces* **2020**, *7*, 1902208.
- (743) Back, M.; Casagrande, E.; Brondin, C. A.; Ambrosi, E.; Cristofori, D.; Ueda, J.; Tanabe, S.; Trave, E.; Riello, P. Lanthanide-Doped Bi₂SiO₅@SiO₂ Core–Shell Upconverting Nanoparticles for Stable Ratiometric Optical Thermometry. *ACS Appl. Nano Mater.* **2020**, *3*, 2594–2604.
- (744) Balabhadra, S.; Debasu, M. L.; Brites, C. D. S.; Ferreira, R. A. S.; Carlos, L. D. Upconverting Nanoparticles Working As Primary Thermometers In Different Media. *J. Phys. Chem. C* **2017**, *121*, 13962–13968.
- (745) Nigoghossian, K.; Ouellet, S.; Plain, J.; Messaddeq, Y.; Boudreau, D.; Ribeiro, S. J. L. Upconversion Nanoparticle-decorated Gold Nanoshells for Near-infrared Induced Heating and Thermometry. *J. Mater. Chem. B* **2017**, *5*, 7109–7117.
- (746) Shang, Y.; Han, Q.; Hao, S.; Chen, T.; Zhu, Y.; Wang, Z.; Yang, C. Dual-Mode Upconversion Nanoprobe Enables Broad-Range Thermometry From Cryogenic to Room Temperature. *ACS Appl. Mater. Interfaces* **2019**, *11*, 42455–42461.
- (747) Lei, P.; Liu, X.; Dong, L.; Wang, Z.; Song, S.; Xu, X.; Su, Y.; Feng, J.; Zhang, H. Lanthanide Doped Bi₂O₃ Upconversion Luminescence Nanospheres for Temperature Sensing and Optical Imaging. *Dalton T.* **2016**, *45*, 2686–2693.
- (748) Kaczmarek, A. M.; Kaczmarek, M. K.; Van Deun, R. Er³⁺-to-Yb³⁺ and Pr³⁺-to-Yb³⁺ Energy Transfer for Highly Efficient Near-infrared Cryogenic Optical Temperature Sensing. *Nanoscale* **2019**, *11*, 833–837.
- (749) Suo, H.; Zhao, X.; Zhang, Z.; Guo, C. 808 nm Light-Triggered Thermometer–Heater Upconverting Platform Based on Nd³⁺-Sensitized Yolk–Shell GdOF@SiO₂. *ACS Appl. Mater. Interfaces* **2017**, *9*, 43438–43448.
- (750) Labrador-Páez, L.; Pedroni, M.; Speghini, A.; García-Solé, J.; Haro-González, P.; Jaque, D. Reliability of Rare-earth-doped Infrared Luminescent Nanothermometers. *Nanoscale* **2018**, *10*, 22319–22328.
- (751) Skripka, A.; Benayas, A.; Marin, R.; Canton, P.; Hemmer, E.; Vetrone, F. Double Rare-earth Nanothermometer in aqueous Media: Opening the Third Optical Transparency Window to Temperature Sensing. *Nanoscale* **2017**, *9*, 3079–3085.
- (752) Savchuk, O. A.; Carvajal, J. J.; Pujol, M. C.; Barrera, E. W.; Massons, J.; Aguilo, M.; Diaz, F. Ho,Yb:KLu(WO₄)₂ Nanoparticles: A Versatile Material for Multiple Thermal Sensing Purposes by Luminescent Thermometry. *J. Phys. Chem. C* **2015**, *119*, 18546–18558.
- (753) Pang, T.; Wang, J. Controllable Upconversion Luminescence and Temperature Sensing Behavior in NaGdF₄:Yb³⁺/Ho³⁺/Ce³⁺ Nano-phosphors. *Mater. Res. Express* **2018**, *5*, 015049.
- (754) Wang, C.; Lin, H.; Xiang, X.; Cheng, Y.; Huang, Q.; Gao, Y.; Cui, X.; Wang, Y. CsPbBr₃/EuPO₄ Dual-phase Devitrified Glass for Highly Sensitive Self-calibrating Optical Thermometry. *J. Mater. Chem. C* **2018**, *6*, 9964–9971.
- (755) Huang, F.; Chen, D. Synthesis of Mn²⁺:Zn₂SiO₄–Eu³⁺:Gd₂O₃ Nanocomposites for Highly Sensitive Optical Thermometry Through the Synergistic Luminescence from Lanthanide-transition Metal Ions. *J. Mater. Chem. C* **2017**, *5*, 5176–5182.
- (756) Das, S.; Som, S.; Yang, C.-Y.; Chavhan, S.; Lu, C.-H. Structural Evaluations and Temperature Dependent Photoluminescence Characterizations of Eu³⁺-activated SrZrO₃ Hollow Spheres for Luminescence Thermometry applications. *Sci. Rep.* **2016**, *6*, 25787.
- (757) Carrasco, E.; del Rosal, B.; Sanz-Rodríguez, F.; de la Fuente, A. J.; Gonzalez, P. H.; Rocha, U.; Kumar, K. U.; Jacinto, C.; Solé, J. G.; Jaque, D. Intratumoral Thermal Reading During Photo-Thermal Therapy by Multifunctional Fluorescent Nanoparticles. *Adv. Funct. Mater.* **2015**, *25*, 615–626.
- (758) Benayas, A.; del Rosal, B.; Pérez-Delgado, A.; Santacruz-Gómez, K.; Jaque, D.; Hirata, G. A.; Vetrone, F. Nd:YAG Near-

- Infrared Luminescent Nanothermometers. *Adv. Opt. Mater.* **2015**, *3*, 687–694.
- (759) Huang, P.; Zheng, W.; Tu, D.; Shang, X.; Zhang, M.; Li, R.; Xu, J.; Liu, Y.; Chen, X. Unraveling the Electronic Structures of Neodymium in LiLuF₄ Nanocrystals for Ratiometric Temperature Sensing. *Adv. Sci.* **2019**, *6*, 1802282.
- (760) Marciniak, L.; Bednarkiewicz, A.; Stefanski, M.; Tomala, R.; Hreniak, D.; Strek, W. Near Infrared Absorbing Near Infrared Emitting Highly-sensitive Luminescent Nanothermometer Based on Nd³⁺ to Yb³⁺ Energy Transfer. *Phys. Chem. Chem. Phys.* **2015**, *17*, 24315–24321.
- (761) Nikolić, M. G.; Antić, Ž.; Čulubrk, S.; Nedeljković, J. M.; Dramićanin, M. D. Temperature Sensing With Eu³⁺ Doped TiO₂ Nanoparticles. *Sens. Actuators, B* **2014**, *201*, 46–50.
- (762) Liu, Y.; Bai, G.; Lyu, Y.; Hua, Y.; Ye, R.; Zhang, J.; Chen, L.; Xu, S.; Hao, J. Ultrabroadband Tuning and Fine Structure of Emission Spectra in Lanthanide Er-Doped ZnSe Nanosheets for Display and Temperature Sensing. *ACS Nano* **2020**, *14*, 16003–16012.
- (763) Dramićanin, M. D.; Antić, Ž.; Čulubrk, S.; Ahrenkiel, S. P.; Nedeljković, J. M. Self-referenced Luminescence Thermometry With Sm³⁺ Doped TiO₂ Nanoparticles. *Nanotechnology* **2014**, *25*, 485501.
- (764) Cui, Y.; Song, R.; Yu, J.; Liu, M.; Wang, Z.; Wu, C.; Yang, Y.; Wang, Z.; Chen, B.; Qian, G. Dual-Emitting MOF/Dye Composite for Ratiometric Temperature Sensing. *Adv. Mater.* **2015**, *27*, 1420–1425.
- (765) Yang, Y.; Chen, L.; Jiang, F.; Yu, M.; Wan, X.; Zhang, B.; Hong, M. A Family of Doped Lanthanide Metal–organic Frameworks for Wide-range Temperature Sensing and Tunable White Light Emission. *J. Mater. Chem. C* **2017**, *5*, 1981–1989.
- (766) Zhou, Y.; Yan, B. Ratiometric Detection of Temperature Using Responsive Dual-emissive MOF Hybrids. *J. Mater. Chem. C* **2015**, *3*, 9353–9358.
- (767) Li, L.; Zhu, Y.; Zhou, X.; Brites, C. D. S.; Ananias, D.; Lin, Z.; Paz, F. A. A.; Rocha, J.; Huang, W.; Carlos, L. D. Visible-Light Excited Luminescent Thermometer Based on Single Lanthanide Organic Frameworks. *Adv. Funct. Mater.* **2016**, *26*, 8677–8684.
- (768) Lian, X.; Zhao, D.; Cui, Y.; Yang, Y.; Qian, G. A Near Infrared Luminescent Metal–organic Framework for Temperature Sensing in the Physiological Range. *Chem. Commun.* **2015**, *51*, 17676–17679.
- (769) Wang, Y.; Chen, B.; Wang, F. Overcoming Thermal Quenching in Upconversion Nanoparticles. *Nanoscale* **2021**, *13*, 3454–3462.
- (770) Zhou, J.; del Rosal, B.; Jaque, D.; Uchiyama, S.; Jin, D. Advances and Challenges for Fluorescence Nanothermometry. *Nat. Methods* **2020**, *17*, 967–980.
- (771) Zhou, Y.; Cheng, Y.; Huang, Q.; Xu, J.; Lin, H.; Wang, Y. Abnormal Thermally Enhanced Upconversion Luminescence of Lanthanide-doped Phosphors: Proposed Mechanisms and Potential applications. *J. Mater. Chem. C* **2021**, *9*, 2220–2230.
- (772) Shi, R.; Martinez, E. D.; Brites, C. D.; Carlos, L. D. Thermal Enhancement of Upconversion Emission in Nanocrystals: a Comprehensive Summary. *Phys. Chem. Chem. Phys.* **2021**, *23*, 20–42.
- (773) Cui, X.; Cheng, Y.; Lin, H.; Huang, F.; Wu, Q.; Wang, Y. Size-dependent Abnormal Thermo-enhanced Luminescence of Ytterbium-doped Nanoparticles. *Nanoscale* **2017**, *9*, 13794–13799.
- (774) Zhou, J.; Wen, S.; Liao, J.; Clarke, C.; Tawfik, S. A.; Ren, W.; Mi, C.; Wang, F.; Jin, D. Activation of the Surface Dark-layer to Enhance Upconversion in a Thermal Field. *Nat. Photonics* **2018**, *12*, 154–158.
- (775) Wang, Z.; Christiansen, J.; Wezendonk, D.; Xie, X.; van Huis, M. A.; Meijerink, A. Thermal Enhancement and Quenching of Upconversion Emission in Nanocrystals. *Nanoscale* **2019**, *11*, 12188–12197.
- (776) Hu, Y.; Shao, Q.; Zhang, P.; Dong, Y.; Fang, F.; Jiang, J. Mechanistic Investigations on the Dramatic Thermally Induced Luminescence Enhancement in Upconversion Nanocrystals. *J. Phys. Chem. C* **2018**, *122*, 26142–26152.
- (777) Lei, L.; Chen, D.; Li, C.; Huang, F.; Zhang, J.; Xu, S. Inverse Thermal Quenching Effect in Lanthanide-doped Upconversion Nanocrystals for anti-counterfeiting. *J. Mater. Chem. C* **2018**, *6*, 5427–5433.
- (778) Mi, C.; Zhou, J.; Wang, F.; Lin, G.; Jin, D. Ultrasensitive Ratiometric Nanothermometer With Large Dynamic Range and Photostability. *Chem. Mater.* **2019**, *31*, 9480–9487.
- (779) Maturi, F. E.; Brites, C. D. S.; Ximenes, E. C.; Mills, C.; Olsen, B.; Jaque, D.; Ribeiro, S. J. L.; Carlos, L. D. Going Above and Beyond: A Tenfold Gain in the Performance of Luminescence Thermometers Joining Multiparametric Sensing and Multiple Regression. *Laser Photonics Rev.* **2021**, *15*, 2100301.
- (780) Ximenes, E. C.; Santos, W. Q.; Rocha, U.; Kagola, U. K.; Sanz-Rodríguez, F.; Fernández, N.; Gouveia-Neto, A. d. S.; Bravo, D.; Domingo, A. M.; del Rosal, B.; et al. Unveiling *In Vivo* Subcutaneous Thermal Dynamics by Infrared Luminescent Nanothermometers. *Nano Lett.* **2016**, *16*, 1695–1703.
- (781) Sekiyama, S.; Umezawa, M.; Kuraoka, S.; Ube, T.; Kamimura, M.; Soga, K. Temperature Sensing of Deep Abdominal Region in Mice by Using Over-1000 nm Near-Infrared Luminescence of Rare-Earth-Doped NaYF₄ Nanothermometer. *Sci. Rep.* **2018**, *8*, 16979.
- (782) Wang, T.; Xiao, T.; Fan, Y.; He, F.; Li, Y.; Peng, Y.; Wang, Q.; Yin, Z.; Yang, Z.; Qiu, J.; et al. Abnormally Heat-enhanced Yb Excited State Lifetimes in Bi₇F₁₁O₅ Nanocrystals and the Potential applications in Lifetime Luminescence Nanothermometry. *J. Mater. Chem. C* **2019**, *7*, 13811–13817.
- (783) Suta, M.; Antić, Ž.; Đorđević, V.; Kuzman, S.; Dramićanin, M. D.; Meijerink, A. Making Nd³⁺ a Sensitive Luminescent Thermometer for Physiological Temperatures—An Account of Pitfalls in Boltzmann Thermometry. *Nanomaterials* **2020**, *10*, 543.
- (784) Lacam, A.; Chateau, C. High-pressure Measurements at Moderate Temperatures in a Diamond anvil Cell With a New Optical Sensor: SrB₄O₇:Sm²⁺. *J. Appl. Phys.* **1989**, *66*, 366–372.
- (785) Xu, C.-N.; Watanabe, T.; Akiyama, M.; Zheng, X.-G. Direct View of Stress Distribution in Solid by Mechanoluminescence. *Appl. Phys. Lett.* **1999**, *74*, 2414–2416.
- (786) Chandra, V. K.; Chandra, B. P.; Jha, P. Self-recovery of Mechanoluminescence in ZnS:Cu and ZnS:Mn Phosphors by Trapping of Drifting Charge Carriers. *Appl. Phys. Lett.* **2013**, *103*, 161113.
- (787) Zhang, H.; Peng, D.; Wang, W.; Dong, L.; Pan, C. Mechanically Induced Light Emission and Infrared-Laser-Induced Upconversion in the Er-Doped CaZnOS Multifunctional Piezoelectric Semiconductor for Optical Pressure and Temperature Sensing. *J. Phys. Chem. C* **2015**, *119*, 28136–28142.
- (788) Zhang, J.-C.; Long, Y.-Z.; Yan, X.; Wang, X.; Wang, F. Creating Recoverable Mechanoluminescence in Piezoelectric Calcium Niobates Through Pr³⁺ Doping. *Chem. Mater.* **2016**, *28*, 4052–4057.
- (789) Chen, C.; Zhuang, Y.; Tu, D.; Wang, X.; Pan, C.; Xie, R.-J. Creating Visible-to-near-infrared Mechanoluminescence in Mixed-anion Compounds SrZn₂S₂O and SrZnSO. *Nano Energy* **2020**, *68*, 104329.
- (790) Mei, S.; Guo, Y.; Lin, X.; Dong, H.; Sun, L.-D.; Li, K.; Yan, C.-H. Experimental and Simulation Insights into Local Structure and Luminescence Evolution in Eu³⁺-Doped Nanocrystals Under High Pressure. *J. Phys. Chem. Lett.* **2020**, *11*, 3515–3520.
- (791) Lay, A.; Wang, D. S.; Wisser, M. D.; Mehlenbacher, R. D.; Lin, Y.; Goodman, M. B.; Mao, W. L.; Dionne, J. A. Upconverting Nanoparticles as Optical Sensors of Nano- to Micro-Newton Forces. *Nano Lett.* **2017**, *17*, 4172–4177.
- (792) Zhuang, Y.; Tu, D.; Chen, C.; Wang, L.; Zhang, H.; Xue, H.; Yuan, C.; Chen, G.; Pan, C.; Dai, L.; Xie, R.-J. Force-induced Charge Carrier Storage: a New Route for Stress Recording. *Light-Sci. Appl.* **2020**, *9*, 182.
- (793) Xie, L.; Qin, Y.; Chen, H.-Y. Polymeric Optodes Based on Upconverting Nanorods for Fluorescent Measurements of pH and Metal Ions in Blood Samples. *Anal. Chem.* **2012**, *84*, 1969–1974.
- (794) Yan, L.; Chang, Y.-N.; Yin, W.; Liu, X.; Xiao, D.; Xing, G.; Zhao, L.; Gu, Z.; Zhao, Y. Biocompatible and Flexible Graphene

- Oxide/upconversion Nanoparticle Hybrid Film for Optical pH Sensing. *Phys. Chem. Chem. Phys.* **2014**, *16*, 1576–1582.
- (795) Näreoja, T.; Deguchi, T.; Christ, S.; Peltomaa, R.; Prabhakar, N.; Fazeli, E.; Perälä, N.; Rosenholm, J. M.; Arppe, R.; Soukka, T.; et al. Ratiometric Sensing and Imaging of Intracellular pH Using Polyethylenimine-Coated Photon Upconversion Nanoprobes. *Anal. Chem.* **2017**, *89*, 1501–1508.
- (796) Tsai, E. S.; Joud, F.; Wiesholler, L. M.; Hirsch, T.; Hall, E. A. H. Upconversion Nanoparticles as Intracellular pH Messengers. *Anal. Bioanal. Chem.* **2020**, *412*, 6567–6581.
- (797) Ding, C.; Cheng, S.; Zhang, C.; Xiong, Y.; Ye, M.; Xian, Y. Ratiometric Upconversion Luminescence Nanoprobe With Near-Infrared Ag₂S Nanodots as the Energy Acceptor for Sensing and Imaging of pH *In Vivo*. *Anal. Chem.* **2019**, *91*, 7181–7188.
- (798) Wang, S.; Feng, J.; Song, S.; Zhang, H. A Long-wave Optical pH Sensor Based on Red Upconversion Luminescence of NaGdF₄ Nanotubes. *RSC Adv.* **2014**, *4*, 55897–55899.
- (799) Radunz, S.; Andresen, E.; Würth, C.; Koerd, A.; Tschiche, H. R.; Resch-Genger, U. Simple Self-Referenced Luminescent pH Sensors Based on Upconversion Nanocrystals and pH-Sensitive Fluorescent BODIPY Dyes. *Anal. Chem.* **2019**, *91*, 7756–7764.
- (800) Zhao, J.; Li, Y.; Yu, M.; Gu, Z.; Li, L.; Zhao, Y. Time-Resolved Activation of pH Sensing and Imaging *In Vivo* by a Remotely Controllable DNA Nanomachine. *Nano Lett.* **2020**, *20*, 874–880.
- (801) Ma, T.; Ma, Y.; Liu, S.; Zhang, L.; Yang, T.; Yang, H.-R.; Lv, W.; Yu, Q.; Xu, W.; Zhao, Q.; et al. Dye-conjugated Upconversion Nanoparticles for Ratiometric Imaging of Intracellular pH Values. *J. Mater. Chem. C* **2015**, *3*, 6616–6620.
- (802) Li, H.; Dong, H.; Yu, M.; Liu, C.; Li, Z.; Wei, L.; Sun, L.-D.; Zhang, H. NIR Ratiometric Luminescence Detection of pH Fluctuation in Living Cells With Hemicyanine Derivative-Assembled Upconversion Nanophosphors. *Anal. Chem.* **2017**, *89*, 8863–8869.
- (803) Du, S.; Hernández-Gil, J.; Dong, H.; Zheng, X.; Lyu, G.; Bañobre-López, M.; Gallo, J.; Sun, L.-d.; Yan, C.-h.; Long, N. J. Design and Validation of a New Ratiometric Intracellular pH Imaging Probe Using Lanthanide-doped Upconverting Nanoparticles. *Dalton T.* **2017**, *46*, 13957–13965.
- (804) Mahata, M. K.; Lee, K. T. Development of Near-infrared Sensitized Core-shell-shell Upconverting Nanoparticles as pH-responsive Probes. *Nanoscale Adv.* **2019**, *1*, 2372–2381.
- (805) Lei, L.; Xia, H.; Lim, C.-K.; Xu, S.; Wang, K.; Du, Y.; Prasad, P. N. Modulation of Surface Energy Transfer Cascade for Reversible Photoluminescence pH Sensing. *Chem. Mater.* **2019**, *31*, 8121–8128.
- (806) Laguna, M.; Escudero, A.; Núñez, N. O.; Becerro, A. I.; Ocaña, M. Europium-doped NaGd(WO₄)₂ Nanophosphors: Synthesis, Luminescence and Their Coating With Fluorescein for pH Sensing. *Dalton T.* **2017**, *46*, 11575–11583.
- (807) Zhu, Y.; Cui, S.; Wang, Y.; Liu, M.; Lu, C.; Mishra, A.; Xu, W. Enhanced Rare Earth Photoluminescence in Inverse Opal Photonic Crystals and Its application for pH Sensing. *Nanotechnology* **2016**, *27*, 405202.
- (808) Mondal, T. K.; Mondal, S.; Ghorai, U. K.; Saha, S. K. White Light Emitting Lanthanide Based Carbon Quantum Dots as Toxic Cr (VI) and pH Sensor. *J. Colloid Interface Sci.* **2019**, *553*, 177–185.
- (809) Li, Y.-J.; Wang, Y.-L.; Liu, Q.-Y. The Highly Connected MOFs Constructed From Nonanuclear and Trinuclear Lanthanide-Carboxylate Clusters: Selective Gas Adsorption and Luminescent pH Sensing. *Inorg. Chem.* **2017**, *56*, 2159–2164.
- (810) Huang, S.-Z.; Liu, S.-S.; Zhang, H.-j.; Han, Z.; Zhao, G.; Dong, X.-Y.; Zang, S.-Q. Dual-Functional Proton-Conducting and pH-Sensing Polymer Membrane Benefiting From a Eu-MOF. *ACS Appl. Mater. Interfaces* **2020**, *12*, 28720–28726.
- (811) Lu, Y.; Yan, B. A Ratiometric Fluorescent pH Sensor Based on Nanoscale Metal-organic Frameworks (MOFs) Modified by Europium(III) Complexes. *Chem. Commun.* **2014**, *50*, 13323–13326.
- (812) Han, Y.-H.; Tian, C.-B.; Li, Q.-H.; Du, S.-W. Highly Chemical and Thermally Stable Luminescent Eu_xTb_{1-x} MOF Materials for Broad-range pH and Temperature Sensors. *J. Mater. Chem. C* **2014**, *2*, 8065–8070.
- (813) Li, H.-Y.; Wei, Y.-L.; Dong, X.-Y.; Zang, S.-Q.; Mak, T. C. W. Novel Tb-MOF Embedded With Viologen Species for Multi-Photofunctionality: Photochromism, Photomodulated Fluorescence, and Luminescent pH Sensing. *Chem. Mater.* **2015**, *27*, 1327–1331.
- (814) Wang, X.; Chang, H.; Xie, J.; Zhao, B.; Liu, B.; Xu, S.; Pei, W.; Ren, N.; Huang, L.; Huang, W. Recent Developments in Lanthanide-based Luminescent Probes. *Coord. Chem. Rev.* **2014**, *273*, 201–212.
- (815) Guan, Y.; Qu, S.; Li, B.; Zhang, L.; Ma, H.; Zhang, L. Ratiometric Fluorescent Nanosensors for Selective Detecting Cysteine With Upconversion Luminescence. *Biosens. Bioelectron.* **2016**, *77*, 124–130.
- (816) Ni, J.; Shan, C.; Li, B.; Zhang, L.; Ma, H.; Luo, Y.; Song, H. Assembling of a Functional Cyclodextrin-decorated Upconversion Luminescence Nanoplatform for Cysteine-sensing. *Chem. Commun.* **2015**, *51*, 14054–14056.
- (817) Wu, Q.; Fang, A.; Li, H.; Zhang, Y.; Yao, S. Enzymatic-induced Upconversion Photoinduced Electron Transfer for Sensing Tyrosine in Human Serum. *Biosens. Bioelectron.* **2016**, *77*, 957–962.
- (818) Zhao, L.; Peng, J.; Chen, M.; Liu, Y.; Yao, L.; Feng, W.; Li, F. Yolk-Shell Upconversion Nanocomposites for LRET Sensing of Cysteine/Homocysteine. *ACS Appl. Mater. Interfaces* **2014**, *6*, 11190.
- (819) Pan, H.; Xu, S.; Ni, Y. Rare-earth Post-modified Zn-based Coordination Polymer Microspheres: Simple Room-temperature Preparation, Fluorescent Performances and application for Detection of Tryptophane. *Sens. Actuators, B* **2019**, *283*, 731–739.
- (820) Wang, X. R.; Huang, Z.; Du, J.; Wang, X. Z.; Gu, N.; Tian, X.; Li, Y.; Liu, Y. Y.; Huo, J. Z.; Ding, B. Hydrothermal Preparation of Five Rare-Earth (Re = Dy, Gd, Ho, Pr, and Sm) Luminescent Cluster-Based Coordination Materials: The First MOFs-based Ratiometric Fluorescent Sensor for Lysine and Bifunctional Sensing Platform for Insulin and Al³⁺. *Inorg. Chem.* **2018**, *57*, 12885–12899.
- (821) Wu, B.; Cao, Z.; Zhang, Q.; Wang, G. NIR-responsive DNA Hybridization Detection by High Efficient FRET From 10-nm Upconversion Nanoparticles to SYBR Green I. *Sens. Actuators, B* **2018**, *255*, 2853–2860.
- (822) Zhang, K.; Lu, F.; Cai, Z.; Song, S.; Jiang, L.; Min, Q.; Wu, X.; Zhu, J.-J. Plasmonic Modulation of the Upconversion Luminescence Based on Gold Nanorods for Designing a New Strategy of Sensing MicroRNAs. *Anal. Chem.* **2020**, *92*, 11795–11801.
- (823) Mendez-Gonzalez, D.; Lahtinen, S.; Laurenti, M.; López-Cabarcos, E.; Rubio-Retama, J.; Soukka, T. Photochemical Ligation to Ultrasensitive DNA Detection With Upconverting Nanoparticles. *Anal. Chem.* **2018**, *90*, 13385–13392.
- (824) Jesu Raj, J. G.; Quintanilla, M.; Mahmoud, K. A.; Ng, A.; Vetrone, F.; Zourob, M. Sensitive Detection of SsDNA Using an LRET-Based Upconverting Nanohybrid Material. *ACS Appl. Mater. Interfaces* **2015**, *7*, 18257–18265.
- (825) Alonso-Cristobal, P.; Vilela, P.; El-Sagheer, A.; Lopez-Cabarcos, E.; Brown, T.; Muskens, O. L.; Rubio-Retama, J.; Kanaras, A. G. Highly Sensitive DNA Sensor Based on Upconversion Nanoparticles and Graphene Oxide. *ACS Appl. Mater. Interfaces* **2015**, *7*, 12422–12429.
- (826) Tsang, M.-K.; Ye, W.; Wang, G.; Li, J.; Yang, M.; Hao, J. Ultrasensitive Detection of Ebola Virus Oligonucleotide Based on Upconversion Nanoprobe/Nanoporous Membrane System. *ACS Nano* **2016**, *10*, 598–605.
- (827) Vilela, P.; El-Sagheer, A.; Millar, T. M.; Brown, T.; Muskens, O. L.; Kanaras, A. G. Graphene Oxide-Upconversion Nanoparticle Based Optical Sensors for Targeted Detection of mRNA Biomarkers Present in Alzheimer's Disease and Prostate Cancer. *ACS Sensors* **2017**, *2*, 52–56.
- (828) Guo, T.; Deng, Q.; Fang, G.; Gu, D.; Yang, Y.; Wang, S. Upconversion Fluorescence Metal-organic Frameworks Thermo-sensitive Imprinted Polymer for Enrichment and Sensing Protein. *Biosens. Bioelectron.* **2016**, *79*, 341–346.
- (829) Zhang, Y.; Tang, Y.; Liu, X.; Zhang, L.; Lv, Y. A Highly Sensitive Upconverting Phosphors-based off-on Probe for the Detection of Glutathione. *Sens. Actuators, B* **2013**, *185*, 363–369.

- (830) Sun, L.; Wang, T.; Sun, Y.; Li, Z.; Song, H.; Zhang, B.; Zhou, G.; Zhou, H.; Hu, J. Fluorescence Resonance Energy Transfer Between $\text{NH}_2\text{-NaYF}_4\text{:Yb,Er}/\text{NaYF}_4\text{@SiO}_2$ Upconversion Nanoparticles and Gold Nanoparticles for the Detection of Glutathione and Cadmium Ions. *Talanta* **2020**, *207*, 120294.
- (831) Zheng, J.; Wu, Y.; Xing, D.; Zhang, T. Synchronous Detection of Glutathione/hydrogen Peroxide for Monitoring Redox Status *In Vivo* With a Ratiometric Upconverting Nanoprobe. *Nano Res.* **2019**, *12*, 931–938.
- (832) Xu, S.; Xu, W.; Wang, Y.; Zhang, S.; Zhu, Y.; Tao, L.; Xia, L.; Zhou, P.; Song, H. $\text{NaYF}_4\text{:Yb,Tm}$ Nanocrystals and TiO_2 Inverse Opal Composite Films: a Novel Device for Upconversion Enhancement and Solid-based Sensing of avidin. *Nanoscale* **2014**, *6*, 5859–5870.
- (833) Chen, X.; Xu, W.; Jiang, Y.; Pan, G.; Zhou, D.; Zhu, J.; Wang, H.; Chen, C.; Li, D.; Song, H. A Novel Upconversion Luminescence Derived Photoelectrochemical Immunoassay: Ultrasensitive Detection to alpha-fetoprotein. *Nanoscale* **2017**, *9*, 16357–16364.
- (834) Guo, T.; Deng, Q.; Fang, G.; Liu, C.; Huang, X.; Wang, S. Molecularly Imprinted Upconversion Nanoparticles for Highly Selective and Sensitive Sensing of Cytochrome C. *Biosens. Bioelectron.* **2015**, *74*, 498–503.
- (835) Xu, S.; Dong, B.; Zhou, D.; Yin, Z.; Cui, S.; Xu, W.; Chen, B.; Song, H. Paper-based Upconversion Fluorescence Resonance Energy Transfer Biosensor for Sensitive Detection of Multiple Cancer Biomarkers. *Sci. Rep.* **2016**, *6*, 23406.
- (836) Li, X.; Wei, L.; Pan, L.; Yi, Z.; Wang, X.; Ye, Z.; Xiao, L.; Li, H.-W.; Wang, J. Homogeneous Immunosorbent Assay Based on Single-Particle Enumeration Using Upconversion Nanoparticles for the Sensitive Detection of Cancer Biomarkers. *Anal. Chem.* **2018**, *90*, 4807–4814.
- (837) Liu, J.; Xu, S.; Sun, L.; Hu, S.; Sun, J.; Liu, M.; Ma, C.; Liu, H.; Wang, Z.; Yang, Y.; et al. Up-conversion Fluorescence Biosensor for Sensitive Detection of CA-125 Tumor Markers. *J. Rare Earths* **2019**, *37*, 943–948.
- (838) Liu, L.; Zhang, H.; Wang, Z.; Song, D. Peptide-functionalized Upconversion Nanoparticles-based FRET Sensing Platform for Caspase-9 Activity Detection *In Vitro* and *In Vivo*. *Biosens. Bioelectron.* **2019**, *141*, 111403.
- (839) Wang, H.; Lu, Y.; Wang, L.; Chen, H. Detection of Tyramine and Tyrosinase Activity Using Red Region Emission $\text{NaGdF}_4\text{:Yb,Er}/\text{NaYF}_4$ Upconversion Nanoparticles. *Talanta* **2019**, *197*, 558–566.
- (840) Cao, S.; Li, Z.; Zhao, J.; Chen, M.; Ma, N. Rational Engineering a Multichannel Upconversion Sensor for Multiplex Detection of Matrix Metalloproteinase Activities. *ACS Sensors* **2018**, *3*, 1522–1530.
- (841) Li, X.; Zhou, S.; Lu, S.; Tu, D.; Zheng, W.; Liu, Y.; Li, R.; Chen, X. Lanthanide Metal–Organic Framework Nanoprobes for the *In Vitro* Detection of Cardiac Disease Markers. *ACS Appl. Mater. Interfaces* **2019**, *11*, 43989–43995.
- (842) Li, Y.; Jia, D.; Ren, W.; Shi, F.; Liu, C. A Versatile Photoinduced Electron Transfer-Based Upconversion Fluorescent Biosensing Platform for the Detection of Disease Biomarkers and Nerve Agent. *Adv. Funct. Mater.* **2019**, *29*, 1903191.
- (843) Ou, X.; Chen, Y.; Xie, L.; Chen, J.; Zan, J.; Chen, X.; Hong, Z.; He, Y.; Li, J.; Yang, H. X-ray Nanocrystal Scintillator-Based Aptasensor for Autofluorescence-Free Detection. *Anal. Chem.* **2019**, *91*, 10149–10155.
- (844) Wiesholler, L. M.; Genslein, C.; Schroter, A.; Hirsch, T. Plasmonic Enhancement of NIR to UV Upconversion by a Nanoengineered Interface Consisting of $\text{NaYF}_4\text{:Yb,Tm}$ Nanoparticles and a Gold Nanotriangle Array for Optical Detection of Vitamin B12 in Serum. *Anal. Chem.* **2018**, *90*, 14247–14254.
- (845) Hazra, C.; Adusumalli, V. N. K. B.; Mahalingam, V. 3,5-Dinitrobenzoic Acid-Capped Upconverting Nanocrystals for the Selective Detection of Melamine. *ACS Appl. Mater. Interfaces* **2014**, *6*, 7833–7839.
- (846) Cen, Y.; Tang, J.; Kong, X.-J.; Wu, S.; Yuan, J.; Yu, R.-Q.; Chu, X. A Cobalt Oxyhydroxide-modified Upconversion Nanosystem for Sensitive Fluorescence Sensing of ascorbic Acid in Human Plasma. *Nanoscale* **2015**, *7*, 13951–13957.
- (847) Yu, H.; Liu, Q.; Li, J.; Su, Z.-M.; Li, X.; Wang, X.; Sun, J.; Zhou, C.; Hu, X. A Dual-emitting Mixed-lanthanide MOF With High Water-stability for Ratiometric Fluorescence Sensing of Fe^{3+} and ascorbic Acid. *J. Mater. Chem. C* **2021**, *9*, 562–568.
- (848) Gerelkhuu, Z.; Jung, D.; The Huy, B.; Tawfik, S. M.; Conte, M. L.; Conte, E. D.; Lee, Y.-I. Highly Selective and Sensitive Detection of Catecholamines Using $\text{NaLuGdF}_4\text{:Yb}^{3+}/\text{Er}^{3+}$ Upconversion Nanoparticles Decorated With Metal Ions. *Sens. Actuators, B* **2019**, *284*, 172–178.
- (849) Zhou, Y.; Ling, B.; Chen, H.; Wang, L. Mn^{2+} -doped $\text{NaYF}_4\text{:Yb,Er}$ Upconversion Nanoparticles for Detection of Uric Acid Based on the Fenton Reaction. *Talanta* **2018**, *180*, 120–126.
- (850) Yuan, J.; Cen, Y.; Kong, X.-J.; Wu, S.; Liu, C.-L.; Yu, R.-Q.; Chu, X. MnO_2 -Nanosheet-Modified Upconversion Nanosystem for Sensitive Turn-On Fluorescence Detection of H_2O_2 and Glucose in Blood. *ACS Appl. Mater. Interfaces* **2015**, *7*, 10548–10555.
- (851) Wang, D.; Pan, K.; Qu, Y.; Wang, G.; Yang, X.; Wang, D. $\text{BaWO}_4\text{:Ln}^{3+}$ Nanocrystals: Controllable Synthesis, Theoretical Investigation on the Substitution Site, and Bright Upconversion Luminescence as a Sensor for Glucose Detection. *ACS Appl. Nano Mater.* **2018**, *1*, 4762–4770.
- (852) Zhao, J.; Gao, J.; Xue, W.; Di, Z.; Xing, H.; Lu, Y.; Li, L. Upconversion Luminescence-Activated DNA Nanodevice for ATP Sensing in Living Cells. *J. Am. Chem. Soc.* **2018**, *140*, 578–581.
- (853) Rabie, H.; Zhang, Y.; Pasquale, N.; Lagos, M. J.; Batson, P. E.; Lee, K.-B. NIR Biosensing of Neurotransmitters in Stem Cell-Derived Neural Interface Using Advanced Core–Shell Upconversion Nanoparticles. *Adv. Mater.* **2019**, *31*, 1806991.
- (854) Rong, M.; Ye, J.; Chen, B.; Wen, Y.; Deng, X.; Liu, Z.-Q. Ratiometric Fluorescence Detection of Stringent ppGpp Using EuMoS_2 QDs Test Paper. *Sens. Actuators, B* **2020**, *309*, 127807.
- (855) Bhardwaj, N.; Bhardwaj, S.; Mehta, J.; Kim, K.-H.; Deep, A. Highly Sensitive Detection of Dipicolinic Acid With a Water-dispersible Terbium-metal Organic Framework. *Biosens. Bioelectron.* **2016**, *86*, 799–804.
- (856) Zhao, M.; Li, B.; Wu, Y.; He, H.; Zhu, X.; Zhang, H.; Dou, C.; Feng, L.; Fan, Y.; Zhang, F. A Tumor-Microenvironment-Responsive Lanthanide–Cyanine FRET Sensor for NIR-II Luminescence-Life-time In Situ Imaging of Hepatocellular Carcinoma. *Adv. Mater.* **2020**, *32*, 2001172.
- (857) Peng, J.; Samanta, A.; Zeng, X.; Han, S.; Wang, L.; Su, D.; Loong, D. T. B.; Kang, N.-Y.; Park, S.-J.; All, A. H.; et al. Real-Time *In Vivo* Hepatotoxicity Monitoring Through Chromophore-Conjugated Photon-Upconverting Nanoprobes. *Angew. Chem., Int. Ed.* **2017**, *56*, 4165–4169.
- (858) Li, Z.; Liang, T.; Lv, S.; Zhuang, Q.; Liu, Z. A Rationally Designed Upconversion Nanoprobe for *In Vivo* Detection of Hydroxyl Radical. *J. Am. Chem. Soc.* **2015**, *137*, 11179–11185.
- (859) Hao, C.; Wu, X.; Sun, M.; Zhang, H.; Yuan, A.; Xu, L.; Xu, C.; Kuang, H. Chiral Core–Shell Upconversion Nanoparticle@MOF Nanoassemblies for Quantification and Bioimaging of Reactive Oxygen Species *In Vivo*. *J. Am. Chem. Soc.* **2019**, *141*, 19373–19378.
- (860) Wang, F.; Qu, X.; Liu, D.; Ding, C.; Zhang, C.; Xian, Y. Upconversion Nanoparticles- MoS_2 Nanoassembly as a Fluorescent Turn-on Probe for Bioimaging of Reactive Oxygen Species in Living Cells and Zebrafish. *Sens. Actuators, B* **2018**, *274*, 180–187.
- (861) Zou, X.; Liu, Y.; Zhu, X.; Chen, M.; Yao, L.; Feng, W.; Li, F. An Nd^{3+} -sensitized Upconversion Nanophosphor Modified With a Cyanine Dye for the Ratiometric Upconversion Luminescence Bioimaging of Hypochlorite. *Nanoscale* **2015**, *7*, 4105–4113.
- (862) Liu, Y.; Jia, Q.; Zhai, X.; Mao, F.; Jiang, A.; Zhou, J. Rationally Designed Pure-inorganic Upconversion Nanoprobes for Ultra-highly Selective Hydrogen Sulfide Imaging and Elimination *In Vivo*. *Chem. Sci.* **2019**, *10*, 1193–1200.
- (863) Liu, S.; Zhang, L.; Yang, T.; Yang, H.; Zhang, K. Y.; Zhao, X.; Lv, W.; Yu, Q.; Zhang, X.; Zhao, Q.; et al. Development of Upconversion Luminescent Probe for Ratiometric Sensing and

- Bioimaging of Hydrogen Sulfide. *ACS Appl. Mater. Interfaces* **2014**, *6*, 11013–11017.
- (864) Zhang, X.; Hu, Q.; Xia, T.; Zhang, J.; Yang, Y.; Cui, Y.; Chen, B.; Qian, G. Turn-on and Ratiometric Luminescent Sensing of Hydrogen Sulfide Based on Metal–Organic Frameworks. *ACS Appl. Mater. Interfaces* **2016**, *8*, 32259–32265.
- (865) Liu, J.; Liu, Y.; Bu, W.; Bu, J.; Sun, Y.; Du, J.; Shi, J. Ultrasensitive Nanosensors Based on Upconversion Nanoparticles for Selective Hypoxia Imaging *In Vivo* Upon Near-Infrared Excitation. *J. Am. Chem. Soc.* **2014**, *136*, 9701–9709.
- (866) Xu, S.; Zhang, X.; Xu, H.; Dong, B.; Qu, X.; Chen, B.; Zhang, S.; Zhang, T.; Cheng, Y.; Xu, S.; Song, H. Silane Modified Upconversion Nanoparticles With Multifunctions: Imaging, Therapy and Hypoxia Detection. *Sci. Rep.* **2016**, *6*, 22350.
- (867) Wang, Y.; Xu, W.; Lei, L.; Chen, L.; Ye, R.; Xu, S. Photoluminescent NaGdF₄@NaYF₄:Ce/Tb Inert-core/active-shell Nanoparticles for Selective and Ultra-sensitive Cu²⁺ Ions Sensing. *J. Lumin.* **2021**, *235*, 118024.
- (868) Zhang, Y.; Xu, S.; Li, X.; Zhang, J.; Sun, J.; Tong, L.; Zhong, H.; Xia, H.; Hua, R.; Chen, B. Improved LRET-based Detection Characters of Cu²⁺ Using Sandwich Structured NaYF₄@NaYF₄:Er³⁺/Yb³⁺@NaYF₄ Nanoparticles as Energy Donor. *Sens. Actuators, B* **2018**, *257*, 829–838.
- (869) Sarkar, S.; Chatti, M.; Adusumalli, V. N. K. B.; Mahalingam, V. Highly Selective and Sensitive Detection of Cu²⁺ Ions Using Ce(III)/Tb(III)-Doped SrF₂ Nanocrystals as Fluorescent Probe. *ACS Appl. Mater. Interfaces* **2015**, *7*, 25702–25708.
- (870) Zhao, J.; Wang, Y.-N.; Dong, W.-W.; Wu, Y.-P.; Li, D.-S.; Zhang, Q.-C. A Robust Luminescent Tb(III)-MOF With Lewis Basic Pyridyl Sites for the Highly Sensitive Detection of Metal Ions and Small Molecules. *Inorg. Chem.* **2016**, *55*, 3265–3271.
- (871) Liu, J.; Kaczmarek, A. M.; Van Deun, R. Downshifting/upconversion NaY(MoO₄)₂ Luminescent Materials as Highly Sensitive Fluorescent Sensors for Pb²⁺ Ions Detection. *Sens. Actuators, B* **2018**, *255*, 2163–2169.
- (872) Xu, S.; Xu, S.; Zhu, Y.; Xu, W.; Zhou, P.; Zhou, C.; Dong, B.; Song, H. A Novel Upconversion, Fluorescence Resonance Energy Transfer Biosensor (FRET) for Sensitive Detection of Lead Ions in Human Serum. *Nanoscale* **2014**, *6*, 12573–12579.
- (873) Huynh, T. V.; Anh, N. T. N.; Darmanto, W.; Doong, R.-A. Erbium-doped Graphene Quantum Dots With Up- and Down-conversion Luminescence for Effective Detection of Ferric Ions in Water and Human Serum. *Sens. Actuators, B* **2021**, *328*, 129056.
- (874) Chen, M.; Kutsanedzie, F. Y. H.; Cheng, W.; Agyekum, A. A.; Li, H.; Chen, Q. A Nanosystem Composed of Upconversion Nanoparticles and N, N-diethyl-p-phenylenediamine for Fluorimetric Determination of Ferric Ion. *Microchim. Acta* **2018**, *185*, 378.
- (875) Wei, R.; Wei, Z.; Sun, L.; Zhang, J. Z.; Liu, J.; Ge, X.; Shi, L. Nile Red Derivative-Modified Nanostructure for Upconversion Luminescence Sensing and Intracellular Detection of Fe³⁺ and MR Imaging. *ACS Appl. Mater. Interfaces* **2016**, *8*, 400–410.
- (876) Zhou, L.-J.; Deng, W.-H.; Wang, Y.-L.; Xu, G.; Yin, S.-G.; Liu, Q.-Y. Lanthanide–Potassium Biphenyl-3,3′-disulfonyl-4,4′-dicarboxylate Frameworks: Gas Sorption, Proton Conductivity, and Luminescent Sensing of Metal Ions. *Inorg. Chem.* **2016**, *55*, 6271–6277.
- (877) Dong, X.-Y.; Wang, R.; Wang, J.-Z.; Zang, S.-Q.; Mak, T. C. W. Highly Selective Fe³⁺ Sensing and Proton Conduction in a Water-stable Sulfonate–carboxylate Tb–organic-framework. *J. Mater. Chem. A* **2015**, *3*, 641–647.
- (878) Chu, H.; Yao, D.; Chen, J.; Yu, M.; Su, L. Double-Emission Ratiometric Fluorescent Sensors Composed of Rare-Earth-Doped ZnS Quantum Dots for Hg²⁺ Detection. *ACS Omega* **2020**, *5*, 9558–9565.
- (879) Gu, B.; Zhou, Y.; Zhang, X.; Liu, X.; Zhang, Y.; Marks, R.; Zhang, H.; Liu, X.; Zhang, Q. Thiazole Derivative-modified Upconversion Nanoparticles for Hg²⁺ Detection in Living Cells. *Nanoscale* **2016**, *8*, 276–282.
- (880) Wang, H.; Wang, X.; Liang, M.; Chen, G.; Kong, R.-M.; Xia, L.; Qu, F. A Boric Acid-Functionalized Lanthanide Metal–Organic Framework as a Fluorescence “Turn-on” Probe for Selective Monitoring of Hg²⁺ and CH₃Hg⁺. *Anal. Chem.* **2020**, *92*, 3366–3372.
- (881) He, L.; Yang, L.; Zhu, H.; Dong, W.; Ding, Y.; Zhu, J.-J. A Highly Sensitive Biosensing Platform Based on Upconversion Nanoparticles and Graphene Quantum Dots for the Detection of Ag⁺. *Methods Appl. Fluoresc.* **2017**, *5*, 024010.
- (882) Hao, J.-N.; Yan, B. Ag⁺-sensitized Lanthanide Luminescence in Ln³⁺ Post-functionalized Metal–organic Frameworks and Ag⁺ Sensing. *J. Mater. Chem. A* **2015**, *3*, 4788–4792.
- (883) Peng, J.; Xu, W.; Teoh, C. L.; Han, S.; Kim, B.; Samanta, A.; Er, J. C.; Wang, L.; Yuan, L.; Liu, X.; et al. High-Efficiency *In Vitro* and *In Vivo* Detection of Zn²⁺ by Dye-Assembled Upconversion Nanoparticles. *J. Am. Chem. Soc.* **2015**, *137*, 2336–2342.
- (884) Ji, G.; Liu, J.; Gao, X.; Sun, W.; Wang, J.; Zhao, S.; Liu, Z. A Luminescent Lanthanide MOF for Selectively and Ultra-high Sensitive Detecting Pb²⁺ Ions in aqueous Solution. *J. Mater. Chem. A* **2017**, *5*, 10200–10205.
- (885) Liu, Y.; Ouyang, Q.; Li, H.; Zhang, Z.; Chen, Q. Development of an Inner Filter Effects-Based Upconversion Nanoparticles–Curcumin Nanosystem for the Sensitive Sensing of Fluoride Ion. *ACS Appl. Mater. Interfaces* **2017**, *9*, 18314–18321.
- (886) Sun, C.; Gradziński, M. Fluorescence Sensing of Cyanide anions Based on Au-modified Upconversion Nanoassemblies. *Analyst* **2021**, *146*, 2152–2159.
- (887) Oh, J.; Jeon, I.; Kim, D.; You, Y.; Baek, D.; Kang, S. J.; Lee, J. Highly Stable Upconverting Nanocrystal–Polydiacetylenes Nanoplates for Orthogonal Dual Signaling-Based Detection of Cyanide. *ACS Appl. Mater. Interfaces* **2020**, *12*, 4934–4943.
- (888) Li, Z.; Yuan, H.; Yuan, W.; Su, Q.; Li, F. Upconversion Nanoprobes for Biodetections. *Coord. Chem. Rev.* **2018**, *354*, 155–168.
- (889) Bigdeli, A.; Ghasemi, F.; Abbasi-Moayed, S.; Shahrajabian, M.; Fahimi-Kashani, N.; Jafarinejad, S.; Farahmand Nejad, M. A.; Hormozi-Nezhad, M. R. Ratiometric Fluorescent Nanoprobes for Visual Detection: Design Principles and Recent Advances - A Review. *Anal. Chim. Acta* **2019**, *1079*, 30–58.
- (890) Zhou, J.; Li, C.; Li, D.; Liu, X.; Mu, Z.; Gao, W.; Qiu, J.; Deng, R. Single-molecule Photoreaction Quantitation Through Intraparticle-surface Energy Transfer (i-SET) Spectroscopy. *Nat. Commun.* **2020**, *11*, 4297.
- (891) Liu, X.; Li, X.; Qin, X.; Xie, X.; Huang, L.; Liu, X. Hedgehog-Like Upconversion Crystals: Controlled Growth and Molecular Sensing at Single-Particle Level. *Adv. Mater.* **2017**, *29*, 1702315.
- (892) Shaikh, F. I.; Chikhale, L. P.; Patil, J. Y.; Mulla, I. S.; Suryavanshi, S. S. Enhanced Acetone Sensing Performance of Nanostructured Sm₂O₃ Doped SnO₂ Thick Films. *J. Rare Earths* **2017**, *35*, 813–823.
- (893) Hu, J.; Sun, Y.; Xue, Y.; Zhang, M.; Li, P.; Lian, K.; Zhuiykov, S.; Zhang, W.; Chen, Y. Highly Sensitive and Ultra-fast Gas Sensor Based on CeO₂-loaded In₂O₃ Hollow Spheres for ppb-level Hydrogen Detection. *Sens. Actuators, B* **2018**, *257*, 124–135.
- (894) Yadav, A. K.; Singh, R. K.; Singh, P. Fabrication of Lanthanum Ferrite Based Liquefied Petroleum Gas Sensor. *Sens. Actuators, B* **2016**, *229*, 25–30.
- (895) Chen, Y.; Wang, D.; Qin, H.; Zhang, H.; Zhang, Z.; Zhou, G.; Gao, C.; Hu, J. CO₂ Sensing Properties and Mechanism of PrFeO₃ and NdFeO₃ Thick Film Sensor. *J. Rare Earths* **2019**, *37*, 80–87.
- (896) Zhang, Y.; Ma, C.; Yang, X.; Song, Y.; Liang, X.; Zhao, X.; Wang, Y.; Gao, Y.; Liu, F.; Liu, F.; et al. NASICON-based Gas Sensor Utilizing MMnO₃ (M: Gd, Sm, La) Sensing Electrode for Triethylamine Detection. *Sens. Actuators, B* **2019**, *295*, 56–64.
- (897) Xu, X. L.; Chen, Y.; Ma, S. Y.; Li, W. Q.; Mao, Y. Z. Excellent Acetone Sensor of La-doped ZnO Nanofibers With Unique Bead-like Structures. *Sens. Actuators, B* **2015**, *213*, 222–233.
- (898) Gawali, S. R.; Patil, V. L.; Deonikar, V. G.; Patil, S. S.; Patil, D. R.; Patil, P. S.; Pant, J. Ce Doped NiO Nanoparticles as Selective NO₂ Gas Sensor. *J. Phys. Chem. Solids* **2018**, *114*, 28–35.

- (899) Singh, G.; Virpal; Singh, R. C. Highly Sensitive Gas Sensor Based on Er-doped SnO₂ Nanostructures and Its Temperature Dependent Selectivity Towards Hydrogen and Ethanol. *Sens. Actuators, B* **2019**, *282*, 373–383.
- (900) Balamurugan, C.; Song, S. J.; Lee, D. W. Porous Nanostructured GdFeO₃ Perovskite Oxides and Their Gas Response Performance to NO_x. *Sens. Actuators, B* **2018**, *272*, 400–414.
- (901) Addabbo, T.; Bertocci, F.; Fort, A.; Gregorkiewicz, M.; Mugnaini, M.; Spinicci, R.; Vignoli, V. Gas Sensing Properties of YMnO₃ Based Materials for the Detection of NO_x and CO. *Sens. Actuators, B* **2017**, *244*, 1054–1070.
- (902) Rasouli Jamnani, S.; Milani Moghaddam, H.; Leonardi, S. G.; Donato, N.; Neri, G. Synthesis and Characterization of Sm₂O₃ Nanorods for application as a Novel CO Gas Sensor. *Appl. Surf. Sci.* **2019**, *487*, 793–800.
- (903) Zito, C. A.; Perfecto, T. M.; Dippel, A.-C.; Volanti, D. P.; Koziej, D. Low-Temperature Carbon Dioxide Gas Sensor Based on Yolk–Shell Ceria Nanospheres. *ACS Appl. Mater. Interfaces* **2020**, *12*, 17745–17751.
- (904) Balamurugan, C.; Lee, D. W. Perovskite Hexagonal YMnO₃ Nanopowder as p-type Semiconductor Gas Sensor for H₂S Detection. *Sens. Actuators, B* **2015**, *221*, 857–866.
- (905) Ma, C.; Hao, X.; Yang, X.; Liang, X.; Liu, F.; Liu, T.; Yang, C.; Zhu, H.; Lu, G. Sub-ppb SO₂ Gas Sensor Based on NASICON and La_xSm_{1-x}FeO₃ Sensing Electrode. *Sens. Actuators, B* **2018**, *256*, 648–655.
- (906) Dong, X.; Cheng, X.; Zhang, X.; Sui, L.; Xu, Y.; Gao, S.; Zhao, H.; Huo, L. A Novel Coral-shaped Dy₂O₃ Gas Sensor for High Sensitivity NH₃ Detection at Room Temperature. *Sens. Actuators, B* **2018**, *255*, 1308–1315.
- (907) Hastir, A.; Kohli, N.; Singh, R. C. Temperature Dependent Selective and Sensitive Terbium Doped ZnO Nanostructures. *Sens. Actuators, B* **2016**, *231*, 110–119.
- (908) Hastir, A.; Kohli, N.; Singh, R. C. Comparative Study on Gas Sensing Properties of Rare Earth (Tb, Dy and Er) Doped ZnO Sensor. *J. Phys. Chem. Solids* **2017**, *105*, 23–34.
- (909) Rong, Q.; Zhang, Y.; Wang, C.; Zhu, Z.; Zhang, J.; Liu, Q. A High Selective Methanol Gas Sensor Based on Molecular Imprinted Ag-LaFeO₃ Fibers. *Sci. Rep.* **2017**, *7*, 12110.
- (910) Yu, K.; Hu, J.; Li, X.; Zhang, L.; Lv, Y. Camellia-like NiO: A Novel Cataluminescence Sensing Material for H₂S. *Sens. Actuators, B* **2019**, *288*, 243–250.
- (911) Ramalho, J. F.; Carlos, L. D.; André, P. S.; Ferreira, R. A. mOptical Sensing for the Internet of Things: A Smartphone-Controlled Platform for Temperature Monitoring. *Adv. Photonics Res.* **2021**, *2*, 2000211.
- (912) Mayer, M.; Baeumner, A. J. A Megatrend Challenging analytical Chemistry: Biosensor and Chemosensor Concepts Ready for the Internet of Things. *Chem. Rev.* **2019**, *119*, 7996–8027.
- (913) Hu, Y.; Jensen, J. O.; Cleemann, L. N.; Brandes, B. A.; Li, Q. Synthesis of Pt–Rare Earth Metal Nanoalloys. *J. Am. Chem. Soc.* **2020**, *142*, 953–961.
- (914) Tou, M.; Mei, Y.; Bai, S.; Luo, Z.; Zhang, Y.; Li, Z. Depositing CdS Nanoclusters on Carbon-modified NaYF₄:Yb,Tm Upconversion Nanocrystals for NIR-light Enhanced Photocatalysis. *Nanoscale* **2016**, *8*, 553–562.
- (915) Rodriguez, J. A.; Liu, P.; Hrbek, J.; Evans, J.; Perez, M. Water Gas Shift Reaction on Cu and Au Nanoparticles Supported on CeO₂(111) and ZnO(0001): Intrinsic Activity and Importance of Support Interactions. *Angew. Chem., Int. Ed.* **2007**, *46*, 1329–1332.
- (916) Si, R.; Flytzani-Stephanopoulos, M. Shape and Crystal-plane Effects of Nanoscale Ceria on the Activity of Au-CeO₂ Catalysts for the Water-gas Shift Reaction. *Angew. Chem., Int. Ed.* **2008**, *47*, 2884–2929.
- (917) Shan, W.; Feng, Z.; Li, Z.; Zhang, J.; Shen, W.; Li, C. Oxidative Steam Reforming of Methanol on Ce_{0.9}Cu_{0.1}O₇ Catalysts Prepared by Deposition-precipitation, Coprecipitation, and Complexation-combustion Methods. *J. Catal.* **2004**, *228*, 206–217.
- (918) Kaneko, H.; Miura, T.; Ishihara, H.; Taku, S.; Yokoyama, T.; Nakajima, H.; Tamaura, Y. Reactive Ceramics of CeO₂–MO_x (M = Mn, Fe, Ni, Cu) for H₂ Generation by Two-step Water Splitting Using Concentrated Solar Thermal Energy. *Energy* **2007**, *32*, 656–663.
- (919) Meng, Q.-L.; Lee, C.-i.; Ishihara, T.; Kaneko, H.; Tamaura, Y. Reactivity of CeO₂-based Ceramics for Solar Hydrogen Production via a Two-step Water-splitting Cycle With Concentrated Solar Energy. *Int. J. Hydrogen Energy* **2011**, *36*, 13435–13441.
- (920) Carrettin, S.; Concepcion, P.; Corma, A.; Lopez Nieto, J. M.; Puentes, V. F. Nanocrystalline CeO₂ Increases the Activity of Au for CO Oxidation by Two Orders of Magnitude. *Angew. Chem., Int. Ed.* **2004**, *43*, 2538–2540.
- (921) Guzman, J.; Carrettin, S.; Fierro-Gonzalez, J. C.; Hao, Y.; Gates, B. C.; Corma, A. CO Oxidation Catalyzed by Supported Gold: Cooperation Between Gold and Nanocrystalline Rare-earth Supports Forms Reactive Surface Superoxide and Peroxide Species. *Angew. Chem.* **2005**, *117*, 4856–4859.
- (922) Shapovalov, V.; Metiu, H. Catalysis by Doped Oxides: CO Oxidation by Au,Ce_{1-x}O₂. *J. Catal.* **2007**, *245*, 205–214.
- (923) Zhang, S.; Li, Y.; Huang, J.; Lee, J.; Kim, D. H.; Frenkel, A. I.; Kim, T. Effects of Molecular and Electronic Structures in CoO_x/CeO₂ Catalysts on NO Reduction by CO. *J. Phys. Chem. C* **2019**, *123*, 7166–7177.
- (924) Zhang, L.; Li, L.; Cao, Y.; Yao, X.; Ge, C.; Gao, F.; Deng, Y.; Tang, C.; Dong, L. Getting Insight into the Influence of SO₂ on TiO₂/CeO₂ for the Selective Catalytic Reduction of NO by NH₃. *Appl. Catal., B* **2015**, *165*, 589–598.
- (925) Schmidt, P. O.; Rosenband, T.; Langer, C.; Itano, W. M.; Bergquist, J. C.; Wineland, D. J. Spectroscopy Using Quantum Logic. *Science* **2005**, *309*, 749–752.
- (926) Bera, P.; Priolkar, K. R.; Gayen, A.; Sarode, P. R.; Hegde, M. S.; Emura, S.; Kumashiro, R.; Jayaram, V.; Subbanna, G. N. Ionic Dispersion of Pt over CeO₂ by the Combustion Method: Structural Investigation by XRD, TEM, XPS, and EXAFS. *Chem. Mater.* **2003**, *15*, 2049–2060.
- (927) Gayen, A.; Priolkar, K. R.; Sarode, P. R.; Jayaram, V.; Hegde, M. S.; Subbanna, G. N.; Emura, S. Ce_{1-x}Rh_xO_{2-δ} Solid Solution Formation in Combustion-Synthesized Rh/CeO₂ Catalyst Studied by XRD, TEM, XPS, and EXAFS. *Chem. Mater.* **2004**, *16*, 2317–2328.
- (928) Baidya, T.; Gayen, A.; Hegde, M. S.; Ravishanker, N.; Dupont, L. Enhanced Reducibility of Ce_{1-x}Ti_xO₂ Compared to That of CeO₂ and Higher Redox Catalytic Activity of Ce_{1-x-y}Ti_xPt_yO_{2-δ} Compared to That of Ce_{1-x}Pt_xO_{2-δ}. *J. Phys. Chem. B* **2006**, *110*, 5262–5272.
- (929) Perezalonso, F.; Meliancabrera, I.; Lopezgranados, M.; Kapteijn, F.; Fierro, J. Synergy of Fe_xCe_{1-x}O₂ Mixed Oxides for N₂O Decomposition. *J. Catal.* **2006**, *239*, 340–346.
- (930) Bera, P.; Priolkar, K. R.; Sarode, P. R.; Hegde, M. S.; Emura, S.; Kumashiro, R.; Lalla, N. P. Structural Investigation of Combustion Synthesized Cu/CeO₂ Catalysts by EXAFS and Other Physical Techniques: Formation of a Ce_{1-x}Cu_xO_{2-δ} Solid Solution. *Chem. Mater.* **2002**, *14*, 3591–3601.
- (931) Cargnello, M.; Doan-Nguyen, V. V. T.; Gordon, T. R.; Diaz, R. E.; Stach, E. A.; Gorte, R. J.; Fornasiero, P.; Murray, C. B. Control of Metal Nanocrystal Size Reveals Metal-Support Interface Role for Ceria Catalysts. *Science* **2013**, *341*, 771–773.
- (932) Lykhach, Y.; Kozlov, S. M.; Skala, T.; Tovt, A.; Stetsovych, V.; Tsud, N.; Dvorak, F.; Johaneck, V.; Neitzel, A.; Myslivecek, J.; et al. Counting Electrons on Supported Nanoparticles. *Nat. Mater.* **2016**, *15*, 284–288.
- (933) Tian, Z.; Yao, T.; Qu, C.; Zhang, S.; Li, X.; Qu, Y. Photolyase-Like Catalytic Behavior of CeO₂. *Nano Lett.* **2019**, *19*, 8270–8277.
- (934) Janoš, P.; Kurán, P.; Pilařová, V.; Trögl, J.; Štátný, M.; Pelant, O.; Henych, J.; Bakardjieva, S.; Životský, O.; Kormunda, M.; et al. Magnetically Separable Reactive Sorbent Based on the CeO₂/γ-Fe₂O₃ Composite and Its Utilization for Rapid Degradation of the Organophosphate Pesticide Parathion Methyl and Certain Nerve Agents. *Chem. Eng. J.* **2015**, *262*, 747–755.

- (935) Chen, Z.; Wang, Y.; Mo, Y.; Long, X.; Zhao, H.; Su, L.; Duan, Z.; Xiong, Y. ZIF-8 Directed Templating Synthesis of CeO₂ Nanoparticles and Its Oxidase-like Activity for Colorimetric Detection. *Sens. Actuators, B* **2020**, *323*, 128625.
- (936) Alizadeh, N.; Salimi, A.; Hallaj, R. Mimicking Peroxidase-like Activity of Co₃O₄-CeO₂ Nanosheets Integrated Paper-based analytical Devices for Detection of Glucose With Smartphone. *Sens. Actuators, B* **2019**, *288*, 44–52.
- (937) Zhu, X.; Gong, Y.; Liu, Y.; Yang, C.; Wu, S.; Yuan, G.; Guo, X.; Liu, J.; Qin, X. Ru@CeO₂ Yolk Shell Nanozymes: Oxygen Supply in Situ Enhanced Dual Chemotherapy Combined With Photothermal Therapy for Orthotopic/subcutaneous Colorectal Cancer. *Biomaterials* **2020**, *242*, 119923.
- (938) Li, Y.; He, X.; Yin, J.-J.; Ma, Y.; Zhang, P.; Li, J.; Ding, Y.; Zhang, J.; Zhao, Y.; Chai, Z.; et al. Acquired Superoxide-Scavenging Ability of Ceria Nanoparticles. *Angew. Chem., Int. Ed.* **2015**, *54*, 1832–1855.
- (939) Zhao, S.; Li, Y.; Liu, Q.; Li, S.; Cheng, Y.; Cheng, C.; Sun, Z.; Du, Y.; Butch, C. J.; Wei, H. An Orally Administered CeO₂@Montmorillonite Nanozyme Targets Inflammation for Inflammatory Bowel Disease Therapy. *Adv. Funct. Mater.* **2020**, *30*, 2004692.
- (940) Yao, T.; Tian, Z.; Zhang, Y.; Qu, Y. Phosphatase-like Activity of Porous Nanorods of CeO₂ for the Highly Stabilized Dephosphorylation Under Interferences. *ACS Appl. Mater. Interfaces* **2019**, *11*, 195–201.
- (941) Vernekar, A. A.; Das, T.; Mugesh, G. Vacancy-Engineered Nanoceria: Enzyme Mimetic Hotspots for the Degradation of Nerve Agents. *Angew. Chem., Int. Ed.* **2016**, *55*, 1412–1416.
- (942) Zhang, J.; Huang, Y.; Jin, L.; Rosei, F.; Vetrone, F.; Claverie, J. P. Efficient Upconverting Multiferoic Core@Shell Photocatalysts: Visible-to-Near-Infrared Photon Harvesting. *ACS Appl. Mater. Interfaces* **2017**, *9*, 8142–8150.
- (943) Boppella, R.; Marques Mota, F.; Lim, J. W.; Kochuveedu, S. T.; Ahn, S.; Lee, J.; Kawaguchi, D.; Tanaka, K.; Kim, D. H. Plasmon and Upconversion Mediated Broadband Spectral Response in TiO₂ Inverse Opal Photocatalysts for Enhanced Photoelectrochemical Water Splitting. *ACS Appl. Energy Mater.* **2019**, *2*, 3780–3790.
- (944) Kasinathan, K.; Kennedy, J.; Elayaperumal, M.; Henini, M.; Malik, M. Photodegradation of Organic Pollutants RhB Dye Using UV Simulated Sunlight on Ceria Based TiO₂ Nanomaterials for antibacterial applications. *Sci. Rep.* **2016**, *6*, 38064.
- (945) Shang, H.; Huang, S.; Li, H.; Li, M.; Zhao, S.; Wang, J.; Ai, Z.; Zhang, L. Dual-site Activation Enhanced Photocatalytic Removal of NO With Au/CeO₂. *Chem. Eng. J.* **2020**, *386*, 124047.
- (946) Rajendran, S.; Khan, M. M.; Gracia, F.; Qin, J.; Gupta, V. K.; Arumainathan, S. Ce³⁺-ion-induced Visible-light Photocatalytic Degradation and Electrochemical Activity of ZnO/CeO₂ Nanocomposite. *Sci. Rep.* **2016**, *6*, 31641.
- (947) Wang, M.; Shen, M.; Jin, X.; Tian, J.; Li, M.; Zhou, Y.; Zhang, L.; Li, Y.; Shi, J. Oxygen Vacancy Generation and Stabilization in CeO_{2-x} by Cu Introduction With Improved CO₂ Photocatalytic Reduction Activity. *ACS Catal.* **2019**, *9*, 4573–4581.
- (948) Qin, W.; Zhang, D.; Zhao, D.; Wang, L.; Zheng, K. Near-infrared Photocatalysis Based on YF₃: Yb³⁺, Tm³⁺/TiO₂ Core/shell Nanoparticles. *Chem. Commun.* **2010**, *46*, 2304–2306.
- (949) Li, C.; Wang, F.; Zhu, J.; Yu, J. C. NaYF₄:Yb,Tm/CdS Composite as a Novel Near-infrared-driven Photocatalyst. *Appl. Catal., B* **2010**, *100*, 433–439.
- (950) Zhang, J.; Huang, Y.; Jin, L.; Rosei, F.; Vetrone, F.; Claverie, J. P. Efficient Upconverting Multiferoic Core@Shell Photocatalysts: Visible-to-Near-Infrared Photon Harvesting. *ACS Appl. Mater. Interfaces* **2017**, *9*, 8142–8150.
- (951) Huang, S.; Zhu, N.; Lou, Z.; Gu, L.; Miao, C.; Yuan, H.; Shan, A. Near-infrared Photocatalysts of BiVO₄/CaF₂:Er³⁺, Tm³⁺, Yb³⁺ With Enhanced Upconversion Properties. *Nanoscale* **2014**, *6*, 1362–1368.
- (952) Zhang, F.; Zhang, C. L.; Wang, W. N.; Cong, H. P.; Qian, H. S. Titanium Dioxide/Upconversion Nanoparticles/Cadmium Sulfide Nanofibers Enable Enhanced Full-Spectrum Absorption for Superior Solar Light Driven Photocatalysis. *ChemSusChem* **2016**, *9*, 1449–1454.
- (953) Li, J.; Cushing, S. K.; Meng, F.; Senty, T. R.; Bristow, A. D.; Wu, N. Plasmon-induced Resonance Energy Transfer for Solar Energy Conversion. *Nat. Photonics* **2015**, *9*, 601–607.
- (954) Wang, W.; Li, Y.; Kang, Z.; Wang, F.; Yu, J. C. A NIR-driven Photocatalyst Based on α -NaYF₄:Yb,Tm@TiO₂ Core-shell Structure Supported on Reduced Graphene Oxide. *Appl. Catal., B* **2016**, *182*, 184–192.
- (955) Chen, C. K.; Chen, H. M.; Chen, C. J.; Liu, R. S. Plasmon-enhanced Near-infrared-active Materials in Photoelectrochemical Water Splitting. *Chem. Commun.* **2013**, *49*, 7917–7919.
- (956) Xu, H.; Li, H.; Xu, L.; Wu, C.; Sun, G.; Xu, Y.; Chu, J. Enhanced Photocatalytic Activity of Ag₃VO₄ Loaded With Rare-Earth Elements Under Visible-Light Irradiation. *Ind. Eng. Chem. Res.* **2009**, *48*, 10771–10778.
- (957) Sordello, F.; Berruti, I.; Gionco, C.; Paganini, M. C.; Calza, P.; Minero, C. Photocatalytic Performances of Rare Earth Element-doped Zinc Oxide Toward Pollutant Abatement in Water and Wastewater. *Appl. Catal., B* **2019**, *245*, 159–166.
- (958) Xie, Y.; Yuan, C.; Li, X. Photocatalytic Degradation of X-3B Dye by Visible Light Using Lanthanide Ion Modified Titanium Dioxide Hydrosol System. *Colloids Surf., A* **2005**, *252*, 87–94.
- (959) Wang, J.; Wang, H.; Zuo, S.; Jin, X.; Zheng, B.; Deng, R.; Liu, W.; Wang, J. Synergistic Effects of Lanthanide Surface Adhesion and Photon-upconversion for Enhanced Near-infrared Responsive Photodegradation of Organic Contaminants in Wastewater. *Environ. Sci.: Nano* **2020**, *7*, 3333–3342.
- (960) Jeong, K.-Y.; Hwang, M.-S.; Kim, J.; Park, J.-S.; Lee, J. M.; Park, H.-G. Recent Progress in Nanolaser Technology. *Adv. Mater.* **2020**, *32*, 2001996.
- (961) Park, W.; Lu, D.; Ahn, S. Plasmon Enhancement of Luminescence Upconversion. *Chem. Soc. Rev.* **2015**, *44*, 2940–2962.
- (962) Molina, P.; Yraola, E.; Ramírez, M. O.; Tserkezis, C.; Plaza, J. L.; Aizpuru, J.; Bravo-Abad, J.; Bausá, L. E. Plasmon-Assisted Nd³⁺-Based Solid-State Nanolaser. *Nano Lett.* **2016**, *16*, 895–899.
- (963) Kataria, M.; Yadav, K.; Nain, A.; Lin, H.-I.; Hu, H.-W.; Paul Inbaraj, C. R.; Chang, T.-J.; Liao, Y.-M.; Cheng, H.-Y.; Lin, K.-H.; et al. Self-Sufficient and Highly Efficient Gold Sandwich Upconversion Nanocomposite Lasers for Stretchable and Bio-applications. *ACS Appl. Mater. Interfaces* **2020**, *12*, 19840–19854.
- (964) Wang, T.; Siu, C. K.; Yu, H.; Wang, Y.; Li, S.; Lu, W.; Hao, J.; Liu, H.; Teng, J. H.; Lei, D. Y.; et al. Influence of Plasmonic Effect on the Upconversion Emission Characteristics of NaYF₄ Hexagonal Microrods. *Inorg. Chem.* **2018**, *57*, 8200–8204.
- (965) Fernandez-Bravo, A.; Wang, D.; Barnard, E. S.; Teitelboim, A.; Tajon, C.; Guan, J.; Schatz, G. C.; Cohen, B. E.; Chan, E. M.; Schuck, P. J.; et al. Ultralow-threshold, Continuous-wave Upconverting Lasing From Subwavelength Plasmons. *Nat. Mater.* **2019**, *18*, 1172–1176.
- (966) Jin, L.; Wu, Y.; Wang, Y.; Liu, S.; Zhang, Y.; Li, Z.; Chen, X.; Zhang, W.; Xiao, S.; Song, Q. Mass-Manufactured Lanthanide-Based Ultraviolet B Microlasers. *Adv. Mater.* **2019**, *31*, 1807079.
- (967) Chen, X.; Jin, L.; Kong, W.; Sun, T.; Zhang, W.; Liu, X.; Fan, J.; Yu, S. F.; Wang, F. Confining Energy Migration in Upconversion Nanoparticles Towards Deep Ultraviolet Lasing. *Nat. Commun.* **2016**, *7*, 10304.
- (968) Jin, L. M.; Chen, X.; Siu, C. K.; Wang, F.; Yu, S. F. Enhancing Multiphoton Upconversion From NaYF₄:Yb/Tm@NaYF₄ Core-shell Nanoparticles via the Use of Laser Cavity. *ACS Nano* **2017**, *11*, 843–849.
- (969) Liu, Y.; Teitelboim, A.; Fernandez-Bravo, A.; Yao, K.; Altoe, M. V.P.; Aloni, S.; Zhang, C.; Cohen, B. E.; Schuck, P. J.; Chan, E. M. Controlled Assembly of Upconverting Nanoparticles for Low-Threshold Microlasers and Their Imaging in Scattering Media. *ACS Nano* **2020**, *14*, 1508–1519.
- (970) Fan, H. H.; Guo, L.; Li, K. F.; Wong, M. S.; Cheah, K. W. Exceptionally Strong Multiphoton-Excited Blue Photoluminescence and Lasing From Ladder-Type Oligo(p-phenylene)s. *J. Am. Chem. Soc.* **2012**, *134*, 7297–7300.

- (971) Poddubny, A.; Iorsh, I.; Belov, P.; Kivshar, Y. Hyperbolic Metamaterials. *Nat. Photonics* **2013**, *7*, 948–957.
- (972) Haider, G.; Lin, H.-I.; Yadav, K.; Shen, K.-C.; Liao, Y.-M.; Hu, H.-W.; Roy, P. K.; Bera, K. P.; Lin, K.-H.; Lee, H.-M.; et al. A Highly-Efficient Single Segment White Random Laser. *ACS Nano* **2018**, *12*, 11847–11859.
- (973) Deng, R.; Qin, F.; Chen, R.; Huang, W.; Hong, M.; Liu, X. Temporal Full-colour Tuning Through Non-steady-state Upconversion. *Nat. Nanotechnol.* **2015**, *10*, 237–242.
- (974) Park, B. J.; Hong, A. R.; Park, S.; Kyung, K.-U.; Lee, K.; Seong Jang, H. Flexible Transparent Displays Based on Core/shell Upconversion Nanophosphor-incorporated Polymer Waveguides. *Sci. Rep.* **2017**, *7*, 45659.
- (975) Gao, L.; Shan, X.; Xu, X.; Liu, Y.; Liu, B.; Li, S.; Wen, S.; Ma, C.; Jin, D.; Wang, F. Video-rate Upconversion Display From Optimized Lanthanide Ion Doped Upconversion Nanoparticles. *Nanoscale* **2020**, *12*, 18595–18599.
- (976) Zheng, K.; Han, S.; Zeng, X.; Wu, Y.; Song, S.; Zhang, H.; Liu, X. Rewritable Optical Memory Through High-Registry Orthogonal Upconversion. *Adv. Mater.* **2018**, *30*, 1801726.
- (977) Zhai, Y.; Yang, X.; Wang, F.; Li, Z.; Ding, G.; Qiu, Z.; Wang, Y.; Zhou, Y.; Han, S.-T. Infrared-Sensitive Memory Based on Direct-Grown MoS₂-Upconversion-Nanoparticle Heterostructure. *Adv. Mater.* **2018**, *30*, 1803563.
- (978) Tan, H.; Gong, G.; Xie, S.; Song, Y.; Zhang, C.; Li, N.; Zhang, D.; Xu, L.; Xu, J.; Zheng, J. Upconversion Nanoparticles@Carbon Dots@Meso-SiO₂ Sandwiched Core-shell Nanohybrids With Tunable Dual-mode Luminescence for 3D Anti-counterfeiting Barcodes. *Langmuir* **2019**, *35*, 11503–11511.
- (979) Sun, T.; Xu, B.; Chen, B.; Chen, X.; Li, M.; Shi, P.; Wang, F. Anti-counterfeiting Patterns Encrypted With Multi-mode Luminescent Nanotaggants. *Nanoscale* **2017**, *9*, 2701–2705.
- (980) Huang, H.; Chen, J.; Liu, Y.; Lin, J.; Wang, S.; Huang, F.; Chen, D. Lanthanide-Doped Core@Multishell Nanoarchitectures: Multimodal Excitable Upconverting/Downshifting Luminescence and High-Level Anti-Counterfeiting. *Small* **2020**, *16*, 2000708.
- (981) Zhang, C.; Zhou, H.-P.; Liao, L.-Y.; Feng, W.; Sun, W.; Li, Z.-X.; Xu, C.-H.; Fang, C.-J.; Sun, L.-D.; Zhang, Y.-W.; et al. Luminescence Modulation of Ordered Upconversion Nanopatterns by a Photochromic Diarylethene: Rewritable Optical Storage With Nondestructive Readout. *Adv. Mater.* **2010**, *22*, 633–637.
- (982) Zhuang, Y.; Lv, Y.; Wang, L.; Chen, W.; Zhou, T.-L.; Takeda, T.; Hirotsaki, N.; Xie, R.-J. Trap Depth Engineering of SrSi₂O₂N₂:Ln²⁺,Ln³⁺ (Ln²⁺ = Yb, Eu; Ln³⁺ = Dy, Ho, Er) Persistent Luminescence Materials for Information Storage Applications. *ACS Appl. Mater. Interfaces* **2018**, *10*, 1854–1864.
- (983) Ruan, J.; Yang, Z.; Huang, A.; Zhang, H.; Qiu, J.; Song, Z. Thermochromic Reaction-Induced Reversible Upconversion Emission Modulation for Switching Devices and Tunable Upconversion Emission Based on Defect Engineering of WO₃:Yb³⁺,Er³⁺ Phosphor. *ACS Appl. Mater. Interfaces* **2018**, *10*, 14941–14947.
- (984) Boyer, J.-C.; Carling, C.-J.; Gates, B. D.; Branda, N. R. Two-Way Photoswitching Using One Type of Near-Infrared Light, Upconverting Nanoparticles, and Changing Only the Light Intensity. *J. Am. Chem. Soc.* **2010**, *132*, 15766–15772.
- (985) Wu, T.; Boyer, J.-C.; Barker, M.; Wilson, D.; Branda, N. R. A “Plug-and-Play” Method to Prepare Water-Soluble Photoresponsive Encapsulated Upconverting Nanoparticles Containing Hydrophobic Molecular Switches. *Chem. Mater.* **2013**, *25*, 2495–2502.
- (986) Wang, J.-Y.; Chen, C.; He, C.; Zheng, Z.-Y.; Wang, C.; Hong, D.-L.; He, X.-T.; Luo, Y.-H.; Sun, B.-W. Ultrathin Two-dimensional Nanosheets Meet Upconverting Nanoparticles: in Situ Near-infrared Triggered Molecular Switching. *J. Mater. Chem. C* **2019**, *7*, 3965–3972.
- (987) Lee, J.; Bisso, P. W.; Srinivas, R. L.; Kim, J. J.; Swiston, A. J.; Doyle, P. S. Universal Process-inert Encoding architecture for Polymer Microparticles. *Nat. Mater.* **2014**, *13*, 524–529.
- (988) You, M.; Lin, M.; Wang, S.; Wang, X.; Zhang, G.; Hong, Y.; Dong, Y.; Jin, G.; Xu, F. Three-dimensional Quick Response Code Based on Inkjet Printing of Upconversion Fluorescent Nanoparticles for Drug anti-counterfeiting. *Nanoscale* **2016**, *8*, 10096–10104.
- (989) Meruga, J. M.; Baride, A.; Cross, W.; Kellar, J. J.; May, P. S. Red-green-blue Printing Using Luminescence-upconversion Inks. *J. Mater. Chem. C* **2014**, *2*, 2221–2227.
- (990) Wang, C.; Jin, Y.; Yuan, L.; Wu, H.; Ju, G.; Li, Z.; Liu, D.; Lv, Y.; Chen, L.; Hu, Y. A Spatial/temporal Dual-mode Optical Thermometry Platform Based on Synergetic Luminescence of Ti⁴⁺-Eu³⁺ Embedded Flexible 3D Micro-rod arrays: High-sensitive Temperature Sensing and Multi-dimensional High-level Secure anti-counterfeiting. *Chem. Eng. J.* **2019**, *374*, 992–1004.
- (991) Ding, M.; Chen, D.; Ma, D.; Liu, P.; Song, K.; Lu, H.; Ji, Z. Tuning the Upconversion Luminescence Lifetimes of KYb₂F₇:Ho³⁺ Nanocrystals for Optical Multiplexing. *ChemPhysChem* **2015**, *16*, 3784–3789.
- (992) Liu, X.; Chen, Z.-H.; Zhang, H.; Fan, Y.; Zhang, F. Independent Luminescent Lifetime and Intensity Tuning of Upconversion Nanoparticles by Gradient Doping for Multiplexed Encoding. *Angew. Chem.* **2021**, *133*, 7117–7121.
- (993) Han, Y.; Li, H.; Wang, Y.; Pan, Y.; Huang, L.; Song, F.; Huang, W. Upconversion Modulation Through Pulsed Laser Excitation for Anti-counterfeiting. *Sci. Rep.* **2017**, *7*, 1320.
- (994) Liu, H.; Jayakumar, M. K. G.; Huang, K.; Wang, Z.; Zheng, X.; Ågren, H.; Zhang, Y. Phase angle Encoded Upconversion Luminescent Nanocrystals for Multiplexing applications. *Nanoscale* **2017**, *9*, 1676–1686.
- (995) Liu, H.; Xu, J.; Wang, H.; Liu, Y.; Ruan, Q.; Wu, Y.; Liu, X.; Yang, J. K. W. Tunable Resonator-Upconverted Emission (TRUE) Color Printing and Applications in Optical Security. *Adv. Mater.* **2019**, *31*, 1807900.
- (996) Li, M.; Yao, W.; Liu, J.; Tian, Q.; Liu, L.; Ding, J.; Xue, Q.; Lu, Q.; Wu, W. Facile Synthesis and Screen Printing of Dual-mode Luminescent NaYF₄:Er,Yb (Tm)/carbon Dots for anti-counterfeiting applications. *J. Mater. Chem. C* **2017**, *5*, 6512–6520.
- (997) Han, Y.; Gao, C.; Wang, Y.; Ju, D.; Zhou, A.; Song, F.; Huang, L.; Huang, W. Spatially Confined Luminescence Process in Tip-modified Heterogeneous-structured Microrods for High-level anti-counterfeiting. *Phys. Chem. Chem. Phys.* **2018**, *20*, 9516–9522.
- (998) Sandhyarani, A.; Kokila, M. K.; Darshan, G. P.; Basavaraj, R. B.; Daruka Prasad, B.; Sharma, S. C.; Lakshmi, T. K. S.; Nagabhushana, H. Versatile Core-shell SiO₂@SrTiO₃:Eu³⁺, Li⁺ Nanopowders as Fluorescent Label for the Visualization of Latent Fingerprints and anti-counterfeiting applications. *Chem. Eng. J.* **2017**, *327*, 1135–1150.
- (999) Ding, M.; Dong, B.; Lu, Y.; Yang, X.; Yuan, Y.; Bai, W.; Wu, S.; Ji, Z.; Lu, C.; Zhang, K.; et al. Energy Manipulation in Lanthanide-Doped Core-Shell Nanoparticles for Tunable Dual-Mode Luminescence Toward Advanced Anti-Counterfeiting. *Adv. Mater.* **2020**, *32*, 2002121.
- (1000) Xu, J.; Zhang, B.; Jia, L.; Fan, Y.; Chen, R.; Zhu, T.; Liu, B. Dual-Mode, Color-Tunable, Lanthanide-Doped Core-Shell Nanoarchitectures for Anti-Counterfeiting Inks and Latent Fingerprint Recognition. *ACS Appl. Mater. Interfaces* **2019**, *11*, 35294–35304.
- (1001) Zhao, J.; Jin, D.; Schartner, E. P.; Lu, Y.; Liu, Y.; Zvyagin, A. V.; Zhang, L.; Dawes, J. M.; Xi, P.; Piper, J. A.; et al. Single-nanocrystal Sensitivity Achieved by Enhanced Upconversion Luminescence. *Nat. Nanotechnol.* **2013**, *8*, 729–734.
- (1002) Chen, B.; Liu, Y.; Xiao, Y.; Chen, X.; Li, Y.; Li, M.; Qiao, X.; Fan, X.; Wang, F. Amplifying Excitation-Power Sensitivity of Photon Upconversion in a NaYbF₄:Ho Nanostructure for Direct Visualization of Electromagnetic Hotspots. *J. Phys. Chem. Lett.* **2016**, *7*, 4916–4921.
- (1003) Wang, Y.; Lei, L.; Ye, R.; Jia, G.; Hua, Y.; Deng, D.; Xu, S. Integrating Positive and Negative Thermal Quenching Effect for Ultrasensitive Ratiometric Temperature Sensing and Anti-counterfeiting. *ACS Appl. Mater. Interfaces* **2021**, *13*, 23951–23959.
- (1004) Ramalho, J. F.; Correia, S. F.; Fu, L.; Dias, L. M.; Adão, P.; Mateus, P.; Ferreira, R. A. S.; André, P. S. Super Modules-based Active QR Codes for Smart Trackability and IoT: a Responsive-banknotes Case Study. *NPJ. Flexible Electronics* **2020**, *4*, 11.

- (1005) Yang, C.; Jiang, J.; Liu, X.; Yin, C.; Deng, C. Rare Earth Ions Doped Polyaniline/cobalt Ferrite Nanocomposites via a Novel Coordination-oxidative Polymerization-hydrothermal Route: Preparation and Microwave-absorbing Properties. *J. Magn. Magn. Mater.* **2016**, *404*, 45–52.
- (1006) Luo, J.; Xu, Y.; Mao, H. Magnetic and Microwave Absorption Properties of Rare Earth Ions (Sm^{3+} , Er^{3+}) Doped Strontium Ferrite and Its Nanocomposites With Polypyrrole. *J. Magn. Magn. Mater.* **2015**, *381*, 365–371.
- (1007) Guo, F.; Li, R.; Xu, J.; Zou, L.; Gan, S. Electromagnetic Properties and Microwave Absorption Enhancement of $\text{Ba}_{0.85}\text{RE}_{0.15}\text{Co}_2\text{Fe}_{16}\text{O}_{27}$ -polyaniline Composites: RE = Gd, Tb, Ho. *Colloid Polym. Sci.* **2014**, *292*, 2173–2183.
- (1008) Mang, C.; Ma, Z.; Luo, J.; Rao, M.; Zhang, X.; Peng, Z. Electromagnetic Wave Absorption Properties of Cobalt-zinc Ferrite Nanoparticles Doped With Rare Earth Elements. *J. Rare Earths* **2021**, *39*, 1415–1426.
- (1009) Chen, H.; Zhao, B.; Zhao, Z.; Xiang, H.; Dai, F.-Z.; Liu, J.; Zhou, Y. Achieving Strong Microwave Absorption Capability and Wide Absorption Bandwidth Through a Combination of High Entropy Rare Earth Silicide Carbides/Rare Earth Oxides. *J. Mater. Sci. Technol.* **2020**, *47*, 216–222.
- (1010) Gao, S.; Wang, G.-S.; Guo, L.; Yu, S.-H. Tunable and Ultraefficient Microwave Absorption Properties of Trace N-Doped Two-Dimensional Carbon-Based Nanocomposites Loaded With Multi-Rare Earth Oxides. *Small* **2020**, *16*, 1906668.
- (1011) Wei, W.; Liu, X.; Lu, W.; Zhang, H.; He, J.; Wang, H.; Hou, Y. Light-weight Gadolinium Hydroxide@polypyrrole Rare-Earth Nanocomposites With Tunable and Broadband Electromagnetic Wave Absorption. *ACS Appl. Mater. Interfaces* **2019**, *11*, 12752–12760.
- (1012) Qiao, Z.; Pan, S.; Xiong, J.; Cheng, L.; Yao, Q.; Lin, P. Magnetic and Microwave Absorption Properties of La-Nd-Fe Alloys. *J. Magn. Magn. Mater.* **2017**, *423*, 197–202.
- (1013) Li, Q.; Liu, J.; Zhao, Y.; Zhao, X.; You, W.; Li, X.; Che, R. Matryoshka Doll"-Like CeO_2 Microspheres With Hierarchical Structure To Achieve Significantly Enhanced Microwave Absorption Performance. *ACS Appl. Mater. Interfaces* **2018**, *10*, 27540–27547.
- (1014) Mitta, S. B.; Dugasani, S. R.; Reddeppa, M.; Vellampatti, S.; Gnapareddy, B.; Kim, M.-D.; Park, S. H. DNA Nanostructures Doped With Lanthanide Ions for Highly Sensitive UV Photodetectors. *Colloids Surf., B* **2019**, *175*, 212–220.
- (1015) Ghosh, S.; Chiang, W. C.; Fakhri, M. Y.; Wu, C. T.; Chen, R. S.; Chattopadhyay, S. Ultrasensitive Broadband Photodetector Using Electrostatically Conjugated MoS_2 -Upconversion Nanoparticle Nanocomposite. *Nano Energy* **2020**, *67*, 104258.
- (1016) Kwon, S. J.; Lee, G. Y.; Jung, K.; Jang, H. S.; Park, J.-S.; Ju, H.; Han, I. K.; Ko, H. A Plasmonic Platform With Disordered Array of Metal Nanoparticles for Three-Order Enhanced Upconversion Luminescence and Highly Sensitive Near-Infrared Photodetector. *Adv. Mater.* **2016**, *28*, 7899–7909.
- (1017) Zhang, X.; Yang, S.; Zhou, H.; Liang, J.; Liu, H.; Xia, H.; Zhu, X.; Jiang, Y.; Zhang, Q.; Hu, W.; et al. Perovskite–Erbium Silicate Nanosheet Hybrid Waveguide Photodetectors at the Near-Infrared Telecommunication Band. *Adv. Mater.* **2017**, *29*, 1604431.
- (1018) Huang, X.; Han, S.; Huang, W.; Liu, X. Enhancing Solar Cell Efficiency: the Search for Luminescent Materials as Spectral Converters. *Chem. Soc. Rev.* **2013**, *42*, 173–201.
- (1019) Nadort, A.; Zhao, J.; Goldys, E. M. Lanthanide Upconversion Luminescence at the Nanoscale: Fundamentals and Optical Properties. *Nanoscale* **2016**, *8*, 13099–13130.
- (1020) Niu, W.; Chen, H.; Chen, R.; Huang, J.; Palaniappan, A.; Sun, H.; Liedberg, B. G.; Tok, A. I. Y. Synergetically Enhanced Near-Infrared Photoresponse of Reduced Graphene Oxide by Upconversion and Gold Plasmon. *Small* **2014**, *10*, 3637–3643.
- (1021) Ding, N.; Xu, W.; Zhou, D.; Pan, G.; Li, D.; Ji, Y.; Chen, X.; Yang, D.; Bai, X.; Ma, C.-G.; et al. Upconversion Ladder Enabled Super-sensitive Narrowband Near-Infrared Photodetectors Based on Rare Earth Doped Fluorine Perovskite Nanocrystals. *Nano Energy* **2020**, *76*, 105103.
- (1022) Kataria, M.; Yadav, K.; Cai, S.-Y.; Liao, Y.-M.; Lin, H.-I.; Shen, T. L.; Chen, Y.-H.; Chen, Y.-T.; Wang, W.-H.; Chen, Y.-F. Highly Sensitive, Visible Blind, Wearable, and Omnidirectional Near-Infrared Photodetectors. *ACS Nano* **2018**, *12*, 9596–9607.
- (1023) Zhao, X.; Song, L.; Zhao, R.; Tan, M. C. High-Performance and Flexible Shortwave Infrared Photodetectors Using Composites of Rare Earth-Doped Nanoparticles. *ACS Appl. Mater. Interfaces* **2019**, *11*, 2344–2351.
- (1024) Shkir, M.; Ashraf, I. M.; Khan, A.; Khan, M. T.; El-Toni, A. M.; AlFaify, S. A Facile Spray Pyrolysis Fabrication of Sm:CdS Thin Films for High-Performance Photodetector Applications. *Sens. Actuators, A* **2020**, *306*, 111952.
- (1025) Babamoradi, M.; Sadeghi, H.; Azimirad, R.; Safa, S. Enhancing Photoresponsivity of Ultraviolet Photodetectors Based on ZnO/ZnO:Eu ($x = 0, 0.2, 1, 5$ and 20 at.%) Core/Shell Nanorods. *Optik* **2018**, *167*, 88–94.
- (1026) Mondal, S.; Ghosh, A.; Piton, M. R.; Gomes, J. P.; Felix, J. F.; Gobato, Y. G.; Galeti, H. V. A.; Choudhuri, B.; Dhar Dwivedi, S. M. M.; Henini, M.; Mondal, A.; et al. Investigation of Optical and Electrical Properties of Erbium-doped TiO_2 Thin Films for Photodetector Applications. *J. Mater. Sci.: Mater. El.* **2018**, *29*, 19588–19600.
- (1027) Hsu, C.-L.; Wu, H.-Y.; Fang, C.-C.; Chang, S.-P. Solution-Processed UV and Visible Photodetectors Based on Y-Doped ZnO Nanowires With TiO_2 Nanosheets and Au Nanoparticles. *ACS Appl. Energy Mater.* **2018**, *1*, 2087–2095.
- (1028) Shkir, M.; Ashraf, I. M.; Chandekar, K. V.; Yahia, I. S.; Khan, A.; Algarni, H.; AlFaify, S. A Significant Enhancement in Visible-light Photodetection Properties of Chemical Spray Pyrolysis Fabricated CdS Thin Films by Novel Eu Doping Concentrations. *Sens. Actuators, A* **2020**, *301*, 111749.
- (1029) Seferis, I. E.; Zeler, J.; Michail, C.; Valais, I.; Fountos, G.; Kalyvas, N.; Bakas, A.; Kandarakis, I.; Zych, E. On the Response of Semitransparent Nanoparticulated Films of LuPO_4 :Eu in Polyenergetic X-ray Imaging Applications. *Appl. Phys. A: Mater. Sci. Process.* **2016**, *122*, 526.
- (1030) Kumar, V.; Luo, Z. A Review on X-ray Excited Emission Decay Dynamics in Inorganic Scintillator Materials. *Photonics* **2021**, *8*, 71.
- (1031) Gupta, S. K.; Zuniga, J. P.; Abdou, M.; Thomas, M. P.; De Alwis Goonatilake, M.; Guiton, B. S.; Mao, Y. Lanthanide-doped Lanthanum Hafnate Nanoparticles as Multicolor Phosphors for Warm White Lighting and Scintillators. *Chem. Eng. J.* **2020**, *379*, 122314.
- (1032) Sen, S.; Tyagi, M.; Sharma, K.; Sarkar, P. S.; Sarkar, S.; Basak, C. B.; Pitale, S.; Ghosh, M.; Gadkari, S. C. Organic–Inorganic Composite Films Based on $\text{Gd}_3\text{Ga}_3\text{Al}_2\text{O}_{12}$:Ce Scintillator Nanoparticles for X-ray Imaging Applications. *ACS Appl. Mater. Interfaces* **2017**, *9*, 37310–37320.
- (1033) Sedov, V.; Kouznetsov, S.; Martyanov, A.; Proydakova, V.; Ralchenko, V.; Khomich, A.; Voronov, V.; Batygov, S.; Kamenskikh, I.; Spassky, D.; et al. Diamond–Rare Earth Composites With Embedded NaGdF_4 :Eu Nanoparticles as Robust Photo- and X-ray-Luminescent Materials for Radiation Monitoring Screens. *ACS Appl. Nano Mater.* **2020**, *3*, 1324–1331.
- (1034) Lee, G.; Struebing, C.; Wagner, B.; Summers, C.; Ding, Y.; Bryant, A.; Thadhani, N.; Shedlock, D.; Star-Lack, J.; Kang, Z. Synthesis and Characterization of a BaGdF_5 :Tb Glass Ceramic as a Nanocomposite Scintillator for X-ray Imaging. *Nanotechnology* **2016**, *27*, 205203.
- (1035) Chen, W.; Cao, J.; Hu, F.; Wei, R.; Chen, L.; Sun, X.; Guo, H. Highly Efficient $\text{Na}_5\text{Gd}_9\text{F}_{32}$:Tb $^{3+}$ Glass Ceramic as Nanocomposite Scintillator for X-ray Imaging. *Opt. Mater. Express* **2018**, *8*, 41–49.
- (1036) Cai, T.; Wang, J.; Li, W.; Hills-Kimball, K.; Yang, H.; Nagaoka, Y.; Yuan, Y.; Zia, R.; Chen, O. Mn $^{2+}$ /Yb $^{3+}$ Codoped CsPbCl $_3$ Perovskite Nanocrystals With Triple-Wavelength Emission for Luminescent Solar Concentrators. *Adv. Sci.* **2020**, *7*, 2001317.

- (1037) Liu, Q.; Liu, H.; Li, D.; Qiao, W.; Chen, G.; Ågren, H. Microlens Array Enhanced Upconversion Luminescence at Low Excitation Irradiance. *Nanoscale* **2019**, *11*, 14070–14078.
- (1038) van der Ende, B. M.; Aarts, L.; Meijerink, A. Lanthanide Ions as Spectral Converters for Solar Cells. *Phys. Chem. Chem. Phys.* **2009**, *11*, 11081–11095.
- (1039) Chander, N.; Khan, A. F.; Chandrasekhar, P. S.; Thouti, E.; Swami, S. K.; Dutta, V.; Komarala, V. K. Reduced Ultraviolet Light Induced Degradation and Enhanced Light Harvesting Using $\text{YVO}_4:\text{Eu}^{3+}$ Down-shifting Nano-phosphor Layer in Organometal Halide Perovskite Solar Cells. *Appl. Phys. Lett.* **2014**, *105*, 033904.
- (1040) Kumar, V.; Swami, S. K.; Kumar, A.; Ntwaeaborwa, O. M.; Dutta, V.; Swart, H. C. Eu^{3+} Doped Down Shifting TiO_2 Layer for Efficient Dye-Sensitized Solar Cells. *J. Colloid Interface Sci.* **2016**, *484*, 24–32.
- (1041) Jiang, L.; Zheng, J.; Chen, W.; Huang, Y.; Hu, L.; Hayat, T.; Alsaedi, A.; Zhang, C.; Dai, S. High-Performance Perovskite Solar Cells With a Weak Covalent $\text{TiO}_2:\text{Eu}^{3+}$ Mesoporous Structure. *ACS Appl. Energy Mater.* **2018**, *1*, 93–102.
- (1042) Jin, J.; Li, H.; Chen, C.; Zhang, B.; Bi, W.; Song, Z.; Xu, L.; Dong, B.; Song, H.; Dai, Q. Improving Efficiency and Light Stability of Perovskite Solar Cells by Incorporating $\text{YVO}_4:\text{Eu}^{3+}$, Bi^{3+} Nanophosphor into the Mesoporous TiO_2 Layer. *ACS Appl. Energy Mater.* **2018**, *1*, 2096–2102.
- (1043) Chander, N.; Khan, A. F.; Komarala, V. K. Improved Stability and Enhanced Efficiency of Dye Sensitized Solar Cells by Using Europium Doped Yttrium Vanadate Down-shifting Nanophosphor. *RSC Adv.* **2015**, *5*, 66057–66066.
- (1044) Sun, T.; Chen, X.; Jin, L.; Li, H.-W.; Chen, B.; Fan, B.; Moine, B.; Qiao, X.; Fan, X.; Tsang, S.-W.; et al. Broadband Ce(III)-Sensitized Quantum Cutting in Core-Shell Nanoparticles: Mechanistic Investigation and Photovoltaic Application. *J. Phys. Chem. Lett.* **2017**, *8*, 5099–5104.
- (1045) Shao, W.; Lim, C.-K.; Li, Q.; Swihart, M. T.; Prasad, P. N. Dramatic Enhancement of Quantum Cutting in Lanthanide-Doped Nanocrystals Photosensitized With an Aggregation-Induced Enhanced Emission Dye. *Nano Lett.* **2018**, *18*, 4922–4926.
- (1046) Liu, W.; Zhang, J.; Hao, Z.; Xiang, G.; Zhang, L.; Zhang, X.; Pan, G.; Luo, Y.; Zhao, H.; Wu, H. Near-infrared Quantum Cutting and Energy Transfer Mechanism in $\text{Lu}_2\text{O}_3:\text{Tm}^{3+}/\text{Yb}^{3+}$ Phosphor for High-efficiency Photovoltaics. *J. Mater. Sci.: Mater. El.* **2017**, *28*, 8017–8022.
- (1047) Erickson, C. S.; Crane, M. J.; Milstein, T. J.; Gamelin, D. R. Photoluminescence Saturation in Quantum-Cutting Yb^{3+} -Doped $\text{CsPb}(\text{Cl}_{1-x}\text{Br}_x)_3$ Perovskite Nanocrystals: Implications for Solar Downconversion. *J. Phys. Chem. C* **2019**, *123*, 12474–12484.
- (1048) de Jong, M.; Meijerink, A.; Rabouw, F. T. Non-Poissonian Photon Statistics From Macroscopic Photon Cutting Materials. *Nat. Commun.* **2017**, *8*, 15537.
- (1049) Zhou, D.; Liu, D.; Jin, J.; Chen, X.; Xu, W.; Yin, Z.; Pan, G.; Li, D.; Song, H. Semiconductor Plasmon-Sensitized Broadband Upconversion and Its Enhancement Effect on the Power Conversion Efficiency of Perovskite Solar Cells. *J. Mater. Chem. A* **2017**, *5*, 16559–16567.
- (1050) Meng, F.; Luo, Y.; Zhou, Y.; Zhang, J.; Zheng, Y.; Cao, G.; Tao, X. Integrated Plasmonic and Upconversion Starlike $\text{Y}_2\text{O}_3:\text{Er}/\text{Au}@/\text{TiO}_2$ Composite for Enhanced Photon Harvesting in Dye-sensitized Solar Cells. *J. Power Sources* **2016**, *316*, 207–214.
- (1051) Meng, F.-L.; Wu, J.-J.; Zhao, E.-F.; Zheng, Y.-Z.; Huang, M.-L.; Dai, L.-M.; Tao, X.; Chen, J.-F. High-efficiency Near-infrared Enabled Planar Perovskite Solar Cells by Embedding Upconversion Nanocrystals. *Nanoscale* **2017**, *9*, 18535–18545.
- (1052) Guo, Q.; Wu, J.; Yang, Y.; Liu, X.; Jia, J.; Dong, J.; Lan, Z.; Lin, J.; Huang, M.; Wei, Y.; et al. High Performance Perovskite Solar Cells Based on $\beta\text{-NaYF}_4:\text{Yb}^{3+}/\text{Er}^{3+}/\text{Sc}^{3+}@/\text{NaYF}_4$ Core-shell Upconversion Nanoparticles. *J. Power Sources* **2019**, *426*, 178–187.
- (1053) Roh, J.; Yu, H.; Jang, J. Hexagonal $\beta\text{-NaYF}_4:\text{Yb}^{3+}$, Er^{3+} Nanoprisim-Incorporated Upconverting Layer in Perovskite Solar Cells for Near-Infrared Sunlight Harvesting. *ACS Appl. Mater. Interfaces* **2016**, *8*, 19847–19852.
- (1054) He, M.; Pang, X.; Liu, X.; Jiang, B.; He, Y.; Snaith, H.; Lin, Z. Monodisperse Dual-Functional Upconversion Nanoparticles Enabled Near-Infrared Organolead Halide Perovskite Solar Cells. *Angew. Chem.* **2016**, *128*, 4352–4356.
- (1055) Luoshan, M.; Bai, L.; Bu, C.; Liu, X.; Zhu, Y.; Guo, K.; Jiang, R.; Li, M.; Zhao, X. Surface Plasmon Resonance Enhanced Multi-shell-modified Upconversion $\text{NaYF}_4:\text{Yb}^{3+}$, $\text{Er}^{3+}@/\text{SiO}_2@/\text{Au}@/\text{TiO}_2$ Crystallites for Dye-sensitized Solar Cells. *J. Power Sources* **2016**, *307*, 468–473.
- (1056) Zhou, Z.; Wang, J.; Nan, F.; Bu, C.; Yu, Z.; Liu, W.; Guo, S.; Hu, H.; Zhao, X.-Z. Upconversion Induced Enhancement of Dye Sensitized Solar Cells Based on Core-shell Structured $\beta\text{-NaYF}_4:\text{Er}^{3+}$, $\text{Yb}^{3+}@/\text{SiO}_2$ Nanoparticles. *Nanoscale* **2014**, *6*, 2052–2055.
- (1057) Chen, X.; Xu, W.; Song, H.; Chen, C.; Xia, H.; Zhu, Y.; Zhou, D.; Cui, S.; Dai, Q.; Zhang, J. Highly Efficient $\text{LiYF}_4:\text{Yb}^{3+}$, Er^{3+} Upconversion Single Crystal Under Solar Cell Spectrum Excitation and Photovoltaic Application. *ACS Appl. Mater. Interfaces* **2016**, *8*, 9071–9079.
- (1058) Bai, J.; Zhao, R.; Han, G.; Li, Z.; Diao, G. Synthesis of 1D Upconversion $\text{CeO}_2:\text{Er}$, Yb Nanofibers via Electrospinning and Their Performance in Dye-sensitized Solar Cells. *RSC Adv.* **2015**, *5*, 43328–43333.
- (1059) Bai, J.; Duan, P.; Wang, X.; Han, G.; Wang, M.; Diao, G. Upconversion Luminescence Enhancement by Fe^{3+} Doping in $\text{CeO}_2:\text{Yb}/\text{Er}$ Nanomaterials and Their Application in Dye-sensitized Solar Cells. *RSC Adv.* **2020**, *10*, 18868–18874.
- (1060) Luitel, H. N.; Mizuno, S.; Tani, T.; Takeda, Y. Broadband-sensitive $\text{Ni}^{2+}-\text{Er}^{3+}$ Based Upconverters for Crystalline Silicon Solar Cells. *RSC Adv.* **2016**, *6*, 55499–55506.
- (1061) Bi, W.; Wu, Y.; Chen, C.; Zhou, D.; Song, Z.; Li, D.; Chen, G.; Dai, Q.; Zhu, Y.; Song, H. Dye Sensitization and Local Surface Plasmon Resonance-Enhanced Upconversion Luminescence for Efficient Perovskite Solar Cells. *ACS Appl. Mater. Interfaces* **2020**, *12*, 24737–24746.
- (1062) Hao, S.; Shang, Y.; Li, D.; Ågren, H.; Yang, C.; Chen, G. Enhancing Dye-sensitized Solar Cell Efficiency Through Broadband Near-infrared Upconverting Nanoparticles. *Nanoscale* **2017**, *9*, 6711–6715.
- (1063) Yu, J.; Yang, Y.; Fan, R.; Wang, P.; Dong, Y. Enhanced Photovoltaic Performance of Dye-sensitized Solar Cells Using a New Photoelectrode Material: Upconversion $\text{YbF}_3\text{-Ho}/\text{TiO}_2$ Nanoheterostructures. *Nanoscale* **2016**, *8*, 4173–4180.
- (1064) Li, Y.; Zhao, L.; Xiao, M.; Huang, Y.; Dong, B.; Xu, Z.; Wan, L.; Li, W.; Wang, S. Synergic Effects of Upconversion Nanoparticles $\text{NaYbF}_4:\text{Ho}^{3+}$ and ZrO_2 Enhanced the Efficiency in Hole-conductor-free Perovskite Solar Cells. *Nanoscale* **2018**, *10*, 22003–22011.
- (1065) Lee, S.-M.; Dhar, P.; Chen, H.; Montenegro, A.; Liaw, L.; Kang, D.; Gai, B.; Benderskii, A. V.; Yoon, J. Synergistically Enhanced Performance of Ultrathin Nanostructured Silicon Solar Cells Embedded in Plasmonically Assisted, Multispectral Luminescent Waveguides. *ACS Nano* **2017**, *11*, 4077–4085.
- (1066) Shao, W.; Chen, G.; Ohulchanskyy, T. Y.; Yang, C.; Ågren, H.; Prasad, P. N. A Core-multiple Shell Nanostructure Enabling Concurrent Upconversion and Quantum Cutting for Photon Management. *Nanoscale* **2017**, *9*, 1934–1941.
- (1067) de la Mora, M. B.; Amelines-Sarria, O.; Monroy, B. M.; Hernández-Pérez, C. D.; Lugo, J. E. Materials for Downconversion in Solar Cells: Perspectives and Challenges. *Sol. Energy Mater. Sol. Cells* **2017**, *165*, 59–71.
- (1068) Trupke, T.; Green, M. A.; Würfel, P. Improving Solar Cell Efficiencies by Down-conversion of High-energy Photons. *J. Appl. Phys.* **2002**, *92*, 1668–1674.
- (1069) Eilers, J. J.; Biner, D.; van Wijngaarden, J. T.; Krämer, K.; Güdel, H. U.; Meijerink, A. Efficient Visible to Infrared Quantum Cutting Through Downconversion With the $\text{Er}^{3+}-\text{Yb}^{3+}$ Couple in $\text{Cs}_3\text{Y}_2\text{Br}_9$. *Appl. Phys. Lett.* **2010**, *96*, 151106.

- (1070) Gao, G.; Wondraczek, L. Near-infrared Down-conversion in Mn^{2+} - Yb^{3+} Co-doped Zn_2GeO_4 . *J. Mater. Chem. C* **2013**, *1*, 1952–1958.
- (1071) Deng, K.; Gong, T.; Hu, L.; Wei, X.; Chen, Y.; Yin, M. Efficient Near-infrared Quantum Cutting in NaYF_4 : Ho^{3+} , Yb^{3+} for Solar Photovoltaics. *Opt. Express* **2011**, *19*, 1749–1754.
- (1072) Yu, D.-C.; Martín-Rodríguez, R.; Zhang, Q.-Y.; Meijerink, A.; Rabouw, F. T. Multi-photon Quantum Cutting in Gd_2O_3 : Tm^{3+} to Enhance the Photo-response of Solar Cells. *Light: Sci. Appl.* **2015**, *4*, No. e344.
- (1073) Xu, Y.; Zhang, X.; Dai, S.; Fan, B.; Ma, H.; Adam, J.-I.; Ren, J.; Chen, G. Efficient Near-Infrared Down-Conversion in Pr^{3+} - Yb^{3+} Codoped Glasses and Glass Ceramics Containing LaF_3 Nanocrystals. *J. Phys. Chem. C* **2011**, *115*, 13056–13062.
- (1074) An, Y.-T.; Labbé, C.; Cardin, J.; Morales, M.; Goubilleau, F. Highly Efficient Infrared Quantum Cutting in Tb^{3+} - Yb^{3+} Codoped Silicon Oxynitride for Solar Cell Applications. *Adv. Opt. Mater.* **2013**, *1*, 855–862.
- (1075) Jia, J.; Dong, J.; Lin, J.; Lan, Z.; Fan, L.; Wu, J. Improved Photovoltaic Performance of Perovskite Solar Cells by Utilizing Down-conversion NaYF_4 : Eu^{3+} Nanophosphors. *J. Mater. Chem. C* **2019**, *7*, 937–942.
- (1076) Santana-Alonso, A.; Yanes, A. C.; Méndez-Ramos, J.; del-Castillo, J.; Rodríguez, V. D. Down-shifting by Energy Transfer in Dy^{3+} - Tb^{3+} Co-doped YF_3 -based Sol-gel Nano-glass-ceramics for Photovoltaic Applications. *Opt. Mater.* **2011**, *33*, 587–591.
- (1077) Li, Q.; Lin, J.; Wu, J.; Lan, Z.; Wang, Y.; Peng, F.; Huang, M. Improving Photovoltaic Performance of Dye-sensitized Solar Cell by Downshift Luminescence and P-doping Effect of Gd_2O_3 : Sm^{3+} . *J. Lumin.* **2013**, *134*, 59–62.
- (1078) Lee, K.-T.; Park, J.-H.; Kwon, S. J.; Kwon, H.-K.; Kyhm, J.; Kwak, K.-W.; Jang, H. S.; Kim, S. Y.; Han, J. S.; Lee, S.-H.; et al. Simultaneous Enhancement of Upconversion and Downshifting Luminescence via Plasmonic Structure. *Nano Lett.* **2015**, *15*, 2491–2497.
- (1079) Alexandre, M.; Chapa, M.; Haque, S.; Mendes, M. J.; Águas, H.; Fortunato, E.; Martins, R. Optimum Luminescent Down-Shifting Properties for High Efficiency and Stable Perovskite Solar Cells. *ACS Appl. Energy Mater.* **2019**, *2*, 2930–2938.
- (1080) Correia, S. F. H.; de Zea Bermudez, V.; Ribeiro, S. J. L.; André, P. S.; Ferreira, R. A. S.; Carlos, L. D. Luminescent Solar Concentrators: Challenges for Lanthanide-based Organic–inorganic Hybrid Materials. *J. Mater. Chem. A* **2014**, *2*, 5580–5596.
- (1081) Shalav, A.; Richards, B. S.; Trupke, T.; Krämer, K. W.; Güdel, H. U. Application of NaYF_4 : Er^{3+} Up-converting Phosphors for Enhanced Near-infrared Silicon Solar Cell Response. *Appl. Phys. Lett.* **2005**, *86*, 013505.
- (1082) Martín-Rodríguez, R.; Fischer, S.; Ivaturi, A.; Froehlich, B.; Krämer, K. W.; Goldschmidt, J. C.; Richards, B. S.; Meijerink, A. Highly Efficient IR to NIR Upconversion in Gd_2O_3 : Er^{3+} for Photovoltaic Applications. *Chem. Mater.* **2013**, *25*, 1912–1921.
- (1083) Shan, G.-B.; Demopoulos, G. P. Near-Infrared Sunlight Harvesting in Dye-Sensitized Solar Cells Via the Insertion of an Upconverter- TiO_2 Nanocomposite Layer. *Adv. Mater.* **2010**, *22*, 4373–4377.
- (1084) Shan, G.-B.; Assaoudi, H.; Demopoulos, G. P. Enhanced Performance of Dye-Sensitized Solar Cells by Utilization of an External, Bifunctional Layer Consisting of Uniform β - NaYF_4 : Er^{3+} / Yb^{3+} Nanoplatelets. *ACS Appl. Mater. Interfaces* **2011**, *3*, 3239–3243.
- (1085) Zou, W.; Visser, C.; Maduro, J. A.; Pshenichnikov, M. S.; Hummelen, J. C. Broadband Dye-sensitized Upconversion of Near-infrared Light. *Nat. Photonics* **2012**, *6*, 560–564.
- (1086) Shen, B.; Yu, C.; Baker, A. A.; McCall, S. K.; Yu, Y.; Su, D.; Yin, Z.; Liu, H.; Li, J.; Sun, S. Chemical Synthesis of Magnetically Hard and Strong Rare Earth Metal Based Nanomagnets. *Angew. Chem., Int. Ed.* **2019**, *58*, 602–606.
- (1087) Lee, J.; Kim, J.; Kim, D.; Lee, G.; Oh, Y.-B.; Hwang, T.-Y.; Lim, J.-H.; Cho, H.-B.; Kim, J.; Choa, Y.-H. Exchange-Coupling Interaction in Zero- and One-Dimensional $\text{Sm}_2\text{Co}_{17}$ / FeCo Core-Shell Nanomagnets. *ACS Appl. Mater. Interfaces* **2019**, *11*, 26222–26227.
- (1088) Liu, Y.; Wang, D.; Shi, J.; Peng, Q.; Li, Y. Magnetic Tuning of Upconversion Luminescence in Lanthanide-Doped Bifunctional Nanocrystals. *Angew. Chem.* **2013**, *125*, 4462–4465.
- (1089) Reddy, L. H.; Arias, J. L.; Nicolas, J.; Couvreur, P. Magnetic Nanoparticles: Design and Characterization, Toxicity and Biocompatibility, Pharmaceutical and Biomedical Applications. *Chem. Rev.* **2012**, *112*, 5818–5878.
- (1090) Wu, L.; Mendoza-Garcia, A.; Li, Q.; Sun, S. Organic Phase Syntheses of Magnetic Nanoparticles and Their Applications. *Chem. Rev.* **2016**, *116*, 10473–10512.
- (1091) De Silva, C. R.; Smith, S.; Shim, I.; Pyun, J.; Gutu, T.; Jiao, J.; Zheng, Z. Lanthanide(III)-Doped Magnetite Nanoparticles. *J. Am. Chem. Soc.* **2009**, *131*, 6336–6337.
- (1092) Aghazadeh, M.; Ganjali, M. R. Samarium-doped Fe_3O_4 Nanoparticles With Improved Magnetic and Supercapacitive Performance: a Novel Preparation Strategy and Characterization. *J. Mater. Sci.* **2018**, *53*, 295–308.
- (1093) Wang, L.; Wang, J.; Wang, Z.; He, C.; Lyu, W.; Yan, W.; Yang, L. Enhanced Antimonate (Sb(V)) Removal From Aqueous Solution by La-doped Magnetic Biochars. *Chem. Eng. J.* **2018**, *354*, 623–632.
- (1094) Qi, Z.; Joshi, T. P.; Liu, R.; Liu, H.; Qu, J. Synthesis of Ce(III)-doped Fe_3O_4 Magnetic Particles for Efficient Removal of Antimony From Aqueous Solution. *J. Hazard. Mater.* **2017**, *329*, 193–204.
- (1095) Zhang, H.; Peng, S.; Rong, C.-b.; Liu, J. P.; Zhang, Y.; Kramer, M. J.; Sun, S. Chemical Synthesis of Hard Magnetic SmCo Nanoparticles. *J. Mater. Chem.* **2011**, *21*, 16873–16876.
- (1096) Shen, B.; Yu, C.; Su, D.; Yin, Z.; Li, J.; Xi, Z.; Sun, S. A New Strategy to Synthesize Anisotropic SmCo_5 Nanomagnets. *Nanoscale* **2018**, *10*, 8735–8740.
- (1097) Wu, Q.; Cong, L.; Yue, M.; Li, C.; Ma, Z.; Ma, X.; Wang, Y. A Unique Synthesis of Rare-earth-Co-based Single Crystal Particles by “Self-aligned” Co Nano-arrays. *Nanoscale* **2020**, *12*, 13958–13963.
- (1098) Dai, G.; Zhong, Z.; Wu, X.; Zhan, S.; Hu, S.; Hu, P.; Hu, J.; Wu, S.; Han, J.; Liu, Y. Magnetic Tuning of Upconversion Luminescence in Au/NaGdF_4 : $\text{Yb}^{3+}/\text{Er}^{3+}$ Nanocomposite. *Nanotechnology* **2017**, *28*, 155702.
- (1099) Freysoldt, C.; Grabowski, B.; Hickel, T.; Neugebauer, J.; Kresse, G.; Janotti, A.; Van De Walle, C. G. First-Principles Calculations for Point Defects in Solids. *Rev. Mod. Phys.* **2014**, *86*, 253–305.
- (1100) Liu, X.; Yi, Z.; Qin, X.; Liu, H.; Huang, W.; Liu, X. Tuning Long-Lived Mn(II) Upconversion Luminescence through Alkaline-Earth Metal Doping and Energy-Level Tailoring. *Adv. Opt. Mater.* **2019**, *7*, 1900519.
- (1101) Lou, B.; Wen, J.; Ning, L.; Yin, M.; Ma, C.; Duan, C. Understanding the defect levels and photoluminescence in a series of bismuth-doped perovskite oxides: First-principles study. *Phys. Rev. B: Condens. Matter Phys.* **2021**, *104*, 115101.
- (1102) Yao, G.; Berry, M. T.; May, P. S.; Kilin, D. DFT Calculation of Russell-Saunders Splitting for Lanthanide Ions Doped in Hexagonal (β)- NaYF_4 Nanocrystals. *J. Phys. Chem. C* **2013**, *117*, 17177–17185.
- (1103) Wang, Z.; Chu, I. H.; Zhou, F.; Ong, S. P. Electronic Structure Descriptor for the Discovery of Narrow-Band Red-Emitting Phosphors. *Chem. Mater.* **2016**, *28*, 4024–4031.
- (1104) Xu, H.; Han, S.; Deng, R.; Su, Q.; Wei, Y.; Tang, Y.; Qin, X.; Liu, X. Anomalous Upconversion Amplification Induced by Surface Reconstruction in Lanthanide Sublattices. *Nat. Photonics* **2021**, *15*, 732–737.
- (1105) Qin, X.; Liu, X.; Huang, W.; Bettinelli, M.; Liu, X. Lanthanide-Activated Phosphors Based on 4f-5d Optical Transitions: Theoretical and Experimental Aspects. *Chem. Rev.* **2017**, *117*, 4488–4527.

(1106) Zhou, J.; Huang, B.; Yan, Z.; Bünzli, J. C. G. Emerging Role of Machine Learning in Light-Matter Interaction. *Light Sci. Appl.* **2019**, *8*, 84.

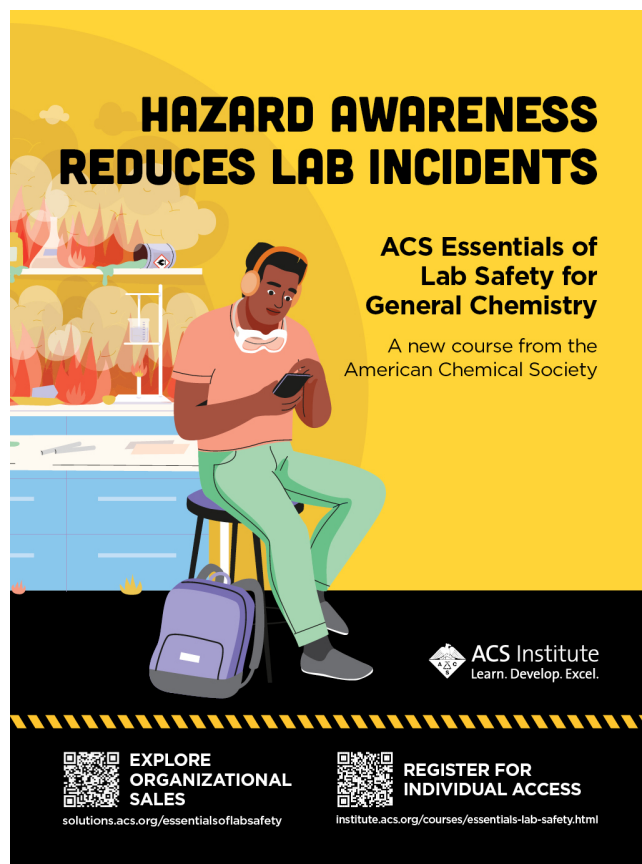
(1107) Schmidt, J.; Marques, M. R. G.; Botti, S.; Marques, M. A. L. Recent Advances and Applications of Machine Learning in Solid-State Materials Science. *npj Comput. Mater.* **2019**, *5*, 83.

(1108) Huang, B.; von Lilienfeld, O. A. Quantum Machine Learning Using Atom-in-Molecule-Based Fragments Selected on the Fly. *Nat. Chem.* **2020**, *12*, 945–951.

(1109) Genty, G.; Salmela, L.; Dudley, J. M.; Brunner, D.; Kokhanovskiy, A.; Kobtsev, S.; Turitsyn, S. K. Machine Learning and Applications in Ultrafast Photonics. *Nat. Photonics* **2021**, *15*, 91–101.

(1110) Yi, Z.; Gao, H.; Ji, X.; Yeo, X.; Chong, S. Y.; Mao, Y.; Luo, B.; Shen, C.; Han, S.; Wang, J.; et al. Mapping Drug-Induced Neuropathy through In-Situ Motor Protein Tracking and Machine Learning. *J. Am. Chem. Soc.* **2021**, *143*, 14907–14915.

(1111) Han, S.; Deng, R.; Gu, Q.; Ni, L.; Huynh, U.; Zhang, J.; Yi, Z.; Zhao, B.; Tamura, H.; Pershin, A.; et al. Lanthanide-doped Inorganic Nanoparticles Turn Molecular Triplet Excitons Bright. *Nature* **2020**, *587*, 594–599.



HAZARD AWARENESS REDUCES LAB INCIDENTS

**ACS Essentials of
Lab Safety for
General Chemistry**

A new course from the
American Chemical Society

ACS Institute
Learn. Develop. Excel.

EXPLORE
ORGANIZATIONAL
SALES
solutions.acs.org/essentialsoflabsafety

REGISTER FOR
INDIVIDUAL ACCESS
institute.acs.org/courses/essentials-lab-safety.html